

# **Experimental study of gaseous heat transfer in microchannels with integrated temperature sensors**

zur Erlangung des akademischen Grades eines  
DOKTORS DER INGENIEURWISSENSCHAFTEN (Dr.-Ing.)

der Fakultät für Chemieingenieurwesen und Verfahrenstechnik des  
Karlsruher Instituts für Technologie (KIT)

genehmigte  
DISSERTATION

von  
Msc Alice Vittoriosi  
aus Arezzo, Italien

Referent: Prof. Dr.-Ing. Roland Dittmeyer

Korreferent: Prof. Dr.-Ing. Stéphane Colin

Korreferent: Prof. Dr.-Ing. Karlheinz Schaber

Tag der mündlichen Prüfung: 26.09.2012





# Abstract

Thanks to the recent technological advances of micro- and nano-machining, the miniaturization of mechanical and electrical devices has become a common procedure to achieve process intensification and efficiency enhancement. To answer the increasing need of reliable experimental data for flows in microstructured devices, two different techniques for integrating temperature sensors in microchannels have been developed, compared and characterized. The two designs rely on different measuring principles, the first deriving directly from IC fabrication techniques and the second being based on conventional commercial sensors. Both offer an insight in microchannel heat transfer. The main feature of the proposed experimental approach is the flexibility towards different applications, overcoming the traditional material limitations of microelectronics derived sensors and allowing the employment of exchangeable microchannel sections. To validate the integrated sensor systems, heat transfer of gases in a single microchannel was chosen as study case. Different tests were undertaken to characterize the measuring systems and highlight the main features of each approach. Moreover, different microchannel materials were tested to study the effects of the surface characteristics on the heat transfer processes at microscales. Finally, the obtained experimental data were compared with CFD simulations. The results were in good agreement. Whereas conventional sensors result in simpler and more robust technologies, IC-based sensors offer higher sensitivities and potentials (e.g. for particular flow regimes, such as rarefied gases, where very small quantities are to be measured). However, silicon microsensors are also very fragile, can only stand limited working conditions and need further design optimization. The present work can be considered as a step toward the full integration of sensors in microfluidic devices and the achievement of online processes control in micro devices.



# Zusammenfassung

Die technologischen Fortschritte der letzten Zeit im Bereich der Mikro- und Nanofertigung haben die erfolgreiche Miniaturisierung von mechanischen und elektromechanischen Bauelementen zu einer Alltäglichkeit werden lassen. Diese miniaturisierten Einheiten erlauben höhere Effizienz und eine Intensivierung der Prozesse innerhalb von Mikrostrukturapparaten. Gleichzeitig steigt jedoch der Bedarf an präzisen experimentellen Daten zur Beschreibung des fluidischen Verhaltens von Flüssigkeiten und Gasen innerhalb von Mikrostrukturen. In der vorliegenden Arbeit wird die Entwicklung zweier unterschiedlicher Möglichkeiten zur Integration von Sensoren in mikrostrukturierte Systeme beschrieben. Die charakteristischen Eigenschaften der Sensoren werden aufgezeigt und verglichen. Die beiden Ansätze basieren auf unterschiedlichen Messprinzipien. Zum einen werden die genannten Sensoren mit aus der Halbleitertechnik bekannten Herstellungsprozessen gefertigt, zum anderen werden kommerzielle erhältliche, jedoch miniaturisierte Sensorelemente in einem speziellen Aufbau verwendet. Mit beiden Systemen ist die Charakterisierung der Wärmeübertragung innerhalb von Mikrokanalanordnungen möglich. Der entscheidende Vorteil des in dieser Arbeit vorgestellten Messsystems ist seine Flexibilität in Bezug auf die unterschiedlichsten Anwendungen. Hiermit werden die Materialgrenzen der klassischen Siliziumtechnik umgangen und die Anwendung austauschbarer Mikrostrukturen aus unterschiedlichen Materialien möglich. Um das Potential der entwickelten Sensortechnologie zu evaluieren wurde der Wärmeübergang in Gasströmungen innerhalb eines einzelnen Mikrokanals als Beispielprozess verwendet. Mit unterschiedlichen Testbedingungen wurden die Sensorsysteme erprobt und ihre Leistungsfähigkeit ermittelt. Darüberhinaus wurden unterschiedliche Materialien mit integrierten Mikrokanälen getestet. Auf diese Weise konnte der Einfluß des Materials und der Oberflächenbeschaffenheit auf den Wärmeübergang an den Gasstrom ermittelt werden. Die experimentellen Ergebnisse wurden mit Ergebnissen aus CFD-Simulationen verglichen. Beide Ergebnisse zeigten gute Übereinstimmung. Während das Messsystem mit konventionellen Sensoren einfacher und robuster aufgebaut ist, zeigen die IC-basierenden Sensorsysteme eine höhere Empfindlichkeit. Diese Systeme sind daher auch besser geeignet, um Messungen unter unkonventionellen Prozessbedingungen durchzuführen, z.B. in verdünnten Gasströmungen, in denen der Massenstrom sehr gering ist. Leider sind die auf Silizium basierenden Chip-Sensoren auch sehr fragil und nur für einen eingeschränkten Prozessparameterbereich einsatzfähig. Eine Designoptimierung für diese Systeme sollte in Zukunft erfolgen. Die vorliegende Arbeit kann als erster Schritt in die Richtung der vollständigen Integration von Sensorsystemen in mikrofluidische Apparate angesehen werden. Hiermit rückt eine in-situ-Prozesskontrolle innerhalb von Mikrosystemen ein Stückchen näher.



# Acknowledgments

First and foremost I want to thank my mentor Dr. Juergen Brandner. It has been an honor and a privilege to work with him. I could not have asked for better inspirational, supporting and patient role model to make my Ph.D. experience productive and stimulating. I hope I will be able to treasure his lessons for my future career and life.

I would also like to thank my PhD advisor, Professor Roland Dittmeyer, who provided encouraging and constructive feedbacks. It is no easy task, reviewing a thesis, and I am grateful for his thoughtful and detailed comments.

I owe my most sincere gratitude to Professor Stéphane Colin for his valuable advice and friendly help, even during the tough times in the lab. He has been able to make my time in Toulouse a very fruitful experience for my work. For this I also would like to warmly thank the research group at INSA who welcomed me and shared some long working hours with me: Lucien Baldas, Christine Barrot and my two colleagues Feriel Samouda and Vlassis Leontidis.

I am happy to acknowledge my debt to professor Gian Luca Morini, who first believed in me and encouraged me. I would not have contemplated the road of scientific research if not for his enthusiasm and his inspiring example.

My sincere thanks are due to Martin Jäger, Conrad Grehl and the whole group of design and manufacturing at IMVT for their expertise, ideas and invaluable help, which made the magic in the lab possible. I also wish to thank Silvia and all the colleagues of IMVT for their contribution to my personal and professional time in Karlsruhe.

I am deeply grateful to Dr. Patrick Ruther, Tobias Holzhammer, Dr. Oliver Paul and the team at IMTEK, Freiburg, who helped me in the difficult task of developing and implementing the microelectronic sensors for my experiments. I also acknowledge the kind help of Michael Schultz (IMF-III, KIT) and Richard Thelen (IMT, KIT) for the roughness measurements as well as Peter Schöck (IPE, KIT) for the manufacturing of the PCBs.

I thank all the people part of the GASMEMS project, for making this adventure a very formative experience and a chance for meeting many new colleagues and, most of all, friends. I can not tell how much I enjoyed the time spent together at the various summer schools, workshops and conferences. I am sure our cooperation and friendship will last long, even after the end of the project. In addition I wish to gratefully thank Chloé Prado for her patience, kindness and availability.

My biggest thanks to all my friends, close and dispersed around the world (too many to list here, but you know who you are!). I especially wish to thank Iole, Michela, Fiamma and Coral, my fellows in many journeys and adventures and, above all, my second family. Despite the distance, they have always been there for me, cheering for my successes and supporting me through my difficulties.

Lastly, I would like to thank my family for all their love and encouragement. In particular my mother and my sister, who supported me in all my pursuit and choices. I could not have done it without them, and for this I would like to dedicate this achievement to them.

The work leading to this invention has received funding from the European Union's Seventh Framework Programme (FP7/2007-2013) under grant agreement n° 215504.

© 2012  
All Rights Reserved

“Remember, it’s supposed to be fun!”

Richard Feynman, quoted in *Some time with Feynman*, L.  
Mlodinow, 2003





# Contents

<b>Abstract</b>	<b>iii</b>
<b>Zusammenfassung</b>	<b>v</b>
<b>Acknowledgments</b>	<b>vii</b>
<b>1. Introduction</b>	<b>1</b>
1.1. MEMS and microfluidic systems . . . . .	1
1.2. Gas flows in microchannels . . . . .	2
1.2.1. Micro-effects vs. Scaling-effects . . . . .	3
1.3. Integrated MEMS . . . . .	6
1.4. Objectives of the work . . . . .	7
1.5. Structure of the thesis . . . . .	8
<b>2. Technological background</b>	<b>9</b>
2.1. Materials and fabrication processes for microsystems . . . . .	9
2.1.1. Silicon and silicon compounds . . . . .	9
2.1.2. Polymers . . . . .	13
2.1.3. Glass . . . . .	14
2.1.4. Ceramics . . . . .	15
2.1.5. Metals and mechanical micromachining . . . . .	15
2.1.6. LIGA manufacturing technique . . . . .	18
2.1.7. Assembly and packaging . . . . .	19
2.2. Sensor technology in MEMS . . . . .	20
2.2.1. Temperature Sensors . . . . .	21
2.2.2. Force and pressure sensors . . . . .	28
2.2.3. Optical sensors (photosensors) . . . . .	32
2.2.4. Chemical sensors . . . . .	32
2.2.5. Biosensors and Biomedical sensors . . . . .	34
<b>3. Theoretical overview on gas dynamics and heat transfer</b>	<b>35</b>
3.1. Characteristic length scales for gases . . . . .	35
3.2. Flow models . . . . .	37
<b>4. Experimental Setup</b>	<b>45</b>
4.1. Experimental device . . . . .	45
4.1.1. Silicon micro sensors integration . . . . .	47
4.1.2. Commercial thermocouples integration . . . . .	49
4.2. Selected measurement technique . . . . .	50
4.2.1. Sensor layout . . . . .	51
4.2.2. Data acquisition cables . . . . .	53
4.2.3. Fabrication processes . . . . .	55

4.3. Microchannel materials and manufacturing . . . . .	57
4.4. Test rig and data acquisition system . . . . .	58
<b>5. Experimental results</b>	<b>61</b>
5.1. Leakage tests . . . . .	61
5.2. Surface characterization . . . . .	63
5.2.1. Scanning electron microscopy . . . . .	65
5.2.2. Contact (stylus) profilometry . . . . .	67
5.2.3. Chromatic white light sensor . . . . .	71
5.3. Microsensors characterization . . . . .	77
5.3.1. Chip contact resistances and noise analysis . . . . .	77
5.3.2. Calibration of the RTDs . . . . .	79
5.3.3. Calibration of the thermopiles . . . . .	86
5.3.4. PEEK-cover tests . . . . .	95
5.3.5. Comparative approach . . . . .	98
5.4. Heat transfer analysis . . . . .	100
5.4.1. Microchannel material effects . . . . .	100
5.4.2. Roughness effects . . . . .	105
<b>6. Numerical results</b>	<b>107</b>
6.1. Geometries and physical models . . . . .	108
6.2. Isothermal flow analysis . . . . .	110
6.3. Simplified simulation of the membrane behavior . . . . .	113
6.4. Full simulation of the membrane behavior . . . . .	117
6.5. Microchannel material effects . . . . .	122
<b>7. Conclusions and Outlook</b>	<b>127</b>
7.1. Conclusions . . . . .	127
7.2. Outlook . . . . .	129
<b>Bibliography</b>	<b>131</b>
<b>Appendix</b>	<b>137</b>
A. Test-rig Specifications . . . . .	137
B. Material properties for the CFD simulations . . . . .	139
B.1. Isothermal flow analysis simulations . . . . .	139
B.2. Simplified simulations of the membrane behavior . . . . .	140
B.3. Full simulations of the membrane behavior . . . . .	141
B.4. Microchannel material effects simulations . . . . .	142
<b>List of Publications</b>	<b>143</b>

# List of Figures

1.1.	The scale of things, in meters. . . . .	1
1.2.	Principal science and engineering disciplines involved in microsystem design and manufacturing. . . . .	3
1.3.	Comparison between experimental friction factors for gases. . . . .	4
1.4.	Comparison between correlations for the Nusselt number of gases. . . . .	4
2.1.	Example for decision tree as basis for manufacturing of microstructure devices. . . . .	10
2.2.	Examples of silicon structures. . . . .	11
2.3.	General procedure of photolithography . . . . .	12
2.4.	Available manufacturing technologies for polymers. . . . .	14
2.5.	Examples of polymer structures. . . . .	14
2.6.	Example of microstructured pieces obtained by ceramic micro injection molding. . . . .	16
2.7.	Microdrilling hard metals tools (tungsten carbide) and micro drilled piece in stainless steel. . . . .	16
2.8.	Micromill in hard metal (tungsten carbide) and stainless steel microchannels realized by precision micromilling. . . . .	17
2.9.	Detail of microturning in diamond and copper microstructure obtained by precision microturning technique. . . . .	17
2.10.	Microdevice realized by the selective laser melting technique (SLM). . . . .	18
2.11.	Example of structures realized with the LIGA manufacturing technique. . . . .	18
2.12.	Three steps of the diffusion bonding assembling technique. . . . .	20
2.13.	MEMS as a microsensor (a) and as microactuator (b). . . . .	21
2.14.	Thermal circuit with the two branches A and B (of different conducting materials), measured temperature $T_2$ and reference temperature $T_1$ . . . . .	22
2.15.	Structure of a typical integrated p-type silicon/aluminum thermopile. . . . .	23
2.16.	Thermal flow sensor working principle. . . . .	24
2.17.	Temperature dependence of the specific resistivity for some metals. . . . .	25
2.18.	Temperature dependence of the charge carrier density $\rho_n$ and the specific resistivity $\rho_{sp}$ for n-doped semiconductors. . . . .	25
2.19.	Adjustable specific resistivity of magnetite ( $\text{Fe}_3\text{O}_4$ ) for different mixtures of Spinel insulant. . . . .	26
2.20.	Possible configurations of resistor connections. . . . .	27
2.21.	Wheatstone bridge circuit configuration for a sensor. . . . .	29
2.22.	Serpentine-type coil for a strain gauge. . . . .	30
2.23.	Silicon piezoresistor based pressure sensor. . . . .	31
2.24.	Examples of optical sensing devices. . . . .	33
3.1.	Characteristic length scales at the molecular level. . . . .	35
3.2.	Limits of the approximations for gas flow modeling. . . . .	38
3.3.	Molecular and continuum flow models. . . . .	38
3.4.	Knudsen number regimes and main applicable models. . . . .	39

3.5. Maxwell model for collisions between molecules and solid wall. . . . .	41
3.6. Gas flow regimes for usual microsystems. . . . .	44
4.1. Multilayer experimental device. . . . .	46
4.2. Separated layers of the experimental device (left) and mounted device (right). . . . .	47
4.3. Schematic view of the PTFE chip support and the microchannel foil with a detail of the assembly cross section. . . . .	48
4.4. PTFE holder foil with installed silicon sensor chip and data acquisition cables. . . . .	49
4.5. PEEK cover with embedded thermocouples. . . . .	49
4.6. Possible structures for thermopiles fabricated on silicon substrates. . . . .	50
4.7. Schematic layout of the integrated measuring system. . . . .	51
4.8. Silicon sensor chip layout. . . . .	52
4.9. Cable layout. . . . .	53
4.10. Disc tool for cable lifting, positioning and bonding. . . . .	53
4.11. Detail of two different bonding areas on the chip. . . . .	54
4.12. Printed circuit board (PCB) adapters and mounted PCBs. . . . .	54
4.13. Fabrication steps for the silicon sensors. . . . .	55
4.14. Picture of a sensing unit and of the backside of the chip. . . . .	56
4.15. Fabrication steps for the polyimide cables. . . . .	57
4.16. Microchannel test sections. . . . .	58
4.17. Experimental test rig. . . . .	59
4.18. Insulation volume. . . . .	60
4.19. Pictures of the test rig. . . . .	60
5.1. Leak test results. . . . .	62
5.2. Main characteristics of a surface sample. . . . .	64
5.3. Distinction between the different characteristics of a surface profile. . . . .	64
5.4. Graphical representation of the mean arithmetic roughness ( $R_a$ ). . . . .	65
5.5. SEM pictures of a milled stainless steel microchannel. . . . .	66
5.6. SEM pictures of a milled copper microchannel. . . . .	67
5.7. SEM pictures of a milled PEEK microchannel. . . . .	68
5.8. SEM pictures of an etched stainless steel microchannel. . . . .	69
5.9. Schematic measuring principle for mechanical profilometry. . . . .	69
5.10. Screen shots from the profilometer measurements. . . . .	70
5.11. Measurement principle for the chromatic white light (CWL) sensing technique. . . . .	71
5.12. CWL scans of the micromachined stainless steel channel section. . . . .	72
5.13. CWL scans of the micromachined copper channel section. . . . .	72
5.14. CWL scans of the micromachined PEEK channel section. . . . .	72
5.15. CWL scans of the etched stainless steel channel section. . . . .	72
5.16. Results of the average roughness measurements with CWL sensor technique. . . . .	73
5.17. 2D and 3D surfaces produced by the CWL sensor for the micromachined stainless steel microchannel. . . . .	74
5.18. 2D and 3D surfaces produced by the CWL sensor for the micromachined copper microchannel. . . . .	74
5.19. 2D and 3D surfaces produced by the CWL sensor for the micromachined PEEK microchannel. . . . .	75
5.20. 2D and 3D surfaces produced by the CWL sensor for the etched stainless steel microchannel. . . . .	75
5.21. Cross section profiles calculated from the CWL 3D surfaces for the different test sections. . . . .	76
5.22. Thermopile basic noise with a chip-cable assembly with suboptimal conditions. . . . .	79

5.23. Thermopile basic noise with a chip-cable assembly bonded with optimized conditions to avoid short-cuts and contact cross-talking. . . . .	79
5.24. Working contacts of a tested sensor chip. . . . .	80
5.25. Relative position between the heating blocks and the RTDs. . . . .	81
5.26. Calibration of a RTD. . . . .	82
5.27. Least square fitting for the calibration of a RTD. . . . .	83
5.28. Relative positions of the embedded thermocouples, the integrated sensors and the device heating blocks. . . . .	84
5.29. Axial temperature distributions as registered by the PEEK cover. . . . .	84
5.30. Relative positions of the heating blocks and the thermopiles TE7R and TE8R. . . . .	88
5.31. Experimental sequence for the calibration of the thermopile TE7R. . . . .	88
5.32. Average reference temperature and voltage signals for the thermopile TE7R. . . . .	89
5.33. Test sequence for the calibration of the thermopile TE8R. . . . .	89
5.34. Average temperatures and voltage signals for the thermopile TE8R. . . . .	90
5.35. Calibration linear fitting for the thermopiles TE7R and TE8R. . . . .	91
5.36. Schematic layout for the two thermopile test sequences. . . . .	92
5.37. Test sequences results for the thermopile TE5L. . . . .	92
5.38. Test sequences results for the thermopile TE6R. . . . .	93
5.39. Test sequences results for the thermopile TE7R. . . . .	93
5.40. Test sequences results for the thermopile TE8R. . . . .	94
5.41. Test sequence performed with the PEEK cover and an imposed mass flow rate of 100 ml/min. . . . .	96
5.42. Test sequence with the PEEK cover, with an imposed mass flow rate of 200 ml/min. . . . .	97
5.43. Test sequence for the PEEK cover at three different temperatures imposed on the heating blocks. . . . .	97
5.44. Comparison between the data from the integrated thermopiles and the PEEK cover thermocouples close to the microchannel entrance. . . . .	99
5.45. Comparison between the data from the integrated thermopiles and the PEEK cover thermocouples for the first unheated block. . . . .	99
5.46. Comparison between the data from the integrated thermopiles and the PEEK cover thermocouples for the second unheated block. . . . .	100
5.47. Axial temperature distribution for the machined stainless steel microchannel. . . . .	101
5.48. Axial temperature distribution for the machined copper microchannel. . . . .	102
5.49. Enlargement of Fig. 5.48 to highlight the details of the temperature distribution. . . . .	102
5.50. Axial temperature distribution for the machined PEEK microchannel. . . . .	103
5.51. Axial temperature distribution for the etched stainless steel microchannel. . . . .	104
5.52. Axial temperature distributions recorded with the PEEK cover and microchannels of different materials. . . . .	104
5.53. SEM picture of the stainless steel microchannel surface before and after surface treatment. . . . .	105
5.54. Comparison of the axial temperature distributions for the machined stainless steel microchannel before and after the surface treatment. . . . .	106
6.1. Schematic representation of the channel-chip geometry. . . . .	108
6.2. Schematic layout of the boundary layer option for the geometry meshing. . . . .	109
6.3. Axial velocity close to the channel exit for an isothermal slip flow. . . . .	111
6.4. Axial pressure and Knudsen number distribution calculated for the isothermal and adiabatic membrane models. . . . .	114
6.5. Axial temperature distribution along the microchannel central axis, the chip and the membrane for the isothermal and adiabatic thermal model. . . . .	115

6.6. Temperature distribution across the microchannel inlet cross section. . . . .	115
6.7. Temperature distribution across the microchannel cross section corresponding to the first membrane. . . . .	116
6.8. Temperature distribution across the microchannel cross section corresponding to the second membrane. . . . .	116
6.9. Temperature distribution across the microchannel cross section corresponding to the third membrane. . . . .	117
6.10. Pressure and Knudsen number distributions along the microchannel axis calculated for the boundary conditions encountered during the chip tests. . . . .	119
6.11. Comparison of the axial temperature distributions for the first set of boundary conditions. . . . .	119
6.12. Comparison of the axial temperature distributions for the second set of boundary conditions. . . . .	120
6.13. Comparison between the measured thermopiles voltage differences and the theoretical temperature differences for Period 1. . . . .	121
6.14. Comparison between the measured thermopiles voltage differences and the theoretical temperature differences for Period 2. . . . .	121
6.15. Comparison between the experimental and numerical results for the axial temperature distribution along the machined stainless steel microchannel. . . . .	123
6.16. Comparison between the experimental and numerical results for the axial temperature distribution along the machined copper microchannel. . . . .	123
6.17. Comparison between the experimental and numerical results for the axial temperature distribution along the machined PEEK microchannel. . . . .	124
6.18. Comparison between the theoretical and experimental temperature profiles for the different microchannel materials. . . . .	125

# List of Tables

2.1.	Correlation between physical effects and measured quantities in conventional sensor technology. . . . .	21
2.2.	Sensors types and methods for temperature measurement. . . . .	22
3.1.	Collision force $F$ , viscosity $\mu$ and mean free path $\lambda$ for different IPL collision models. . . . .	36
4.1.	Specifications for the different realized microchannel test sections. . . . .	58
5.1.	Helium leak rate conventional classification. . . . .	63
5.2.	Results of the profilometry analysis of the microchannel test sections. . . .	70
5.3.	Results of the CWL sensor scans for the microchannel sections. . . . .	73
5.4.	Comparison between the average roughnesses of the tested microchannel sections measured with the three different techniques. . . . .	76
5.5.	Calibration coefficients calculated for the working RTDs on the chip. . . . .	83
5.6.	Calibration coefficients for the RTDs calculated with the direct calibration technique and corrected by employing the embedded thermocouples. . . . .	85
6.1.	Specification of the channel geometry created for the CFD simulations. . . .	109
6.2.	Boundary conditions type chosen for the different geometry areas. . . . .	109
6.3.	Details of the four different meshes created with GAMBIT. . . . .	112
6.4.	Boundary conditions imposed for the simulation of the microchannel heat transfer performances. . . . .	113
6.5.	Boundary conditions for the microchannel simulation as recorded during one of the integrated sensors experiments. . . . .	118
A.1.	List of the test-rig parts and instruments. . . . .	137
A.2.	Accuracies of the different instruments as given by vendors. . . . .	138
B.1.	List of material properties used for the isothermal flow simulations (cf. Sec. 6.2). . . . .	139
B.2.	List of material properties used for the simplified simulation of the membrane behavior (cf. Sec. 6.3). . . . .	140
B.3.	List of material properties used for the full simulation of the membrane behavior (cf. Sec. 6.4). . . . .	141
B.4.	List of material properties used for the microchannel material effects simulations (cf. Sec. 6.5). . . . .	142





# 1. Introduction

In his keynote lecture for the “Freeman Scholarship” in 1999 [1], Prof. Gad-el-Hak highlighted the egocentric nature of the universe, where typical sizes of man can be placed almost at the center between the smallest subatomic particles (about  $10^{-26}$  m) and the extent of the observable universe (about  $1.42 \cdot 10^{26}$  m), as represented in Fig. 1.1.

In man’s constant seek for overcoming his limits, broaden his knowledge and improve his achievements, the miniaturization of tools and systems is not a new field. Since the invention of the microscope in the seventeenth century, the direct observation of the micro-world, and the discovery of cells, molecules, atoms and sub-atomic particles, opened the doors to a completely new field of science and research toward the smallest scales. With the advent of transistors (invented in 1948), integrated circuits with sizes down to some tenths of nanometers provided a huge performance increase in communication and information technologies allowing higher speeds, accuracies and less power consumption. Following the development of integrated circuit technology, microfabrication processes have been developed to create miniaturized sensors, actuators, gears, motors, nozzles and others more. These led to the birth and spread of microsystem technologies and microfluidics.

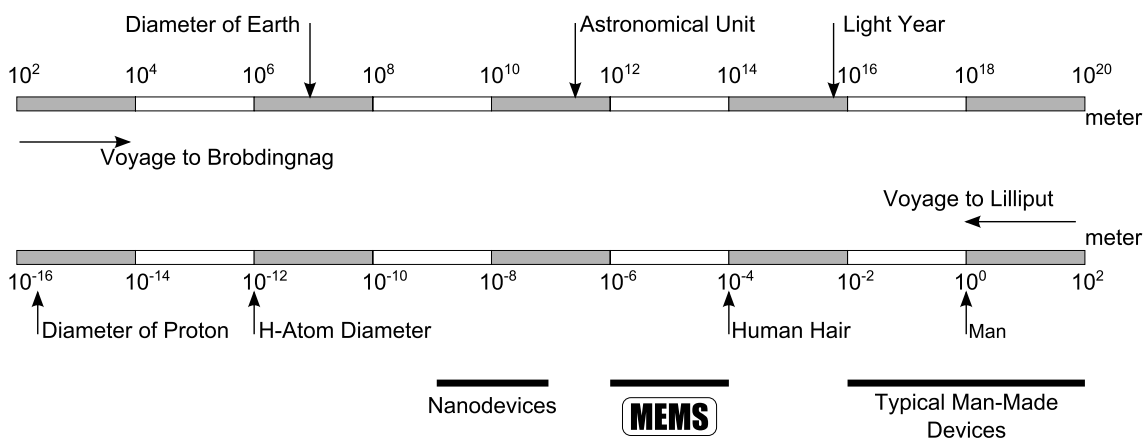


Figure 1.1.: The scale of things, in meters [1].

## 1.1. MEMS and microfluidic systems

Generally speaking, a microsystem can be defined as a system with dimensions of characteristic and functional components being below 1 mm. Microelectromechanical systems

(MEMS) refer to specific microsystems combining electrical and mechanical components, usually involving at least a sensing or an actuating unit, and have been considered by many researchers as the constituting units of microsystems. Following Madou [2], microsystems include three major components: microsensors, actuators and a process unit. Microsystems engineering involves the design, manufacture and packaging of such systems by means of different microfabrication processes specifically developed or adapted for the purpose.

The great appeal of microsystems and MEMS does not only rely on the small reachable sizes. To understand the reasons behind the success of such devices, it is necessary to look at the potentials they offer in enhancing the performances of many technological processes. Thanks to the small mutual distances between the working fluid volumes, mass transfer resistances are low offering fast mixing and good mixing qualities. The characteristic surface-to-volume ratio strongly affects heat transfer efficiencies. Being this ratio much larger for microdevices than for conventional systems, typical heat transfer performances in microstructured heat exchangers can be some orders of magnitude higher than for traditional ones. Moreover, the typical time constants of microsystems are quite small compared to macroscale systems, leading to faster responses and, thus, increased agility which may further lead to higher efficiencies. For specific applications in chemical and process technology, small systems present the advantage that the characteristic extinguishing width of many reactions under usual process conditions is larger than the systems characteristic length itself, allowing safer and better controlled processes.

Early microfluidic devices included constituent parts of gas chromatographs developed at Stanford University [3], and ink-jet printer nozzles developed by IBM [4]. Ever since a large variety of MEMS devices and components has been produced, marking a huge step toward the ultimate miniaturization of machines. Among the different available devices single components such as flow sensors and valves can be mentioned, as well as complex systems consisting of pumps, valves, separation capillaries, micropumps and micromotors. Reviews of available miniaturized devices can be found, e.g., in [5], [6], [7] and [8].

Although MEMS have strong connections with microelectronics, if only for the fact that many MEMS manufacturing processes originate from silicon microelectronics, their development has gone much further than being a simple branch of the IC industry. The possible applications of MEMS and microsystems range from biology, medicine, chemical and process engineering, electronics and communication, to the automotive industry, making microsystem engineering and microfluidics strongly multidisciplinary fields. For these reasons, the design and development of MEMS require the interaction of many disciplines, as illustrated in Fig. 1.2.

## 1.2. Gas flows in microchannels

The rapid growth in MEMS and microsystems markets observed in the last couple of decades has not been matched by corresponding advances in the understanding of the flow physics involved in their operation. However, a great number of studies on liquid and gaseous microchannel flows are available in literature. An extensive review of the main results obtained for heat transfer in microdevices has been presented by Morini in 2004 [10]. The understanding of fluid dynamics and heat transfer for gaseous microflows is more advanced than for liquids, as simplifications in the modeling of the molecular interactions for gases make these simulations more affordable than for liquids. A specific review of works concerning microchannel gas flows has been presented by Rostami [11] and, more recently, by Colin [12], who concentrated on gas heat transfer at microscales. Despite the large number of available theoretical and experimental references, unambiguous conclusions about microflow physics can not be drawn, due to substantial disagreement between

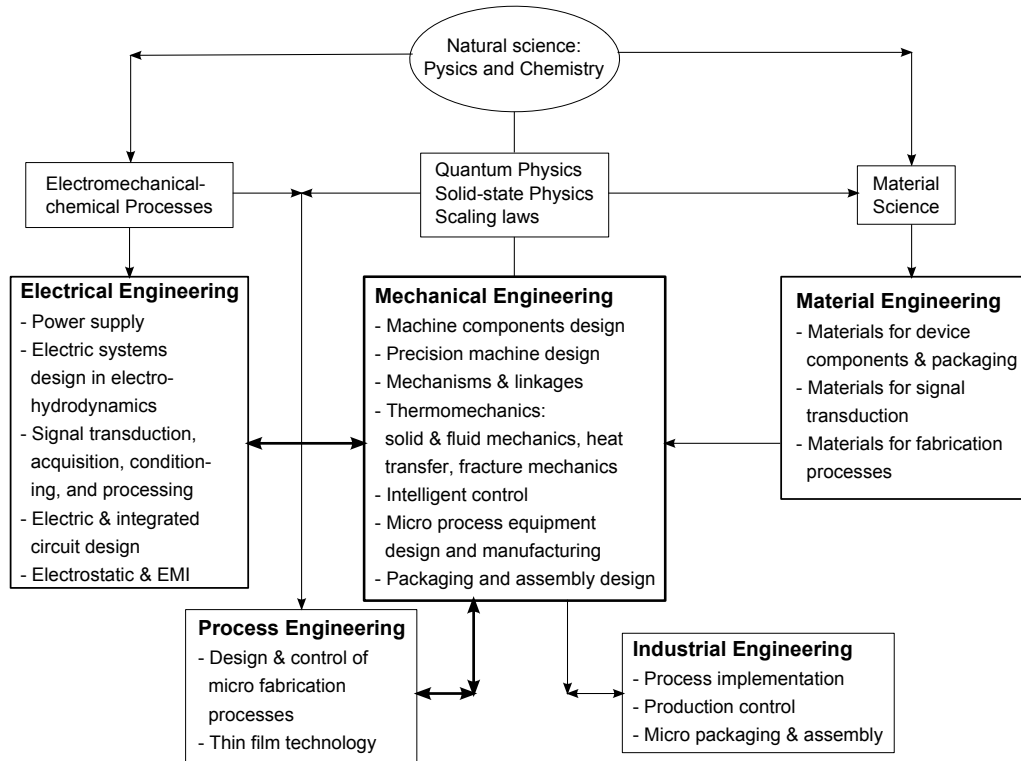


Figure 1.2.: Principal science and engineering disciplines involved in microsystem design and manufacturing [9].

the results obtained by different researchers [10]. As an example for this, Figure 1.3 shows different experimental friction factors for gas flows reported in literature. The deviation of the data from the classical theory is quite large. For this reason a series of corrections to the classical correlations to calculate the friction factor and the Nusselt number for gas flows in microchannels have been proposed. However, none of them is able to explain all the available experimental results. This is well documented in Fig. 1.4, where the deviations of three new proposed correlations from conventional theory and from each other for the Nusselt number of gas flows is represented. Besides these results, non-linear pressure distributions ([13], [14] and [15]) and mass flow rates higher than theoretical ones ([16] and [17]) have also been found.

### 1.2.1. Micro-effects vs. Scaling-effects

In the attempt of explaining the apparently new features of microchannel flows, many authors claimed the existence of some “micro effects”, which would determine the complete reformulation of the theory at the basis of microscale gas flow physics. However, for most situations this appears not to be the case, and it should rather be talked about “scaling effects”. These, as suggested by Guo and Li [23], appear because of the dependence on the characteristic length of the different terms in the classical flow models. A review of the different scaling effects for liquid flows in microchannels has been proposed by Morini [24], but his considerations can be easily extended to gas flows. The relative weight of each scaling effect can be evaluated by defining some dimensionless parameters.

The *thermal entrance region* for an internal flow is defined as the portion of the channel where the temperature profile evolves from the entrance profile to the fully developed profile. In this region the average Nusselt number ( $Nu$ ) is not constant for given geometry and thermal boundary conditions, but is a function of the Reynolds number ( $Re$ ). These

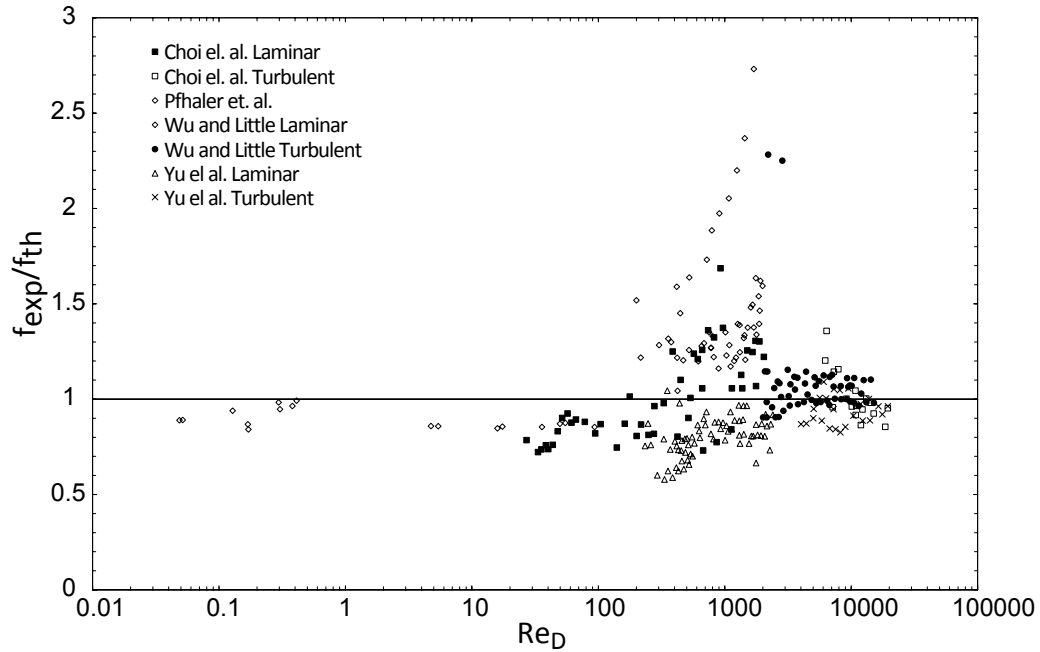


Figure 1.3.: Comparison between experimental friction factors for gases obtained by Choi et al. [18], Pfahler et al. [19], Wu and Little [20] and Yu et al. [21], normalized with the theoretical value from [22]

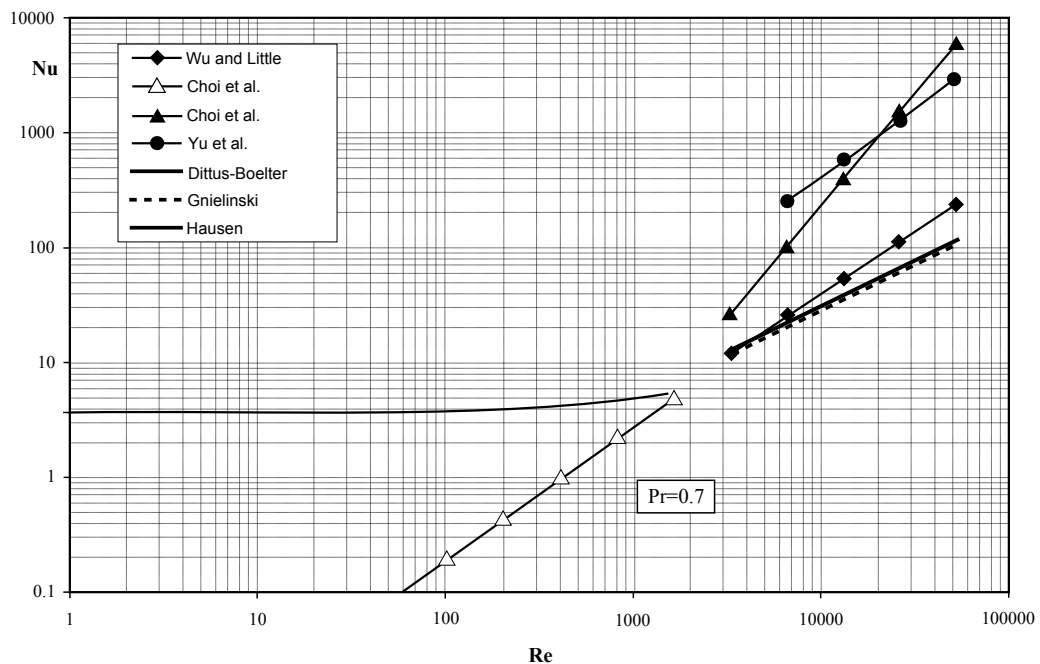


Figure 1.4.: Comparison between classical correlations for the Nusselt number of gases and the new correlations for microchannels proposed by Wu and Little [20], Choi et al. [18] and Yu et al. [21]. (Adapted from [10])

deviations are the higher the larger the diameter-to-length ratio ( $d/L$ ) is. For microchannels this contribution might not be negligible and a threshold has been established in terms of the Graetz number (when  $Gz > 10$  the entrance effects on the Nusselt number cannot be neglected).

*Viscous dissipation* refers to the heat generated by shear between the different parts of

a viscous fluid moving at different velocities. Viscous dissipation is represented by the Brinkman number ( $Br$ ), which depends on the ratio between the square of the fluid velocity and a reference temperature difference. When the product between  $Br$ ,  $Re$  and the friction factor  $f$  is smaller than 0.1, viscous dissipation can be neglected [25]. On the contrary, when viscous dissipation effects are not negligible, the Nusselt number is reduced for large values of the Reynolds number.

*Fluid axial conduction* refers to a heat flux within the fluid along the axis of the channel in the opposite direction of the temperature gradient. The relative weight of this effect is determined by the Peclet number  $Pe$  and, in particular, it can be neglected if  $Pe > 50$  [25].

*Conjugate effects* can play a substantial role in determining the actual heat transfer of gases in microchannels (especially when considering the flow inside commercial micro capillaries). These effects refer to the situation where the relative volume occupied by the solid walls around the channel is not negligible compared to the fluid volume. This can be frequently encountered when the reduction of the channel diameter is achieved by a reduction of the tube inner diameter, while the external diameter is kept at standard size to be compatible with conventional fittings. In this case, parallel to the axial heat conduction within the fluid, heat conduction along the wall, in the opposite direction of the temperature gradient, is established. At low Reynolds numbers, this effect reduces the Nusselt number. Conjugate effects can be neglected when:

$$\left(\frac{\kappa_w}{\kappa_f}\right) \left(\frac{D^2 - d^2}{dl}\right) \frac{1}{RePr} < 10^{-2} \quad (1.1)$$

where  $\kappa_w$  and  $\kappa_f$  are the thermal conductivity of the wall and the fluid respectively,  $D$  and  $d$  are the outer and the inner diameter of the tube, and  $l$  is the microchannel length [25].

Another important aspect to be considered, especially for gaseous microflows, is *compressibility*. Classically, the flow is said to be compressible whenever the Mach number ( $Ma$ ) goes above the threshold of 0.3. However, this is only a necessary but not a sufficient condition, especially when it comes to microdevices. In some microflows the pressure drop due to the shear stress and the flow acceleration may be large even though the average  $Ma$  remains sufficiently low [26, 27]. This results in a non negligible density variation which leads to non linear pressure profiles.

Another effect of compressibility is that the fully developed flow may not be reached and the Nusselt number may increase as an effect of the acceleration. A common error done when incorrectly treating gas flows as incompressible is considering the pressure evolution along the channel as linear. On the contrary many experimental studies (see, e.g., [13], [14] and [25]) confirmed that, as an effect of compressibility, the pressure distribution might be highly nonlinear. As a rule of thumb for gas flows in microchannels it can be said that the flow must be treated as compressible if at least one of the following inequalities is satisfied [28]:

$$\begin{cases} Ma_e > 0.3 \\ \frac{\Delta p}{p_i} > 0.05 \end{cases} \quad (1.2)$$

where the subscript  $e$  and  $i$  stand for exit and inlet quantities, respectively.

The characteristics of the channel walls, such as *roughness*, which for conventionally sized channels can often be neglected, may become relevant when the overall dimensions are reduced. This is because at microscale the relative influence of the surface quality on the

channel sizes drastically increases. Due to the typical irregular distribution of the dimensions and the shapes of roughness profiles, the integration of surface quality in analytical and numerical models is rather difficult. On the other hand, an accurate experimental characterization of roughness effects has not been univocal so far. Only few works can be found treating the influence of surface quality in microchannels systematically. Tang et al. [29] performed an experimental study for different kinds of microchannels and micro tubes. The authors reported a deviation of the friction factor depending on the roughness level. In the work of Turner et al. [15] on the contrary, a substantial independence of the friction factor on roughness was reported.

As already pointed out, “micro-effects” in the true sense of the word are properly only those effects which require a re-formulation of the conventional continuum equations (i.e. Navier-Stokes and Fourier equations). The small length-scales of microdevices may indeed invalidate the continuum approximations or the thermodynamic equilibrium hypothesis. This is true, e.g., for non-newtonian fluids, for which the relationship between stress and strain rate and heat flux and temperature gradient is not linear, or for rarefied gases, encountered at low pressures or at very small scales. The latter case is very likely to happen for gas flows in MEMS and will be further discussed in Section 3.2.

A final aspect which can neither be considered a “scaling” nor a “micro” effect, but which has nevertheless a great influence on the correctness of experimental results, is the treatment of *uncertainties*. The actual values of channel dimensions can vary a lot from their nominal values, while the measured pressure and temperature variations can change if the measurement position is changed (as a consequence of strong entrance effects). All these contributions may add together and lead to large variations in the final results, and must therefore be carefully considered and taken into account. Celata [30] demonstrated how an improper negligence of the experimental uncertainties could lead to a complete misinterpretation of the results and consequently to an incorrect claim for “new effects” at microscale.

### 1.3. Integrated MEMS

Taking advantage of the IC technology, silicon microfabrication techniques and traditional measuring principles have been combined to produce microscale sensors for a variety of applications [31]. Besides the evident reduction in size, on-chip electronics presents also a reduction of the sensitivity to interferences [32], increased response frequencies and the possibility of combination with control and actuation systems [8].

Shear stress sensors [33], anemometers [34], pressure transducers [35] and temperature sensors [36] are some examples of the available micro sensors for “large-scale” applications. However, one of the most appealing features of these systems is the possibility of integrating them in microsystems. Accessing online and direct information of the flow opens new frontiers in the understanding of the governing physical mechanisms in micro systems.

Integrating sensors in microchannels is not a trivial task, even if precision silicon manufacturing techniques are employed. Usually the quantities to be measured are much smaller than in conventional applications, therefore highly sensitive sensors or signal enhancing techniques are required. On the other hand, the reduced size of the system where the sensors have to be integrated requires even smaller dimensions for the sensors themselves to reduce interferences with the flow behavior. Integrated temperature sensors have been presented, e.g., by Wu, et al. [37], Park, et al. [38] and Xue and Qiu [39]. Low temperature manufacturing processes for integrated sensors employing particular materials for heat transfer studies have also been developed and described, e.g. by Liu, et al. [40] and Ko and Gau [41].

Despite the progress of miniaturized sensors fabrication techniques and the large number of configurations proposed over the years, broad implementation of these systems in terms of integrating the sensors in microscale devices has not been achieved yet. The highly process-specific designs proposed in literature mostly limit the use of the sensors to the single application they have been designed for. Flexible and adaptable designs are still lacking which may be integrated in more versatile microdevices to be used for different applications and environments. Moreover, planar fabrication technologies, which offer great manufacturing potential, limit the employable materials to a few (basically silicon and its compounds and glass).

### 1.4. Objectives of the work

From the presented literature overview it is clear that reliable predictions of the flow behavior of gas microflows are still hard to achieve. The results obtained by different researchers might be limited to their case-study, and should be further validated for other gas species, channel materials and flow conditions (including e.g. rarefaction, compressibility and roughness effects altogether). Extensive experimental campaigns aimed at the validation or confutation of these models should be therefore foreseen.

In addition to that, it should be highlighted that many employed experimental methods are based on measurements at the inlet/outlet of the microstructures. The gas bulk properties are then extrapolated by assuming more or less linear evolutions along the microchannels. However, this method may be source of large uncertainties, which are demonstrated to play a major role in conditioning the final results. Yang et al. [42], e.g., recently pointed out this issue for the calculation of the Nusselt number of a gas flow inside a microtube.

To overcome these limitations, the implementation of integrated sensors appears as the best solution, which, however, has the drawback of offering reduced flexibility in employable materials and configurations.

This work describes a new experimental approach for the local characterization of gas flow heat transfer in microchannels. Starting from the state-of-the-art of MEMS-based designs, a new integrated sensor assembly is proposed, with the aim of broadening the possible applications of integrated measuring systems. To compare the performance of the developed system, a layout for integration of commercial transducers is proposed as well. By comparing the two methods, the potential and the limits of the two approaches are assessed.

The main challenge for the desired system is the possibility of adapting it to different channel materials and geometries avoiding, at the same time, major modifications to the general design layout. This ensures a direct evaluation of the material influence on the heat transfer of gases at microscales. As the measuring technique is fixed, the results from different tests can be directly compared and do not depend on the specific experimental setup with which they have been obtained. Moreover, by providing internal measurement points, the indirect extrapolation of data from external measurements is avoided and more reliable results can be produced.

By proving the flexibility of the integrated measurement techniques, the feasibility of broad implementation of MEMS in technological processes for online monitoring (and control) of the process parameters can be demonstrated.

The principal objectives of this work can be summarized as follows:

- Design and manufacturing of integrated temperature microsensors with silicon fabrication technologies.

- Development of an integration technique to include the silicon microsensor assemblies in microchannels made from different materials.
- Development of an integration technique to include commercial thermocouples in a microchannels.
- Design and implementation of a new experimental device for heat transfer studies of gas flows in microchannels.
- Characterization of the two integrated measuring systems and comparison of their performance.
- Test of different channel materials with the integrated measurement system.
- Evaluation of channel material and wall surface characteristic effects on the heat transfer performance.

The present work has been part of a "Marie Curie" *Initial Training Network* (INT) named GASMEMS and was funded by the European Commission. The Network includes different European academic and industrial institutions with the aim of promoting research in the field of gas microflows. Within GASMEMS, the project involved the cooperation of one major partner, the Institute of Micro Process Engineering (IMVT) at the Karlsruhe Institute of Technology (KIT), and two secondary partners: the National Institute of Applied Sciences (INSA) of Toulouse, and the Technical University of Dresden.

## 1.5. Structure of the thesis

The structure of the thesis is as follows. In Chapter 2 an overview of the typical materials and manufacturing processes employed for microstructured devices and MEMS is given. An extended description of the different sensor technologies adaptable for MEMS and microsystems in general is also included. Chapter 3 presents a theoretical background for gas flow physics, with particular attention to the different flow models, their validity and limitations. In Chapter 4 the microchannel experimental device, the test rig and the employed measuring techniques are described in detail. Chapter 5 presents the obtained experimental results and the related discussion. After reporting the preliminary experimental data, the tests with the integrated measuring systems are described and the related results are given. The comparison between the two measuring techniques is shown. Finally, the data from experimental campaigns with different microchannel materials are presented to investigate the effects of the wall thermal properties and roughness on the temperature profile development. Chapter 6 presents the results from CFD simulations in terms of integrated sensor behavior and microchannel material effects. In both cases comparison with the experimental data is done. Concluding remarks and hints for future developments are included in Chapter 7.



## 2. Technological background

To successfully design and implement a process with MEMS technology, suitable materials, manufacturing techniques, sensing and actuating methods must be chosen.

### 2.1. Materials and fabrication processes for microsystems

The main fabrication techniques employed to produce MEMS have their roots in microelectronics technology. It is no wonder then that the development of MEMS accelerated strongly in the 1990s, taking advantage of the integrated circuit revolution of the previous decades. However, the design and the fabrication of MEMS, and in general of microsystems, may differ a lot from conventional microelectronics manufacturing techniques. Moreover, integration of microstructured components in technological processes usually means integration of different materials in a single system, each providing a specific function. A good knowledge of the variety of available materials and their main properties as well as of the principal manufacturing techniques is mandatory when dealing with designing, realization and implementation of microsystems. A series of process parameters must be examined to verify the compatibility with the chosen material and the overall design feasibility with the available manufacturing techniques. Temperature and pressure boundary conditions, e.g., must be known to verify that the materials can sustain them. Finally, the kind of process occurring in the structures and the fluid with which the structure would eventually come in contact (liquids, gases, reactant species) must be known since corrosion, fouling or material incompatibilities might arise. In conclusions, the choice of a material for a particular application is not an a-priori step of the device fabrication, but relies rather a process-oriented approach. On the other hand, the choice of the manufacturing technique is related to the chosen material, but also to the required specification of the structure to be realized. As a representative example, a typical decision tree to be followed for the realization of a metallic microstructure device is given in Fig. 2.1. According to the application the structure may slightly change, but the fundamental scheme stays valid for microsystems design in general.

#### 2.1.1. Silicon and silicon compounds

Silicon (Si) is among the most abundant elements on Earth. Many mature industrial processes are available to refine sand and produce single crystal Si wafered substrates, having large areas and very low defect densities. The combination of integrated-circuit (IC) processing and silicon micromachining techniques has marked the advent and development

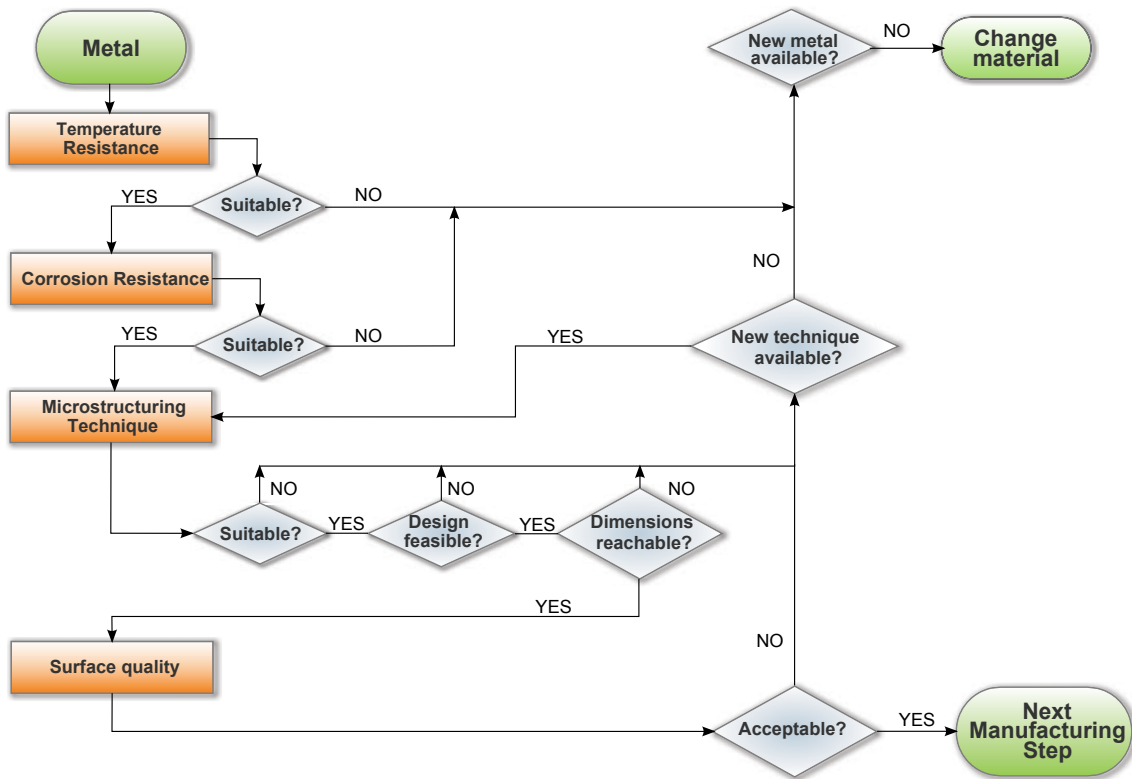


Figure 2.1.: Example for decision tree as basis for manufacturing of microstructure devices [43].

of MEMS, positioning silicon as primary choice material [9]. The main features of Si making it a good candidate to be used for MEMS substrates are:

- Si has about the same Young's modulus as steel (about  $2 \cdot 10^5$  MPa) but is as light as aluminum with a mass density of about  $2.3 \text{ g/cm}^3$ .
- It is mechanically stable and can be integrated into electronics on the same substrate.
- It presents a high melting point (about twice that of aluminum) which makes it dimensionally stable even at high temperatures.
- Its coefficient of thermal expansion is smaller than those of steel and aluminum.
- It presents almost no mechanical hysteresis making it a perfect candidate for sensors and actuators.
- Fabrication processes and treatments of Si are well established and documented, and a great flexibility of design and manufacturing is available.

Single-crystal Si, as many other semiconductors, can be easily doped with impurities to alter its electrical and thermal conductivity. Phosphorous (P) is a common dopant for n-type Si and Boron (B) is used to produce p-type Si. Silicon doping can be performed either by thermal diffusion of the doping atoms (following Fick's law) or by ionic implantation (accelerating and focusing a dopant ion beam on the Si substrate) [9]. In MEMS applications single-crystal Si is a very versatile material both for bulk and surface micro-machining applications. In the first case a variety of well characterized anisotropic etches and etch-mask materials are available, while in the second case the single-crystal Si can be used as a mechanical platform for the fabrication of device structures (which can be made either from Si or from different materials).

Bulk micromachining of Si involves the removal of materials from the substrate to form the desired three-dimensional geometry of the microstructure. The commonly used techniques to perform bulk micromachining employ wet or dry etching together with etch masks and etch stops [44]. Etching involves the exposure of a substrate to a chemical etchant covered by a protection mask. The part of the substrate not covered by the mask is dissolved and removed by the etchants. One of the most important features of etching is the directionality of the process. Isotropic etching refers to the cases where the etchants attack the material uniformly in all directions. On the contrary, anisotropic etching presents higher etch rates in some preferential directions, depending on the crystal orientation [9]. For wet etching, usual isotropic etchants are acidic agents (e.g. HF), while alkaline chemicals (e.g. KOH) are used for anisotropic wet etching. Alternatives to wet etching are the dry etching techniques, which often involve the employment of a plasma of ionized gases, along with neutral particles to remove material from the etch surface. Reactive ion etching (RIE) is the most commonly used dry etch processes to pattern Si. RIE is highly directional, thus enabling direct pattern transfer from the masking material to the etched Si surface. In particular, deep reactive ion etching (DRIE) has been largely employed as it can produce very high aspect ratio structures, with almost perfect vertical walls [2]. In Fig. 2.2 examples of etched structures in silicon are presented.

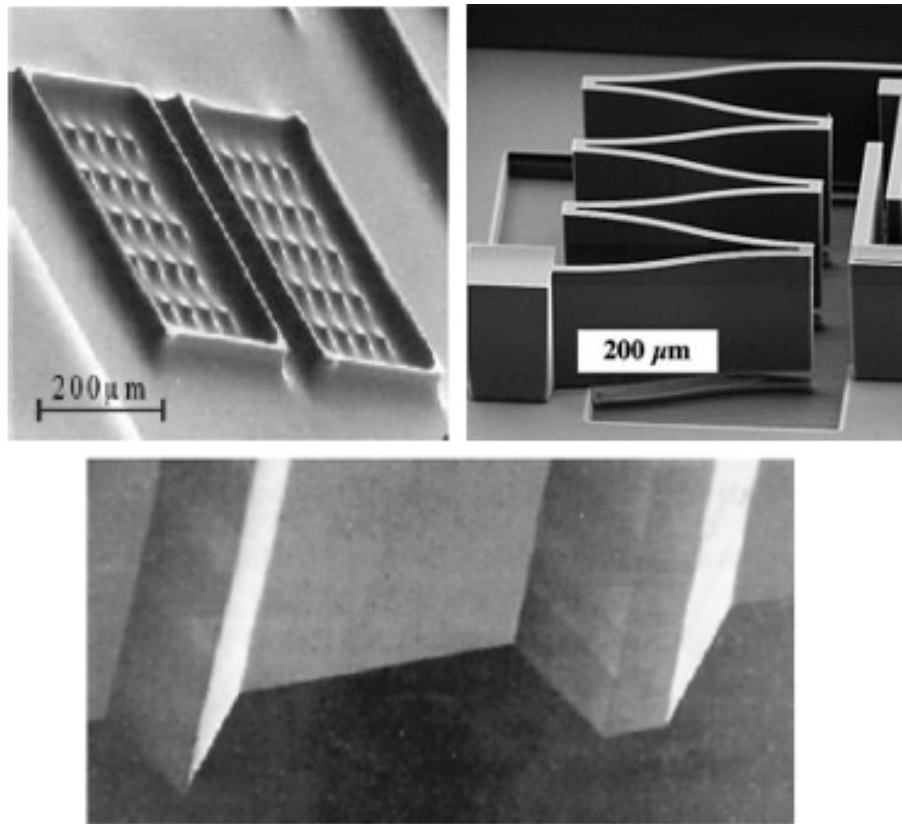


Figure 2.2.: Examples of silicon structures. From the top-left corner in clockwise direction: isotropically etched microtips on (111) silicon [45]; MEMS actuator realized with DRIE [46]; structures obtained with anisotropic etching of a (100) silicon wafer employing a rectangular mask [47].

In contrast to bulk micromachining, in which material is removed from the substrate by means of physical or chemical processes, surface micromachining involves only the top of the substrate usually by means of patterning, modifying or adding material layer by layer.

To obtain patterned structures with etching techniques, the substrate surfaces need to be worked according to the pattern to be transferred. Photolithography is the most reliable technique to obtain patterns on substrates up to submicrometer resolution. It involves the coating of the substrate with a photosensitive film (photoresist) which is then exposed to a set of light through a transparent patterned mask. The solubility of the photoresist changes when exposed to light, becoming more soluble under light (positive photoresist) or more soluble under shadow (negative photoresist) [2]. Figure 2.3 shows the main steps of a photolithography process.

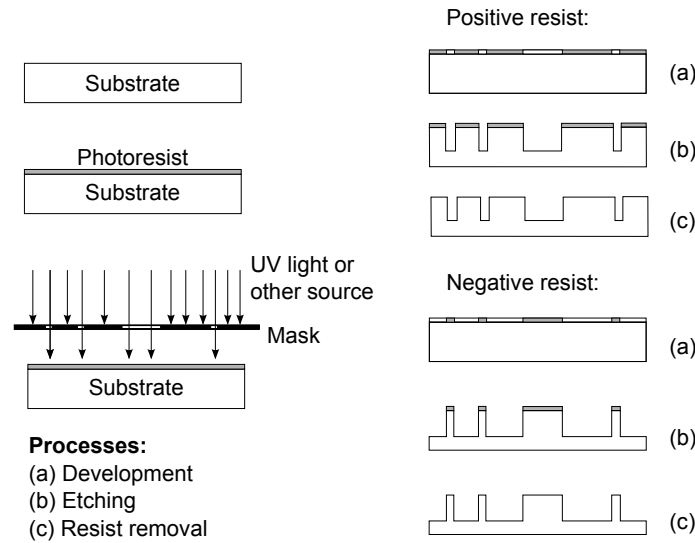


Figure 2.3.: General procedure of photolithography [9].

A common technique used to modify the Si substrate surface is thermal oxidation. In particular this process is used to produce silicon dioxide ( $\text{SiO}_2$ ) layers [44].  $\text{SiO}_2$  can be used as a thermal and electrical insulator, as a mask in the etching of silicon substrates (due to its strong resistance to many etchants, excluding HF) or as a sacrificial layer in surface micromachining [9].  $\text{SiO}_2$  can be grown thermally on Si substrate, by placing it into a furnace tube, where an oxygen flow is blown and proper temperature conditions are imposed [2].

Another technique to cover a Si substrate is the chemical vapor deposition (CVD). CVD can be used to deposit different organic or inorganic thin-film materials by means of convective heat and mass transfer as well as diffusion with chemical reactions. The reactants are carried over the heated substrate surface within a carrier gas flow. The necessary energy for the reaction to take place is directly given by the surface high temperature (where dissociation, adsorption and desorption of reactants and products take place) [2]. Among the materials that can be deposited by CVD the most commonly used in MEMS are  $\text{SiO}_2$ , Si in polycrystalline form (polysilicon) and Si nitride ( $\text{Si}_3\text{N}_4$ ) [9].

Polysilicon is made out of grains whose orientations vary according to the deposition conditions. It is widely used in MEMS fabrication technology as it presents mechanical properties comparable to single-crystal Si. The required deposition and etching technology are already available from the IC industry. Also the resistivity of polysilicon can be altered by impurity doping, using the same techniques as developed for single-crystal Si [9].

Silicon nitride ( $\text{Si}_3\text{N}_4$ ) is used as electrical insulation (presenting a resistivity of about  $10^6 \Omega \cdot \text{cm}$ ), surface passivation or etch mask (as it present a strong resistance to oxidation and to many etchants) [9].

Several modified CVD processes have been developed to obtain better results in terms of rate of growth or quality of the deposited film. Among these, plasma enhanced chemical vapor deposition (PECVD) and low pressure chemical vapor deposition (LPCVD) are the most common [9]. In PECVD the reaction energy is not provided anymore by a heated substrate, but transferred with a RF-plasma, which avoid damage of the surfaces at high temperatures [2]. LPCVD is used to increase the rate of deposition and to obtain a more uniform deposit [2]. Finally, when the precursor of the material to be deposited is introduced in solid form and then evaporated or transported onto the target surface, the process is named physical vapor deposition (PVD) [9]. Differently from CVD, PVD coating does not involve the growth of layers with chemical reactions, but is mainly based on physical processes such as high temperature evaporation or plasma sputtering. PVD process usually requires vacuum environments and include four different steps: evaporation, transportation, reaction and deposition. PVD is often used to deposit thin metallic films on substrate surfaces. These can be required to conduct electricity from sensors or to supply electricity to actuators. Aluminum (Al) is probably the most widely used metal for these applications. Aluminum thin films can be used in combination with polymers (e.g. polyimide) so that they can be sputter-deposited at low temperatures [9].

To broaden the range of silicon MEMS applications, which is by its nature limited by the material physical properties, alternate materials have been developed. In particular, the operating temperatures of Si-devices are limited to 200 °C and in general harsh environmental conditions are to be avoided, including, e.g. high-temperature, high-radiation, high-wear and highly acidic or basic chemical environments (Si is dissolved as an hydroxocomplex in most solutions at most value of PH). To be used under such conditions, silicon carbide (SiC) has been recognized as a potential substitute for Si or as a protection layer of components against high temperatures. SiC layers can be deposited using different techniques, among which the most commonly employed are LPCVD or APCVD (atmospheric pressure chemical vapor deposition) [9].

### 2.1.2. Polymers

Polymers are a large class of materials that include three major categories: duromers, thermoplastics and elastomers. Polymers have become increasingly popular for MEMS and microfluidic systems for a series of reasons:

- Many polymer materials present a higher mechanical yield strain than silicon, which makes them appealing for those applications where a robust material is required [48].
- Polymers are in general significantly cheaper than other materials. Moreover, since some of the manufacturing processes do not require clean room facilities, fabrication costs can also be significantly reduced [43].
- Polymers can be available in large dimensions (no wafer restriction as for silicon), thus, polymer MEMS do not have size limits [9].
- A new complete series of manufacturing processes are available for polymers, overcoming the limited sets of fabrication techniques for silicon (see Fig. 2.4) [48].
- Polymers provide good chemical, structural and biological functionalities for many applications, i.e. high corrosion and electrical resistance [48].

Among all polymeric materials thermoplastics are quite diffused and constitute the largest part of polymeric MEMS devices [43]. In general, thermoplastics present weak attractive forces between the constitutive chains, and therefore can be easily re-molded, re-shaped and thus recycled by simple heating processes [43]. The selection of the proper thermoplastic to be employed in MEMS depends largely on the specific application and on the

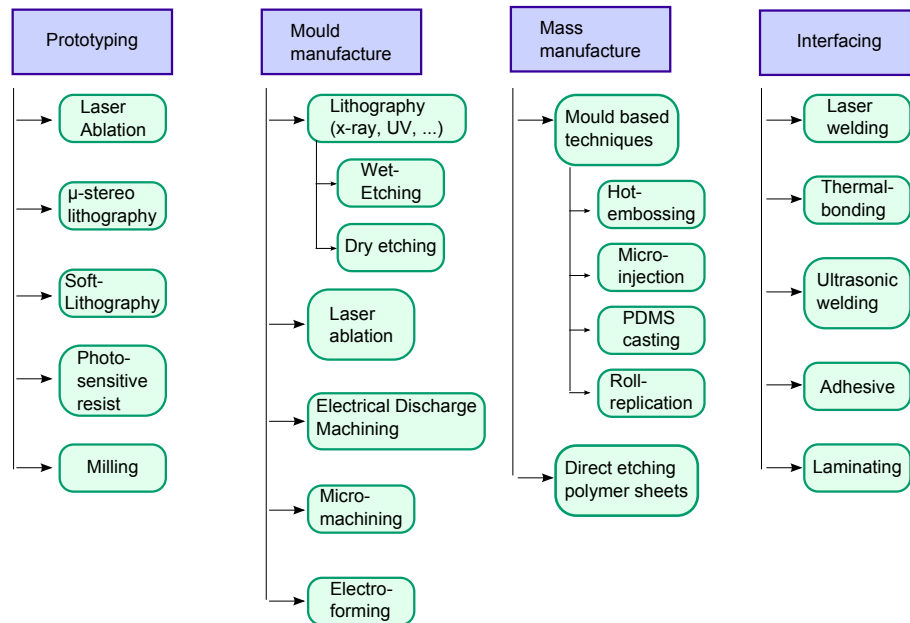


Figure 2.4.: Available manufacturing technologies for polymers [49].

characteristics required by the material. COC (cyclic-olefine-copolymer) presents for example excellent optical properties and is thermally quite stable, while PMMA (polymethylmetacrylate) is quite inexpensive and has a low glass transition temperature. A particular class of polymers are the so called high-performance polymers, among which is, e.g., PEEK (polyetheretherketone). PEEK offers the high chemical and mechanical resistances, and it can be safely used up to temperatures higher than 150 °C [48].

Some classes of polymers can be structured with conventional clean room techniques employed also for silicon structures. Among these the most diffused is photolithography. Other available manufacturing techniques for polymers MEMS are molding, hot embossing, laser micromachining and micro-stereolithography (for which an overview is given in [43]). Figure 2.5 presents examples of polymeric microstructures.

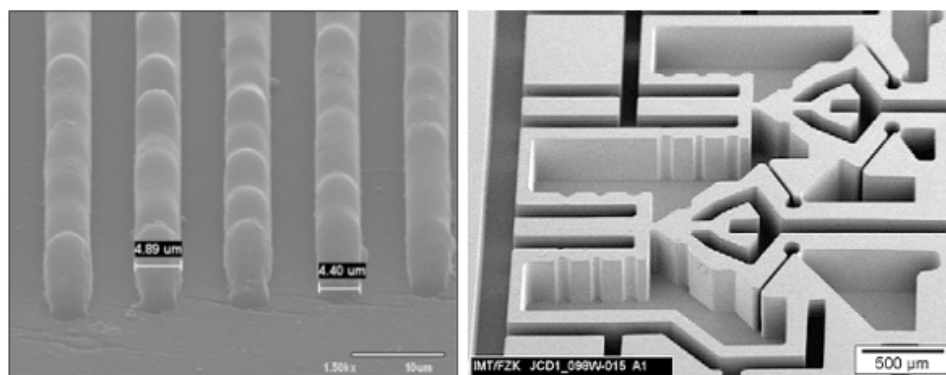


Figure 2.5.: Examples of polymer structures. Micro-injection molded structures (left) [50] and hot-embossed high aspect ratio structures (right) [51].

### 2.1.3. Glass

Glass is a monolithic non-crystalline solid consisting mainly of  $\text{SiO}_2$ . Glass often contains additives or impurities that modify its properties such as mechanical stability, optical transparency, etc. [48].

The precise fabrication of microstructures out of glass is quite challenging, and controlled surface qualities and geometries are difficult to achieve. Moreover, glass is a brittle material and cracks often arise during manufacturing or thermal processing. Some of the processes originally developed for silicon technology can be adapted to manufacture glass structures [52]. Isotropic wet etching of glass is possible by using hydrofluoric acid (HF) as an etchant. Since HF eventually also attacks the material used as mask, only limited depth can be reached for etched structures (usually 10-300  $\mu\text{m}$ ) [52]. To obtain higher aspect ratios and fairly vertical structure walls, plasma dry etching and ion etching can be combined into the deep reactive ion etching technique (DRIE) [48].

Micro-mechanical machining of glass is strongly limited by the intrinsically brittle nature of the material. Cutting processes may often result in damages and fractures. Special techniques like powder blasting and micro-ultra-sonic machining (MUSM), or laser micro-machining can be however exploited to create glass microstructures [52]. Finally, also hot embossing of glass is possible [48].

### 2.1.4. Ceramics

Most structural ceramics are characterized by high thermal and chemical stability, which makes them a suitable material for microdevices working under harsh chemical and thermal conditions (typically very high temperature processes involving corrosive reactants) [52]. Ceramics excel metals in their compression strength but have a lower tensile strength and elasticity. Due to their mechanical properties and their high melting point, molding processes and joining techniques established for other materials can not be transferred to ceramics [52]. While some shaping processes, such as laser machining, electrical discharge manufacturing or micromechanical machining are applied to sintered state ceramics, many other processes developed for creating structures in ceramics start from ceramic powders [52].

Ceramic injection molding (CIM) is a well-established technique for manufacturing ceramic structures with a resolution within the micrometer range [52]. Structures obtained with the CIM technique are shown in Fig. 2.6.

### 2.1.5. Metals and mechanical micromachining

Metals are a class of materials particularly appealing for microsystem applications, for they present very high temperature stabilities and chemical resistances, and at the same time can be manufactured with a broad variety of well established techniques which, according to the necessity, can range from cheap large scale production to ultra precision micromachining. Moreover, metals usually present excellent heat transfer performance, which makes them suitable for applications, where huge amounts of heat must be transferred in small volumes. Among metallic materials different kinds of stainless steels, Nickel-base-alloys, Titanium, or “noble” metals, are just some of the possible choices [43].

The different available manufacturing processes for metals can be classified as abrasive methods, where mechanical micromachining, laser machining and wet chemical etching play a major role, and non abrasive methods, such as e.g. selective laser melting [53]. These manufacturing techniques have not necessarily been developed specifically for microsystem technology, but they have been adapted to meet the needs of MEMS in terms of feasibility of complex structures, required geometrical tolerances and superficial roughness.

Mechanical micromachining is a very flexible and common method to manufacture prototypes and small-scale series microsystems. It consists of the ablation of metallic material from a substrate surface with proper tools made out of, e.g., diamond, titanium, or hard metals [53]. Precision or ultra-precision micromachining allows the creation of complex

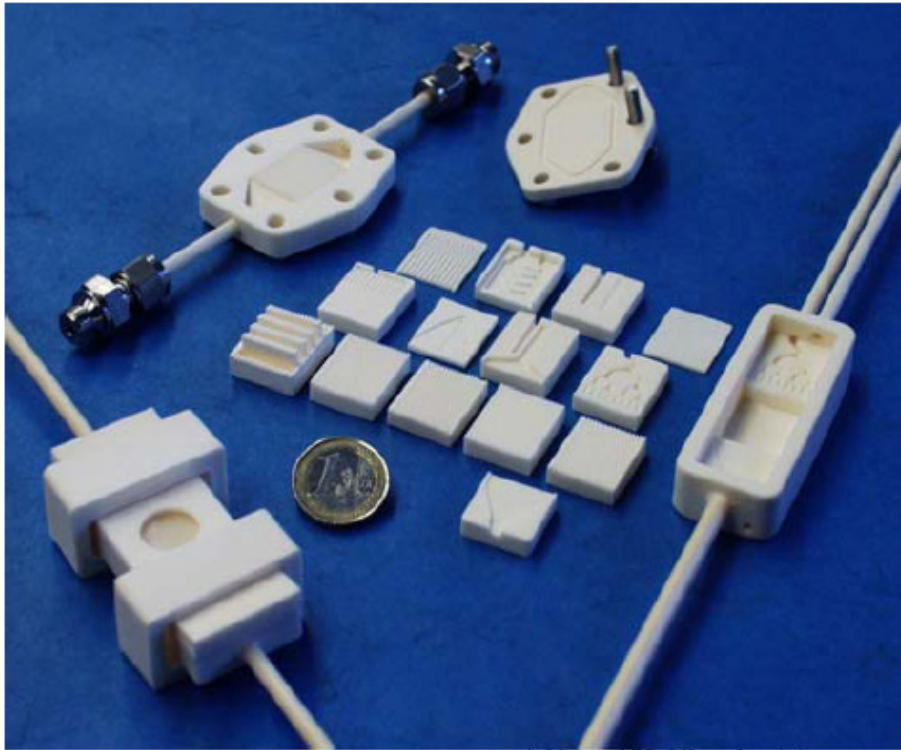


Figure 2.6.: Example of microstructured pieces obtained by ceramic micro injection molding [52].

geometrical structures with precisely defined dimensions (above  $10\ \mu\text{m}$  for precision machining and below  $1\ \mu\text{m}$  for ultra-precision machining). Drilling, turning and milling are the most commonly used processes employed to create microstructures with mechanical micromachining [43]. To meet the required tolerances, special efforts and machining strategies are necessary which compensate effects such as tool deflection. The reachable aspect ratios and minimum structure dimensions are limited by the tool dimensions themselves as well as by the material used. With the state-of-the-art available tools, the smallest dimensions are about  $10\ \mu\text{m}$ , with maximum aspect ratios of about 5 for turning, while the aspect ratio can reach 40 for drilling techniques. However, these parameters are strongly affected by the choice of metal and by the geometrical details to be realized. Examples of micromachining tools and realized structures are given in Fig. 2.7 - 2.9.

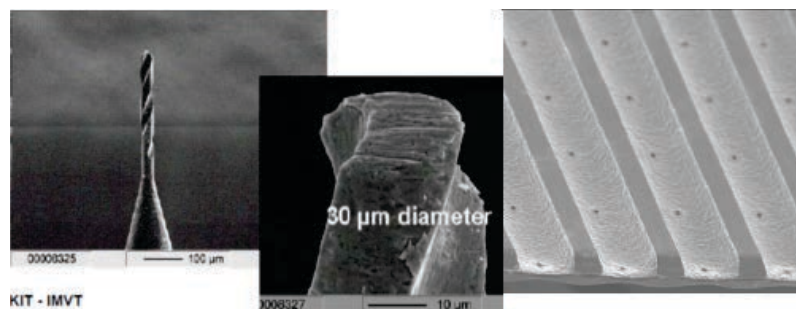


Figure 2.7.: Microdrilling hard metals tools (tungsten carbide) and micro drilled piece in stainless steel [43].

Another important parameter to be controlled is the surface roughness. With surface optimization techniques (i.e. electropolishing, plating or metal coating) very high surface



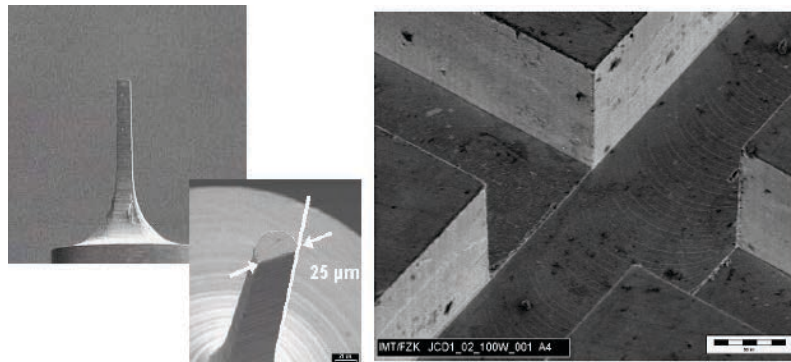


Figure 2.8.: Micromill in hard metal (tungsten carbide) and stainless steel microchannels realized by precision micromilling [43].

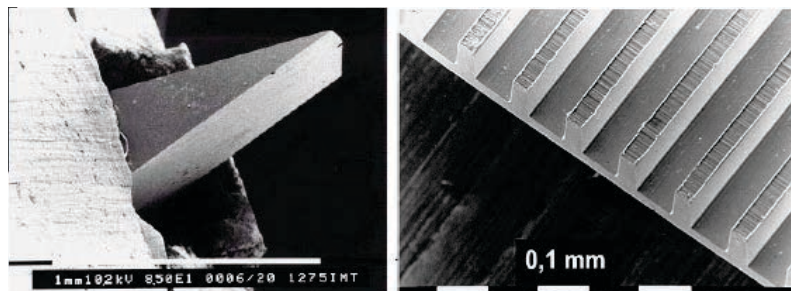


Figure 2.9.: Detail of microturning in diamond and copper microstructure obtained by precision microturning technique [43].

qualities (down to some 10 nm roughness) can be reached, also depending on the metal or alloy used [53].

Besides mechanical micromachining, laser precision machining is also available to create microstructures in metals. Laser machining includes three different processes: cutting, drilling and microstructuring [53]. Laser-assisted microstructuring or micropatterning can be realized with different processes, namely ablation via sublimation, ablation via laser-cutting, ablation via melt ejection and laser-micro-caving (LMC) [43]. While ablation techniques are not very precise and lead to debris formation and contamination, LMC, which can be described as a laser-induced oxidation of the surface, allows a cleaner patterning of metals, with a reduced amount of debris and melt [43].

Another technique adapted to micromachining of metals is the so called selective laser melting (SLM). SLM is based on the micro-stereolithography technique adopted for rapid-prototyping of polymers. This technique has the main advantage of allowing the creation of 3D structures without requiring bonding or assembling. On the other hand the achievable surface qualities are quite poor, and the gas tightness of the obtained structures is usually insufficient (cf. Fig. 2.10) [43].

A final technology to be mentioned and commonly used to create microstructure in metals is etching. Both wet chemical etching and dry etching are available for metals and represent a valid alternative to mechanical micromachining. In particular, the manufacturing of complicated geometries or channel arrays is easier with etching techniques [53]. As a drawback, valid in particular for wet chemical etching, the achievable resolutions and surface qualities are poor. Moreover, as wet chemical etching is an isotropic process, the structure cross sections typically present a semi-elliptical shape, while the smallest achievable dimensions are limited by the fact that the etching extends isotropically below

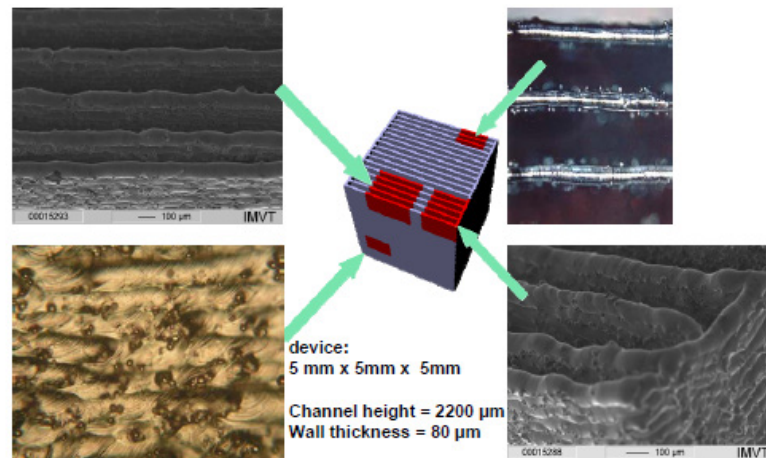


Figure 2.10.: Microdevice realized by the selective laser melting technique (SLM) starting from steel powder, with details of the obtained structure with the typical poor surface quality [53].

the mask and the obtained openings are defined by the mask width plus twice the etching depth (this mainly limits the aspect ratio that can be obtained with wet chemical etching) [53].

### 2.1.6. LIGA manufacturing technique

The LIGA process for manufacturing microstructured devices is radically different from the other fabrication processes, offering great potential in creating microstructures of different materials and with high aspect ratio and previously unachievable absolute tolerances [54]. The term LIGA is an acronym for the German terms *Lithografie* (Lithography), *Galvanoformung* (Electroforming) and *Abformung* (Molding), which represents the three main steps of the manufacturing technique firstly developed at the Nuclear Research Center Karlsruhe (now Karlsruhe Institute of technology). A detailed description of the different steps of the LIGA process is given in [2].

For most applications the structures obtained with LIGA are used as molds for subsequent injection molding. Indeed, as the manufacturing process is slow and very costly, to allow LIGA to be an economically viable micromachining alternative it is necessary to succeed in replicating the structure without remaking the primary models [54]. Examples of structures obtained with the LIGA process are shown in Fig. 2.11.

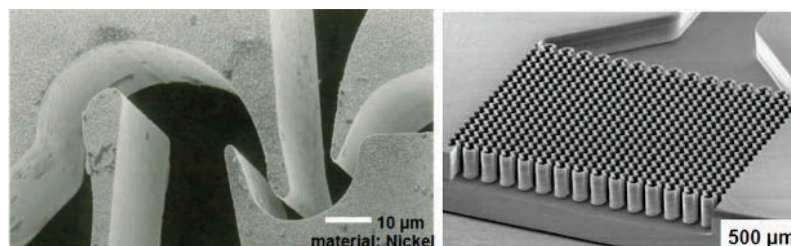


Figure 2.11.: Example of structures realized with the LIGA manufacturing technique. On the left: complex 3D geometry of a nozzle for the separation of uranium obtained in nickel [55]. On the right: high aspect ratio structures for a micromixer in nickel [56].

### 2.1.7. **Assembly and packaging**

After the manufacturing of the microstructures with any of the above described processes, the second necessary step for the realization of microsystems is assembly and packaging. While the assembly of devices at macroscales does not present major problems, this step may present some critical issues when coming to microscales. Many problems are related to the required tolerances and surface qualities to achieve good alignment and sealing of the assembled structures [43]. Small misalignments during the assembling/bonding phase might result in severe geometrical deformation of the final structures. An improper surface quality or the formation of burrs during the microfabrication step are two of the main reasons for structure misalignment and therefore must be accurately controlled during the structure manufacturing. Alignment techniques to avoid errors might be mechanical (e.g. alignment pins) or automated (e.g. using laser diodes and photosensors) [43]. Another aspect to be carefully considered is related to tolerances. Insufficient manufacturing tolerances lead to misfit or too tightly fit components, resulting in fitting over-stress and premature failure of the assembly. On the other hand, excessive tolerances may result in loose fits.

According to the employed material, different assembly and packaging techniques are available. For silicon structures, bonding is usually the adopted process for assembly. Among the available bonding methods, adhesive bonding, anodic bonding and fusion bonding are the most common [44].

For the adhesive bonding an intermediate layer of polymeric material (usually PMMA) or glass is used to cover the wafer surface. Successively, the two parts to be bonded are brought in contact and heated.

In the anodic bonding a substrate of glass or Pyrex<sup>®</sup> is joined to the silicon substrate by using a strong electric field while the two pieces are heated (above 450 °C). A ion exchange between the two materials is established resulting in a permanent bond.

Finally, fusion bonding results in a cross-oxidation of the silicon over the bonding interface. To enhance this process, special activation techniques for the oxide or on the wafer surface are available [44].

For microstructures made out of polymers the easiest assembly technique is direct gluing [43]. However, some polymers have no adhesive surface and require additional processes to modify it. Moreover, draining of the glue in the microstructure and clogging of microchannels might occur. By controlling the dosage of the glue or by creating special cavities in the structures it is possible to overcome some of these issues.

As alternative to gluing, welding is another interesting technique. In this case no additional material is required since the polymer itself is activated to diffuse into the counterpart. For this purpose solvents, ultrasonic vibrations or laser sources can be used [43]. Laser-transmission welding in particular is a powerful tool for welding transparent or opaque polymers with structural details down to 10  $\mu\text{m}$ . These techniques requires usually the application of resins with absorbing dyes or special absorbing nanolayers over the polymer surface [43].

A possible process to assemble ceramic or glass structures when direct bonding can not be used (e.g. when two materials with different coefficients of thermal expansions must be joined) is soldering. In this case an intermediate material (usually vitreous or glass-ceramic sealant) is used between the two parts to create joints which can stand relatively high temperatures (which must nevertheless always be below the melting temperature of the glass) [52].

A particular technique to assemble materials (primarily metals) is diffusion bonding, which has the advantage of not requiring any additional material (like soldering or brazing) and creates stable microstructured devices from single micromachined metal foils [43]. The process starts from a stack of metal foils with the desired arrangement which is then positioned in an evacuation furnace, pressed with a prescribed force and heated up to above 2/3 of the material melting temperature. Under these conditions the material at the adjacent interface diffuse into each other creating very stable and insolvable connections. The three main steps of the diffusion bonding technique are shown in Fig. 2.12. While for many metals the use of diffusion bonding is already well established, some aluminum or chromium alloys (which generate a protective layer on top of the surfaces) or materials with high melting temperatures (e.g. tungsten) are not suitable to be joined with this technique.

Nonoxide ceramics can also be directly employed for diffusion bonding processes, while oxide ceramics need an intermediate layer to facilitate the bonding. In general, the control of the process parameters is not trivial and small contamination of the material composition may lead to failure. Finally the presence of large burr deriving from previous manufacturing steps must be avoided.

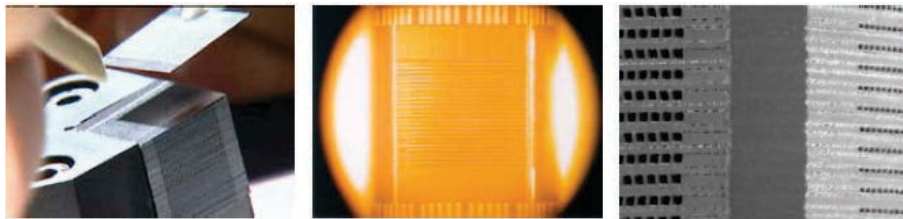


Figure 2.12.: Three steps of the diffusion bonding assembling technique. From the left: stacking of single foils, heating-up and pressing of the foil stack, final monolithic structure [53].

When diffusion bonding can not be used, laser welding can be employed as an alternative [43]. Laser deep penetration welding or conduction welding are both available laser-assisted techniques which can be employed. In the first case high aspect ratios can be achieved, while the second ensure small heat-affected zones (more suitable for micropackaging). Temporal laser pulse shaping has also been adopted to combine the advantages of the two different methods, allowing the manufacturing of completely laser-based devices. When multi-foil assemblies are not required, or when the joining should be reversible (the structures should be opened and re-closed), straightforward conventional techniques of packaging such as clamping and screwing can be used, employing O-rings or gaskets for sealing.

## 2.2. Sensor technology in MEMS

With the increasing number of scientific and industrial applications of MEMS, microdevices and microreaction technology, the requirement for precise analytical techniques for measurement and control of key process parameters of the ongoing processes is becoming a standard. For this reason, suitable sensors and analytical tools have to be developed and integrated in microstructured devices without disturbing and degrading the performance of the analytical technique or of the entire device.

Thanks to the spreading of IC technology, the miniaturization of sensors has become possible and a variety of different configurations has been established [9]. Microsensors have the advantages of being sensitive and accurate with minimal amount of required

sample substance [8]. The small dimensions achievable with IC surface machining processes allows the integration of a sensing and even an actuating element and a signal transduction unit in a single device which can be considered as a core unit of a microelectromechanical system [9]. This principle is illustrated in Fig. 2.13.

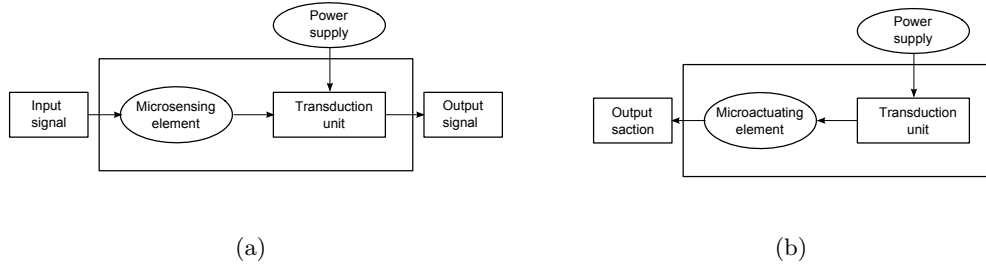


Figure 2.13.: MEMS as a microsensor (a) and as microactuator (b) [9].

Despite the fact that integration of sensors in microsystems as inline analytical tools is a relatively new field, the basic working principles of microsensors are well known, as they directly derive from the conventional sensor technology. A good understanding of these principles is therefore important to be able to further develop microsensors and their integration in microsystems.

Sensors can be generally classified according to the measured quantity or to the physical effect they are based on (as illustrated in Tab. 2.1).

Table 2.1.: Correlation between physical effects and measured quantities in conventional sensor technology [57].

	Effect							
	Thermal	Optical	Magnetic	Piezo-resistance	Piezoelectric	Pyroelectric	Chemical	Electrical
Quantity								
Position		X	X	X	X			X
Force				X	X			X
Pressure				X	X			X
Temperature	X	X				X		X
Light	X	X			X	X		X
Gas		X					X	X
Magnetic field			X					X

### 2.2.1. Temperature Sensors

The exact measuring of temperature is one of the most important challenges of sensor technology. The large number of temperature dependent physical processes leads to a broad range of possible methods and components which are suitable for measuring temperatures (see Tab. 2.2).

Table 2.2.: Sensors types and methods for temperature measurement (adapted from [57]).

	Range in °C	Remarks
Thermoelement	-200...+1600	small voltage signal, expensive electronics, Zero-point compensation
Thermistors	-270...+850	small voltage signal, expensive electronics
Si-elements	-50...+150	resistance, transistors, lower temperature limit given by the body housing, cheap sensing element
PTC-Thermistor	-30...+350	steep temperature threshold, cheap, robust
NTC-Thermistor	-50...+350	Exponential characteristic curve, compromise between precision and price
Photodiode	0...+4000	remote measurement, below +400 °C semiconductor with small energy gap
Pyroelectric detector	0...+4000	remote measurement, high sensitivity, dynamic measure
Strain thermometer	-200...+1000	liquid working fluid, bi-metal, punctual measurement
Gas thermometer	-250...+1000	Physical measurement, very complex, pressure measurement
Color T-measurement	-30...+1600	Color change of e.g. liquid crystals
Quartz thermometer	-40...+300	Digital output signal

### Thermoelements

If two metallic conductors of different materials are brought in intimate contact, it is possible to measure a temperature-dependent voltage difference, the so called thermal voltage generated by the Seebeck effect (for a complete description of the physical phenomenon see [58]). Figure 2.14 shows a high-impedance instrument reading the voltage  $V$  which corresponds to the temperature  $T_2$  at the measuring point reduced by the constant reference junction temperature  $T_1$ . This relationship is expressed by Eq. 2.1, where  $\alpha_s$  is the Seebeck coefficient expressed in V/K.

$$\Delta V = \alpha_s \Delta T \quad (2.1)$$

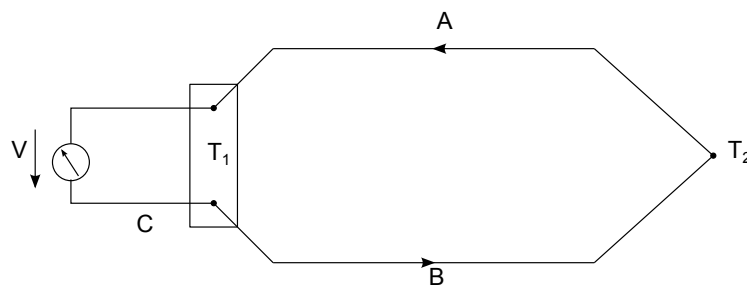


Figure 2.14.: Thermal circuit with the two branches A and B (of different conducting materials), measured temperature  $T_2$  and reference temperature  $T_1$ .



The Seebeck coefficient is a bulk material property which can be expressed as:

$$\nabla E_F/q = \alpha_s \nabla T \quad (2.2)$$

where  $E_F$  is the Fermi energy and  $q$  is the elementary charge. From Eq. 2.2 it is evident that there will be no gradient in the Fermi energy and thus in the electrical potential, unless a temperature gradient is present.

To obtain high voltage signals, materials with large Seebeck coefficients should be used for thermocouples. Low-doped semiconductors are well suited to this purpose. However, some issues in the employment of these materials might arise:

- the position of the measuring point should be relatively far away from the position of the reference point as otherwise a mutual influence in the heat conduction could result in a distortion of the measurement.
- the supply lines to the measuring point should be robust and resistant to mechanical stress to avoid failure during assembly and disassembly.

Both conditions are difficult to meet with semiconductor materials: the bridging of large distances is difficult due to the single-crystalline structure and the brittle nature of semiconductors, which make them susceptible to breakage. Nevertheless, thanks to the advances in semiconductor fabrication technologies, it has been possible to manufacture microsensors on silicon substrates based on the Seebeck effect, which are also compatible with MEMS technologies [36].

Based on the same principle as thermocouples (the Seebeck effect), thermopiles are temperature-difference transducers particularly suitable for MEMS applications. In Fig. 2.15 the schematic concept of an integrated silicon thermopile is shown.

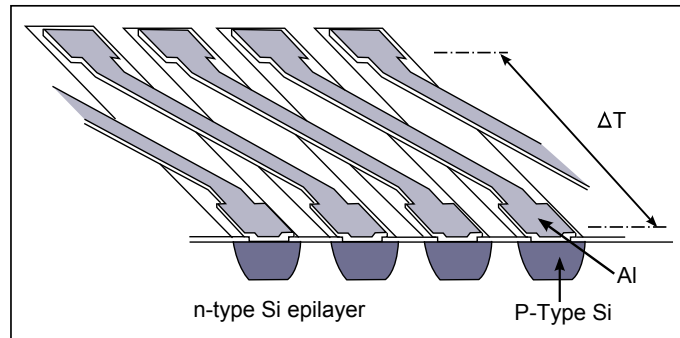


Figure 2.15.: Structure of a typical integrated p-type silicon/aluminum thermopile.

The typical structure of such transducers consists of many thermocouples (e.g. p-type silicon-aluminum junctions) connected in series (*thermocouple cascade*). The different junctions experience the same temperature gradient, resulting in an enhanced sensitivity of the sensor and a high output. Sensitivities of about 5-50 mV/K are common for miniaturized thermopiles. An important parameter for thermopiles is the characteristic resistance, which depends on the number of stripes, the length of the stripes in squares (length-width ratio) and the electrical sheet resistance. Typical values for the resistance range between 10-100 k $\Omega$  [36].

Among the various possible applications of miniaturized thermopiles, silicon flow sensors are particularly interesting [32]. The thermal conductance from the hot to the cold region of the thermopile is lowered by heat conduction from the sensor to the ambient. If the sensor is placed within a fluid flow, the heat transfer and thus the temperature difference

between the hot and the cold region are related to the fluid velocity. By measuring the temperature difference between two fixed points, in between which a heater is placed, it is possible to derive the velocity of the flow, as schematically represented in Fig. 2.16.

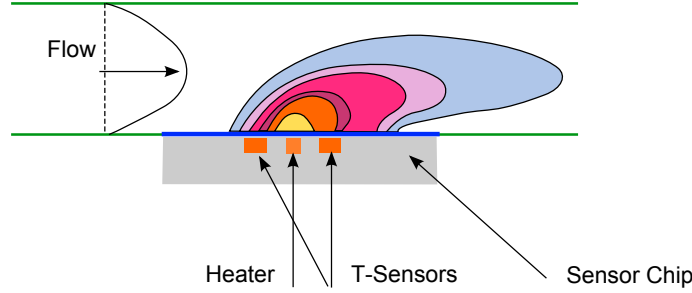


Figure 2.16.: Thermal flow sensor working principle.

### Thermistors

The working principle of thermistors is based on the temperature dependence of the electric resistance. The resistance  $R$  of macroscopically homogeneous components of length  $d$  and cross section  $A$  depends on geometrical and material properties and can be evaluated by the location-independent values of the specific conductivity  $\sigma_{sp}$  or the specific resistivity  $\rho_{sp}$  as given in Eq. 2.3 [58].

$$R = \rho_{sp} \cdot \frac{d}{A} = \frac{1}{\sigma_{sp}} \cdot \frac{d}{A} \quad (2.3)$$

Ignoring the temperature variation of the geometrical parameters (which is negligible with respect to the electric properties variations), the temperature dependence of the material resistance is given by:

$$\frac{\partial R}{\partial T} = \frac{\partial \rho_{sp}}{\partial T} \cdot \frac{d}{A} = -\frac{1}{\sigma_{sp}^2} \frac{\partial \sigma_{sp}}{\partial T} \cdot \frac{d}{A} \quad (2.4)$$

The temperature dependence of the specific resistivity varies for the different material classes. In the following a short overview for metals, semiconductors and ceramics is given since these are the most commonly employed materials for the fabrication of thermistors.

In metals the conductivity is mainly influenced by two opposite phenomena. On one hand the electron density increases with increasing temperature because of the broadening of the Fermi-Dirac distribution, which affects the effective conductivity of the charge carriers (positive contribution to the conductivity), while on the other hand the electron mobility decreases with increasing temperature for lattice scattering phenomena (negative contribution to the conductivity). However, the negative contribution generally prevails and the general behavior of the specific resistance against temperature is therefore positive (i.e. the specific resistance increases with increasing temperature as shown in Fig. 2.17). For this reason metallic thermistors are usually referred to as Positive Temperature Coefficient (PTC) resistors [58]. Figure 2.17 also shows that the resistivity temperature dependence of many common metals usually presents a linear behavior.

A very different behavior than that of metals is exhibited by semiconductor materials, for which both coefficients in Eq. 2.3 strongly depend on the temperature. In particular, the temperature dependence of the resistivity does not show a linear behavior as in metals (see Fig. 2.18). Within the working range of Si-temperature sensors, which extends from  $-50$  to  $+150$  °C, the mobility of charge carriers decreases with increasing temperature due



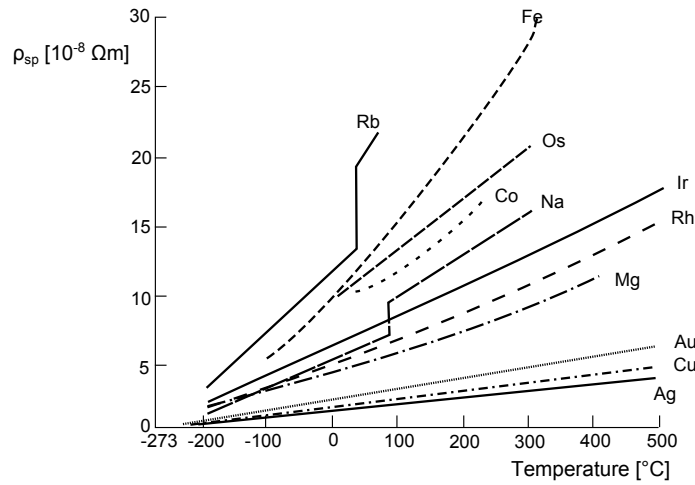


Figure 2.17.: Temperature dependence of the specific resistivity for some metals [58].

to the thermal lattice scattering, causing an increase in the resistivity. At higher temperatures intrinsic conduction predominates, i.e. when the thermal production of charge carrier pairs outbalances the lattice scattering, and the resistivity, after reaching a maximum value, decreases [58].

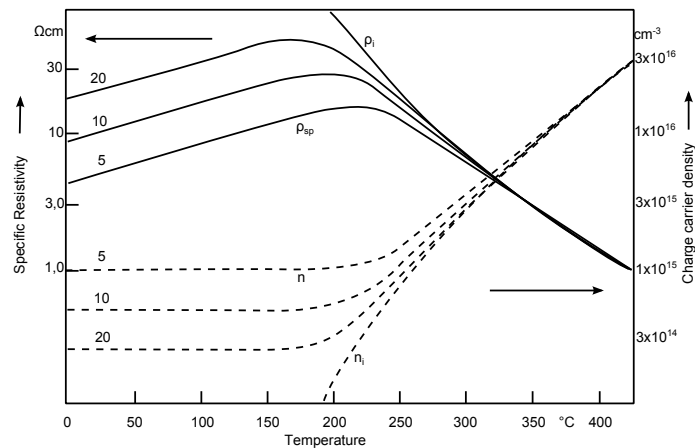


Figure 2.18.: Temperature dependence of the charge carrier density  $\rho_n$  and the specific resistivity  $\rho_{sp}$  for n-doped semiconductors [57].

The major advantage of silicon temperature sensors is that they can be produced with the help of advanced semiconductor technology quite inexpensively. Because of the small chip size of the sensors, the simultaneous production of a large number of sensors per wafer is possible.

In many ceramic materials the temperature dependence of electrical conductivity is similar to that of semiconductors, but some ceramics have an almost metallic conductivity. Through the production of mixed crystals of more and less conductive ceramics the temperature coefficient can be varied continuously, which is a great advantage for the manufacturing of temperature sensors (see Fig. 2.19) [58].

Depending on the behavior of the specific resistivity with temperature, ceramic thermistors can be classified as negative temperature coefficient (NTC) resistors, when the electron mobility increases while the electron density is constant and the resistivity consequently decreases with increasing temperature, or as positive temperature coefficient (PTC) resis-

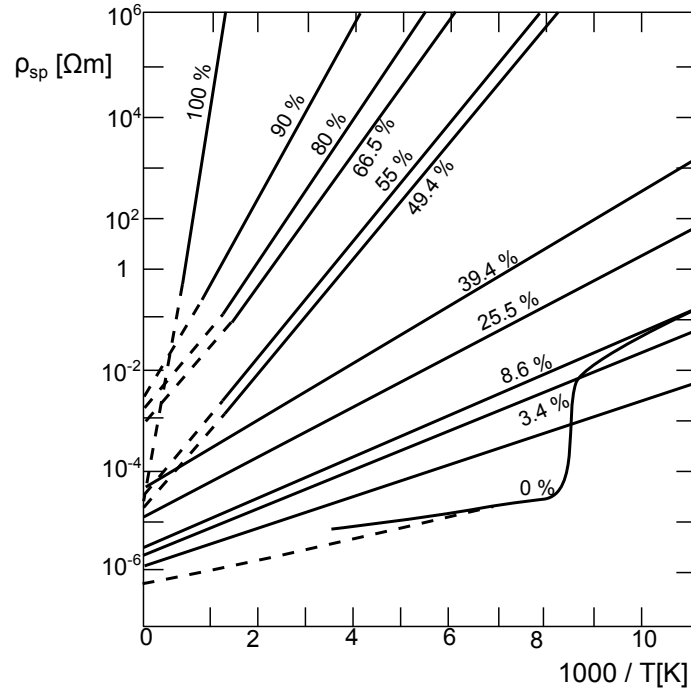


Figure 2.19.: Adjustable specific resistivity of magnetite ( $\text{Fe}_3\text{O}_4$ ) for different mixtures of Spinel insulant [58].

tors, when for special grain boundary effects the specific resistivity increases with increasing temperature.

Regardless of the constituting material, all kinds of thermistors need a bias current to allow the detection of the resistance signal. With a current-carrying measurement (in contrast to the nearly currentless measurement with thermocouples), the voltage drop on the measuring leads always to relatively large measurement errors (i.e. the error order of magnitude is comparable to that of the measured quantity itself). However, by smartly designing the wiring for the sensor contacts, the error can be reduced or avoided [58]. In Fig. 2.20, four possible layouts are illustrated. The easiest one is the 2-wire configuration, which however leads to the highest uncertainties. 4- or 3-wire configurations are therefore preferred, where the ones with a Wheatstone-bridge layout have the drawback of requiring bridge resistors with defined and known temperature coefficients. In some cases this problem can be overcome by placing the bridge resistors out of the sensor area, at a defined and constant temperature.

### Diodes and transistors

The DC characteristic of a pn-diode has a strong temperature dependency as shown by the Shockley equation:

$$I = I_S \left( \exp \frac{eV}{k_B T} - 1 \right), \quad (2.5)$$

where  $e$  is the charge of an electron,  $V$  is the voltage and  $k_B$  is the Boltzmann constant. For the saturation current  $I_S$  the following relationship applies:

$$I_S = AT^\alpha \exp \left( -\frac{E_{go}}{kT} \right). \quad (2.6)$$

In Eq. 2.6,  $A$  is a constant and  $E_{go}$  is the band gap extrapolated at  $T=0$  K. In the exponent  $\alpha$  doping ratio and geometry factors are taken into account as well as the temperature

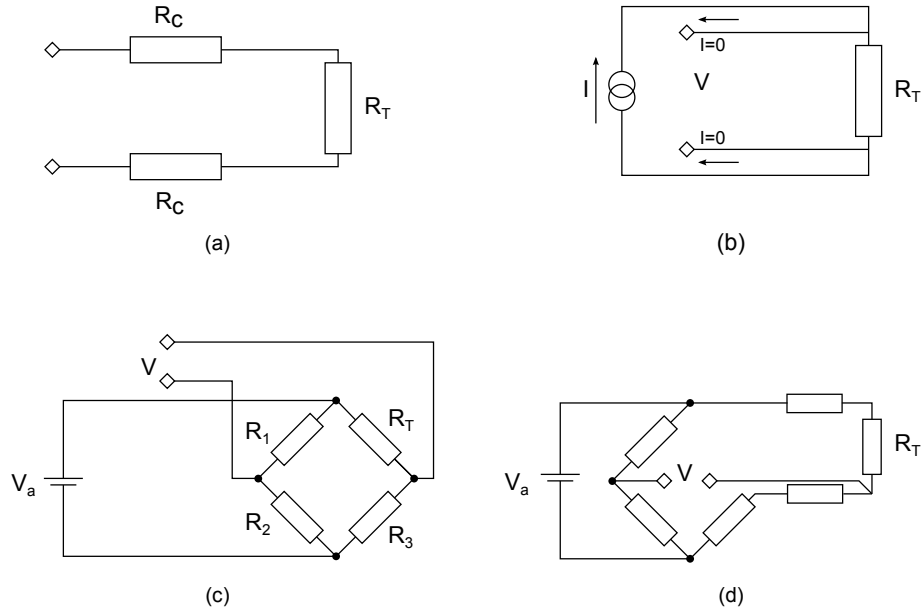


Figure 2.20.: Possible configurations of resistor connections. a. 2-wire configuration. b. 4-wire configuration with voltage measurement on the sensor resistance. c. 4-wire configuration with Wheatstone-bridge layout. d. 3-wire configuration with Wheatstone-bridge layout.

variation of the diffusion constant. When the polarity is in the forward direction, the temperature dependence is, according to Eq. 2.5, particularly high. As  $eV \gg kT$  the temperature response of  $V$  can be rewritten (neglecting the unitary term) as:

$$\left(\frac{\partial V}{\partial T}\right)_I = -\frac{E_{g0}/e - V}{T} - \frac{\alpha k}{e}. \quad (2.7)$$

By using a bipolar transistor (which is operated by connecting the base and collector as a diode) instead of a diode, the exponent  $\alpha$  can be particularly high with appropriate current gain.

Silicon transistors have proven to be suitable as temperature sensors as they present an appropriate band gap, a favorable sensitivity and a good material robustness even under harsh conditions [58]. Unfortunately, manufacturing tolerances have a great influence on the temperature dependence due to effects of the local crystal quality and surface effects on the saturation current. The differences in the base-emitter voltage for the same collector current and room temperature as well as the scattering of the temperature coefficients compromise the interchangeability of the sensors and thus prevented the widespread use of transistor temperature sensors. An electronic signal processing with transistor temperature sensors is only economically feasible if the process does not have to be adjusted individually for each sensor, i.e. if the sensor characteristics from item to item have sufficiently small fluctuations and are also stable over longer periods [57].

### Other temperature measurement techniques

Besides the most common techniques which can be used to measure temperatures and which have already been described, other physical effects can be exploited for this purpose. In the following a list of them with a short description of the working principle is given, while a more detailed analysis can be found, e.g., in [58].

*Pyroelectric temperature sensors* are based on the so-called pyroelectric effect, for which the polarization of certain materials (e.g. ferroelectric materials) depends on the temper-

ature. If two initially neutral metal electrodes are coated with a ferroelectric material in between, when activated by a temperature difference a potential difference will be created by the ferroelectric dipole charge, resulting in a measurable external voltage. The voltage difference remains constant only with a precise insulation of the sensor and by using a extremely high input impedance amplifier.

*Quartz crystal oscillators* are widely used as building blocks for the production of electrical vibrations with constant frequencies. With a different embodiment, they can also be used as very sensitive temperature measurement instruments with frequency-analogue output signals. The temperature coefficient of the resonant frequency of quartz crystals may be in fact considerably increased by the choice of special crystallographic cut angles relative to the electrical and optical axis. The great advantage of quartz temperature sensors relies on the analog frequency output signal which, by using an electronic divider, can be read with an accuracy up to one Hertz. This provides temperature resolutions far below 1 K.

*Fiber-optic temperature sensors* have been increasingly used for the simplification of optical radiation transport. These systems can be exploited for temperature measurements, as many typical optical properties (absorption, fluorescence, etc.) of materials have a characteristic temperature dependence, which can be scanned by an optical fiber, transmitted and analyzed. Critical for practical applications is the neutral transmission behavior: the sensor signal should be as little dependent on the structure and on the fiber-optic transmission length as possible. This can be achieved by measuring the intensity ratio of different fluorescence lines with different temperature dependencies or by measuring of the temporal distribution decay curves.

*Mechanical temperature sensors* include all those temperature sensors that exploit the thermal expansion of gases, liquids or solids (e.g., the common mercury thermometer), while an example for a *chemical temperature sensor* is the exploitation of the ability of various chemical compounds to change their color either abruptly or continuously (thermal paints) at a certain temperature or within a given temperature interval.

### 2.2.2. Force and pressure sensors

Along with temperature measurement, force and pressure measurements have the greatest technical importance. The basic effect of most force and pressure sensor is the elastic deformation of a solid body: in this case the external mechanical forces act against the interatomic bonding forces, and a reversible change in shape is produced as a response [58]. Plastic deformations are usually undesirable for pressure sensors, as the cycling change of the sensor characteristics can eventually lead to a fatigue fracture.

#### Piezoresistive sensors

The change in shape of a conductor under the influence of a mechanical force affects the electrical resistance of the body itself and can therefore be used as the basis for the production of resistive pressure sensors. Piezoresistors refer to sensors whose resistivity changes with applied strain. Metal resistors change their resistance in response to strain mainly due to the shape deformation mechanism. Such resistors are technically called strain gauges. The resistivity of silicon (and other semiconductors) changes as a function of strain. Silicon is therefore a true piezoresistor [59].

In a piezoresistor the resistance  $R$  changes linearly with the applied strain:

$$\frac{\Delta R}{R} = G \cdot \frac{\Delta L}{L}, \quad (2.8)$$

where the proportional constant  $G$  is called the gauge factor of a piezoresistor.

Although the resistance is usually measured along the resistors longitudinal axis, the applied strain may contain three primary vector components: one along the longitudinal axis of the resistor and two arranged  $90^\circ$  to the longitudinal axis and each other [59]. For this reason a piezoresistive element behaves differently towards longitudinal and transverse strain components. The change of the measured resistance under the longitudinal stress component is called longitudinal piezoresistivity, while the relative change of measured resistance to the longitudinal strain is called the longitudinal gauge factor. Similarly, the transverse piezoresistivity and the transverse gauge factor can be defined. The longitudinal and transverse strains are often present at the same time, though, for any given piezoresistive material, one of them may play a clearly dominating role. The total resistance change is the sum of all changes under longitudinal and transverse stress.

Most piezoresistors are temperature-sensitive. For the purpose of eliminating this effect the Wheatstone bridge configuration for the sensor circuit is particularly effective (see Fig. 2.21) [59].

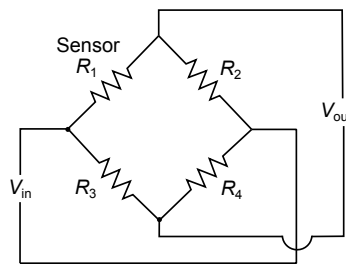


Figure 2.21.: Wheatstone bridge circuit configuration for a sensor.

The output voltage is related to the input voltage according to the relation given in Eq. 2.9.

$$V_{out} = \left( \frac{R_2}{R_1 + R_2} - \frac{R_4}{R_3 + R_4} \right) V_{in}. \quad (2.9)$$

Variations of the environmental temperature would cause changes to all resistances in the bridge with the same percentage. Hence, the temperature variations cause the numerators and the denominators of the right-hand terms of Eq. 2.9 to be scaled by an identical factor. The temperature effect is therefore canceled out.

Metal strain gauges are commercially available, often in the form of metal-clad plastic patches that can be glued to surfaces of interest. Resistors are etched into the metal cladding layer. Typically, a zigzagged conductor path is used to effectively increase the length of the resistor and the amount of total resistance in a given area (Fig. 2.22).

Some of the criteria to select a metal strain gauge include accuracy, long-term stability, cyclic endurance, range of operational temperature, ease of installation, tolerable amounts of elongation and stability in a harsh environment. To satisfy these requirements commercial metal strain gauges are often not made of pure metal thin films but of tailored metal alloys [59]. For conventional applications of strain gauges as pressure sensors, thin wire strain gauges are fixed on macroscopic bodies (spring bellows) so that the mechanical stress and strain are transferred from the surface of the spring bellows to the strain gauges. Another common configuration of pressure sensors require the application of strain gauges on membranes to convert the pressure into a measurable force. The use of membranes has the advantage that a thermal load does not directly affect the measurement body where it can cause permanent modifications [58].

For micromachined pressure sensors strain gauges are fabricated on mechanical beams and membranes using monolithic integration processes. Metal resistors are generally deposited

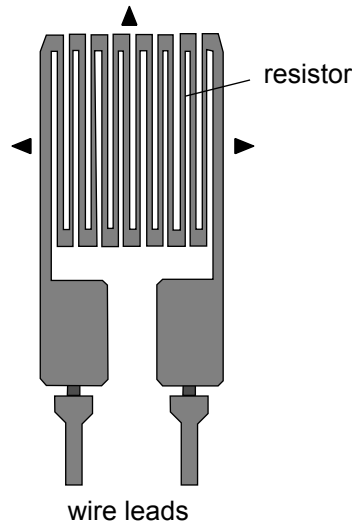


Figure 2.22.: Serpentine-type coil for a strain gauge.

by CVD or sputtering and patterned. Elemental metal thin films can be used as strain gauges in MEMS, even though they do not compare favorably with semiconductor strain gauges in terms of piezoresistive gauge factors. However, metal thin films provide sufficient performance for many applications. Using metal instead of a semiconductor eliminates the need for doping and for long process rows [58].

Semiconductor strain gauges are made by selectively doping silicon. The piezoresistive coefficients of single-crystal silicon are not constant but are influenced by the doping concentration, the type of dopant and the substrate temperature. Appropriate doping concentrations must be carefully selected when designing silicon piezoresistors. For both p- and n-type silicon, the value of the piezoresistive coefficient decreases with increasing temperature and doping concentration [59]. A successful design must balance the needs to have an appreciable resistance value, to maximize the gauge factor, and to minimize temperature effects. The temperature coefficient of resistance (TCR) of a piezoresistor should ideally be as small as possible to minimize effects of temperature variation. For piezoresistors made of doped silicon, the TCR is a function of the doping concentration [59].

For MEMS piezoresistors, polysilicon offers a number of advantages over single-crystalline silicon, including the ability to be deposited on a wide range of substrates. However, the gauge factor of polycrystalline silicon is much smaller than that of single crystalline silicon. It does not depend on the orientation of the resistor within the substrate, but is influenced by growth and annealing conditions. The gauge factors for n- and p-type polycrystalline silicon substrates are strongly influenced by the doping concentration [59].

Bulk microfabricated pressure sensors with thin deformable diaphragms made of single-crystal silicon are within the earliest MEMS products and still dominate the market today. One example is shown in Fig. 2.23 [60]. The piezoresistors are located in the center of four edges, which correspond to regions of maximum tensile stress when the diaphragm is bent by a uniformly applied pressure difference across it. The resistors are connected in a full Wheatstone bridge configuration to compensate thermal offsets. Using microfabrication, the diaphragm thickness can be controlled precisely (typical thicknesses are 25  $\mu\text{m}$  or below).

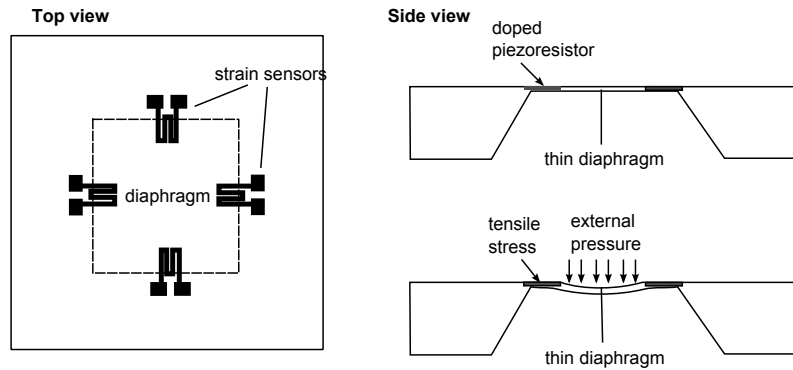


Figure 2.23.: Silicon piezoresistor based pressure sensor.

### Piezoelectric sensors

Piezoelectric sensors, as the name suggests, are based on the piezoelectric effects, according to which the polarization of some materials (piezoelectric materials) changes when they are strained by external forces (i.e. the electrical charges are displaced and accumulate on opposing surfaces of the piezoelectric element). Besides quartz, which is one of the most sensitive and stable piezoelectric materials, also ferroelectric materials (such as polycrystalline piezoceramics) can become piezoelectric by the application of a large electric field [58]. With stiffness similar to that of many metals, piezoelectric materials produce a high output voltage with very little strain. Thus, piezoelectric sensing elements provide an excellent linearity over a wide amplitude range. A final important note about piezoelectric materials is that they can only measure dynamic or changing events. While static events will cause an initial output, this signal will slowly decay (or drain away) based on the time constants of the piezoelectric material or the attached electronics [58].

Depending on how a piezoelectric material is cut, three main modes of operation can be distinguished: compression, longitudinal, and shear.

The compression design features high rigidity, making it useful for implementation in high frequency pressure and force sensors. Its disadvantage is that it is somewhat sensitive to thermal transients.

The simplicity of the longitudinal design is offset by its narrow frequency range and low over-shock survivability.

The shear configuration is typically used in accelerometers as it offers a well balanced blend of wide frequency range, low off axis sensitivity, low sensitivity to base strain and low sensitivity to thermal inputs [58].

Piezoelectric sensors measure in principle only forces. To be used as pressure sensors, the pressure must be converted into a proportional force, e.g. by a membrane. While strain gauges generally measure surface tensions, in piezoelectric sensors the stress state of the entire sensor volume is taken into account (any existing local variations of the power distribution will be averaged).

### Other pressure sensors

*Capacitive pressure sensors* consist of parallel plate capacitors coupled with diaphragms (usually metallic) and exposed to the process pressure on one side and the reference pressure on the other side. Electrodes are attached to the diaphragm and are charged by a high frequency oscillator. The electrodes sense any movement of the diaphragm and this changes the capacitance. The change of capacity creates a change of the electrical field, which results in a voltage proportional to the pressure variation.

*Inductive pressure sensors* are coupled with a diaphragm or a Bourdon tube. A ferromagnetic core is attached to the elastic element and has a primary and two secondary windings. A current is charged to the primary winding. When the core is centered, the same voltage will be induced to the two secondary windings. When the core moves following a pressure change, the voltage ratio between the two secondary windings changes. The difference between the voltages is proportional to the change in pressure.

*Potentiometric sensors* have an arm mechanically attached to the elastic pressure sensing element. When pressure changes the elastic element deforms, causing the arm to move backwards or forwards across a potentiometer, and a resistance measurement is taken. These sensing elements present an optimum working range, but are seemingly limited in their resolution and therefore not very much used.

*Vibrating element pressure sensors* function by measuring a change in resonant frequency of a vibrating element. A current is passed through a wire which induces an electromotive force within the wire. The force is then amplified and causes oscillation of the wire. Pressure affects this mechanism by affecting the wire itself: an increase in pressure decreases the tension within the wire and thus lowers the angular frequency of oscillation.

### 2.2.3. Optical sensors (photosensors)

Devices that can convert optical signals into electronic outputs have been developed and employed in many consumer products (e.g. televisions). The selection of materials for optical sensors is based on the quantum efficiency, which corresponds to the tendency of the material to create electron-hole pairs by the input of photons. Semiconducting materials such as silicon and gallium arsenide or alkali metals such as lithium, sodium, potassium and rubidium are common materials used for optical sensors.

Figure 2.24 illustrates some of the most commonly adopted configurations for optical sensors.

The photovoltaic junction can produce an electric potential when the more transparent semiconductor A is subject to an incident photon energy. The produced voltage can be measured from the change of the electrical resistance in the circuit. The photoconductive device represented in Fig. 2.24-b refers to a sensor made of a material which changes conductivity when exposed to light. Both photodiodes and phototransistors are constituted by arrangements of p- and n- silicon doped layers. These devices can convert incident light into a proportional current signal. All the presented sensor configurations can be miniaturized and have a very short time response in generating electrical signals [9].

### 2.2.4. Chemical sensors

Chemical sensors are used to convert the information about the presence and concentration of specific chemical compounds into an electrical signal. Substances that can be identified with chemical sensors are atoms, ions or molecules in gases, liquids or solids.

Typical examples of chemical sensors are the FIGARO<sup>®</sup> gas sensors. In these devices a metal oxide crystal, such as SnO<sub>2</sub>, is heated to a given temperature in air. As a consequence, oxygen is adsorbed on the crystal surface, creating a negative charge. Inside the sensor, in particular at grain boundaries, the adsorbed oxygen forms a potential barrier which prevents carriers from moving freely. The electrical resistance of the sensor is attributed to this potential barrier. In the presence of a deoxidizing gas, the surface density of the negatively charged oxygen decreases, so the barrier height in the grain boundary is reduced. The reduced barrier height decreases the sensor resistance. The relationship between the sensor resistance and the concentration of deoxidizing gas can be quantified and measured.



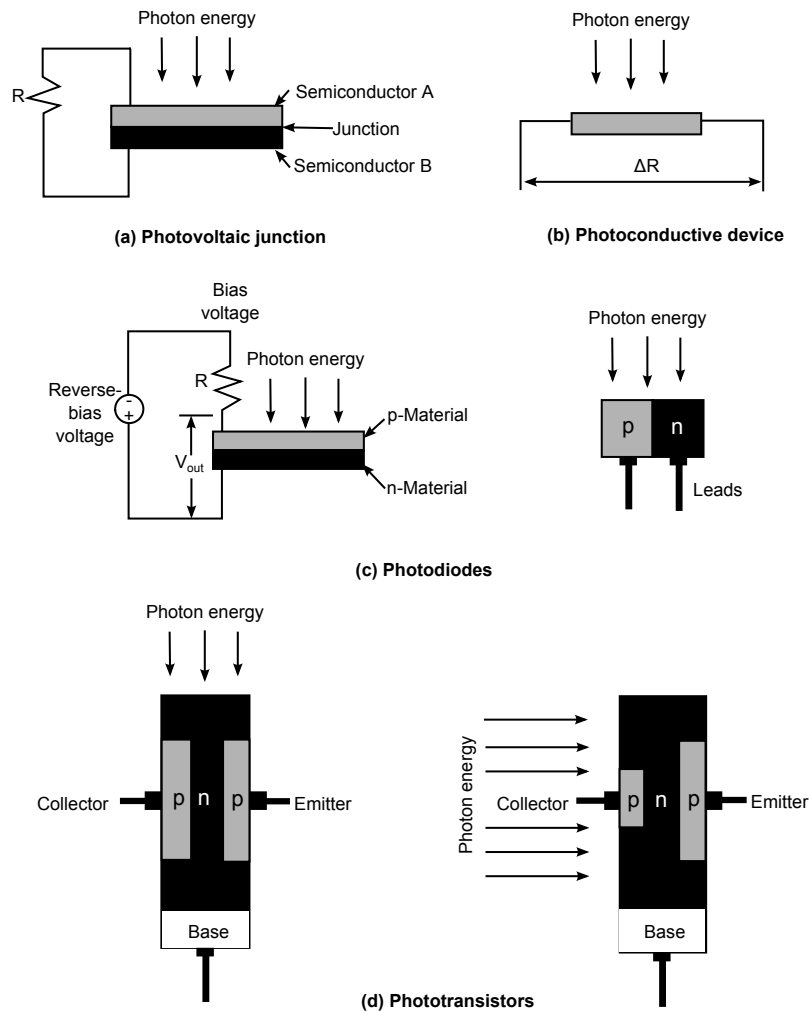


Figure 2.24.: Examples of optical sensing devices [9].

Another typical example of chemical sensor is the oxygen sensor (or lambda sensor) particularly employed in the automotive industry. These sensors are installed in the engine fuel control feedback loop. They are used to balance the fuel mixture, leaning the mixture when the sensor reads rich and enriching the mixture when the sensor reads lean. The zirconium dioxide element in the lambda sensor's tip produces a voltage that varies according to the amount of oxygen in the engine exhaust gases compared to the ambient oxygen level in the outside air. The larger the difference, the higher the sensor's output voltage.

A detailed description of the various chemical sensors and their working principles can be found, e.g., in [58] or in [61]. Here some of the most typically employed sensors are listed and briefly described.

*Chemiresistor sensors* consist of organic polymers with embedded metal inserts. If exposed to certain gases, the electrical conductivity of the polymers changes. An example of a polymer used in chemiresistor sensors is phthalocyanine, which, coupled with copper, can sense ammonia ( $\text{NH}_3$ ) and nitrogen dioxide ( $\text{NO}_2$ ).

*Chemicapacitor sensors* use polymers as dielectric materials in a capacitor. The dielectric constant of the material changes if exposed to certain gases. As a consequence, the material dielectric constant is changed as well. Polyphenylacetylene can be used, e.g., to sense gas species such as  $\text{CO}$ ,  $\text{CO}_2$ ,  $\text{N}_2$  and  $\text{CH}_4$ .

*Chemimechanical sensors* exploit the properties of some polymers whose shape changes when exposed to chemicals. By measuring the change on the dimensions, the presence of these chemicals can be detected. An example is the moisture sensors which employs pyraline.

*Metal oxide gas sensors* work similarly to chemiresistor employing semiconductors (such as SnO<sub>2</sub>) instead of polymers. The change in resistance can be accelerated by exposing the sensor to heat, and consequently enhancing the reactivity of the measurand gas. Better results can further be obtained by depositing metallic catalysts on the sensor surface.

### 2.2.5. Biosensors and Biomedical sensors

The biomedical industry has become one of the major users of MEMS, which are employed as biosensors, bio-instruments and systems for testing and analysis. Microsensors employed for the so called bio-MEMS can be divided into two main groups: biosensors and biomedical sensors. The first group extensively includes all those measuring devices containing biological elements, while biomedical sensors are used to detect biological substances [61].

Biosensors exploit the interaction of the substance to be detected and biologically derived molecules (such as enzymes, antibodies or proteins). The biomolecules are attached to the sensing elements and can alter the output signal whenever they come in contact with the substance in detection.

Biomedical sensors are particularly appealing as they offer the opportunity of quickly and precisely analyzing biological samples. Among the different available biomedical sensors, electrochemical and optical biosensors have a large relevance. They exploit the principle that certain biological substances can release elements during particular chemical reactions which alter the electricity flow pattern of the sensor or generate fluorescence. This principle is used for example in sensors which can measure the glucose concentration in blood samples.

Optical biosensors have numerous applications in biomedical research, health care, pharmaceuticals, environmental monitoring, etc.. There are two main areas of development in optical biosensors. These involve measuring the light output of a luminescent process, or determining changes in light absorption between the reactants and products of a reaction. The two techniques are usually referred to as fluorescence-based detection and label-free detection, respectively [62]. In fluorescence-based detection, the target molecules are labeled with fluorescent tags. The intensity of the fluorescence indicates the presence of the target molecules. In label-free detection, target molecules are not labeled or altered but are detected in their natural forms. A comprehensive review of optical biosensors is given in [63].

### 3. Theoretical overview on gas dynamics and heat transfer

In this section the principal models available to describe fluid dynamics and heat transfer phenomena of gas flows will be presented. The limits and advantages of each model will be discussed as well, with a focus on the limits of the continuum approach in the description of rarefied gases and the possible alternatives to it.

#### 3.1. Characteristic length scales for gases

Molecular interactions play a major role in determining the behavior of matter (e.g. the state of matter depends mainly on the balance between intermolecular forces and molecular thermal energy), and the full understanding of gas flow physics requires to take into account the main characteristics at molecular level. Three characteristic lengths can be identified to describe molecular interactions: the mean molecule diameter  $d$ , the mean molecular spacing  $\delta$  and the mean free path  $\lambda$  (Fig. 3.1) [64]. The mean free path can be described as the average distance traveled by a molecule between two consecutive collisions. For single species gases, the mean free path depends on the mean molecule diameter  $d$  and on the number density  $n = \delta^{-3}$ .

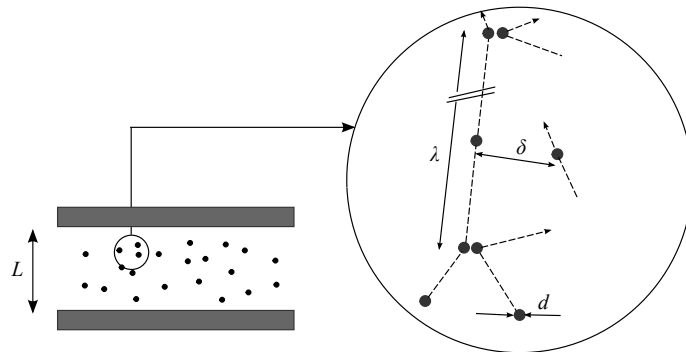


Figure 3.1.: Characteristic length scales at the molecular level [64].

The concept of molecular collisions can be easily understood by using the *hard sphere* model (HS) to represent molecules (i.e. a molecule is represented as a sphere of diameter  $d$ ). A collision is said to happen when the center of a molecule is located inside the sphere

of radius  $d$  with the center of another molecule as its center. Under the hypothesis that only binary collisions take place (and this is more true the more diluted the gas is) the mean free path can be expressed as the ratio between the mean thermal velocity  $\bar{c}$  and the collision rate  $\nu$ :

$$\lambda = \frac{\bar{c}}{\nu} = \frac{\sqrt{8RT/\pi}}{\nu}, \quad (3.1)$$

where the mean thermal velocity, which depends on the temperature  $T$  and on the specific gas constant  $R$ , is calculated from the Boltzmann equation [64].

The calculation of the mean free path depends on the model chosen for describing the elastic binary collisions between two molecules. According to the collision model also different collision rates can be defined. Classical approaches are based on an inverse power law (IPL) model for the force exerted by the two colliding molecules. The general expressions of the mean free path can then be written in terms of fluid viscosity  $\mu$ , density  $\rho$  and temperature  $T$ , as described in Eq. 3.2.

$$\lambda = k_1 \frac{\mu}{\rho\sqrt{RT}} \quad (3.2)$$

The coefficient  $k_1$  is listed for some classic (IPL) collision models in Tab.3.1, along with the corresponding values for the force exponent  $\eta$  and the viscosity exponent  $\omega$ . The parameter  $\alpha$  refers to the deflection angle taken by the molecule after a collision, as introduced by Koura and Matsumoto in 1991 [65].

Table 3.1.: Collision force  $F$ , viscosity  $\mu$  and mean free path  $\lambda$  for different IPL collision models [64].

Model	$F \propto \frac{1}{r^\eta}$ $\eta$	$\mu \propto T^\omega$ $\omega$	$\lambda$ $k_1$
Hard Sphere	$\infty$	$\frac{1}{2}$	$\frac{16}{5\sqrt{2\pi}}$
Variable Hard Sphere	variable	$\omega = \frac{\eta+3}{2(\eta-1)}$	$\frac{2(7-2\omega)(5-2\omega)}{15\sqrt{2\pi}}$
Maxwell Molecules	5	1	$\sqrt{\frac{2}{\pi}}$
Variable Soft Sphere	variable	$\omega = \frac{\eta+3}{2(\eta-1)}$	$\frac{4\alpha(7-2\omega)(5-2\omega)}{5(\alpha+1)(\alpha+2)\sqrt{2\pi}}$

More realistic potential models, which include the long-range attractive part of the force, have also been proposed. The Lennard-Jones potential model is among the most widely used, for its accuracy in the prediction of the diffusion and the viscosity coefficients [64].

As it is clear from the examples reported in Tab. 3.1, the direct calculation of the mean free path requires the knowledge of non-mesurable quantities such as the force exerted between two colliding molecules. Another possibility to obtain the mean free path is to exploit the kinetic theory of gases (see, e.g., [66]), which relates it to measurable quantities like viscosity coefficient  $\mu$ , pressure  $P$ , temperature  $T$ , molecular mass  $m$  and to the Boltzmann constant  $k_B$ , as expressed in Eq. 3.3 [67]. Equation 3.3, which is a specific case of Tab. 3.1 with a modified  $k_1$  from the HS case, can be directly derived from the Chapman-Enskog expansion of the Boltzmann equation [68].

$$\lambda = \frac{\sqrt{\pi}\mu}{2P} \left( \frac{2k_B T}{m} \right)^{1/2} \quad (3.3)$$

### Non-dimensional quantities

In the description of gas flow physics it is particularly convenient to define some dimensionless parameters which allow a quick and effective comparison of the main flow characteristics.

The Reynolds number is the ratio of inertial forces to viscous forces. It is defined as:

$$Re = \frac{\rho u L}{\mu}, \quad (3.4)$$

where  $u$  is a reference velocity and  $L$  is a characteristic length of the flow.

The ratio of the flow velocity to the speed of sound  $a = \sqrt{\gamma RT}$  (where  $\gamma$  is the ratio of the constant pressure and constant volume heat capacities) is the Mach number:

$$Ma = \frac{u}{a} \quad (3.5)$$

Another useful parameter commonly employed in the description of gas flows is the Knudsen number, defined as the ratio of the mean free path to the systems characteristic length:

$$Kn = \frac{\lambda}{L} \quad (3.6)$$

From the definition of  $\lambda$  given in Eq. 3.3 and the expressions in Eqs. 3.4 and 3.5, it is possible to express the Knudsen number as a function of the three dimensionless numbers  $Re$ ,  $Ma$  and  $\gamma$ :

$$Kn = \sqrt{\frac{\pi\gamma}{2}} \frac{Ma}{Re}. \quad (3.7)$$

This allows gas flows to be classified according to some specific characteristics. Turbulent behavior is, e.g., determined with the Reynolds number, while the Mach number is related to the flow compressibility. The Knudsen number finally determines the degree of rarefaction of the flow (see Section 3.2).

## 3.2. Flow models

The different length scales characterizing gas flows and their relative values determine the validity of the assumptions and hypotheses which are the basis of different flow models. This concept is illustrated in Fig. 3.2.

The vertical line represents the boundary between dilute and dense gases. For dilute gases intermolecular forces play no role and the molecules are mostly in free flight in between binary collisions which abruptly change the molecules' directions and speeds.

The gently sloped line indicates the limit of molecular chaos. When averaging over many molecules, statistical fluctuations are negligible when at least  $L/\delta > 100$  (where  $L$  is the characteristic length and  $\delta$  is the mean molecular spacing). The continuum approximation, which regards the fluid as a continuous medium (ignoring its molecular nature), is valid only above of this line. In continuum models the flow characteristics such as density, velocity, stress and heat flux, are defined as averages over fluid elements which are sufficiently large to guarantee a sufficient number of molecules inside them, and at the same time small compared to the scale of the relevant microscopic phenomena of the flow.

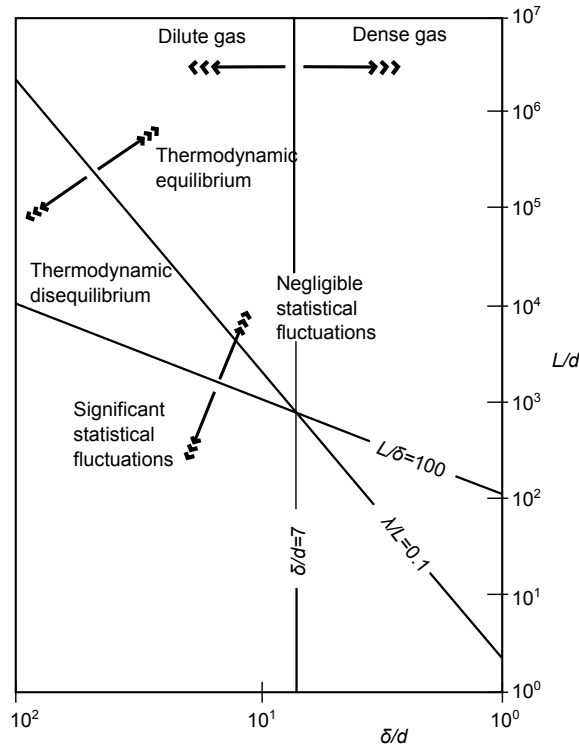


Figure 3.2.: Limits of the approximations for gas flow modeling [64], adapted from [69].

The steeper line in Fig. 3.2 defines the limits of the quasi-thermodynamic equilibrium, implying that the molecules have a sufficient number of collisions to adjust to the changing fluid properties. This limit is governed by the Knudsen number ( $Kn = 0.1$ ).

Fluid models can be classified between continuum and molecular, where the latter consider the fluid as a collection of molecules (see Fig. 3.3).

The well-known Navier-Stokes (NS) equations are an example of a continuum model. They can be applied when both the quasi-thermal equilibrium and the negligible statistical fluctuations hypotheses are met. As they are still quite easy to handle mathematically and well established among the fluid dynamics community, they are the model of choice as long as they are applicable. For gas flows in micro devices, however, this might not be

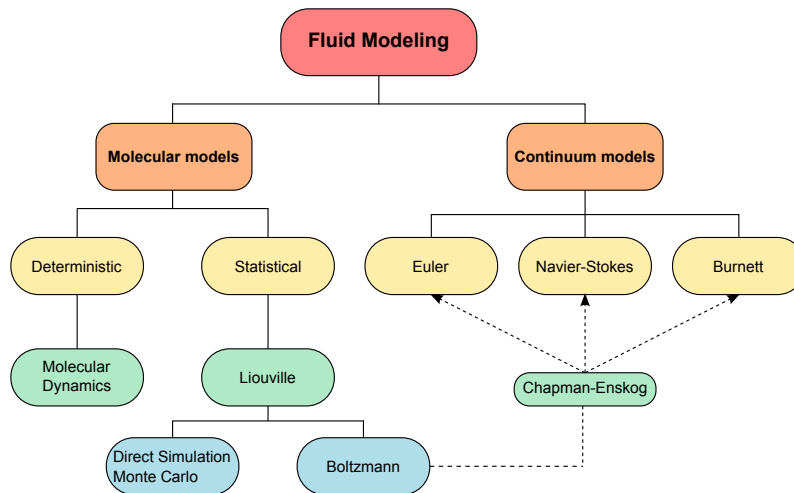


Figure 3.3.: Molecular and continuum flow models [70].

the case, since the mean free path of gases can be rather large (compared to that of liquids and solids) and the Knudsen number might gain larger values than the conventional limit of validity of the NS equations [70]. Moreover, deviations from the continuum behavior might appear fairly before the Knudsen number reaches a value of 0.1. These deviations must be then taken into account and somehow integrated into the NS equations (extending their validity to the actual threshold of  $Kn = 0.1$ ). A quite usual way to determine which model suits the considered gas flow better is based on the Knudsen number. According to its value different flow regimes are identified:

- For  $Kn < 10^{-3}$ , the flow is in the continuum regime. The NS equations with conventional boundary conditions can accurately model these flows.
- For  $10^{-3} < Kn < 10^{-1}$ , the flow is in the slip regime. In this Knudsen range the bulk flow may still be modeled with the NS equations, while close to the gas-solid interface the gas is locally out of equilibrium (this is the *Knudsen layer*, which is a few mean free path lengths thick and therefore can be neglected for smaller  $Kn$ ). In this case the non-equilibrium at the wall can be taken into account by modifying the boundary conditions.
- For  $10^{-1} < Kn < 10$  the flow is in the transitional regime. For  $Kn \approx 1$  the validity of the continuum approach can be extended by use of higher order equation sets such as the Burnett equations. For higher Knudsen numbers the continuum approach is no longer valid but the intermolecular collisions can not be neglected. Statistical approaches such as the direct simulation Monte Carlo (DSMC) method are suitable to model these flows.
- For  $Kn > 10$  the flow is in the free molecular regime and the occurrence of the intermolecular collisions can be neglected compared to the collisions between the gas molecules and the solid walls. Accurate modeling can be obtained by directly solving the Boltzmann equation, where the collision integral is neglected.

The classification of the different flow regimes with the corresponding models is illustrated in Fig 3.4.

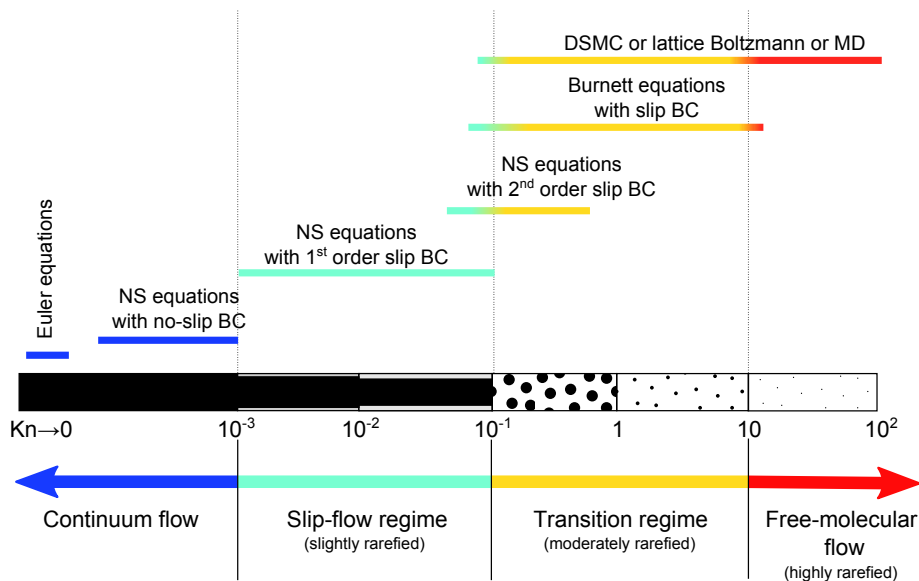


Figure 3.4.: Knudsen number regimes and main applicable models (adapted from [64]).

### Continuum models

For continuum models the conservation of mass, momentum and energy can be expressed with a system of partial differential equations:

$$\frac{\partial \rho}{\partial t} + \frac{\partial}{\partial x_k} (\rho u_k) = 0 \quad (3.8)$$

$$\rho \left( \frac{\partial u_i}{\partial t} + u_k \frac{\partial u_i}{\partial x_k} \right) = -\frac{\partial p}{\partial x_i} + \rho g_i + \frac{\partial}{\partial x_k} \left[ \mu \left( \frac{\partial u_i}{\partial x_k} + \frac{\partial u_k}{\partial x_i} \right) + \delta_{ki} \lambda \frac{\partial u_j}{\partial x_j} \right] \quad (3.9)$$

$$\rho \left( \frac{\partial e}{\partial t} + u_k \frac{\partial e}{\partial x_k} \right) = \frac{\partial}{\partial x_k} \left( \kappa \frac{\partial T}{\partial x_k} \right) - p \frac{\partial u_k}{\partial x_k} + \phi \quad (3.10)$$

where  $\rho$  is the density,  $u_k$  is a component of the velocity vector  $\mathbf{u}$ ,  $p$  is the thermodynamic pressure,  $g_i$  is the body force per unit mass,  $\mu$  and  $\lambda$  are the first and second coefficients of viscosity,  $\delta_{ki}$  is the Kronecker delta,  $e$  is the internal energy,  $\kappa$  is the thermal conductivity,  $T$  is the temperature field and  $\phi$  is the viscous dissipation rate given by:

$$\phi = \frac{1}{2} \mu \left( \frac{\partial u_i}{\partial x_k} + \frac{\partial u_k}{\partial x_i} \right)^2 + \lambda \left( \frac{\partial u_j}{\partial x_j} \right)^2. \quad (3.11)$$

Equations 3.9 are the NS equations expressing the conservation of momentum for a Newtonian fluid. The classical boundary conditions for velocity and temperature are the no-slip and no-temperature-jump boundary conditions:

$$\mathbf{u}|_w = \mathbf{u}_{wall} \quad (3.12)$$

$$T|_w = T_{wall} \quad (3.13)$$

where the subscript “wall” relates to the wall itself, while the subscript “w” refers to the conditions of the fluid at the wall.

The notion of no-slip and no-temperature-jump relates to the fact that there can not be any discontinuity of velocity and temperature [70]. The interactions between a fluid particle and the wall are similar to the interactions among fluid particles and, therefore, no discontinuity is allowed at the wall either. For this reason the fluid must have the same velocity and temperature than the wall. Those two boundary conditions hold as long as the fluid adjacent to the wall is in thermodynamic equilibrium (i.e. there is an infinitely high frequency of collisions between the fluid and the solid surface) [70]. When  $Kn > 0.001$ , the collision frequency is not high enough to ensure equilibrium. One way to cope with this is to introduce a tangential-velocity slip and a temperature jump at the wall.

### Slip boundary conditions

The slip-velocity boundary condition can be expressed in its general form as:

$$\Delta u|_w = u_{fluid} - u_{wall} = \xi \frac{\partial u}{\partial y} \quad (3.14)$$

where  $\xi$  is the slip length which, for some MEMS applications, might not be negligible. For an isothermal dilute monoatomic gas, Eq. 3.14 has been derived rigorously by Maxwell [71]. Gas molecules are modeled as rigid spheres continuously colliding with each other and with the solid walls. For the ideal case of perfectly smooth surfaces, the reflection angle



equals the incident angle, the molecules conserve their tangential momentum and exert no shear on the surface. This situation is referred to as *specular reflection* (see Fig 3.5-a). For extremely rough walls the molecules are reflected randomly and independently from the incident angle (see Fig. 3.5-b).

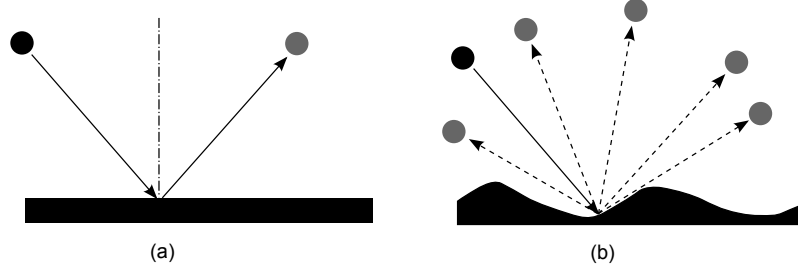


Figure 3.5.: Maxwell model for collisions between molecules and solid wall [64]. (a) specular reflection. (b) diffuse reflection.

This *diffuse reflection* requires a finite slip velocity to balance the shear stress transmitted to the wall. From a force balance near the wall it can be written:

$$u_{gas} - u_{wall} = \lambda \frac{\partial u}{\partial y} \quad (3.15)$$

where the slip length is now replaced by the mean free path. Equation 3.15 can be interpreted by stating that a significant slip occurs only if the mean velocity of the molecules varies appreciably over a distance of one mean free path.

In the case of real walls, some molecules are reflected diffusely and some specularly. The fraction of molecules diffusely reflected defines the *tangential momentum accommodation coefficient* (TMAC),  $\sigma_v$ . The TMAC depends on the gas, on the solid and on the surface characteristics. It has been determined experimentally, e.g., by [72], [73], [16] and [74] (ranging between 0.2 and 1). For a real fluid, Eq.3.15 becomes:

$$u_{gas} - u_{wall} = \frac{2 - \sigma_v}{\sigma_v} \lambda \frac{\partial u}{\partial y} \quad (3.16)$$

Similar considerations have been done for the temperature boundary condition by Smoluchowski [75]. The final set of (first order) slip boundary conditions reads:

$$u_{gas} - u_{wall} = \frac{2 - \sigma_v}{\sigma_v} \lambda \frac{\partial u}{\partial y} + \frac{3}{4} \frac{\mu}{\rho T_{gas}} \left( \frac{\partial T}{\partial x} \right)_w \quad (3.17)$$

$$T_{gas} - T_{wall} = \frac{2 - \sigma_T}{\sigma_T} \left[ \frac{2\gamma}{(\gamma + 1)} \right] \frac{k}{\mu c_v} \lambda \frac{\partial T}{\partial y} \quad (3.18)$$

where  $x$  and  $y$  are the streamwise and normal coordinates,  $T_{gas}$  is the temperature of the gas adjacent to the wall,  $k$  and  $c_v$  are the flow thermal conductivity and the heat capacity at constant volume and  $\gamma$  again is the specific heat capacity ratio. The TMAC  $\sigma_v$  and the *thermal accommodation coefficient* (TAC)  $\sigma_T$  are given by:

$$\sigma_v = \frac{\tau_i - \tau_r}{\tau_i - \tau_w} \quad (3.19)$$

$$\sigma_T = \frac{dE_i - dE_r}{dE_i - dE_w} \quad (3.20)$$

where  $\tau$  is the tangential momentum flux,  $dE$  is an energy flux and the subscripts  $i$ ,  $r$  and  $w$  stand for incident, reflected and solid wall conditions, respectively.

The second term of Eq. 3.17 is the *thermal creep*, which generates a slip velocity in the opposite direction of the tangential heat flux.

First order slip boundary conditions are valid as long as  $0.001 < Kn < 0.1$ . To extend the validity of the NS equations to higher Knudsen, second order boundary conditions have been formulated. The generic form for the velocity boundary condition is given by (where the symbol  $*$  stands for dimensionless quantities [64]):

$$u_{gas}^* - u_{wall}^* = C_1 Kn \frac{\partial u^*}{\partial y^*} \Big|_w - C_2 Kn^2 \frac{\partial^2 u^*}{\partial x^{*2}} \Big|_w \quad (3.21)$$

where  $C_1$  and  $C_2$  denote the general form of the first and second order accommodation coefficients. A complete review of the different proposed models of second order boundary conditions can be found in [64] and [76].

### Molecular models

Molecular models recognize the fluid as a collection of discrete particles, while the macroscopic properties can be computed from the particle information by averaging or weighted averaging processes. The complete description of a gas flow is achieved if for each time  $t$  and each position  $\mathbf{x}$  the number density, the velocity and the internal energy distribution functions are known.

Among the molecular models, deterministic approaches attempt the description of the single molecules and their interactions. *Molecular dynamics* (MD) computer simulations describe the motion of  $N$  molecules in a region of space. Their interactions are imposed in a form of a two-body potential energy, and the time evolution is determined by integrating Newton's equations of motion. As no particular assumption is done, MD is in principle valid for any flow and any range of parameters. However, this approach presents two major drawbacks: the correctness of the result depends strongly on the choice of the potential for the particular fluid-solid combination, and the number of molecules  $N$  that can be realistically simulated on a computer is limited. Many efforts are made to broaden the range of application of MD methods, for example by combining it with other methods and using the deterministic approach only where a high resolution is required (see e.g. [77] and [78]).

An alternative to deterministic approaches are statistical methods. In this case the probability of finding a molecule at a particular position and state is computed. The independent variables of the problem are time, the three spatial coordinates and the three components of the molecular velocity. Extra dimensions are added to the phase space if diatomic or polyatomic molecules are considered, while for gas mixtures separate probability distributions are required for each species.

The Boltzmann equation defines the evolution in time and space of the distribution function  $f(t, \mathbf{x}, \mathbf{v})$  for a gas at equilibrium. For a monoatomic dilute gas it reads as follows:

$$\frac{\partial f}{\partial t} + \mathbf{v} \cdot \frac{\partial f}{\partial \mathbf{x}} + \mathbf{F} \cdot \frac{\partial f}{\partial \mathbf{v}} = Q(f f_*) \quad (3.22)$$

where  $\mathbf{x} = (x, y, z)$  and  $\mathbf{v} = (v_x, v_y, v_z)$  are the position and the molecular velocity vectors, respectively,  $\mathbf{F}$  is the mass force and  $Q(f f_*)$  is the collision integral.

The distribution function represents the number of molecules that in the time instant  $t$  are included inside the domain  $([\mathbf{x}; \mathbf{x} + d\mathbf{x}]; [\mathbf{v}; \mathbf{v} + d\mathbf{v}])$ . The form of the collision integral

depends on the adopted molecular collision model. Details about the formulation of the Boltzmann equation can be found in [79] and [80].

Once a solution for the distribution function  $f$  is obtained, the macroscopic properties (such as the density  $\rho$ , the macroscopic velocity vector  $\mathbf{u}$  and the temperature  $T$ ) of the gas can be obtained by the following weighted integrals:

$$\rho = mn = m \int (nf) d\mathbf{v} \quad (3.23)$$

$$u_i = \int v_i f d\mathbf{v} \quad (3.24)$$

$$\frac{3}{2}kT = \int \frac{1}{2}m u_i u_i f d\mathbf{v} \quad (3.25)$$

The direct solution of the Boltzmann equation is usually not affordable because of the non linearity of the collision integral. Chapman and Cowling [68] proposed a solution of the Boltzmann equation by considering a small perturbation of  $f$  from the equilibrium form (i.e. for  $Kn = 0$ ) and by expanding in series in terms of  $Kn$  (valid for small Knudsen numbers). By considering different orders of the expansion, the different continuum models can be directly derived from the distribution function. The zeroth order of the series expansion corresponds to the Euler equations. The first order brings about the Navier-Stokes/Fourier equations. The second order approximation leads to the Burnett equations, while the third order approximations define the super-Burnett equations.

For the transitional regime, i.e. away from the ranges where either continuous models can be applied or where the direct solution of Eq. 3.22 can be performed, approximate solution methods are required, which attempt the simplification of the collision integral. The different available methods are extensively described in [67].

One of the commonly employed simulation methods in the transitional regime is the direct simulation Monte Carlo (DSMC) method. The main idea is to uncouple the simulations of the intermolecular collisions and of the molecular motion with a time step smaller than the mean collision time. The method considers a large number of randomly selected and statistically representative particles. The statistical error of DSMC is inversely proportional to the square root of the total number of simulated molecules.

### Rarefaction and MEMS

Rarefied gas flows are classically encountered in low-pressure applications, such as high-altitude flights and high-vacuum devices. However, rarefied conditions can be also found in small geometries such as MEMS devices, for which the reduction in the characteristic length produces an increase in the Knudsen number.

To give a concrete example, for air at atmospheric pressure slip occurs if  $L < 100 \mu\text{m}$ , while at 1 mbar absolute pressure slip occurs already for  $L < 100 \text{mm}$ .

Typically, most MEMS using gas flows work between the slip flow and the transitional regimes (see Fig. 3.6), and therefore careful considerations must be done before attempting the modeling of such systems, to correctly evaluate which models suit each situation.

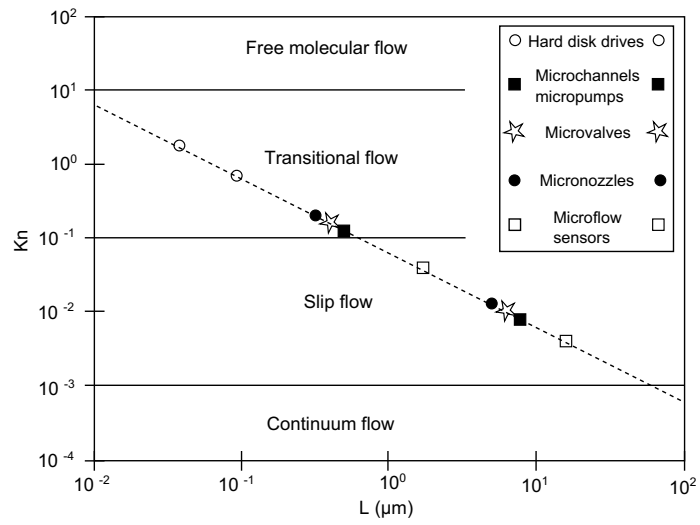


Figure 3.6.: Gas flow regimes for usual microsystems [64], adapted from [81].

## 4. Experimental Setup

To fulfill the goals presented in Section 1.4, a new experimental setup has been designed and realized. The main requirements to be met can be summarized as follows:

- The setup should allow the study of heat transfer performances for gases in microchannels.
- The setup should present easily exchangeable microchannel sections to test different materials without the need of modifying the whole experimental design.
- An integrated temperature measuring system should be established to access direct information on the flow in the microchannel. This should be designed in such a way that integration is possible with in principle any kind of microchannel material.
- Different testing conditions should be achievable, i.e. different rarefaction regimes, ranging from continuum to slip flow, different compressibility levels and variable thermal boundary conditions.

### 4.1. Experimental device

The core of the developed experimental setup is the microstructured device. It presents a multilayer configuration offering a large flexibility of applications: exchangeable channel sections, controllable pressure and thermal boundary conditions, and possibility of integrating different types of sensors. Two possible configurations for the measurement of the temperature profile along a microchannel have been implemented. The first is a MEMS-based integrated measuring system based on planar silicon technology, while the second represents an attempt to employ conventional commercial sensors in the microfluidic device.

The multilayer device has been designed starting from an existing prototype developed at the Institute for Micro Process Engineering (IMVT) at Karlsruhe Institute of Technology (KIT) for two-phase flow studies [82]. The design has been adapted for gas flow studies and for direct integration of the sensors in the microchannels. The MEMS-based measuring system was designed in cooperation with the Institute for Microsystems Engineering (IMTEK) at the University of Freiburg, where the actual fabrication of the system took place in specific clean room facilities. During the project phase, particular attention had to be paid to finding a compromise between leak tightness of the microfluidic device

(microchannel plus sensor assembly), the fulfillment of the desired system flexibility (possibility of exchanging the test sections) and the physical limitations of the sensor assembly (very brittle structure and necessity of electrical access for data acquisition). The characterization of the sensors and the preliminary tests on the multilayer device have been performed during a secondment at the National Institute of Applied Science (INSA) at the University of Toulouse, while the experimental campaign with the different microchannel sections was performed at IMVT.

In Fig. 4.1 the multilayer experimental device is shown. Each layer is designed for a specific functional task, which allows the achievement of the required flexibility. Starting from

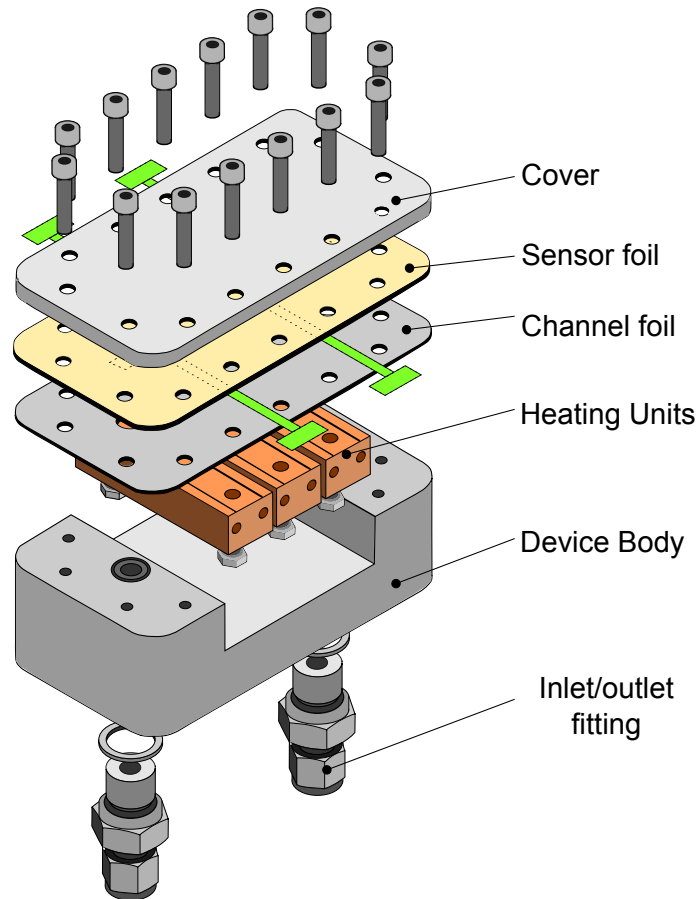


Figure 4.1.: Multilayer experimental device.

the bottom, the device includes standard fittings for the feed and exhaust lines of the gas. The body of the device is made of stainless steel, which gives the device a high thermal inertia and allows the achievement of stable thermal boundary conditions. Within the body frame, three separate copper blocks are installed as heating-cooling units. The spaces between the blocks produce a natural thermal insulation from heat conduction. The use of copper guarantees that the desired boundary conditions are reached quickly thanks to the thermal properties of the material. Each copper block presents two receptacle holes for the installation of electrically powered heating cartridges or of tubes for a liquid heating-cooling loop. On top of each block, two small grooves have been realized for the installation of thermocouples measuring the block temperature right below the microchannel section. These sensors can be connected to the data acquisition system and/or to the power unit supplying the heating elements (when, e.g. a feedback signal is required to automatically control the imposed boundary conditions). The three heating/cooling units can be controlled separately to impose the thermal boundary conditions at the microchannel section:

custom wall temperature distributions (T-boundary conditions) as well as fixed heat flux profiles (h-boundary conditions) can be chosen.

On top of the heating/cooling units the microchannel section is installed. A single three-wall microchannel open on the top is manufactured with the chosen fabrication process on a foil of the desired material. The channel foils can be easily exchanged allowing the test of different geometries, materials and surface characteristics. By leaving the channel top open, it is possible to integrate the measuring system in the channel. This constitutes the upper layer which, as opposed to the channel foil, is fixed for all the experiments. This choice is the result of a compromise between the possibility of exchanging the test sections and the necessity of keeping the integrated measuring system to produce comparable results. Conventional integrated systems require the permanent installation of the sensors in the microchannel which can be either built during the fabrication of the sensors themselves (e.g. silicon channels produced along with the sensors) or bonded on the sensor substrate (e.g. silicon sensor chips bonded on silicon or glass microchannel foils). These configurations do not allow any further modification nor the integration with materials other than silicon or glass (except for some special polymeric compounds). On the contrary, with the present design the channels can be easily closed and re-opened without any permanent bonding, three out of four walls can be of any chosen material, while the last wall is fixed and is constituted by the sensor layer.

The whole device is closed by screws along the entire perimeter of the upper cover. To minimize gas leakage, particular attention must be paid to the sealing between the cover and the microchannel plate, as described in the following. The different parts of the manufactured device are shown in Fig. 4.2.

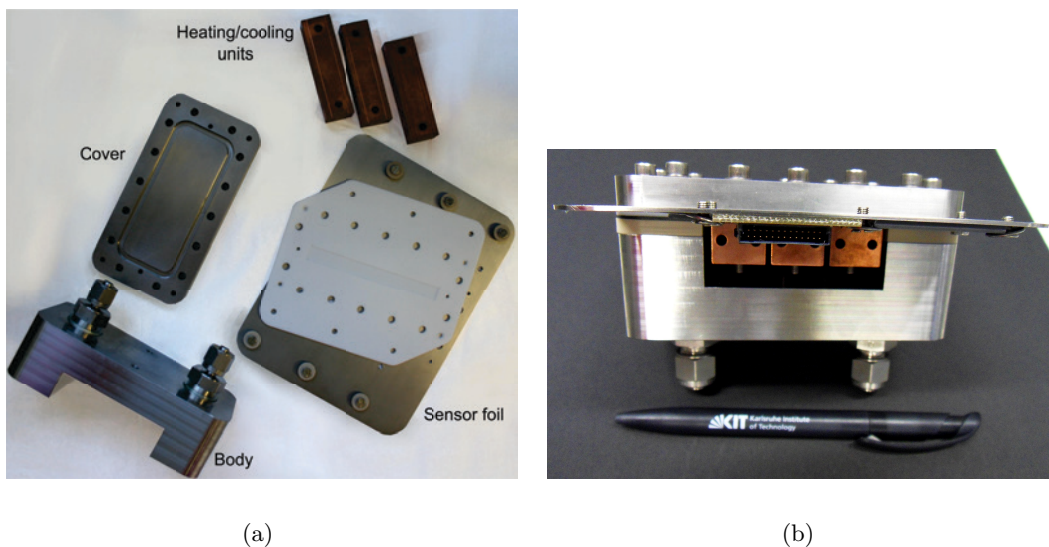


Figure 4.2.: Separated layers of the experimental device (left) and mounted device (right).

The two different configurations used for the integration of temperature sensors in the channel top wall require in the first case the mounting of a silicon chip on top of the microchannel layer, while in the second case the replacement of the device cover with a new one is needed, including embedded thermocouples in it.

#### 4.1.1. Silicon micro sensors integration

The MEMS-based integrated sensors have been designed and manufactured in cooperation with the Institute of Micro Systems Engineering (IMTEK) at the University of Freiburg.

Details about the design and the fabrication processes are given in Section 4.2. The sensors are manufactured on top of a silicon wafer which is then properly cut to create chips covering the entire channel length. By using a single chip configuration instead of integrating small sensor units separated from each other, it is easier to avoid gas leakages, a higher uniformity for the top wall is ensured (avoiding e.g. abrupt material changes), and the connections for the data recording can be directly grouped on the chip instead of being handled separately for each sensor.

To mount the silicon chip on the device frame, a polytetrafluoroethylene (PTFE) foil has been realized which presents a central recess for the chip positioning. Thanks to its elastic properties, the PTFE chip holder also serves as a channel sealing. Indeed, major channel leak tightness problems are caused by the thin cables which exit the device and connect the chip to the data acquisition system (see following sections). The use of conventional O-rings is not possible in this case, since they would break the thin cables. Once the device is closed with the screwing system, the PTFE layer, pressed against the channel foil below, is elastically deformed and acts as a sealing mechanism for the microchannel itself. The sensor and microchannel layers are schematically represented in Fig. 4.3, where a detail of the cross section of the assembly is also given. A picture of the PTFE foil is shown in Fig. 4.4

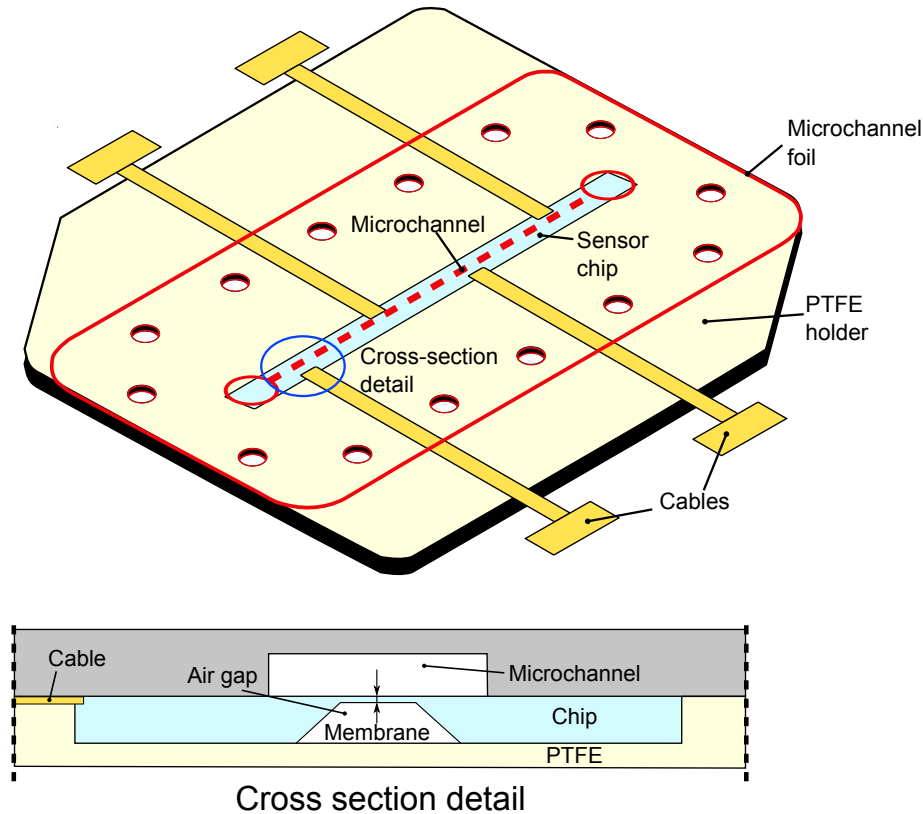


Figure 4.3.: Schematic view of the PTFE chip support and the microchannel foil with a detail of the assembly cross section. For a better understanding of the mutual positions, the layers are represented upsidedown with respect to their real alignment (the chip is mounted above the microchannel layer).

In the fabrication of the PTFE chip holder particular attention to tolerances had to be paid. If the recess is too small, the chip would not fit on it or would experience some pre-imposed stresses from the mounting, which might compromise its stability during the tests. If the recess is too loose, the sensor positioning would not be correct and the sealing



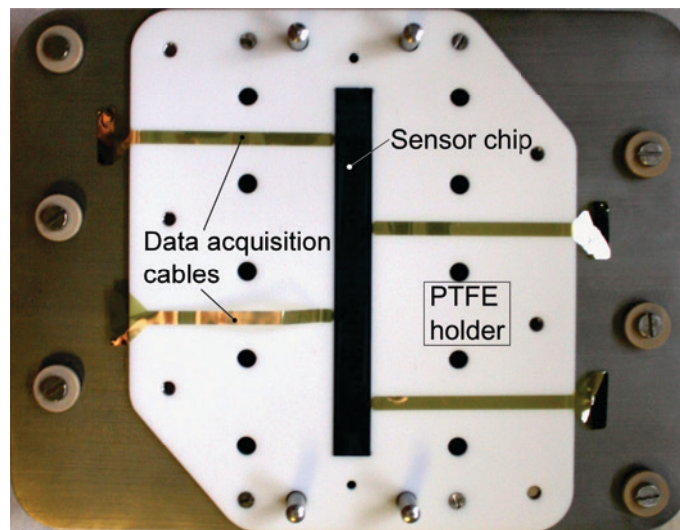


Figure 4.4.: PTFE holder foil with installed silicon sensor chip and data acquisition cables.

of the channel would be compromised.

#### 4.1.2. Commercial thermocouples integration

Normally, the integration of commercial temperature sensors in microchannels should be avoided. Indeed, even the smallest available sizes for the sensing elements are comparable to the channel dimensions, and this would result in major flow disturbances. However, for the present work, a special design for the integration of thermocouples inside a microchannel ensuring minimal interaction with the flow has been developed. The sensor foil and the device cover shown in Fig. 4.1 were replaced by a cover realized in PEEK, along the axis of which 6 type-K thermocouples with  $125\ \mu\text{m}$  sensing tips had been installed with vertical orientation. The sensors are inserted in receptacle holes in the cover, which allow a precise gluing of the tips in the desired positions. In particular, the sensing elements exit at the inner surface of the cover, facing inside of the microchannel once the device is closed. To ensure that the tips are in contact with the gas and do not measure the temperature of the cover bulk material, small recesses have been realized around the sensor endings to expose them to the flow. Figure 4.5 shows the PEEK channel cover and some details of the embedded thermocouples.

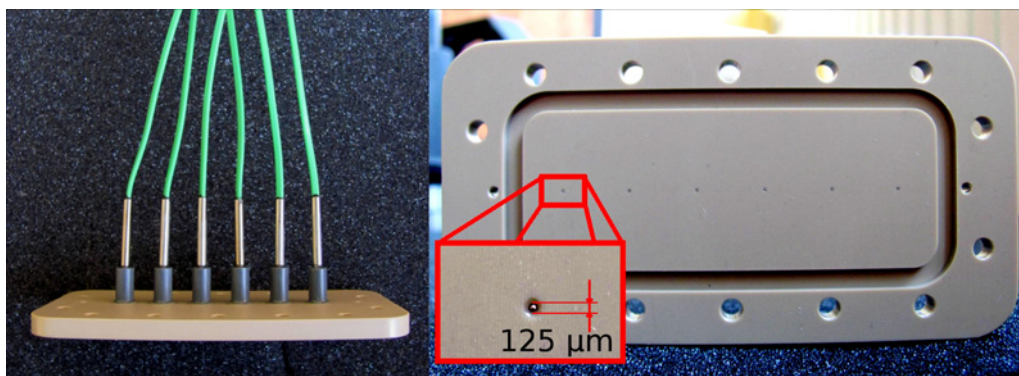


Figure 4.5.: PEEK cover with embedded thermocouples. Cover overview (left) and details of the embedded sensors (right).

## 4.2. Selected measurement technique

The design for the integrated temperature sensors has been chosen from available MEMS-microsensors configurations. Since the main aim of the experimental setup is the measurement of the gas temperature distribution inside a microchannel, it is important to reduce the influence of the environment on the sensors to a minimum. The employment of thermopiles is the most suitable choice, since they allow almost currentless measurements (as opposed to, e.g., thermistors), reducing self-heating effects. The same kind of measurements with a thermistor configuration would result in a joule heating of the sensor substrate up to some degrees, inducing unacceptable errors in the final results.

The main drawback of using thermopiles is that they are temperature difference transducers. This means that a reference temperature measurement is necessary. Moreover, the direct integration of silicon thermopiles in MEMS has some limitations due to the high thermal conductivity of silicon. The thick silicon substrate below the sensor contacts can spoil the overall sensitivity and cause a thermal short-cut. To maximize the achievable temperature increase, silicon micromachining techniques were employed to remove the bulk material below the sensors. This created thin membranes (5-10  $\mu\text{m}$  thick) which increased the thermal resistance of the sensors and, proportionally, the overall sensitivity. The heat generated or absorbed in the “hot” region on the membrane generates a temperature difference with the “cold region”, outside the membrane.

Several structures can be adopted to separate the “hot” and “cold” regions of the sensors, namely closed membranes, cantilever beams and floating membranes (see Fig. 4.6) [36].

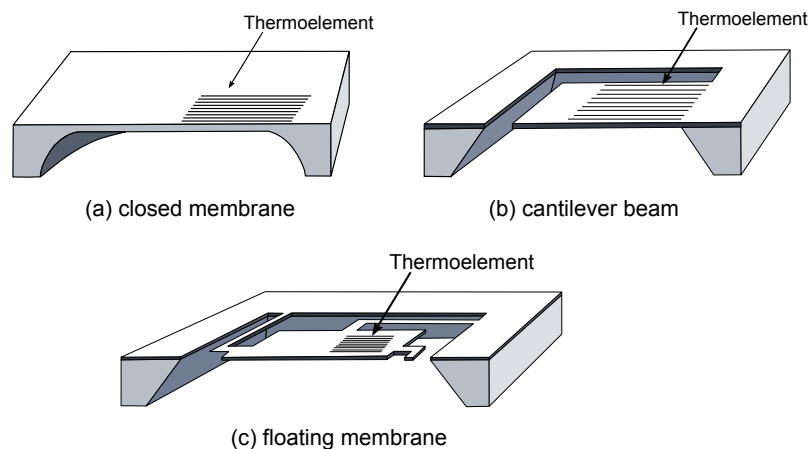


Figure 4.6.: Possible structures for thermopiles fabricated on silicon substrates [36].

In the closed membrane configuration, the cold region is formed by a thick wafer around the etched membrane, which is the hot region of the sensor. This structure is characterized by a low thermal resistance, a small time constant  $T_{60}$  (i.e. the time required for the transducer’s voltage to reach 63.2 % of its final asymptotic value in response to a sudden change in temperature) and the highest resistivity among the possible silicon thermopile configurations.

The cantilever beam configuration, while presenting a relatively high thermal resistance compared to the closed membrane, offers the possibility of having relatively large hot regions. The structure has a medium time constant and sensitivity, while it may present fragility issues.

Finally, the floating membrane configuration refers to the situation where the membrane is held only by a few suspension beams. In this case very large hot areas together with

high sensitivities can be achieved but the fragility (especially during the fabrication) is increased, too. To achieve high thermal resistances the suspension beams are usually made very narrow and long. For this reason the number of strips that can be accommodated by the suspension beams is limited. Consequently, the floating membrane configuration presents the lowest thermopile sensitivity [36]. This effect is however compensated by the high thermal resistances and overall good sensitivities that can be achieved. An example of a floating membrane configuration for a miniaturized thermopile is given in [83], which reports for a sensor area of  $12 \text{ mm}^2$ , a thermal resistance of about  $2000 \text{ K/W}$  for four beams in parallel, and an estimated sensitivity of  $4.8 \text{ mV/K}$  for an eight-strip thermopile.

The closed membrane configuration represents a compromise between high reachable sensitivities and mechanical stability of the structure, and it has therefore been chosen for the present sensor layout. The sensing junctions (“hot”) are positioned in the middle of the membrane, while the reference junctions (“cold”) are positioned on the chip, outside of the membrane. Once the chip is mounted on the PTFE holder and the device is closed, the membrane faces the inner part of the microchannel and is in contact with the gas flow, while the reference junctions remain outside the microchannel. Thanks to the small thermal inertia of the membrane and the insulation gap on its back side, the influence of heat conduction from the chip is strongly reduced. The sensor signal must be interpreted in this case as the difference between the temperature of the chip and that of the gas in contact with the membrane.

To retrieve the gas absolute temperature it is therefore necessary to measure the temperature of the chip. In this case there is no need for a membrane configuration and the influence of self-heating effects is not critical. The best option is to use resistance temperature detectors (RTD), which are a particular class of thermistors with a higher intrinsic linearity. For the signals to be interpreted as reference temperatures, the RTDs should be positioned close to the reference junctions of the thermopiles.

#### 4.2.1. Sensor layout

Following the above mentioned considerations, a design for the integrated measuring system has been developed. Figure 4.7 schematically shows a measuring unit, constituted by a RTD, a thermopile and a membrane creating an air gap on the backside of the thermopile sensing junctions.

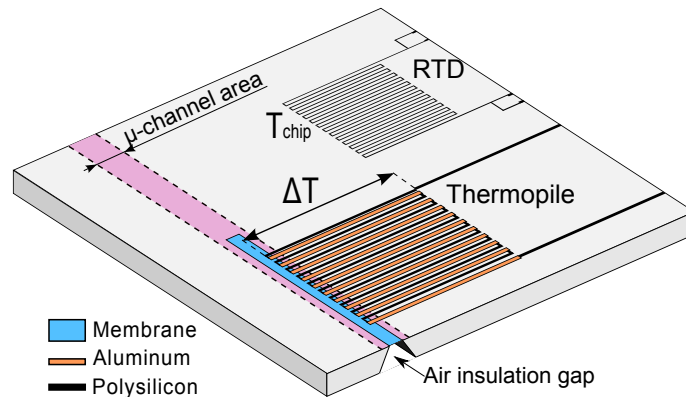


Figure 4.7.: Schematic layout of the integrated measuring system. The thermopile sensing junctions are included into the microchannel with a membrane configuration, while the reference temperature is measured by the RTD fabricated on the chip.

The RTDs present a four wire configuration to reduce noise effects of the lead resistance on the measure (see Section 2.2.1), while the selected material for the contacts is polysilicon.

The thermopiles are constituted by ten polysilicon-aluminum junctions connected in series. Values of the Seebeck coefficients ranging between 50 and 100  $\mu\text{V}/\text{K}$  have been reported in literature for aluminum-polysilicon CMOS thermopiles ([84] and [85]), which should be suitable for the present purposes.

The air gap created by the membrane on the chip backside constitutes an insulating barrier to the heat conduction across the chip, thus allowing the measuring of the temperature difference between the gas in the channel and the chip. The gas temperature at the thermopile position can be obtained as:

$$T_{gas} = T_{chip} \pm \Delta T \quad (4.1)$$

where  $T_{chip}$  is measured by the RTD and  $\Delta T$  is measured by the thermopile.

To allow the measurement of the temperature at different positions, an array of sensing units (membrane, thermopile and RTD) has been manufactured along the silicon chip. In particular, two thermopiles have been manufactured for each membrane (one per side), allowing a redundant measurement for comparison purposes and ensuring at the same time a symmetric thermal conduction profile along the contact leads on the chip. The complete layout of the chip is shown in Fig. 4.8.

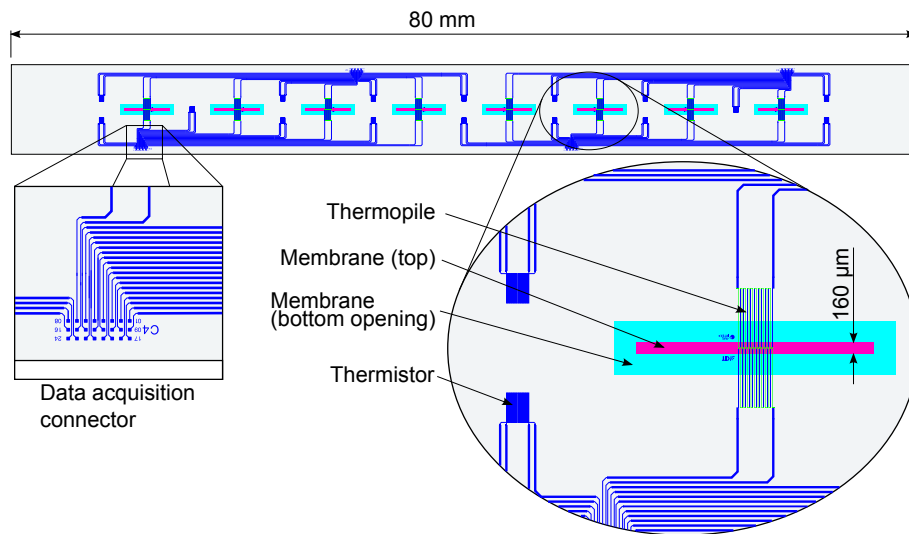


Figure 4.8.: Silicon sensor chip layout with details of the data acquisition connectors (left) and of the thermopile-RTD system (right).

A total number of 16 thermopiles have been manufactured on top of eight thin membranes distributed along the chip axis. 16 RTDs are positioned symmetrically on the chip, close to the thermopiles reference junctions.

During the design phase, the membrane width was chosen considering the major direct effects. Its value is the theoretical lower limit for the microchannel width, since to perform the measurements the entire membrane must be included in the microchannel. On the other hand the smaller the membrane is, the higher the likelihood of having thermal shortcuts becomes. Finally, a compromise value of 160  $\mu\text{m}$  had been chosen, where this is not a critical limit to the overall channel dimensions, since the height of the channel can be freely chosen.

### 4.2.2. Data acquisition cables

The data recorded by the different sensors are transferred by the corresponding leads at four different positions on the chip sides. This creates four data acquisition interfaces (as shown in the detail of Fig. 4.8). From the chip the signals are collected by four thin film polyimide cables ( $15\ \mu\text{m}$  thick), which are bonded in correspondence of the four connectors. The cables exit the device from the sides and are then connected to an adapter built on a printed circuit board (PCB). From here conventional cables can be plugged, transferring the data to a computer for recording and analysis. The schematic layout of the cable and a picture of a chip with two bonded cables are shown in Fig. 4.9.

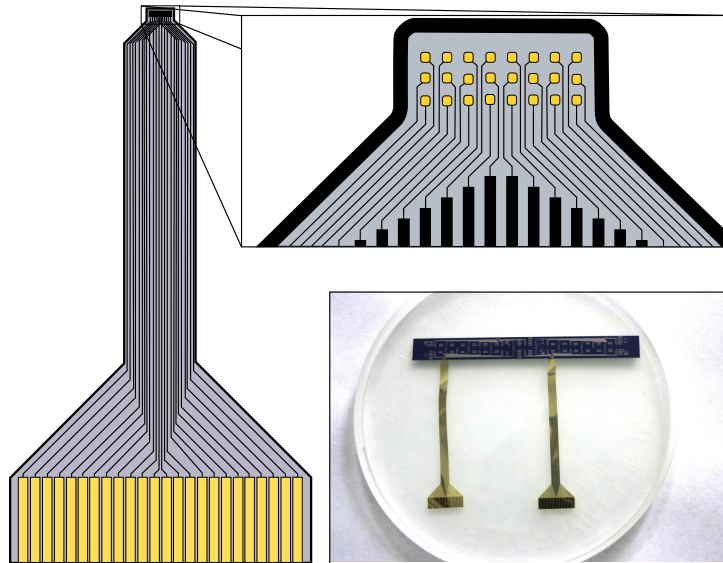


Figure 4.9.: Cable layout with a detail of the contacts on the chip side (top) and a picture of a sensor chip with two cables bonded to one side.

The bonding of the cable onto the Si chip is performed with a flip-chip bonder (Finetech Fineplacer 96 $\lambda$ ), which allows the precise alignment of the two counter pieces and creates temperature-pressure cycles to ensure the bonding of the contact bumps. The pick-up of the cable is performed by applying vacuum and using a tool which consists of a disc with a series of  $25\ \mu\text{m}$  holes (see Fig. 4.10). The disc also ensures a uniform pressure distribution over the contact area during the bonding phase.

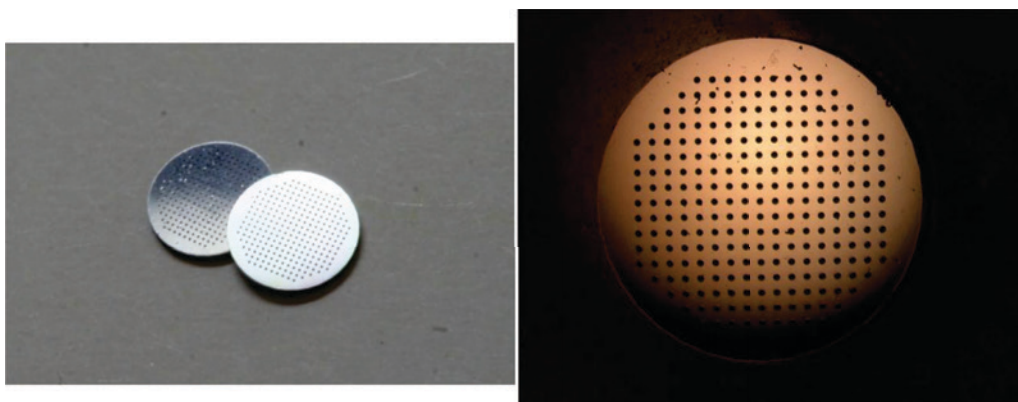


Figure 4.10.: Disc tool for cable lifting, positioning and bonding.



The bonding of the cable is a very delicate step of the chip preparation process, since overpressures or exceeding temperatures could compromise the insulation between the different contacts, creating shortcuts, cross-talking and signal noise. Insufficient pressure and temperature result in missing contacts and sensor failure. The optimal bonding parameters were identified empirically. A bonding temperature of 160 °C and a pressure of 4.83 MPa were applied for a time lapse of 40 s. After 20 s, an ultrasonic pulse with a power of 300 W was applied for 1 s. The force has the most evident effect on the final bonding quality [86]. Figure 4.11 shows the comparison between the bonding areas resulting from two similar processes, one performed with optimal bonding conditions and one with too high pressure during the bonding phase.

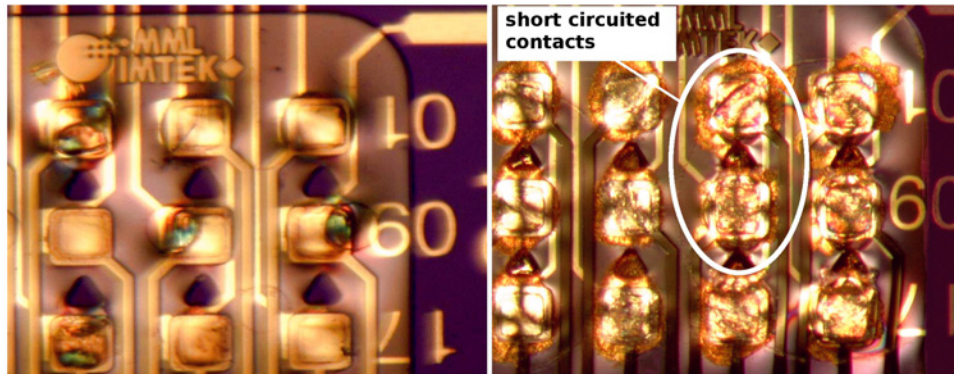


Figure 4.11.: Detail of two different bonding areas on the chip. When the bonding parameters are correctly chosen and controlled the contact areas are clean (left). If pressures higher than 4.83 MPa are applied, the material spurts out of the contact bumps, creating cross-talking and contact shortcuts (right).

The PCB interface which transfers the data from the cable level to the actual data recording system is constituted by two plugs. The first one is a zero insertion force (ZIF) connector working as an interface between the cable and the PCB. The second is a conventional wire-to-board PCB-plug whose pins are connected to the ZIF. A flat cable ending with a D-sub plug finally transfers the data to the computer. A picture of the data acquisition connections and cables is shown in Fig. 4.12.

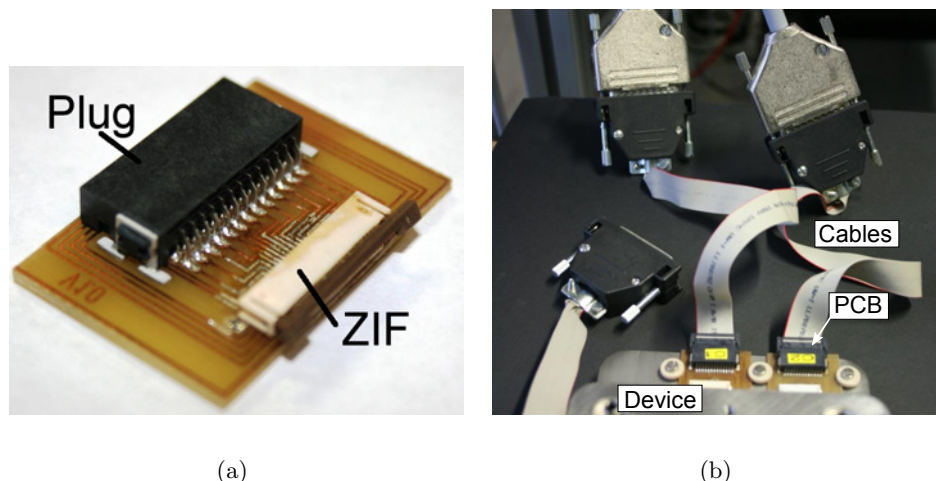


Figure 4.12.: Printed circuit board (PCB) adapters to interface the chip's thin cables (left) and mounted PCBs with flat cables for the connection to the data acquisition units (right).

### 4.2.3. Fabrication processes

#### Sensors fabrication

The different phases of the sensor fabrication procedure are represented in Fig. 4.13 and require a total of five masks. The sensor manufacturing starts with a 4" (100 mm) diameter monocrystalline silicon wafer, which allows the simultaneous fabrication of 8 chips.

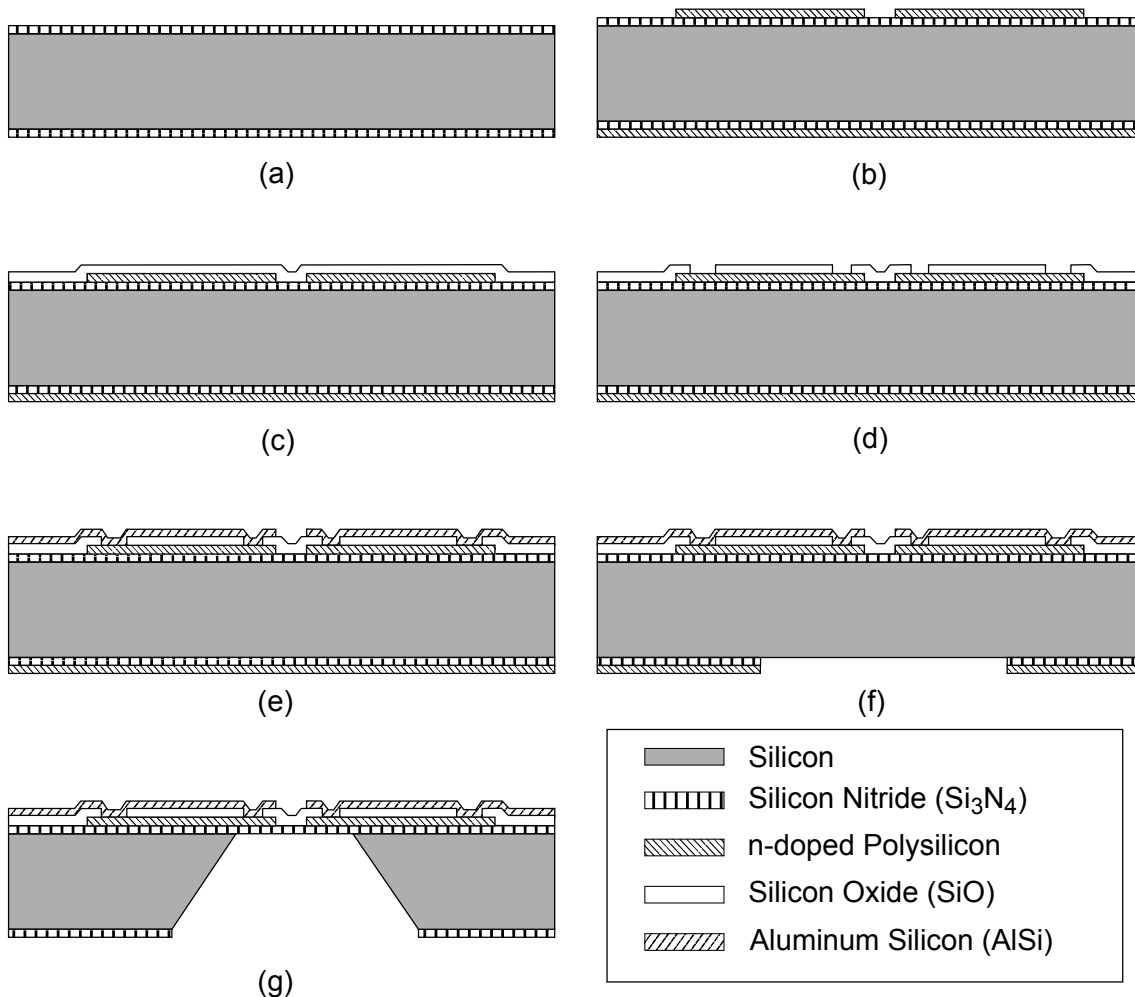


Figure 4.13.: Fabrication steps for the silicon sensors

The fabrication procedure includes the following steps:

- A layer of silicon nitride ( $\text{Si}_3\text{N}_4$ ) is deposited on the wafer as insulation layer with low pressure chemical vapor deposition (LPCVD) (Fig. 4.13-a).
- A layer of n-doped Polysilicon is deposited on the wafer. The dopants are then activated by an annealing process.
- A photoresist layer is deposited and patterned with photolithography. Reactive ion etching (RIE) is used to pattern the polysilicon layer (Fig. 4.13-b).
- A layer of silicon oxide ( $\text{SiO}$ ) is deposited with plasma enhanced chemical vapor deposition (PECVD) serving as a passivation layer between the two thermopile junction materials (Fig. 4.13-c).
- The openings for the contact are realized on the  $\text{SiO}$  by a photolithography process followed by RIE (Fig. 4.13-d).

- Aluminum Silicon (AlSi) is deposited with sputtering.
- The AlSi layer is patterned with photolithography followed by wet chemical etching. The newly created contacts between the AlSi and Polysilicon layers are activated with an annealing process (Fig. 4.13-e).
- To create the membrane, openings on the  $\text{Si}_3\text{N}_4$  and Polysilicon layers on the chip's rear side are created with photolithography and RIE (Fig. 4.13-f).
- The membrane is realized by KOH wet chemical etching (Fig. 4.13-g).
- The wafer is diced to separate the single chips.

Figure 4.14 shows the picture of a sensing unit (membrane, thermopile and RTD) fabricated with the described procedure, along with a detail of the chips rear side, where the typical sloped shape of the etched membrane and the thermopile junctions on the thin layer are visible.

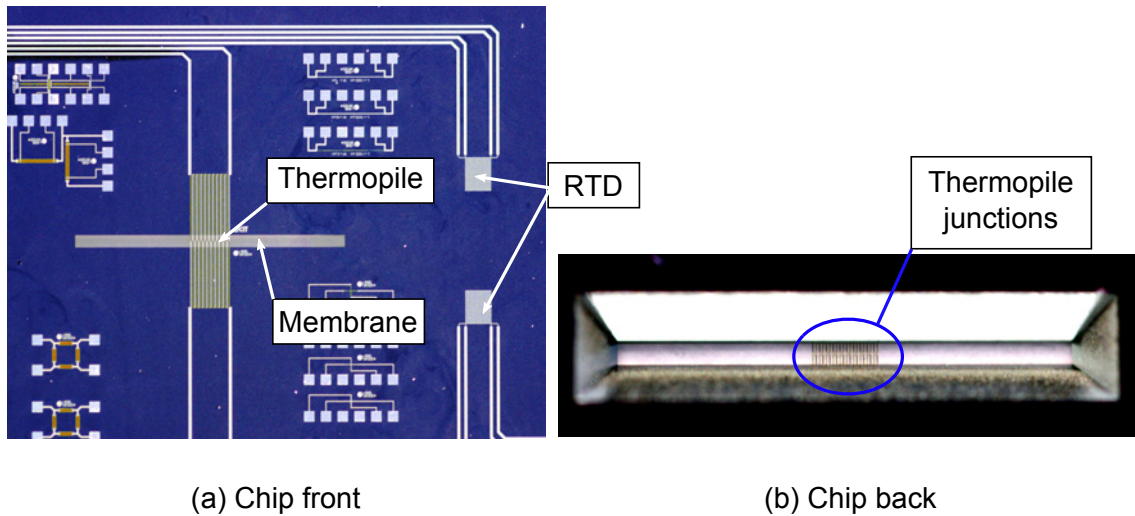


Figure 4.14.: Picture of a sensing unit (left) and of the backside of the chip (right), with details of the thermopile junctions (two colors).

### Cable fabrication

As in the case of the sensors, the thin cables for the data acquisition are fabricated using planar silicon technology, starting from a monocrystalline Si wafer serving as support substrate. The process is represented in Fig. 4.15 and consists of the following steps:

- A first polyimide layer is created on the wafer with spin coating (the polymer solution is deposited on the substrate which is then rotated at high velocity to create a uniform thin layer) and an imidization thermal process (Fig. 4.15-a).
- A photoresist is deposited as sacrificial layer and patterned with photolithography (negative pattern). After the deposition of a layer of Platinum (Pt) the photoresist is removed leaving the patterned metallization on the chip (lift-off) (Fig. 4.15-b).
- A second layer of polyimide is deposited and imidized on top of the metallization (Fig. 4.15-c).
- The two polyimide layers are patterned with photolithography and RIE (Fig. 4.15-d).
- The contacts to the ZIF-connector are realized by depositing gold with electroplating (Fig. 4.15-e).
- The cables are peeled off the silicon wafer (Fig. 4.15-f).



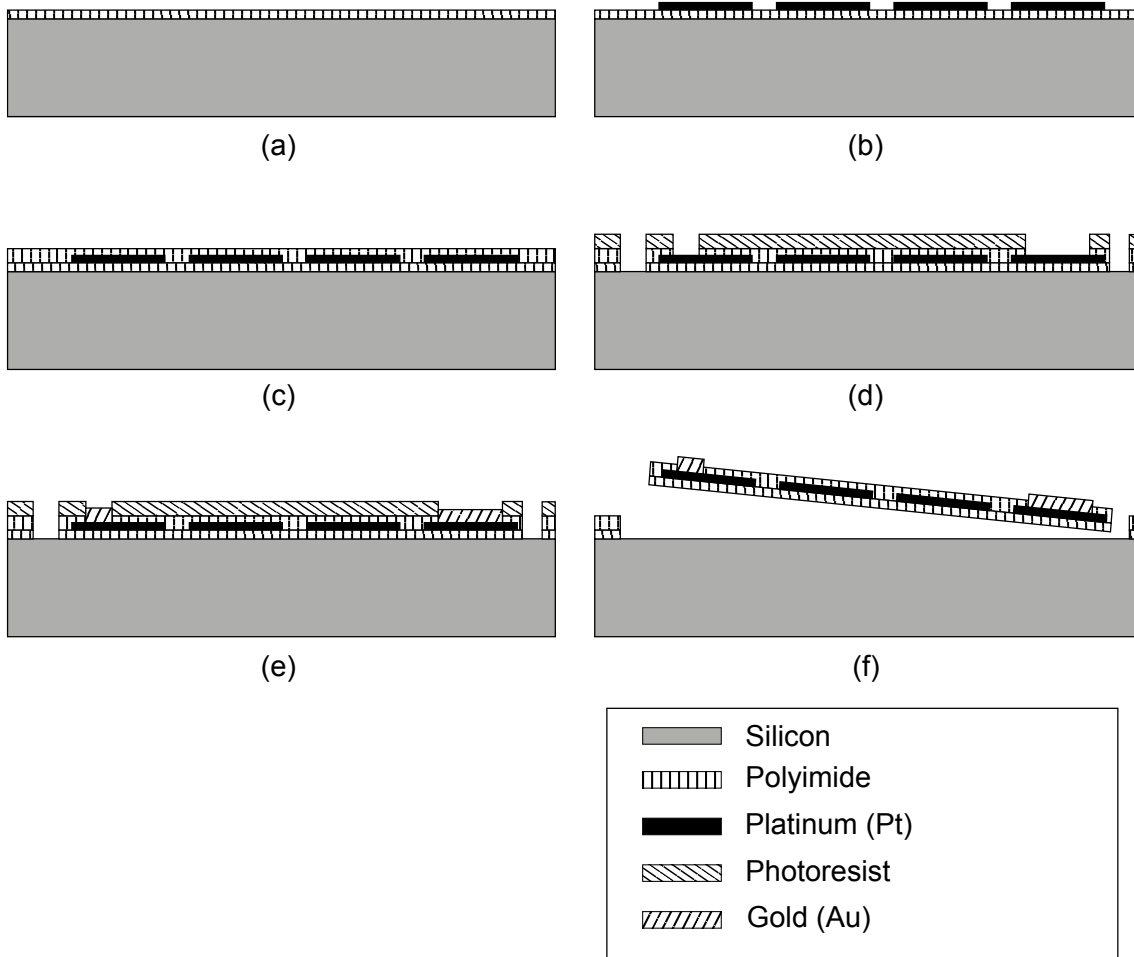


Figure 4.15.: Fabrication steps for the polyimide cables.

### 4.3. Microchannel materials and manufacturing

The realized removable test sections present a single microchannel configuration to allow the integration of the membrane array on the microchannel top. As already mentioned, the microchannel dimensions can not be freely imposed, as the minimum microchannel width corresponds to the membrane width ( $160\ \mu\text{m}$ ). To work in a safe range, a nominal channel width of  $400\ \mu\text{m}$  has been chosen for the test sections, while the channel height has been fixed to  $100\ \mu\text{m}$ . The reason of choosing a relatively small aspect ratio (height-to-width ratio) is that the sensors are included on the channel top wall, and they come in contact only with the upper part of the gas flow. For the recorded values to be representative of the entire cross section (i.e. to be considered representative of the gas bulk temperature at the sensor position), the height should be small enough to assume that the temperature distribution across the channel cross section is rather uniform, compared to the axial temperature variations.

With the available manufacturing techniques four different test sections have been manufactured as listed in Tab. 4.1. The realized test sections are shown in Fig. 4.16.

The average dimensions of the channels have been measured by optical inspection with scanning electron microscopy (SEM), except for the height of the fourth section, which has been calculated considering the mask width and the etching rate.

Table 4.1.: Specifications for the different realized microchannel test sections.

	Material	Manufacturing technique	Section	Average dimensions [ $\mu\text{m}$ ]	
				Width	Height
1	Stainless steel	Mechanical micro-milling	Rectangular	$400 \pm 4$	$110 \pm 4$
2	Copper	Mechanical micro-milling	Rectangular	$405 \pm 4$	$80 \pm 4$
3	PEEK	Mechanical micro-milling	Rectangular	$401 \pm 4$	$108 \pm 4$
4	Stainless steel	Wet chemical etching	Semi-elliptical	$422 \pm 4$	$170 \pm 15$



Figure 4.16.: Microchannel test sections.

#### 4.4. Test rig and data acquisition system

To perform the experiments, the pressure and thermal boundary conditions for the microchannel must be externally imposed and controlled. For this purpose an experimental test-rig has been realized as schematically shown in Fig. 4.17<sup>1</sup>.

The test-rig is built up using 6 mm stainless steel pipes, arranged in two branches, upstream and downstream of the microchannel device, respectively. The whole installation, including the measurement and control devices, forms an open loop between the gas feeding facility and the gas exhaust line. The gas feeding is on the upstream branch, and is followed by a mass flow controller (MFC) for the imposition of given flow rates. The inlet pressure can be measured with three pressure transducers, each presenting a different working range to ensure acceptable uncertainties at all pressure levels (namely 0-1 bar, 0-200 mbar and 0-10 mbar). For the inlet pressure regulation a manual needle valve is installed before the pressure transducers. The inlet temperature is measured by a thermocouple installed in the gas line. The temperature can be regulated, if necessary, with a cross-flow micro heat exchanger, fed with a water flow at the desired temperature.

<sup>1</sup>Technical information about the test rig and the data acquisition system can be found in Appendix A

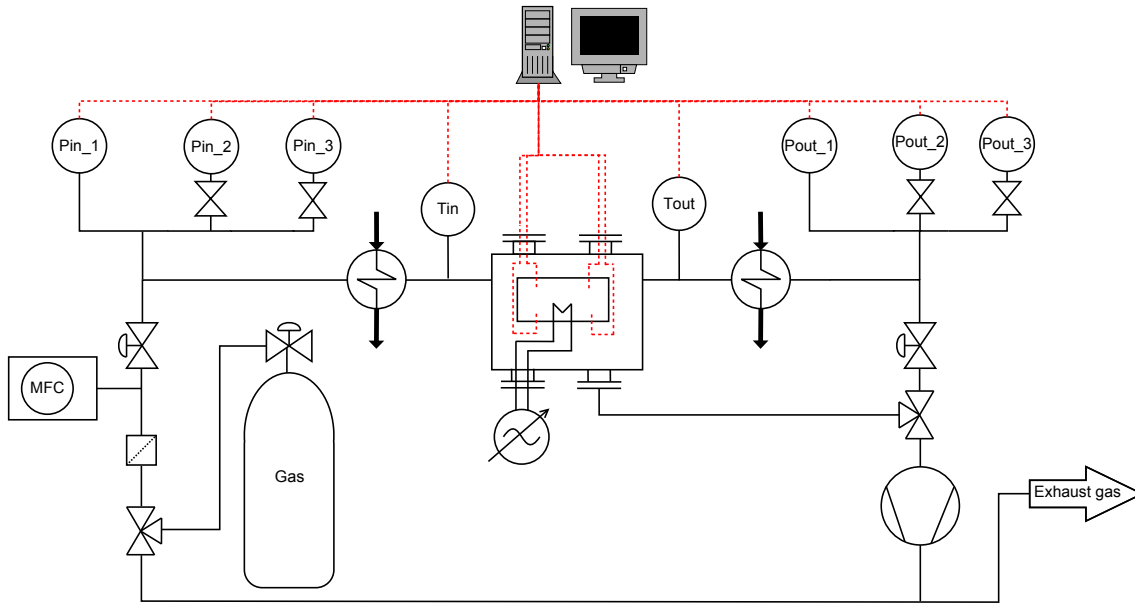


Figure 4.17.: Experimental test rig for the imposition and the control of the boundary conditions for the microchannel device.

The downstream branch includes temperature and pressure measurements, as well as a heat exchanger and a needle valve for temperature and pressure control.

The circuit is connected to a vacuum pump, which allows to achieve pressure ranges below the atmospheric level (to span the slip regime).

The thermal boundary conditions for the microchannel are imposed via the heating elements inside the copper blocks mounted below the test section. The heating cartridges are connected to an external power station with three independent channels. In particular, the temperature below the test section can be regulated by three temperature controllers receiving the signals from the thermocouples installed on the copper block grooves. As the three channels of the power station can work independently, it is easy to impose T-type boundary conditions and given temperature profiles along the microchannel foil.

To reduce the heat losses to the ambient, the microchannel device is installed in a closed volume which can be evacuated by a pump. The insulation volume is closed by a flange system while the gas inlet and outlet lines as well as the electrical connections and the cables for the data acquisition are inserted via sealed flange openings. The insulation volume is shown schematically in Fig. 4.18. With the employed vacuum pump it was possible to keep the volume at an absolute pressure of about 5 mbar during the experiments.

The data acquisition from the integrated sensors and from the test-rig is performed with Field Point<sup>®</sup> modules from National Instruments. Different modules are employed for the recording of the thermocouples, the pressure transducers and the integrated sensor signals. The modules are interfaced with a computer with a LabView<sup>®</sup> application which allows data recording as well as online visualization of the different signals.

Pictures of the experimental test rig are given in Fig. 4.19.

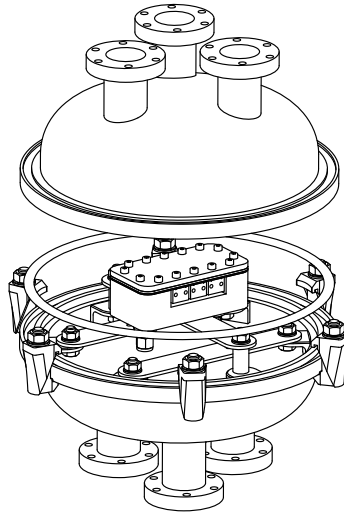


Figure 4.18.: Insulation volume with flange system for the thermal insulation of the experimental device (positioned at the center of the volume).

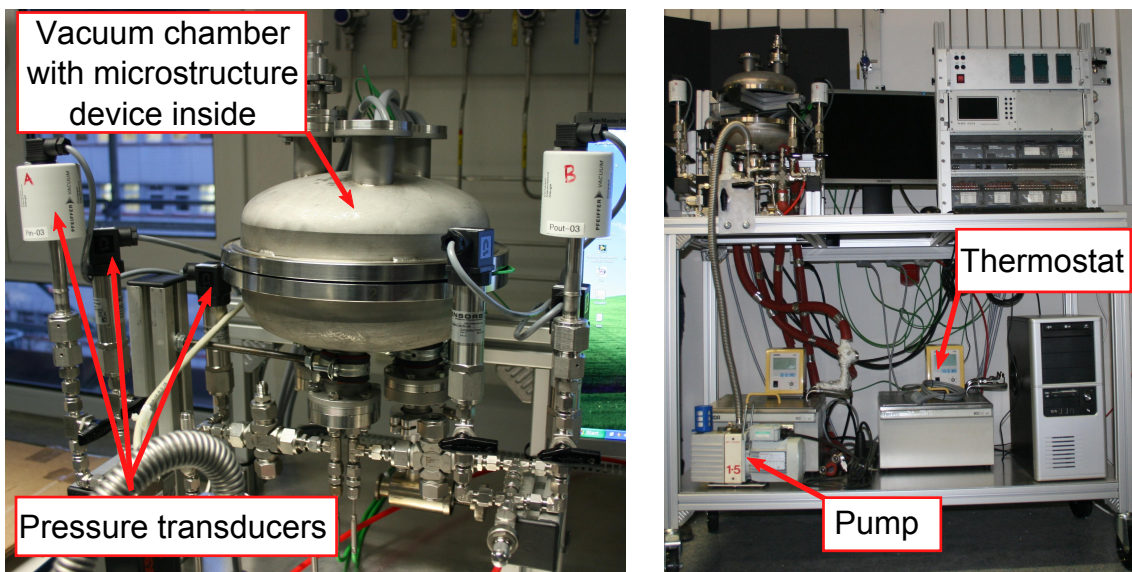


Figure 4.19.: Pictures of the test rig with details of the flange insulation volume, the three pressure transducers for different pressure ranges (upper left corner), the vacuum pump and the thermostat for the pre-heating of the gas (center) the power station and the data acquisition modules (upper right corner).

## 5. Experimental results

After a general characterization of the leak tightness of the microchannel device and the test-rig, a series of tests were performed, to calibrate the integrated microsensors. These tests allowed the comparison between the two different integration designs, as well as the evaluation of their performances, limitations and potentials.

The employment of local measuring systems was of particular interest for the study of material and surface properties effects on the heat transfer performances of the microchannel. To investigate these effects, the surface characteristics of the manufactured microchannel sections were studied. The heat transfer tests have been performed with the same boundary conditions for all the microchannel sections, analyzing then the different resulting temperature profiles.

The main objectives of the experimental campaign performed with the described multilayer device and test rig can be summarized as follows:

- Validation of the measuring principle for the integrated microsensors.
- Completion of tests to study the heat transfer of gases under varying flow conditions (from continuum to early transition) by using the two developed integrated sensor designs.
- Characterization of the influence of the microchannel material and surface characteristics on the microchannel heat transfer performances.

### 5.1. Leakage tests

A series of tests have been performed after the mounting of the experimental circuit to assess whether a sufficient leak tightness could be guaranteed by the rig itself and by the microchannel device with the microsensors chip. In the first case leakages may occur in the fittings between the different circuit parts (i.e. valves, transducers connections, etc.), which must be carefully closed and regularly checked. When the experimental device is mounted, the major leakage source is the sensor assembly itself. Indeed, the necessity of transferring the data out from the device with the polyimide cables did not allow a conventional sealing with O-rings. Despite the use of the PTFE support foil as sealing layer, small leaks could not be avoided. A leak rate of about  $7 \cdot 10^{-3}$  mbar·l/s was measured.

The evaluation of the leak rate with and without the microchannel device has been performed by first evacuating the examined volume and successively recording the pressure

variation with time by the transducers installed in the test-rig. Before the tests beginning, all the fittings and piping were inspected for damages and closed tightly, trying to reduce leaks at a minimum. The test device (without the integrated microsensor assembly) was tested separately and proved to be gas tight (leak rate  $< 1 \cdot 10^{-8}$  mbar·l/s). After the evacuation, the starting pressure inside the circuit was about 0.5 mbar, while the test environment was at atmospheric pressure. The leak rate was calculated for the control volume over which the leak test was performed. The only difference between experiments with and without the microchannel device is given by the microchannel volume. This can be neglected with respect to the rest of the volume enclosed by the test rig (i.e. piping and fittings). The control volume was calculated, considering the overall length of the connections and the average tube diameters, to be about 0.3 liters.

In Fig. 5.1 the pressure variation results for the two tests are shown. The data referring to the inlet and the outlet recordings are plotted.

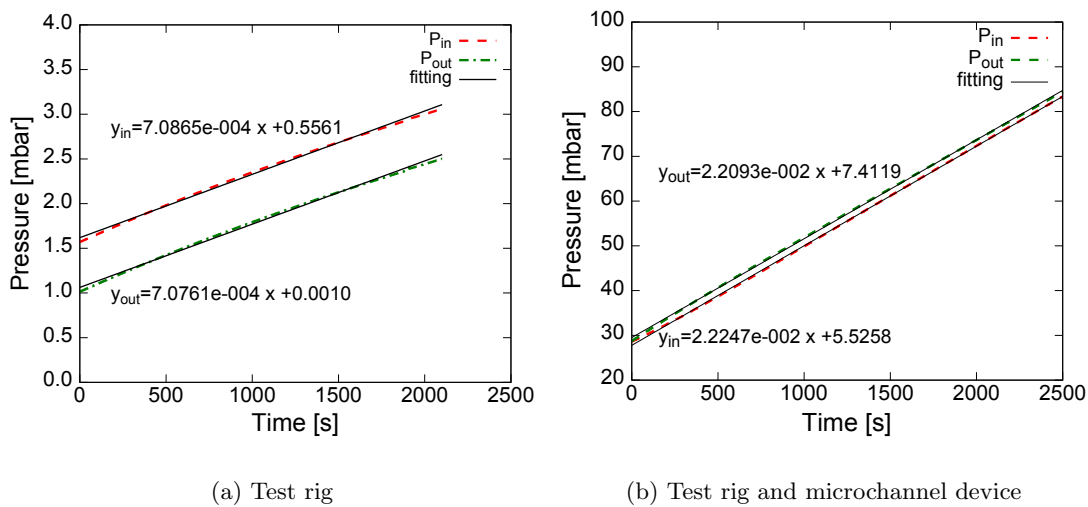


Figure 5.1.: Leak test results for the experimental rig (a) and the experimental rig with the microchannel device and the integrated sensors installed (b).

In the case of the test-rig evacuation the smaller range transducers (i.e. 0-10 mbar) have been employed, while for the tests with the experimental device it has been necessary to switch to the middle range transducers (0-200 mbar). The experimental points have been fitted with a linear regression method, where the first grade coefficient corresponds to the pressure variation in time. The calculated linear fitting equations are given in the plots. For both experiments the pressure drop between the inlet and the outlet was small (there is no imposed gas flow). A substantial increase of the leak rate was encountered when the microchannel device was installed in the circuit.

After converting the obtained data in proper units using the calculated control volume, the following leak rates have been obtained:

$$\begin{aligned} \text{Test-rig leak rate} & \quad 2.124 \cdot 10^{-4} \quad \text{mbar} \cdot \text{l/s} \\ \text{Test-rig + device leak rate} & \quad 6.63 \cdot 10^{-3} \quad \text{mbar} \cdot \text{l/s} \end{aligned}$$

The standard limits defined to classify the tightness of technical systems are shown for comparison in Tab. 5.1 (which, however, refers to helium leak tests). In both cases the recorded leak rates are above the gas-tight threshold. The difference between the two measurements is of course the effect of the microsensor assembly, which introduce an additional

Table 5.1.: Helium leak rate conventional classification [87].

Definition	Leak-rate limit
	mbar·l/sec
Water-tight	$10^{-02}$
Vapor-tight	$10^{-03}$
Bacteria-tight	$10^{-04}$
Oil-tight	$10^{-05}$
Virus-tight	$10^{-06}$
Gas-tight	$10^{-07}$
“Technical-tight”	$10^{-10}$

leak source at the position where the cables exit the device between the microchannel and the PTFE layers. The leakages of the test-rig are mainly located at the thermocouple positions. Indeed, commercial thermocouples present a metal coating of the sensing junction which allows some gas to pass through. The measured leak rate corresponds to about  $3 \cdot 10^{-11}$  kg/s, which represents less than 1 % of the mass flow rates established during the experiments (under continuum flow regime), and can be therefore considered acceptable.

The leak rate has been periodically checked throughout all the performed experiments. The reported values do not significantly change from one test to the other and can be considered representative for the experimental setup itself.

## 5.2. Surface characterization

The influence of surface roughness on the behavior of pipe flows has been studied extensively for well over a century ([88], [89] and [90]), and different methods to evaluate its effects have been proposed over the years. With the development of mini- and microdevices, however, new questions have been raised mainly to assess whether classical conclusions could be extended to these new fields. Given the small characteristic dimensions of microfluidic devices, typical roughness heights may not be negligible as for conventional hydraulic systems (for which roughness usually represents less than 5 % of the overall diameter) [91]. Many works on microstructured systems are available claiming roughness to play a major role in determining, e.g., the occurring of the flow laminar-turbulent transition or enhancing the heat transfer performances due to an increment of the available exchange surface [10].

In general, if a surface sample, as shown in Fig. 5.2, is considered, the main surface features can be distinguished by their characteristic dimensions as:

- Roughness: characteristic short interval structures.
- Waviness: surface structure with longer intervals.
- Form: includes even longer surface structures.

When a surface is analyzed, the actual measured quantity is the *primary profile* (P), consisting of a *waviness profile* (W) and a *roughness profile* (R) (as represented in Fig. 5.3).

To separate the short- and long-wave components, a limiting wavelength, defined as cutoff, is specified as a signal filter. The cutoff must be short enough to exclude long wavelengths and long enough to ensure that relevant texture information are not dismissed [93].

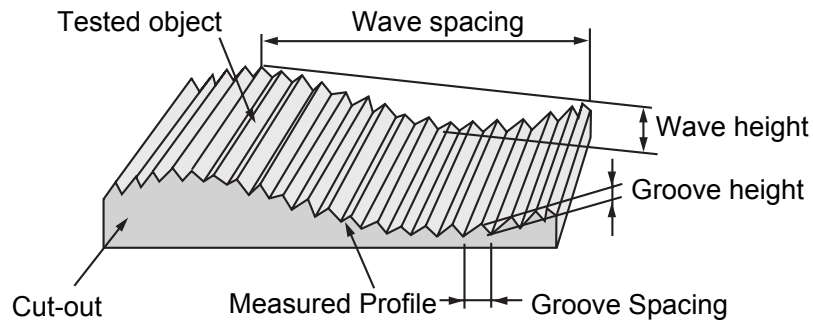


Figure 5.2.: Main characteristics of a surface sample [92].

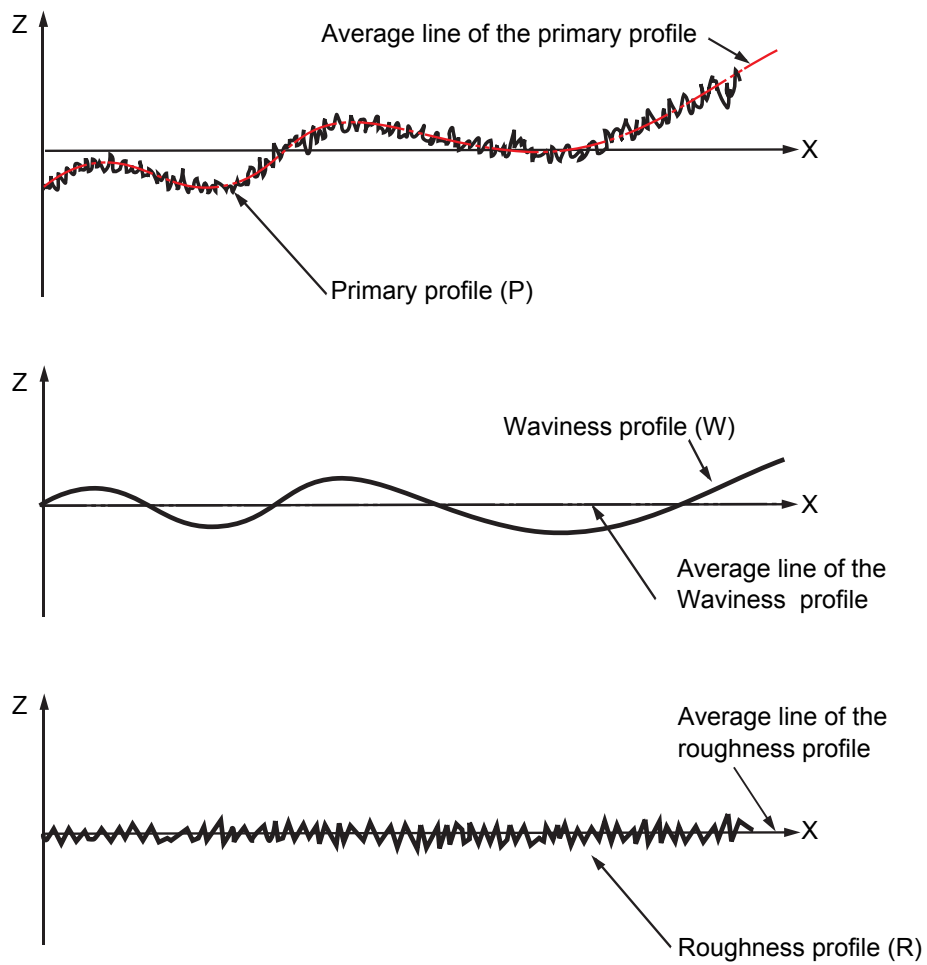


Figure 5.3.: Distinction between the different characteristics of a surface profile [92].



Since most of the fabrication and manufacturing processes are statistical by nature, surface topography relies on the definition of a series of statistical quantities. The number of defined parameters ranges from around 50-100, many of which are included in national standards [94]. The one employed in the following is the *mean arithmetic roughness* ( $R_a$ ), corresponding to the arithmetic mean of all the profile intercepts within the sampling length  $L$ . The mean arithmetic roughness is represented in Fig. 5.4 and is defined, according to [94], as:

$$R_a = \frac{1}{L} \int_0^L |z(x)| dx \quad (5.1)$$

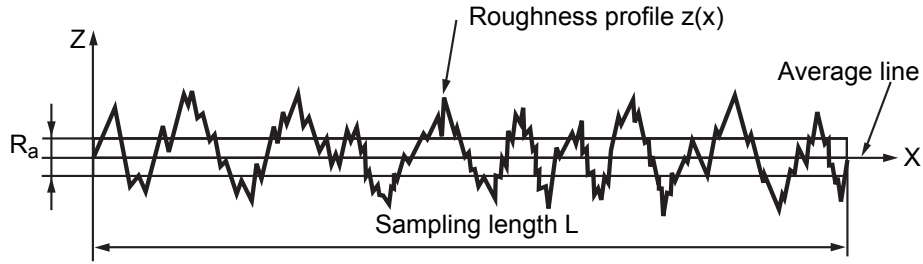


Figure 5.4.: Graphical representation of the mean arithmetic roughness ( $R_a$ ) [92].

Despite the amount of efforts in determining the role of roughness at microscales, univocal conclusions can still not be drawn, one of the main reason for that being the lack of specific techniques to analyze the texture of microstructured surfaces. Indeed, some of the classical evaluation methods are not applicable to microdevices, due to the impossibility of a physical or optical access to the surfaces. Moreover, the description of surface finish by average parameters (such as the mean arithmetic roughness) might not be fully representative of microstructured surfaces, due to the non-uniformities typically originating from micro-manufacturing processes.

For the present work, the open geometry of the manufactured microchannels allowed both optical and contact methods to be employed for the evaluation of surface roughness. As optical techniques, scanning electron microscopy (SEM) and a chromatic white light sensor (CWL) were used, where the first provides a qualitative evaluation of the texture, while the second enables quantitative measurements. As contact method, stylus profilometry was employed, since the characteristic dimensions of the probes allowed the access to the microchannel bottom surfaces. A fairly more accurate technique would have been atomic force microscopy (AFM). In this case, however, the dimensions of the holder of the sensing tip which must be in contact (or in proximity) to the surface, were too big to provide access to the microchannels.

To take local non-uniformities into account, the measurements were performed at different positions along the microchannels, computing then the corresponding local average roughnesses.

### 5.2.1. Scanning electron microscopy

The first method employed for the test section surface characterization is scanning electron microscopy. It is a non invasive method allowing high magnifications and also scanning of large surfaces. Qualitative evaluation of the surface roughness by SEM is often used for cases where the channel aspect ratio does not allow the insertion of probes as, e.g., for atomic force microscopy. Despite its flexibility and relative simplicity, SEM does not

allow a direct quantitative evaluation of roughness (unless an external reference is used) and other methods are therefore needed.

Pictures of the whole channel and of details of the surfaces have been taken to highlight the main characteristics of each section. Some representative pictures referring to the channel sections described in Section 4.3 are shown in Fig. 5.5 - 5.8.

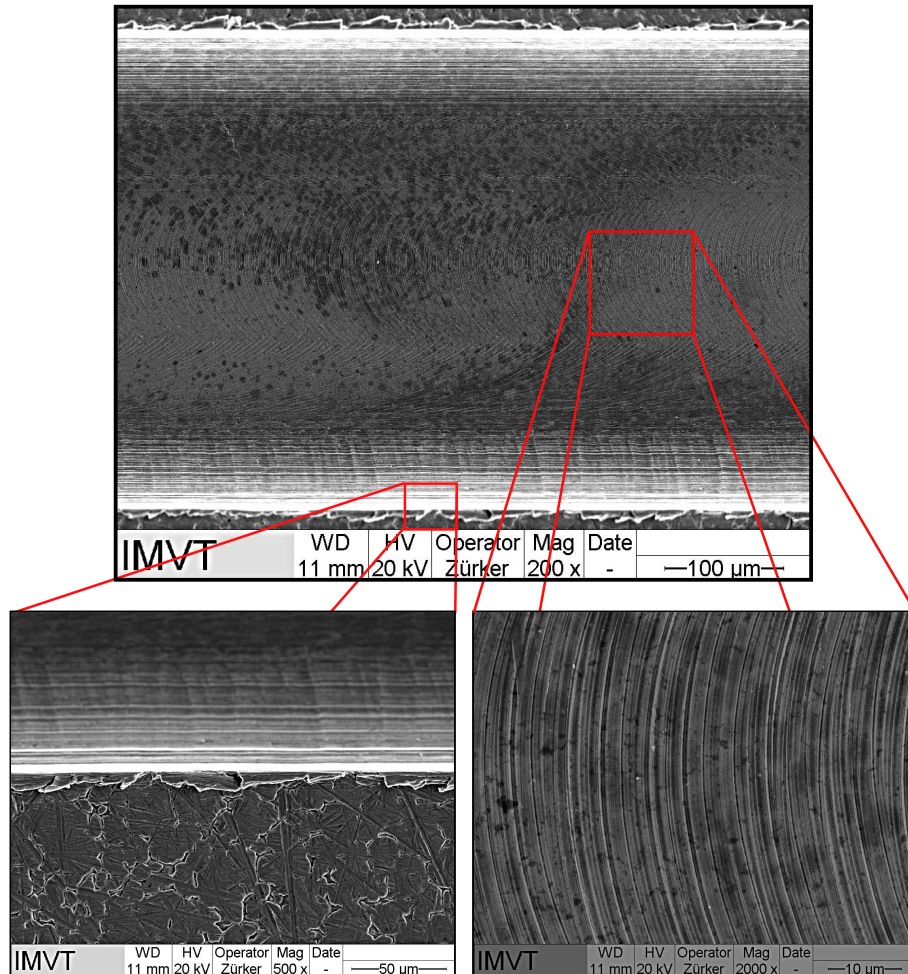


Figure 5.5.: SEM pictures of a milled stainless steel microchannel (top), with details of the channel side and bottom walls (bottom left and right, respectively). Typical manufacturing tool patterns are visible on the bottom wall.

The stainless steel and PEEK test sections prepared with micromachining techniques (Fig. 5.5 and 5.7) show characteristic patterns on the bottom wall, derived from the tools used during the fabrication (i.e., in the specific case, a micro-endmill). The etched channel (Fig. 5.8) does not present any unidirectional manufacturing pattern, as wet chemical etching is an isotropic process. In this case large irregular grains are seen on the channel walls. The channel boundaries in the pictures are not sharp, indicating the typical semi-elliptic cross section of etched microchannels. Finally, also the micromachined copper channel (Fig. 5.6) does not present characteristic fabrication patterns. A possible explanation for the increased roughness (compared to machined stainless steel and PEEK) could be that the thermal stress occurring during the machining led to oxidation on the copper surface. This can cause grains to grow on top of the surface which are then removed by the machining tool, leaving holes and an irregular texture. The phenomenon is enhanced if copper oxide molecules are already included in the metal matrix, as in the present case. These are released at high temperatures and can also cause pitting of the metal surface. The

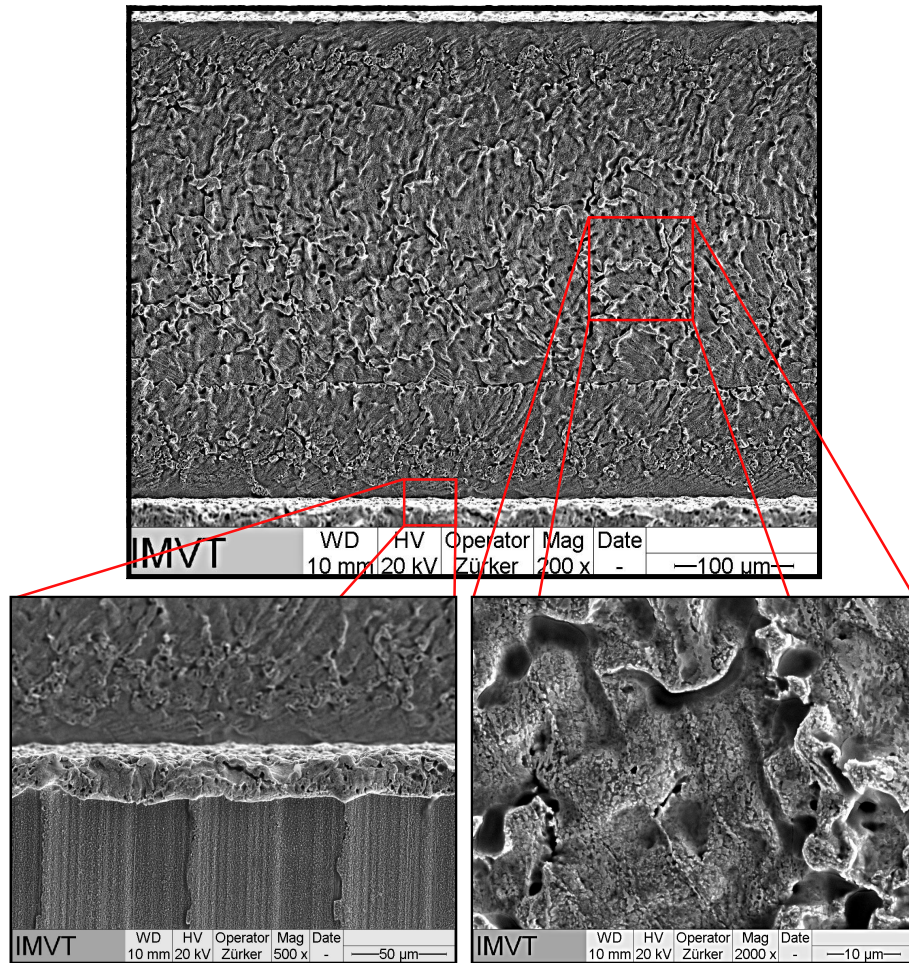


Figure 5.6.: SEM pictures of a milled copper microchannel (top), with details of the channel side and bottom walls (bottom left and right, respectively). The bottom wall shows an irregular and rough surface deriving from material removal during the fabrication.

employment of oxygen free copper (OF-Cu) would strongly reduce this effect and allow a better surface finish.

To obtain more quantitative data about the surface characteristics of the test sections, both contact profilometry and chromatic confocal imaging measurements have been used.

### 5.2.2. Contact (stylus) profilometry

Among the different profilometry techniques (including optical and contact methods), contact (or stylus) profilometry is one of the most commonly used for surface texture measurements [95]. It consists of a diamond stylus brought in contact with the surface to be measured and moved laterally for a pre-defined scanning distance. The profilometer measures the small vertical displacements of the stylus as a function of position, corresponding to the surface variations. A schematic representation of the profilometry measuring principle is shown in Fig. 5.9.

The resolution of the roughness measurement is a function of the stylus diameter and the scanning velocity. In general, contact profilometry enables the recording of detailed surface profiles with excellent resolutions both in the horizontal and the vertical direction. Among the drawbacks of this technique are the fragility of the stylus and the possibility of surface damages occurring from stylus-surface interactions. Moreover, contact profilometry



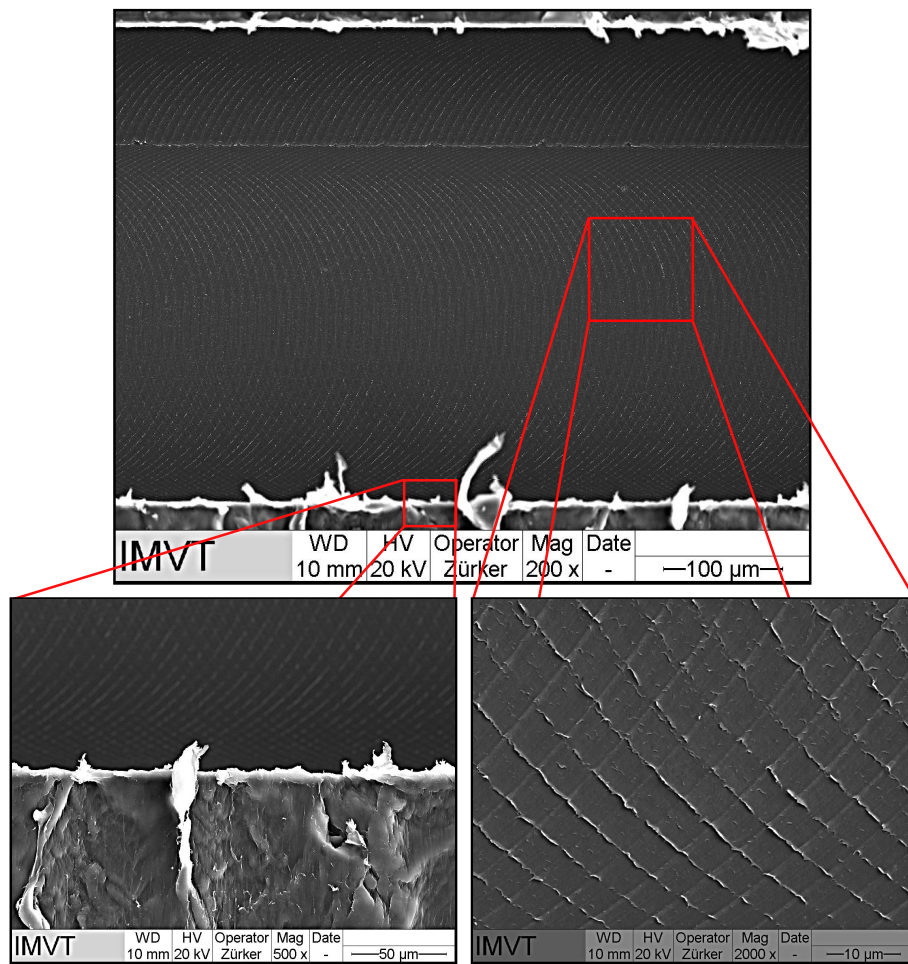


Figure 5.7.: SEM pictures of a milled PEEK microchannel (top), with details of the channel side and bottom walls (bottom left and right, respectively). Manufacturing tool patterns are visible on the bottom wall.

is usually designed for 2D measurements. 3D mapping is becoming increasingly available but requires special and more expensive instrumentations.

For the present analysis a Veeco DEKTAK V220 system, available at the Institute for Microstructure Technology (IMT) at KIT has been employed. A 25 μm radius stylus has been used to scan a length of 1 mm along the axis of the microchannel bottom wall. The measurements returned the primary profile including the waviness and roughness components. These data are automatically analyzed to calculate the mean arithmetic roughness  $R_a$ . Some difficulties for the positioning of the probe along the microchannel axis, performed with the help of a microscope, were encountered because the probe holder had almost the same size as the microchannel.

Two examples of data from a profilometer scan are shown in Fig. 5.10 for the microchannels in copper and PEEK, respectively. On the main box the primary profile, the waviness and the roughness curves are plotted, while the different parameters averaged over the scanning length are reported on the left boxes.

For each tested microchannel material, the values of  $R_a$  averaged over three measurements at different axial positions are given in Tab. 5.2. As observed with SEM, the copper and the etched stainless steel sections show relatively rough surfaces. The micromachined sections in stainless steel and PEEK both present rather low average roughnesses (considering that no post-treatment to improve the surface quality had been performed).

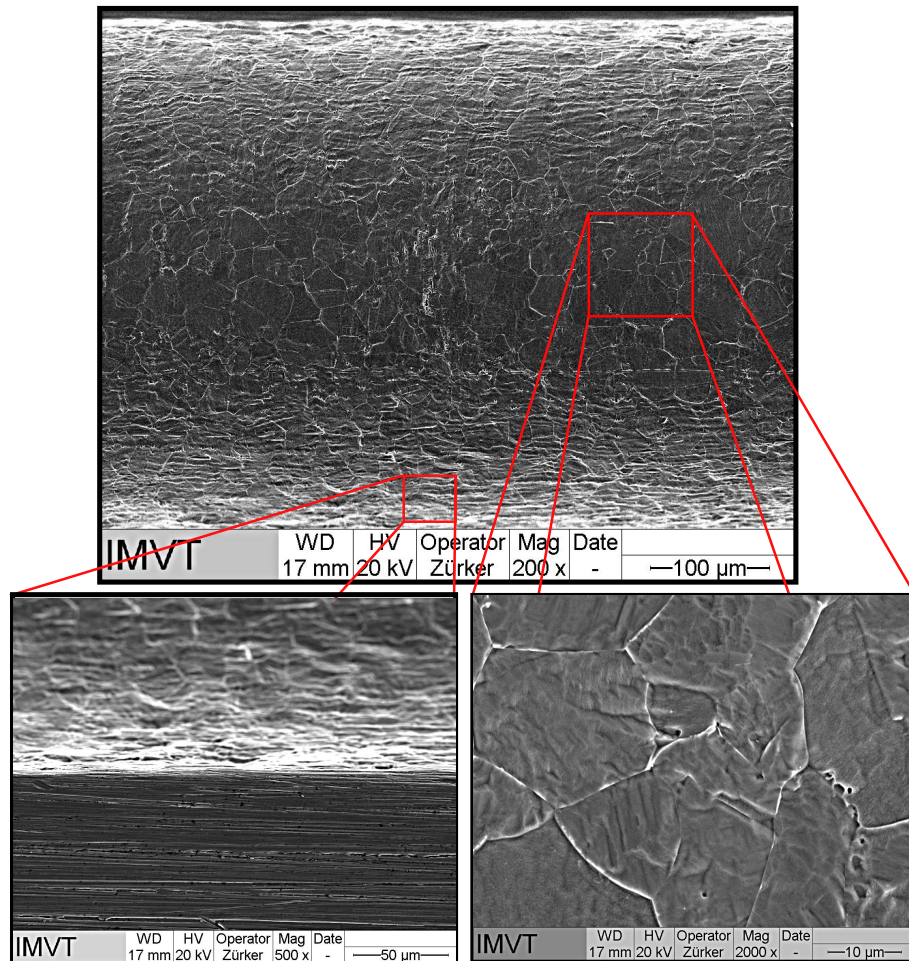


Figure 5.8.: SEM pictures of an etched stainless steel microchannel (top), with details of the channel side and bottom walls (bottom left and right, respectively). The channel surface deriving from the etching process shows typical irregular grains.

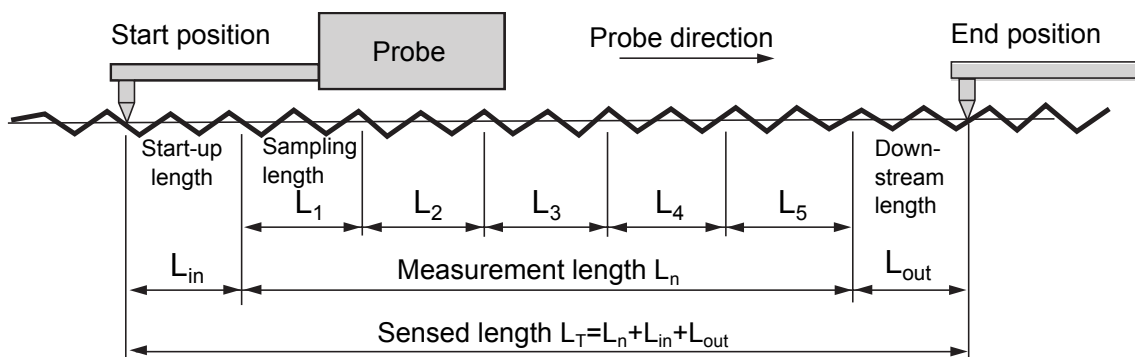
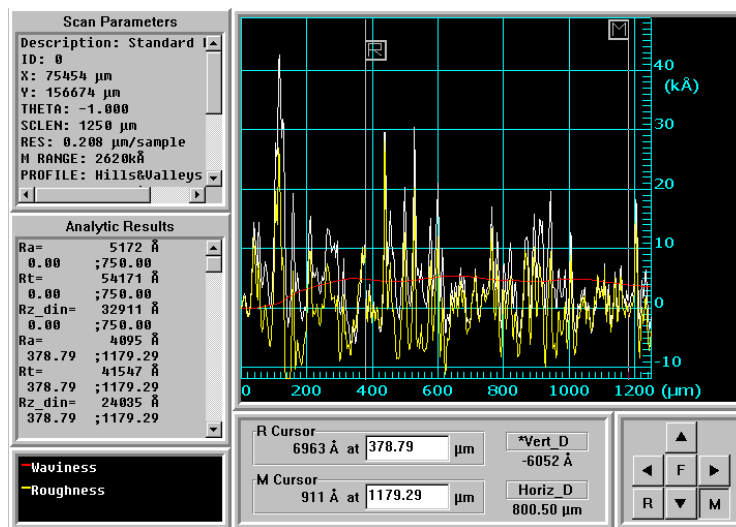
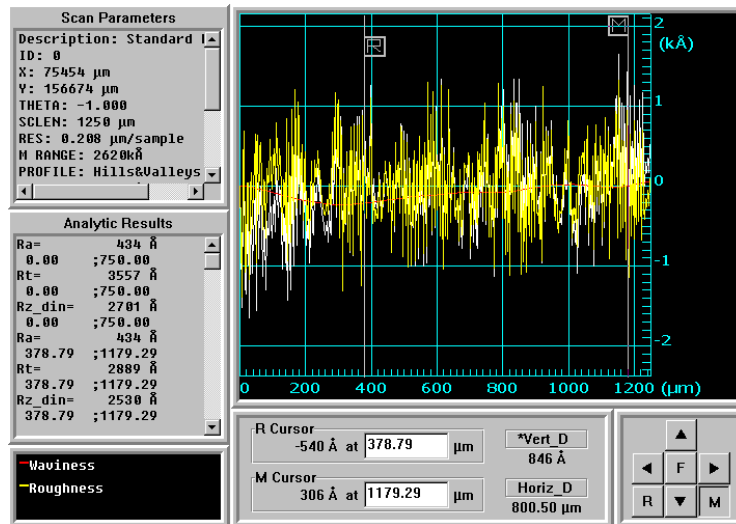


Figure 5.9.: Schematic measuring principle for mechanical profilometry [92].

The values reported in Tab. 5.2 can be considered as representative of the material-manufacturing technique combination. However, they are only indicative since the evaluation was done over small lengths and along the axis only.



(a) Copper



(b) PEEK

Figure 5.10.: Screen shots from the profilometer measurements of two microchannel sections.

Table 5.2.: Results of the profilometry analysis of the microchannel test sections.

Section	Average $R_a$
1 Micromachined stainless steel	0.03 $\mu\text{m}$
2 Micromachined copper	0.52 $\mu\text{m}$
3 Micromachined PEEK	0.04 $\mu\text{m}$
4 Etched Stainless steel	0.32 $\mu\text{m}$

### 5.2.3. Chromatic white light sensor

To overcome the main limitations of the contact evaluation technique, further measurements with chromatic confocal imaging (or chromatic white light - CWL) technique have been performed with a sensor and a measuring station from FRT at the Institute for Material Research (IMF-III) at KIT.

Chromatic white light (CWL) sensors exploit the phenomenon of light aberration to determine the profile of the scanned surfaces. The device consists of a white light source, a measuring head with a lens showing a strongly wavelength-dependent focal length and a spectrometer. The measuring head focuses the light on the surface to be measured, which scatters back parts of the light to the detector. The spectrum of the scattered light presents a peak whose wavelength depends on the height of the target surface and can be used to determine its profile. The CWL measuring principle is shown in Fig. 5.11.

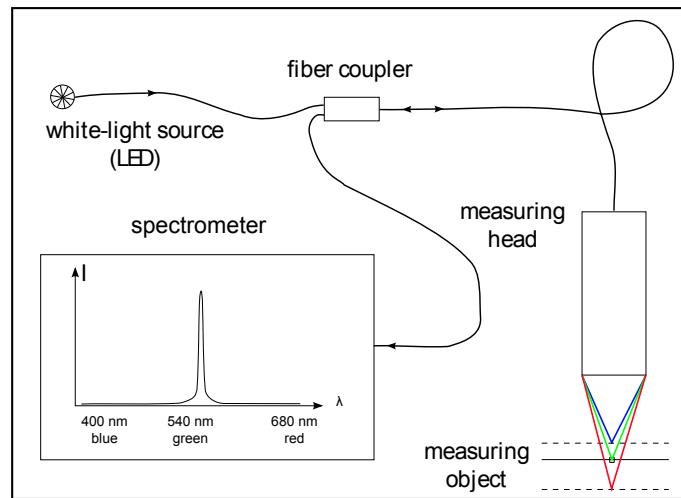


Figure 5.11.: Measurement principle for the chromatic white light (CWL) sensing technique [96].

The CWL sensing method is a non-contact technique allowing very high resolution measurements of 1D and 2D profiles. It also allows the reconstruction of 3D surfaces thanks to a multilevel scanning. The main drawback of this technique is the necessity of providing a direct illumination of the measuring surface. In microstructured systems the structure itself might create shadowed areas inaccessible to the light source.

For the 2D analysis of the microchannels, a scanning length of 5.6 mm has been chosen. This is the value defined in standards for the evaluation of the mean roughness of a technical surface [97]. For an overall characterization of the test sections, three different scans per microchannel have been performed along the central axis: near the inlet, the middle and the outlet, respectively. The results of the scans for the different sections are shown in Fig. 5.12 - 5.15. The data have been filtered to remove the waviness component.

The roughness profiles may significantly vary not only when the material or the manufacturing processes is changed, but also from one part to another along the same microchannel (as it is evident in Fig. 5.13). This effect is mainly caused by wear of the machining tool during the manufacturing process. For this reason it is important, when characterizing microstructured surfaces, to take into account the manufacturing process and assess whether this may influence the uniformity of the surface finish. Tab. 5.3 reports the mean arithmetic roughness  $R_a$  for each scan and the average for the whole microchannels. Figure 5.16 presents the comparison of  $R_a$  between the different microchannel sections.

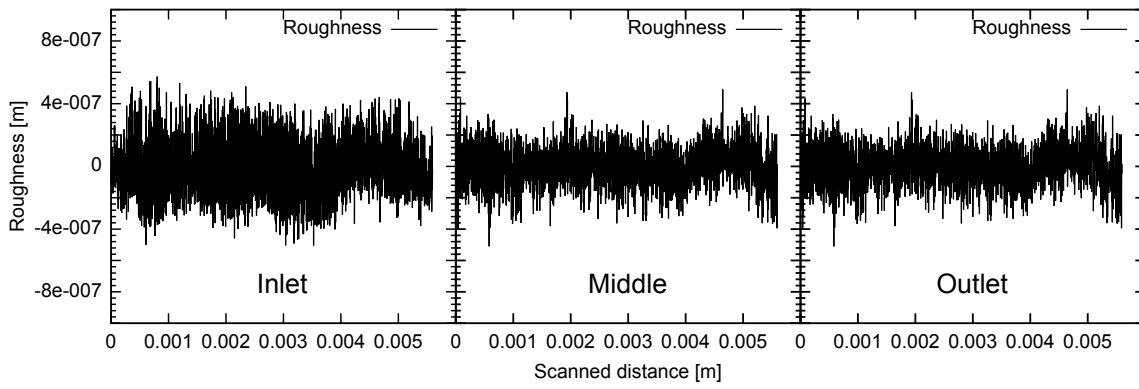


Figure 5.12.: CWL scans of the micromachined stainless steel channel section.

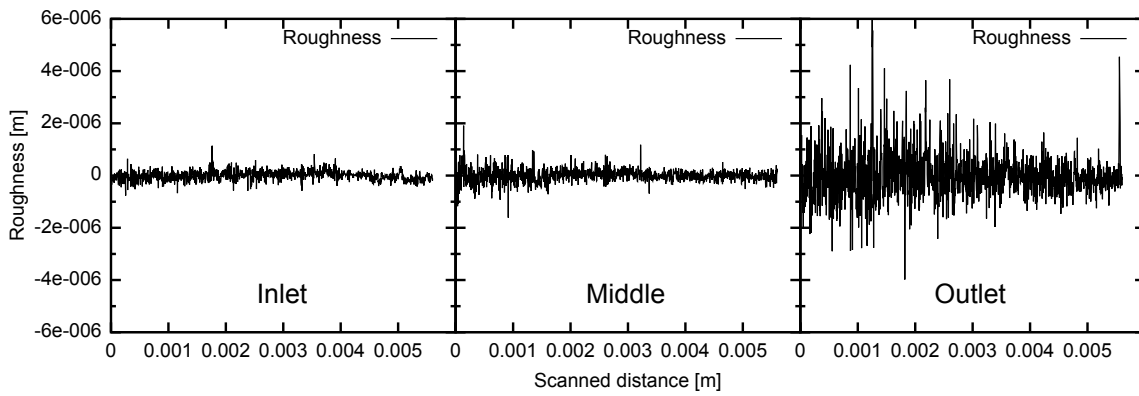


Figure 5.13.: CWL scans of the micromachined copper channel section.

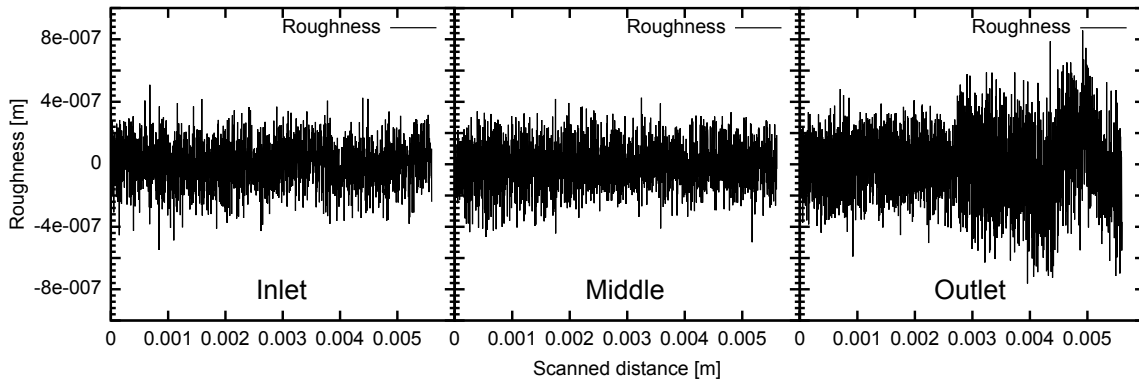


Figure 5.14.: CWL scans of the micromachined PEEK channel section.

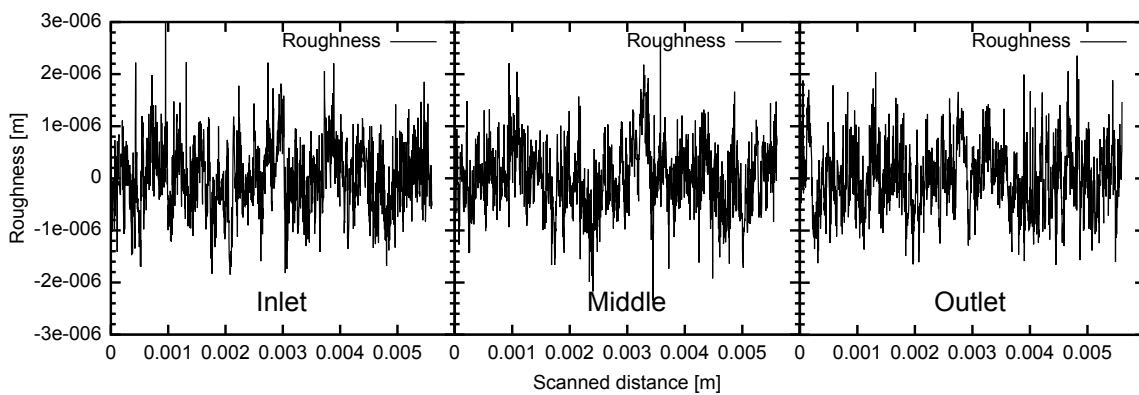


Figure 5.15.: CWL scans of the etched stainless steel channel section.



Table 5.3.: Results of the CWL sensor scans for the microchannel sections. The mean arithmetic roughness for the single scans is reported, along with the average value for each tested microchannel.

Channel		$R_a$ [ $\mu\text{m}$ ]	Average $R_a$ [ $\mu\text{m}$ ]
1 - Micromachined stainless steel	Inlet	0.0771	0.0769
	Middle	0.0809	
	Exit	0.0727	
2 - Micromachined copper	Inlet	0.1463	0.3027
	Middle	0.1685	
	Exit	0.5932	
3 - Micromachined PEEK	Inlet	0.1094	0.1385
	Middle	0.1346	
	Exit	0.1716	
4 Etched stainless steel	Inlet	0.4795	0.4591
	Middle	0.4353	
	Exit	0.4624	

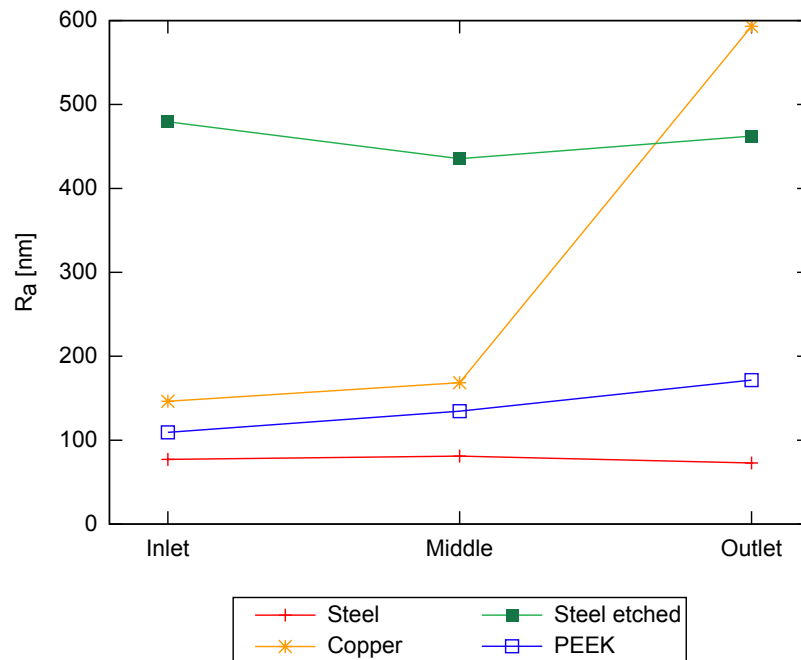


Figure 5.16.: Results of the average roughness measurements with CWL sensor technique. For each microchannel test section three scans have been performed around the inlet, the center and the outlet of the microchannel respectively.

Considering the average  $R_a$  as representative for the whole microchannels might induce rather large errors, as it completely dismisses all the local differences and inhomogeneities. Moreover, the results presented so far only refer to the microchannels axis. For a better representation of the surface characteristics, 3D measurements were performed by using the 3D rendering feature of the CWL device. In this case a rectangular area to be scanned is defined and the device can either provide a 2D color map of the detected heights or reconstruct a 3D profile. Example results for the four different sections types are given in Fig. 5.17 - 5.20.

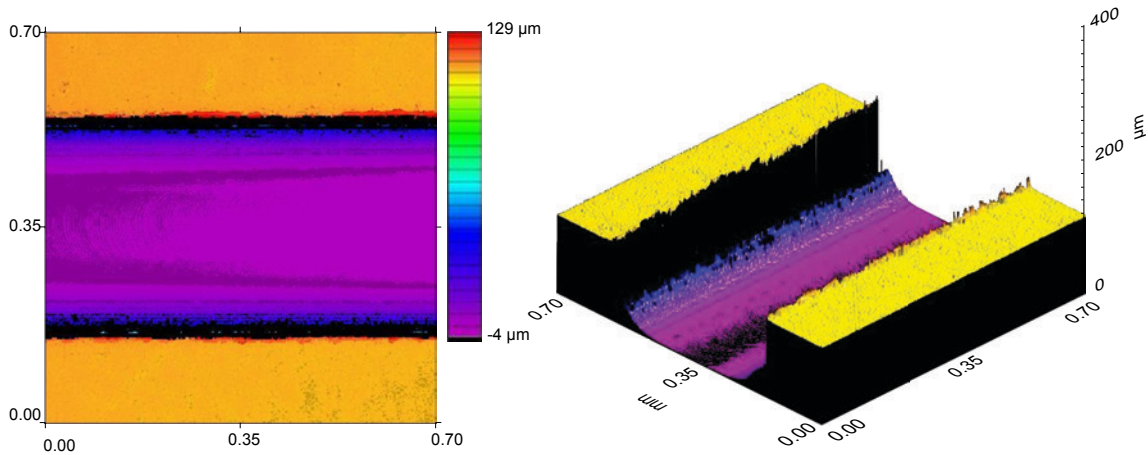


Figure 5.17.: 2D and 3D surfaces produced by the CWL sensor for the micromachined stainless steel microchannel.

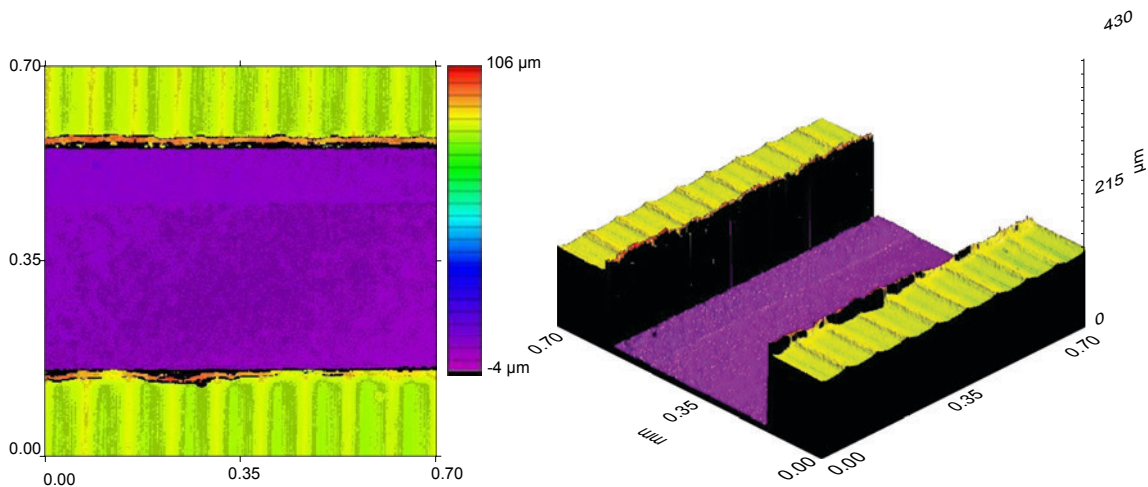


Figure 5.18.: 2D and 3D surfaces produced by the CWL sensor for the micromachined copper microchannel.

The main drawback of this measurement approach is that with rectangular channels, unavoidable shadowing effects from the side walls create blank areas that cannot be scanned by the CWL sensor. If, e.g., the cross section profiles along a line are calculated, the side walls will not appear, as they cannot be optically accessed by the sensor. Figure 5.21 reports some examples of cross section profiles. The shadow areas are marked in red, meaning that the data points contained in them are not reliable and should be neglected.

While the rounded corners of the stainless steel etched microchannel (Fig. 5.21-d) are expected, some minor curvature at the bottom corners of the micromachined stainless

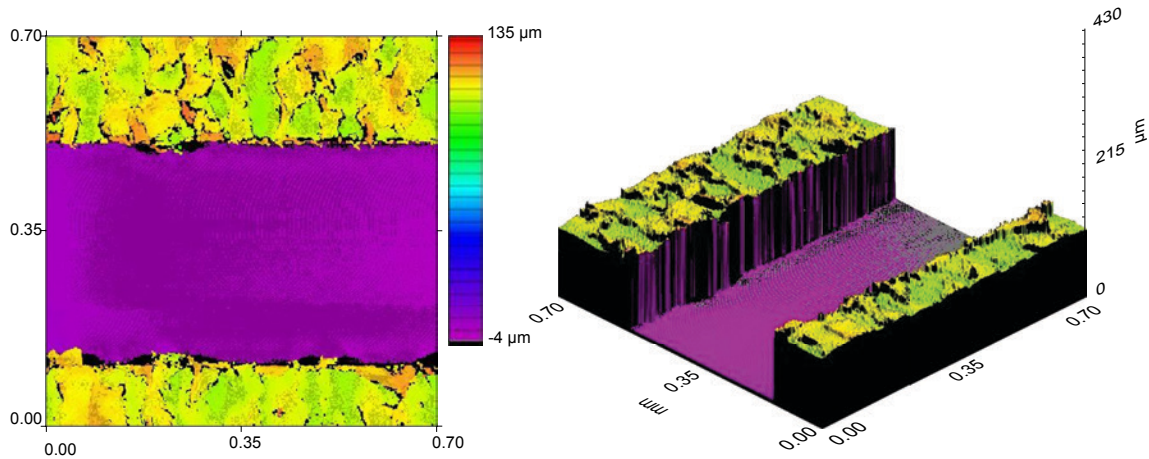


Figure 5.19.: 2D and 3D surfaces produced by the CWL sensor for the micromachined PEEK microchannel.

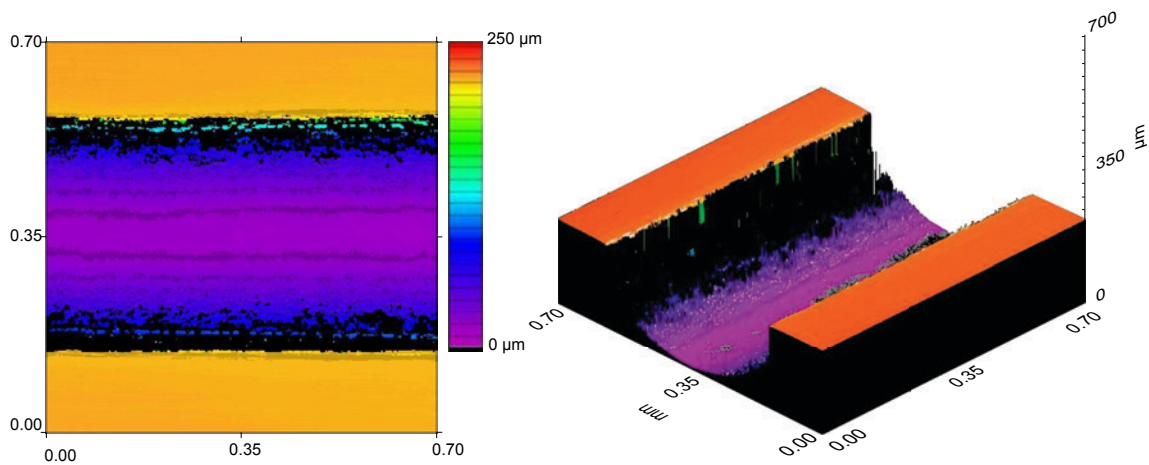


Figure 5.20.: 2D and 3D surfaces produced by the CWL sensor for the etched stainless steel microchannel.

steel section are visible as well (Fig. 5.21-a). These derive from the hard metal tool head (similar to the one showed in Fig. 2.8), which shows rounded edges. For materials like copper and PEEK, on the contrary, diamond tools were employed, which allow better precision and smaller curvature radii at the boundaries. The absence of rounded corners in the copper and PEEK sections (Fig. 5.21-b and -c) is only apparent since the actual channel boundaries cannot be accessed by the optical sensor due to the wall shadowing. The shape defects of the copper and PEEK microchannels are however smaller than for stainless steel, given that the material hardness of steel is higher.

Table 5.4 presents a comparison between the average roughness of each tested section type, calculated from the three described methods. The results for scanning electron microscopy are reported only as orders of magnitude, since the evaluation has been done taking the dimension scale as reference. Quantitative data could be retrieved by employing specific reference scales for SEM roughness measurements, which in this case were not available.

Table 5.4 shows that the results obtained from the three techniques are in general comparable. The largest discrepancies appear for the smallest  $R_a$ , i.e. for the micromachined stainless steel and PEEK sections. In these cases the profilometry measurements give smaller average roughnesses than the CWL sensor. However, the length over which the profilometry data are averaged (1 mm) is shorter than the scanning length set for the CWL

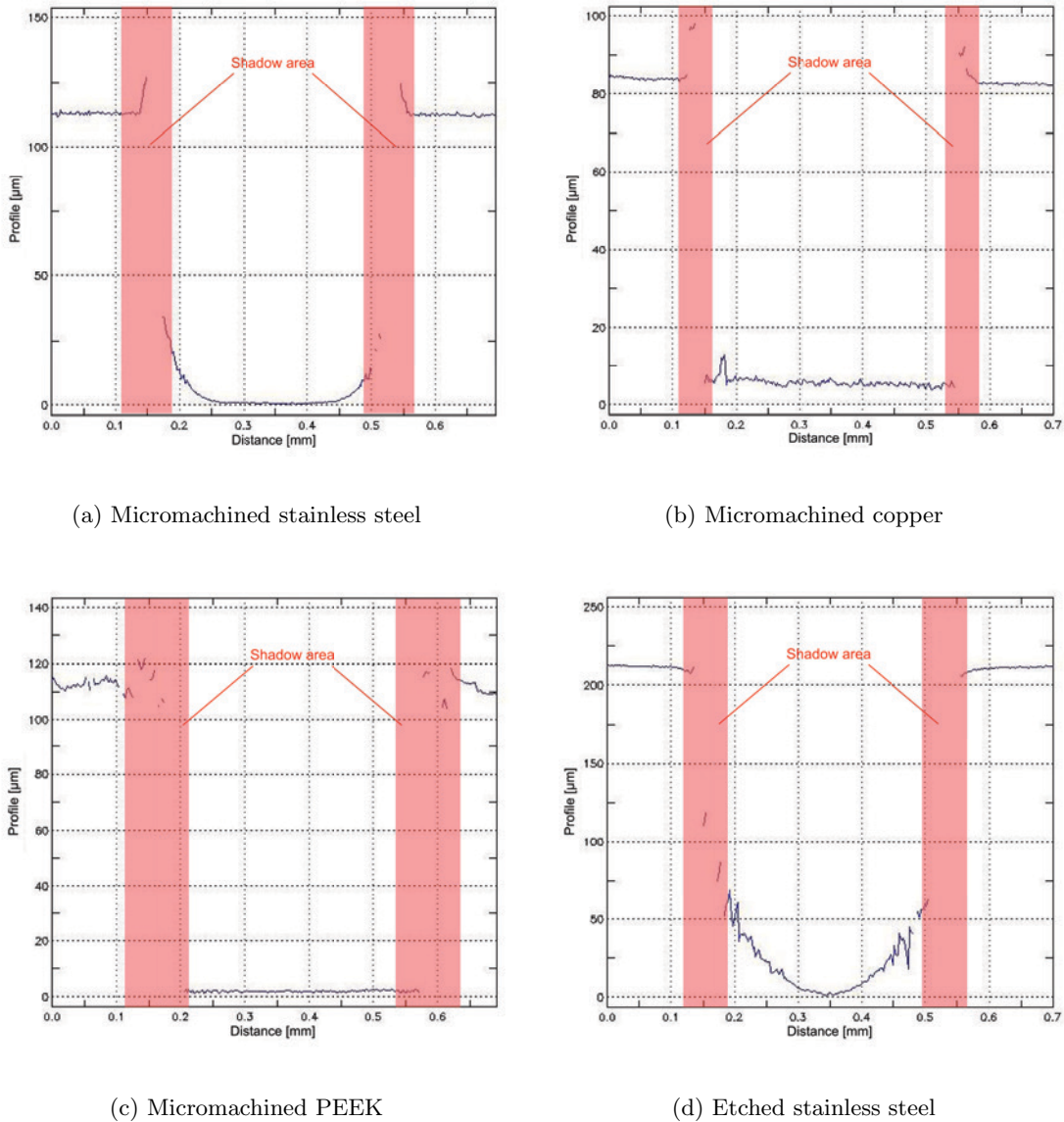


Figure 5.21.: Cross section profiles calculated from the CWL 3D surfaces for the different test sections.

Table 5.4.: Comparison between the average roughnesses of the tested microchannel sections measured with the three different techniques.

Test section	Average $R_a$		
	SEM	Profilometry	CWL sensor
Micromachined stainless steel	$\mathcal{O}(100 \text{ nm})$	28 nm	70 nm
Micromachined copper	$\mathcal{O}(500 \text{ nm})$	517 nm	302 nm
Micromachined PEEK	$\mathcal{O}(100 \text{ nm})$	43 nm	138 nm
Etched stainless steel	$\mathcal{O}(300 \text{ nm})$	315 nm	459 nm

sensor (5.6 mm). Despite the vertical and horizontal resolutions of the two techniques are comparable (i.e. about  $1 \mu\text{m}$  in the x-y direction and in the order of 10 nm in the vertical

direction), the results obtained with profilometry have a more local connotation than those obtained with CWL measurements. Thus, CWL can be considered as more representative of the average characteristics.

Some final remarks about the surface characterization results can be summarized as follows:

- A qualitative characterization (e.g. with SEM imaging technique) is useful to have a first hint on the surface main features and properties.
- Contact profilometry produces quantitative data of the mean roughness and can provide the actual surface topography along linear paths. However, to prevent major damages of the stylus, only short lengths per scan can be analyzed, and a mechanical access to the surfaces must be available (i.e. the technique is not suitable for closed channels or for high aspect ratio structures).
- CWL sensor analysis is a powerful surface characterization technique, providing non-contact measurements and the possibility of 2D and 3D scans. It requires expensive instruments and needs an optical access to the surface. Shadowing problems might be encountered in the case of microstructures, due to the lack of direct illumination.
- The intrinsic features of the microfabrication process as well as the conditions at which the process is carried out have major effects on the resulting roughness. For micromachined pieces, the conditions of the employed tools, the presence of cooling during the process (dry vs. wet) and the machining speed (rotational as well as moving speed) are some of the most influential aspects.
- The choice of employed materials affects the final surface characteristics too. In general, harder materials presents shape defects (i.e. rounded corners structures) but result in smoother surfaces with respect to polymers or other material classes. Nevertheless, if the quality of the metallic matrix is not controlled, thermal processes such as oxidation may occur under particular manufacturing conditions, resulting in very poor finish even for micromachined metals.
- Micromachined surfaces can be characterized by very inhomogeneous properties, with average roughness varying up to one order of magnitude, even over small lengths.

## 5.3. Microsensors characterization

### 5.3.1. Chip contact resistances and noise analysis

Before employing the integrated sensor chip for actual temperature measurements, it is necessary to attest the correct functioning of the electrical connections. Also the basic noise component in the signals must be evaluated along with the main noise sources. In case of very noisy signals, a post process filtering might be required to isolate the meaningful data.

As a first step, the presence of electric contact between the terminals belonging to the same sensor and the electrical insulation between contacts not belonging to the same sensor must be verified. The contact resistance analysis has been performed at two levels: before and after the bonding of the data acquisition cables on the chip.

The resistances of all the contacts of the 4 connectors on the chip sides were measured in special clean room facilities at IMTEK, University of Freiburg (where the chips have been manufactured). By means of an optical microscope, miniaturized contact needles were positioned on two contact terminals and the cross-resistance was measured with a multimeter. Typical contact resistances for working sensors are in the range of 0.3-0.5 k $\Omega$  for the RTDs and 10-15 k $\Omega$  for the thermopiles. The testing of different chips showed good

functioning of the contacts and a proper insulation between non-communicating wires (no interference).

The second control phase has been performed after the bonding of the data acquisition cables on the chip (at the sides), the installation of the chip on the PTFE frame and the connection of the cables to the PCB adapters. The analysis allowed verifying proper cable bonding. A wrong choice of the bonding parameters might result in shortcuts between contacts. This can be verified qualitatively by optical inspection (see Fig. 4.11), or quantitatively by measuring of the contact resistances. Interferences or shortcuts exist whenever a finite resistance between two contacts not belonging to the same sensor is registered.

From the second set of measurements the following conclusions can be drawn:

- After the bonding of the cables, the electrical contact for some sensors was compromised. This might be a result of a non uniform pressure distribution applied during the bonding.
- The working sensors show contact resistances within the same order of magnitude as registered at the chip level, with small increments due to the additional electric resistance of the cables.
- If the optical inspection of the bonding area shows melted material driven out of the original contact position, the insulation of the contacts is not preserved. Finite resistances have been measured also between non communicating terminals. Under these circumstances the functioning of the sensor is not completely compromised, but the signals are characterized by high basic noise level.
- The chips bonded under optimized conditions present “cleaner” bonding areas. The electrical insulation is guaranteed also after cable installation, and the basic noise component in the signal is small.

Figures 5.22 and 5.23 present the registration of thermopile basic noise for two different chips. The first corresponds to a chip-cable assembly bonded under sub-optimal conditions, with interferences registered between the contacts. Figure 5.23 corresponds to an assembly prepared with optimized bonding conditions (see Section 4.2.2). A reduction of about three orders of magnitude of the basic noise was possible.

After installation of the integrated sensor system in the device, the contact resistances have been checked again to verify that the chip integrity is preserved. During mounting chip fractures might occur due to non uniform pressure distributions from the screws combined with pre-imposed mechanical stress in the chip. The fractures usually occurred around the thin membranes or close to defects on the chip surface (e.g. pits on the back side originating from the etching). If the failure involved only part of the assembly (i.e. only one connector or one single sensor got insulated), the chip could still be employed for measurements.

Figure 5.24 shows the evolution of sensor failure during the installation phase for one of the tested chips. Connector C1 was not working after the mounting of the cable, probably due to incorrect bonding. Connector C4, initially working, failed after the installation of the chip in the device, due to a local fracture in correspondence of the connector itself. The dead connections in connector C2 result from a localized failure of either the annealing process for the activation the junction contacts or the bonding of the cable with the sensor bumps.

The experimental results presented in the following sections refer, if not otherwise specified, to the chip of Fig. 5.24. Although two out of four connectors are broken, one half of the chip is entirely working (on both sides) allowing the full characterization of one channel half (or of the entire length if the chip is rotated and two similar experiments are performed).



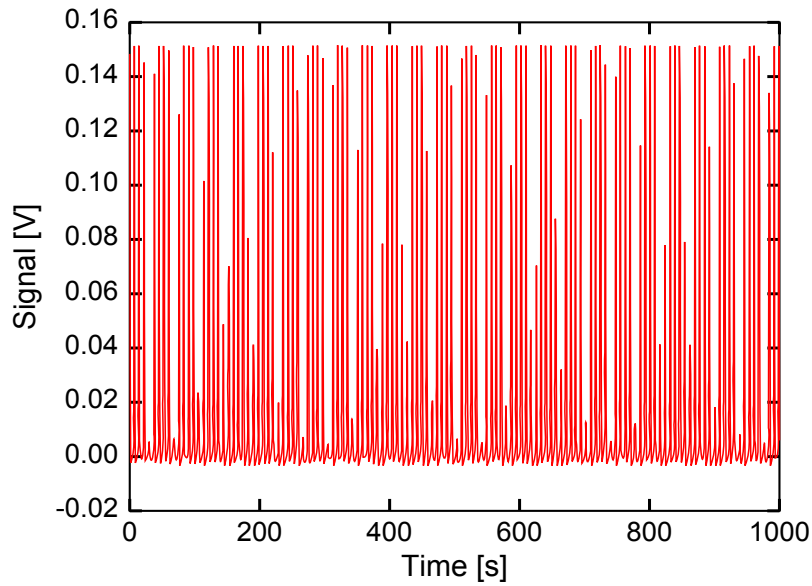


Figure 5.22.: Thermopile basic noise with a chip-cable assembly with suboptimal conditions (cf. Fig. 4.11 (right)).

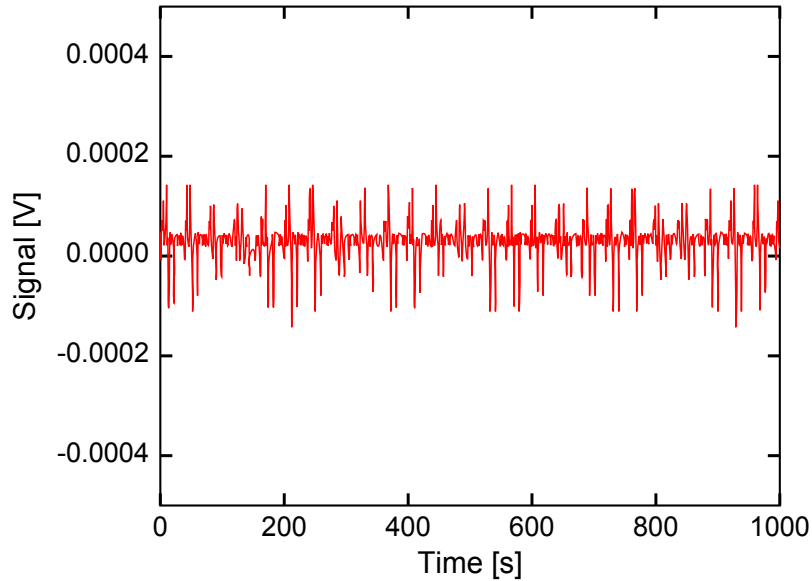


Figure 5.23.: Thermopile basic noise with a chip-cable assembly bonded with optimized conditions to avoid short-cuts and contact cross-talking (cf. Fig. 4.11 (left)).

The high fragility of the silicon chip constitutes one of the major issues for the developed integrated measuring system. It mainly derives from the relatively large dimensions of the whole structure. A configuration with smaller and separated measuring units, integrated on a more resistant supporting frame, would allow the overcoming of this issue. Nevertheless, this would also complicate the manufacturing processes and the data acquisition layout significantly. Moreover, by employing different materials, the microchannel wall would be non-uniform, with possible local disturbances of the flow thermodynamics (e.g. local concentrated head-losses and formation of undesired hot-spots).

### 5.3.2. Calibration of the RTDs

The resistance temperature detectors (RTDs) positioned on the chip to measure the substrate temperatures as a reference for the thermopile “cold” junctions can provide an ab-

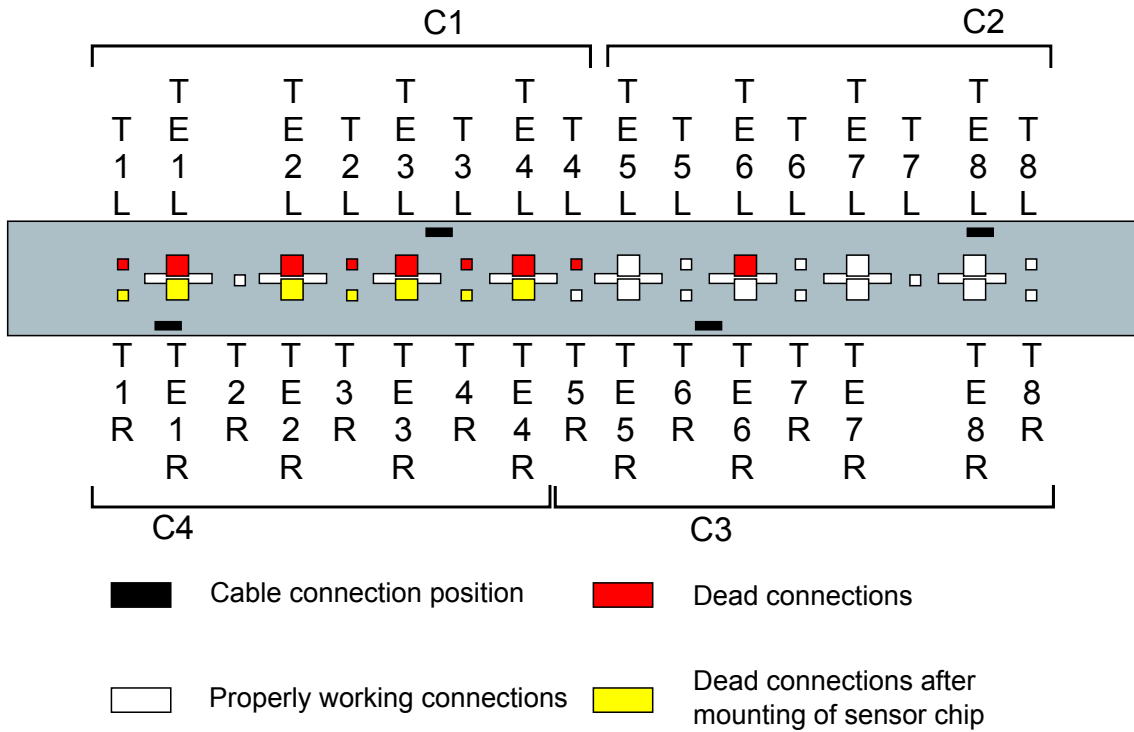


Figure 5.24.: Working contacts of a tested sensor chip. During the closing of the device connector C4 broke, while connector C1 was already insulated after cable bonding.

solute temperature measurement. This allows a direct calibration by simply providing proper reference signals for the chip temperature. For the present experimental layout the reference signals can be obtained by using the thermocouples installed below the channel layer. The relative position of the heating blocks, the reference thermocouples and the RTDs on the chip are shown in Fig. 5.25. The RTDs on the chip’s left side are labeled as “TXL” and those on the right side are labeled as “TXR”, with “X” being the number of the sensor.

If no gas flow is imposed in the microchannel and all three blocks are set to the same temperature, the microchannel and the sensor layers will reach, at steady state, the same temperature. In this case the temperatures registered by the thermocouples on the blocks can be considered as the reference values for the resistance signals recorded by the RTDs on the chip.

The entire procedure for calibration of the RTDs can be summarized as follows:

1. Evacuation of the closed insulation volume.
2. Imposition of the set temperature on the power station controllers.
3. Waiting for the steady state (evaluated by monitoring both the signals of the thermocouples and of the RTDs until they do not show any significant change).
4. Recording of the signals (from reference thermocouples and RTDs).
5. Post processing of the results and calculation of the average reference temperatures and corresponding resistance signals with related errors.
6. Repetition of the procedure for different set points.
7. Calculation of the calibration coefficients by fitting the experimental points.



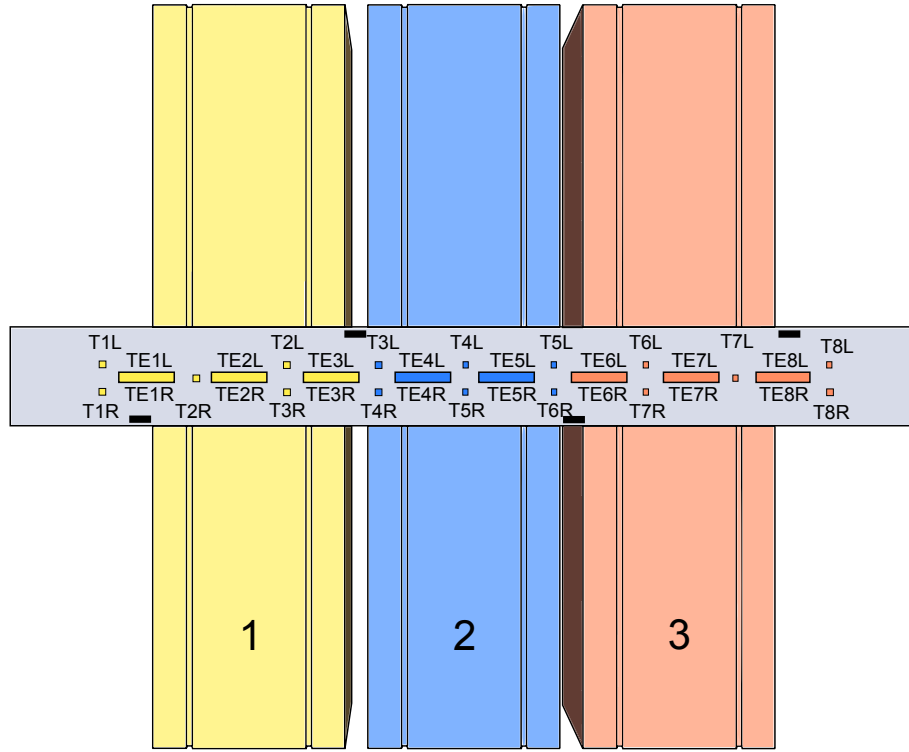


Figure 5.25.: Relative position between the heating blocks, with grooves for the positioning of the reference thermocouples, and the RTDs on the chip.

The set points have been chosen within the mechanical stability limits of the chip. Tests up to 75 °C have been done without any major failure of the chip. However to prevent thermal stresses a temperature window between room temperature and 50 °C has been chosen for the calibration. The validity of the calibration coefficients has been verified up to 65 °C.

Figure 5.26-a shows the comparison between the signals of the reference thermocouples and the RTDs for both the transient and the steady state phases. In general, the RTDs showed a good time response with no detectable delay within the recording frequency of the data acquisition system (1 Hz). In Fig. 5.26-b the averaging of the two signals over the steady state region is reported.

Over small temperature ranges ( $\Delta T \approx 100^\circ\text{C}$ ), the characteristic temperature-resistance relation of RTDs can be considered linear [58]. Figure 5.27 shows the linear least square fitting for the different calibration points. This is done considering a function of the form:

$$T(R) = a \cdot R + b \quad (5.2)$$

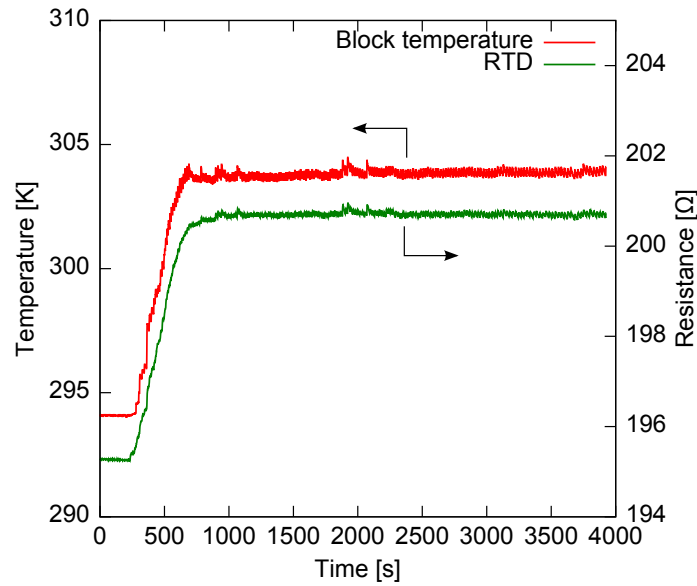
where  $a$  and  $b$  are the fitting coefficients corresponding to the slope and the intercept of the linear function, respectively.

For the general  $i$ -th experimental average temperature ( $T_{avg,i}$ ) the residual from the fitting equation can be calculated as:

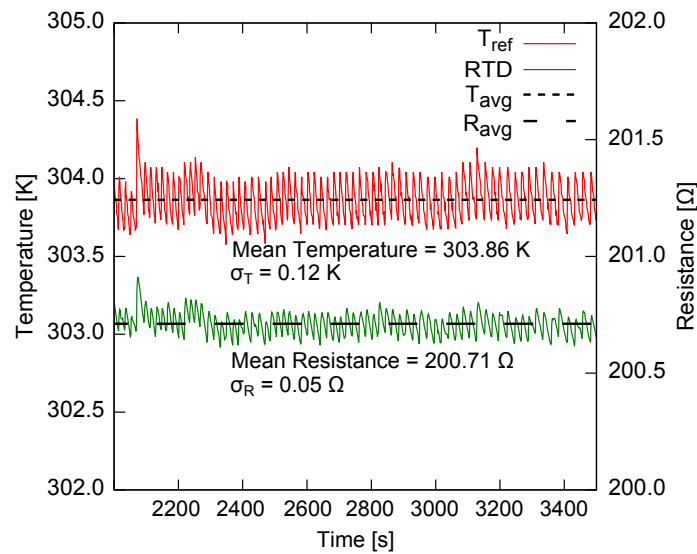
$$r_i = T_{fit,i} - T_{avg,i} \quad (5.3)$$

where  $T_{fit,i}$  is the temperature calculated using Eq. 5.2 with the experimental average resistance ( $R_{avg,i}$ ):

$$T_{fit,i} = T(R_{avg,i}) = a \cdot R_{avg,i} + b \quad (5.4)$$



(a) Signal



(b) Averaging window

Figure 5.26.: Calibration sequence of a RTD for a reference set temperature of 30 °C (a), and average signals calculated over the steady state region (b).

Table 5.5 shows the final calibration coefficients calculated for the tested RTDs. The calculation of the reported uncertainties is described in the following, and includes both the estimated calibration errors and the instrumental uncertainties.

The hypothesis at the basis of the RTDs calibration is the achievement of a uniform and constant temperature distribution along the blocks, the microchannel and the chip. This allows considering the block temperatures as references for the corresponding chip areas. However, the microchannel section is directly heated only partially by the copper blocks. Two areas, close to the entrance and the exit, are heated only by conduction along the chip and the microchannel layers. To assess that this would not invalidate the calibration process, the microchannel top wall temperature was measured in addition with

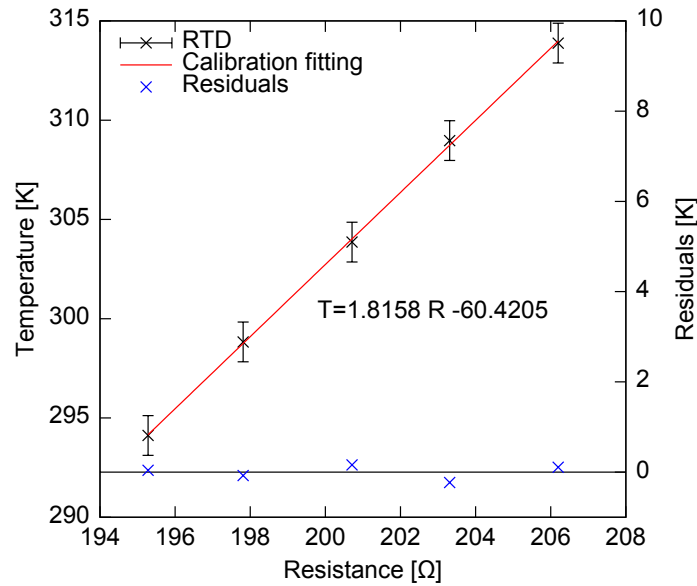


Figure 5.27.: Least square fitting of the calibration experimental points and residuals for a RTD on the silicon chip.

Table 5.5.: Calibration coefficients calculated for the working RTDs on the chip.

RTD	Coefficients		Uncertainty [K]
	Slope	Intercept	
T5L	1.96	-64.77	$\pm 0.74$
T5R	1.93	-58.16	$\pm 0.73$
T6L	1.67	-19.81	$\pm 0.90$
T6R	1.77	-50.75	$\pm 0.69$
T7L	1.74	-67.91	$\pm 0.69$
T7R	1.43	-9.61	$\pm 1.04$
T8L	1.89	-126.38	$\pm 0.74$
T8R	2.12	-162.30	$\pm 0.80$

an alternative method, under the same conditions as imposed for the RTD calibration. For this purpose, the PEEK cover with embedded thermocouples was installed in the device, on top of a plain metal foil (i.e. an unstructured layer of the same material than the microchannel plate). The deviations between the boundary conditions imposed for the two test series were below than 0.5 %, and therefore the obtained data sets could be compared. By considering the relative positions of the embedded thermocouples and the integrated RTDs (Fig. 5.28), it was possible to provide a set of alternative reference temperatures to check the validity of the coefficients found with the direct calibration technique.

Figure 5.29 shows the temperatures recoded by the PEEK cover thermocouples for the same set points imposed during calibration of the RTDs.

Excluding the measurements done at room temperature (no heating), it is clear that a non uniform temperature distribution is established along the channel axis, differently from what assumed for the first calibration. For a given set point, similar temperature profiles have been recorded in different tests, proving the repeatability of the obtained results.

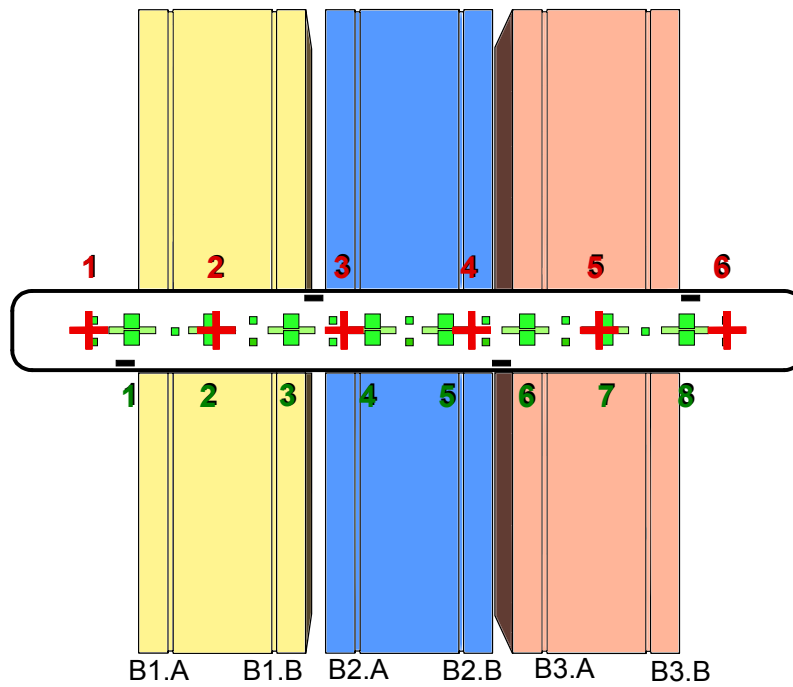


Figure 5.28.: Relative positions of the embedded thermocouples in the PEEK cover (red crosses), the integrated sensors on the silicon chip (green squares) and the device heating blocks.

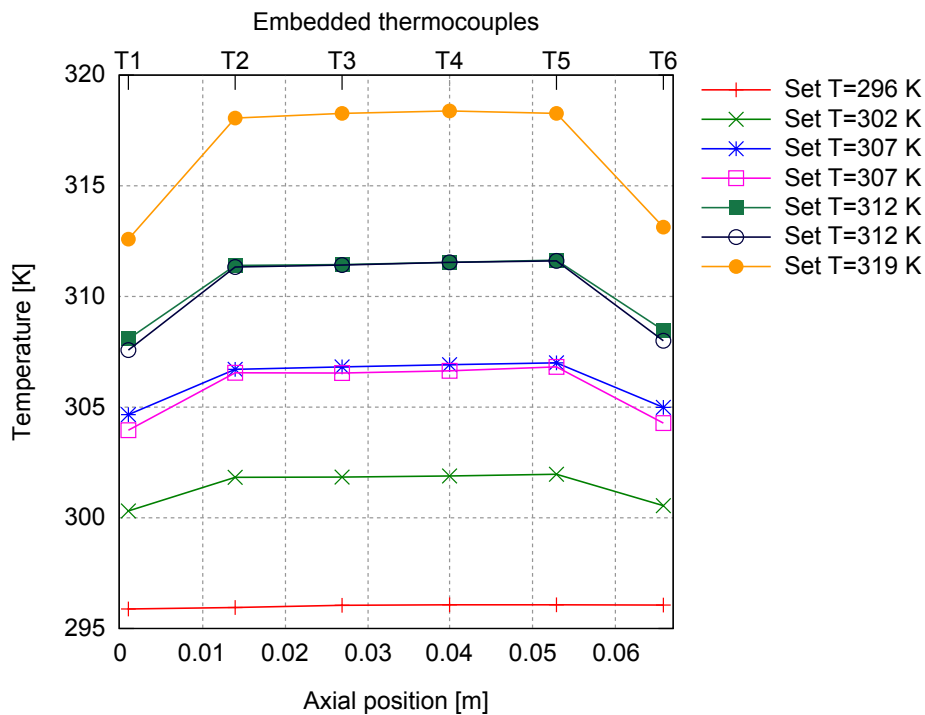


Figure 5.29.: Axial temperature distributions as registered by the PEEK cover embedded thermocouples after imposing different constant temperatures on the heating blocks.

By taking the data from the PEEK cover tests as reference, new calibration coefficients for the RTDs have been calculated. These are reported in Tab. 5.6, along with the ones obtained from the direct calibration. Since this second calibration procedure takes into

account the non uniformity of the axial temperature distribution, the new calculated coefficients were finally employed to transfer the resistance signals into temperature readings.

Table 5.6.: Calibration coefficients for the working RTDs on the chip calculated with the direct calibration technique (black) and corrected by employing the embedded thermocouples on the PEEK cover as reference (red).

RTD	Coefficients				Uncertainty	
	Slope		Intercept		[K]	
T5L	1.96	1.89	-64.77	-51.81	$\pm 0.74$	$\pm 0.73$
T5R	1.93	1.86	-58.16	-45.44	$\pm 0.73$	$\pm 0.73$
T6L	1.67	1.68	-19.81	-33.11	$\pm 0.90$	$\pm 0.69$
T6R	1.77	1.61	-50.75	-8.56	$\pm 0.69$	$\pm 0.83$
T7L	1.74	1.65	-67.91	-49.39	$\pm 0.69$	$\pm 0.69$
T7R	1.43	1.36	-9.61	+6.01	$\pm 1.04$	$\pm 0.97$
T8L	1.89	1.35	-126.38	-4.15	$\pm 0.74$	$\pm 0.68$
T8R	2.12	1.51	-162.30	-29.78	$\pm 0.80$	$\pm 0.70$

### Uncertainty analysis

The uncertainty associated with the temperature measurements of the RTDs and reported in Tab. 5.6 has been calculated considering three different contributes:

- $\Delta T_{ref}$  : the uncertainty associated with the reference signals;
- $\Delta T_{fit}$  : the uncertainty associated with the fitting;
- $\Delta T_{calib}$  : the calibration uncertainty associated with the error propagation of the resistance measurement.

The uncertainty relative to the reference signal originates from two different sources: the instrumental error (i.e. the uncertainty associated with the reference thermocouples and provided by the vendor) and the averaging error (i.e. the error made by considering the temperature constant and equal to its average value). The averaging error is related to the standard deviation ( $\sigma_{mean,T}$ ):

$$\sigma_{mean,T} = \sqrt{\frac{1}{N} \sum_{i=1}^N (T_i - T_{avg})^2}, \quad (5.5)$$

where  $N$  is the number of experimental points,  $T_i$  is the  $i$ -th experimental point and  $T_{avg}$  is the average temperature calculated as:

$$T_{avg} = \frac{1}{N} \sum_{i=1}^N T_i. \quad (5.6)$$

The final uncertainty relative to the temperature reference is taken as the maximum of the instrumental error and twice the standard deviation of the temperature averaging, as expressed in Eq. 5.7.

$$\Delta T_{ref} = \pm \max(|\Delta T_{instr}|; |2\sigma_{mean,T}|) \quad (5.7)$$

The error related to the fitting is calculated as the maximum of the residuals  $r_i$ .

$$\Delta T_{fit} = \pm r_{max} \quad (5.8)$$

$$r_{max} = \max(|r_i|) \quad (5.9)$$

Finally, the uncertainty related to the resistance measurement is calculated applying the error propagation theory [98] for Eq. 5.2. For a single calibration point this contribution is:

$$\Delta T_{calib,i} = \frac{\partial T}{\partial R} \cdot \Delta R_i = a \cdot \Delta R_i \quad (5.10)$$

where  $\Delta R_i$  is the error associated with the resistance measurement. This, as for the reference temperature, is calculated as the maximum between the instrumental error, given by the vendor of the resistance recording device, and the standard deviation of the resistance signal averaging:

$$\Delta R_i = \pm \max(|\Delta R_{instr}|; |2\sigma_{mean,R}|) \quad (5.11)$$

The total error associated with the resistance measurement is taken as the maximum among the errors for the different calibration points:

$$\Delta T_{calib} = \pm \max(|\Delta T_{calib,i}|) \quad (5.12)$$

As the three uncertainty contributions are independent from each other it is possible to calculate the total uncertainty from the sum of the squared contributions:

$$\Delta T_{tot} = \pm \sqrt{\Delta T_{ref}^2 + \Delta T_{fit}^2 + \Delta T_{calib}^2} \quad (5.13)$$

### 5.3.3. Calibration of the thermopiles

In the case of the RTDs it is possible to identify suitable reference signals, as there is a direct resistance-temperature correspondence. The thermopiles, on the contrary, require the imposition of a known and controlled temperature difference over the two junction series, to be used as a reference. With the present setup this means setting a pre-defined temperature gradient between the gas and the chip. This is not a trivial task since the gas temperature evolution along the channel is not known a-priori and the measurement of the actual local gas temperatures is one of the aims of the present work.

A direct calibration of the thermopiles has been attempted by establishing a relatively high flow rate of gas in the microchannel (compared to the flow rates encountered with rarefied flows). The assumption is that the gas acquires a high axial velocity and exits without increasing its temperature. In this case the reference signal is given by the difference between the gas temperature (measured at the inlet and at the outlet of the microchannel to verify if there is any variation) and the chip temperature (measured by the previously calibrated RTDs). A typical sequence consists of the following steps:

1. Acquisition of the zero signal for each sensor to have a reference for the thermopile voltage. This is calculated by averaging the signal recorded in absence of any gas flow in the channel and at room temperature.
2. Evacuation of the insulation volume.
3. Setting of the gas flow at a given mass flow rate and at room temperature.

4. Heating of one copper block to a pre-set temperature (the reason of heating only one block is to attempt the imposition of localized temperature differences at the sensor positions, preventing the heating of the whole chip for conduction effects).
5. Waiting for the steady state to be reached. This phase may take long due to heat conduction in the whole device.
6. Recording of the signals from the RTDs, the thermopiles and the reference thermocouples for the gas temperature (installed at the inlet and outlet of the insulation volume) and the block temperature (positioned on top of the heating blocks).
7. Calculation of the average values of the thermopile voltage, the gas temperature, the chip temperature measured by the RTDs, and the block temperature signals.
8. Calculation of the temperature variation  $\Delta T$  as difference between the chip and the gas temperatures, and the voltage variation  $\Delta V$  as difference between the voltage measured for the considered calibration point and the previously measured zero signal.
9. Repetition for the different blocks and for different set points.
10. Fitting of the experimental points ( $\Delta T$ ,  $\Delta V$ ) and calculation of the calibration coefficients.

The set points have been chosen in a range between room temperature and 40 °C, to avoid thermal stress across the chip and possible membrane fractures. In the following the data related to two thermopiles, namely TE7R and TE8R, will be compared. The relative positions of the sensors, the chip and the heating blocks are shown in Fig. 5.30. The thermopile TE7R is completely included within the heated area (third block), while the membrane of the thermopile TE8R is partially outside. As in the case of the RTDs this might result in a different thermal behavior. The tests were carried out by imposing a temperature of 40 °C on the third block only and a flow rate of nitrogen of 65 ml/min (corresponding to an average residence time of about  $10 \cdot 10^{-3}$  seconds). As chip reference temperatures, the RTDs T7R and T7L for the thermopile TE7R and the RTDs T7L and T8R for the thermopile TE8R have been considered (as indicated in Fig. 5.30).

Figure 5.31 shows the recorded calibration sequence for the thermopile TE7R. The thermopile signal is plotted with the block and the chip temperature profiles along with the gas outlet temperature, recorded outside the device insulation volume. The temperature of the third block is raised with a step from room temperature to the set point. The chip temperature follows the step of the block temperature while the outlet temperature remains constant. This results in a decreasing thermopile signal, i.e. the establishment of a negative temperature difference between the heated chip and the gas ( $\Delta T = T_{gas} - T_{chip} < 0$ ).

To calculate the voltage variation corresponding to the temperature difference across the membrane, the steady state average values of the measured quantities have been calculated (as shown in Fig. 5.32).

The data for the same test sequence relative to the thermopile TE8R are shown in Fig. 5.33. The signal of the RTD positioned inside the chip (T7L) follows the block temperature, while the RTD outside the heated area (T8R) presents some delay for the heating up phase, due to conduction in the axial direction. The thermopile signal varies corresponding to the block temperature step, indicating the establishment of a temperature difference across the membrane. However, in this case the signal increases, indicating a positive gradient ( $\Delta T > 0$ ). The calculated average signals for the thermopile TE8R are shown in 5.34.

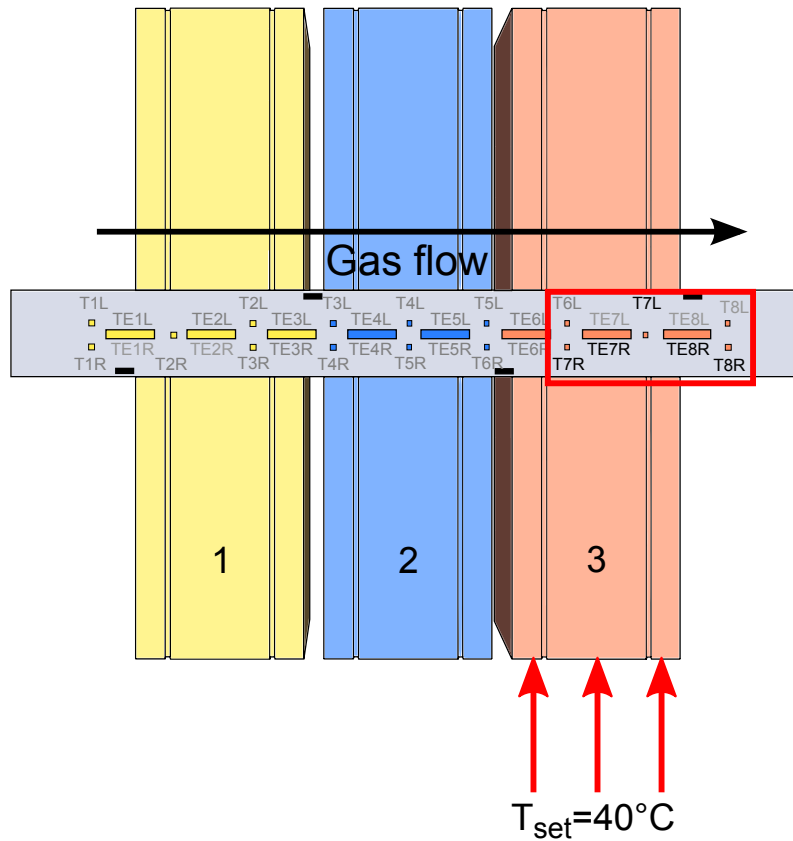


Figure 5.30.: Relative positions of the heating blocks and the chip with the thermopiles TE7R and TE8R analyzed as example.

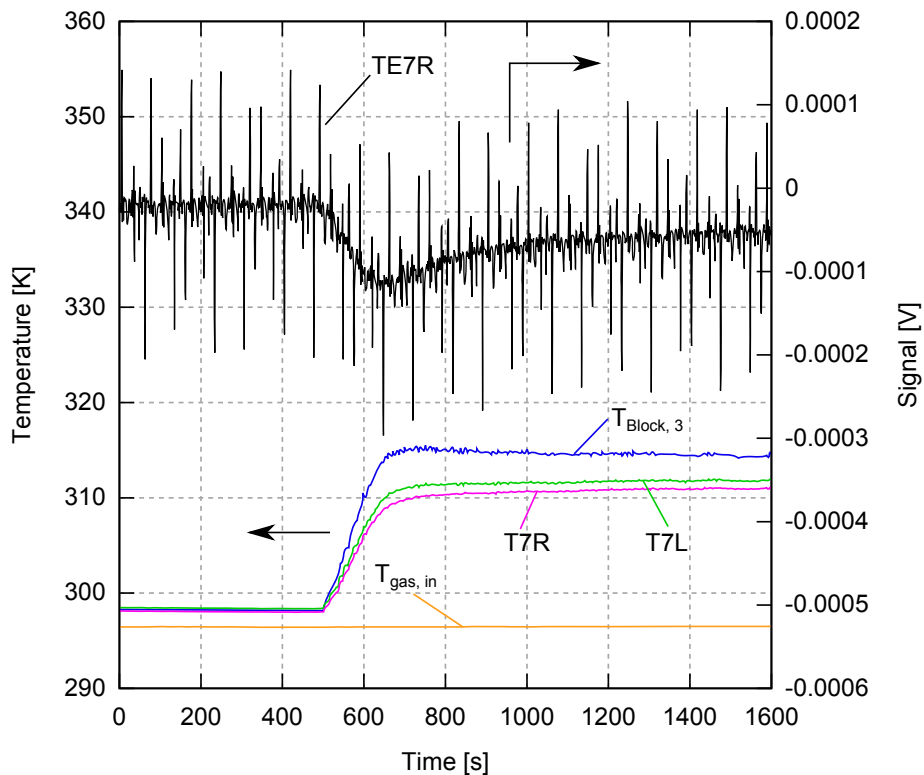


Figure 5.31.: Experimental sequence for the calibration of the thermopile TE7R. The block, initially at room temperature, was heated up to  $40^{\circ}\text{C}$ .



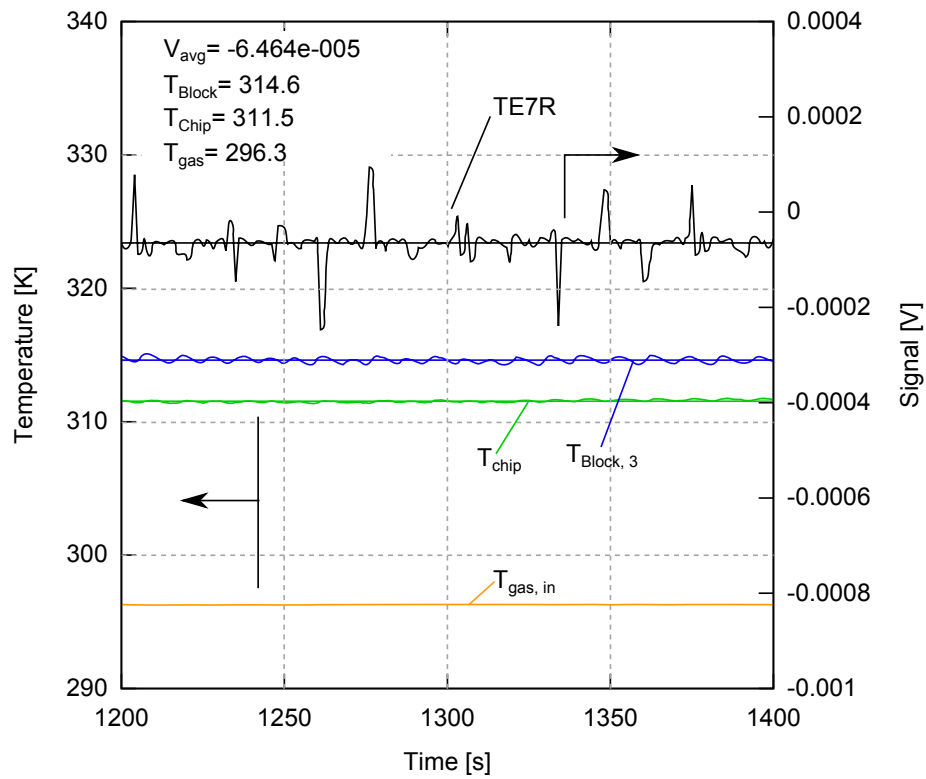


Figure 5.32.: Average reference temperature and voltage signals for the thermopile TE7R, calculated from the sequence shown in Fig. 5.31.

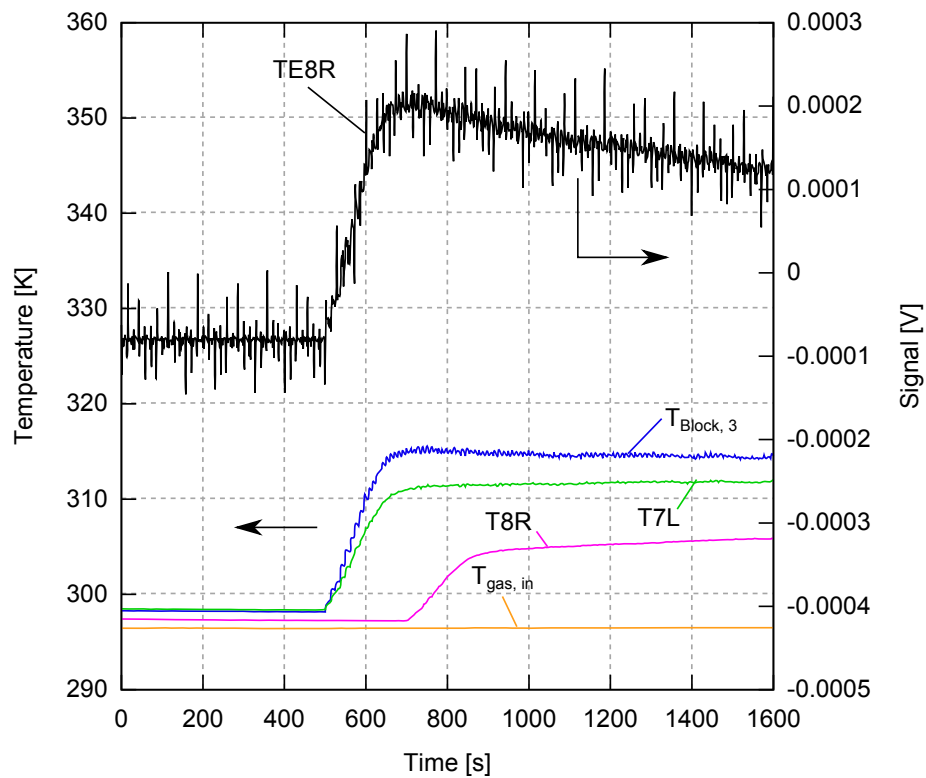


Figure 5.33.: Test sequence for the calibration of the thermopile TE8R. The block, initially at room temperature, was heated up to 40 °C.

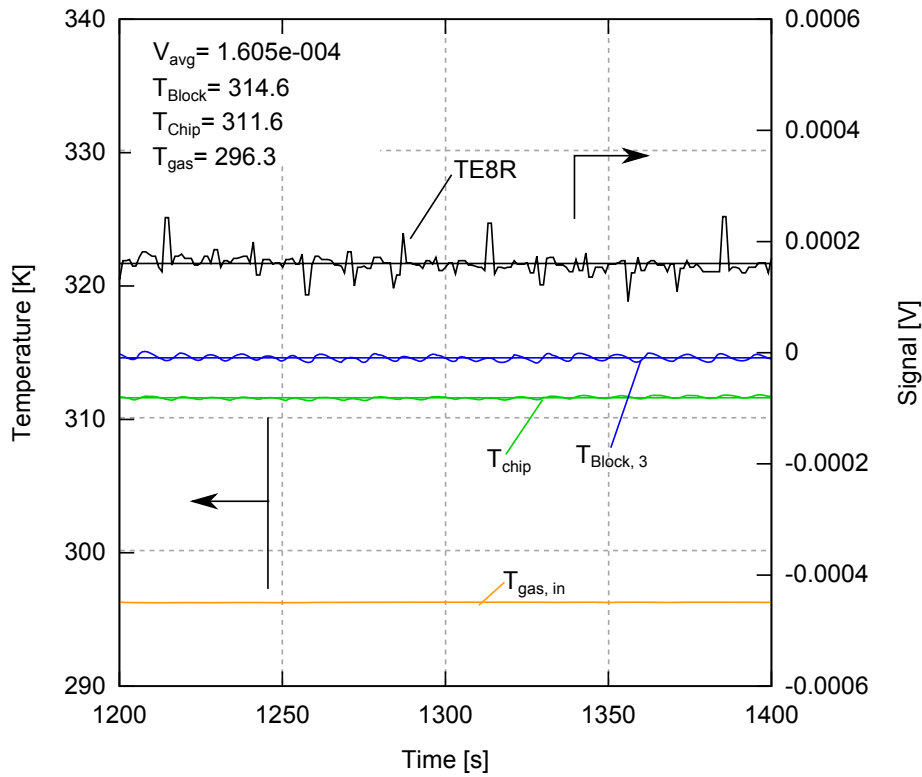


Figure 5.34.: Average temperatures and voltage signals for the thermopile TE8R, calculated from the sequence shown in Fig. 5.33.

The described test procedure was repeated for different temperature set points. The average data were reported in  $\Delta V$ - $\Delta T$  plots, as shown in Fig. 5.35. For each thermopile the voltage difference at each set point ( $\Delta V$ ) was calculated as the difference between the average signal measured with the heated chip ( $V_{avg}$ ) and the signal recorded before the heating ( $V_0$ ). The experimental points were fitted with linear regression. Although for some sensors a good linear trend could be found (cf. Fig. 5.35-a), some other sensors showed larger deviations from the calculated fitting lines (cf. Fig. 5.35-b). Moreover, by repeating the calibration for some points, different fitting equations were found. This lack of repeatability nullifies the validity of the whole calibration.

A possible reason behind the data scattering and the lack of repeatability is the assumption that the temperature of the gas flowing in the microchannel does not increase during the test. Although the temperature at the outlet of the insulation volume was constant, the signals recorded during the tests show a clear sign switch between the two thermopiles TE7R and TE8R. This could be explained assuming a temperature variation of the gas. The negative signal of the thermopile TE7R corresponds to the unheated gas flow reaching the sensors, and the heated chip. The gas reaching the thermopile TE8R has already crossed the whole heated area, while the chip is no more directly heated. In this case the gas temperature is higher than that of the chip, resulting in positive gradient and, thus, a positive  $\Delta V$ . For these reasons, the calibration with the hypothesis of no gas heating along the microchannel can not be considered valid.

Another typical feature of the chip thermal behavior can be observed in Fig. 5.31 and 5.33. After the step corresponding to the block temperature variation, the thermopile signal shows a progressive decrease. Despite the fact that only one block is heated, the chip temperature tends to become uniform due to axial thermal conduction. This results in a progressively smaller temperature difference between the chip and the gas and, thus, in decreasing thermopile signals.

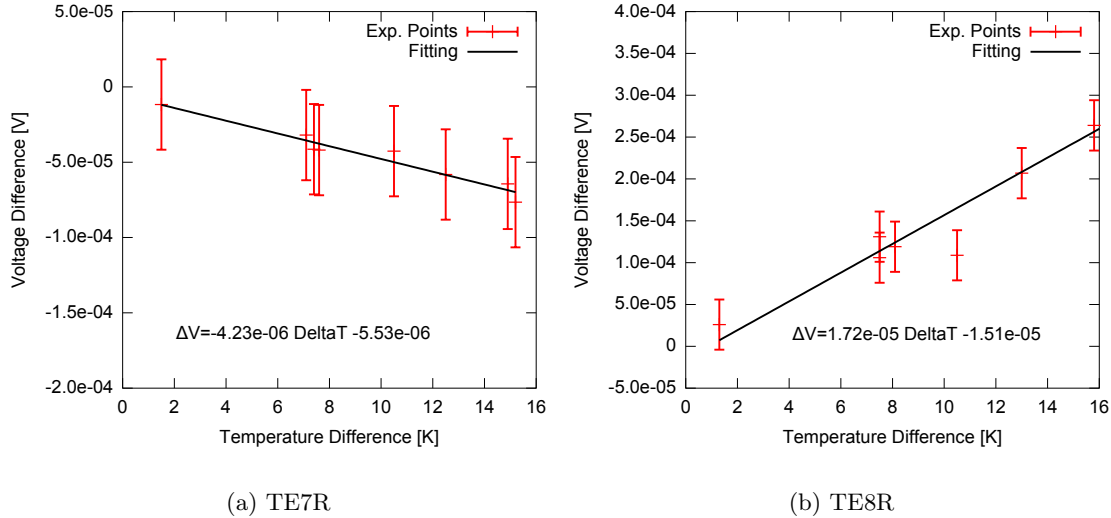


Figure 5.35.: Calibration experimental points and linear fitting for the thermopiles TE7R (a) and TE8R (b). The voltage error bars include the uncertainty of the voltage acquisition instruments.

Since the hypothesis at the basis of the thermopile calibration procedure has been demonstrated to be wrong, a series of tests have been performed, trying to understand the thermal behavior of the microchannel-chip assembly. The tests have been focused on assessing the validity of the employed measuring principle and evaluating the system responses. In this case the temperature of the gas is not known, but is assumed to vary along the microchannel according to the thermal boundary conditions.

Two different test sequences will be compared, differing for the imposed boundary conditions. Both tests present an initial and a final phase with no gas flow. This allows the evaluation of the start-up and shut-down transitories. At the same time the presence of hysteresis effects can be investigated by checking whether the signals fall back to their initial values whenever the gas flow is stopped. The central phase of both tests corresponds to the imposition of a gas flow of nitrogen with a mass flow rate of 100 ml/min and an inlet pressure of 1.5 bar.

In the first test sequence a temperature of 30 °C was set for all three heating blocks and then turned off. In the second case a temperature of 30 °C was imposed on the first block only (close to the gas inlet), while the remaining two were left unheated. Figure 5.36 schematically shows the imposed boundary conditions for the two test sequences.

To compare the obtained results and evaluate the differences of the chip thermal behavior at different axial positions, four sensors have been considered, namely TE5L, TE6R, TE7R and TE8R. Their relative positions are shown in Fig. 5.36. In Fig. 5.37 - 5.40 the comparison of the responses for the two sequences for each sensor are presented.

For the four examined sensors the thermopile average signal with no gas flow is zero, and no hysteresis after the heating of the chip has been detected (i.e., when the gas flow is stopped the thermopile signal falls back to zero). The presence of the gas is recorded by the thermopiles as a negative step ( $\Delta V < 0$ ). The gas inlet temperature is lower than the chip temperature even when the gas is not heated (due to a lower ambient temperature of the gas supply line) and a negative  $\Delta T$  is established across the membranes. In particular the absolute value of  $\Delta V$  increases along the channel becoming higher from TE5L to TE8R. This suggests the presence of a convective effect along the microchannel and a temperature reduction of the gas at the microchannel exit due to the flow expansion.

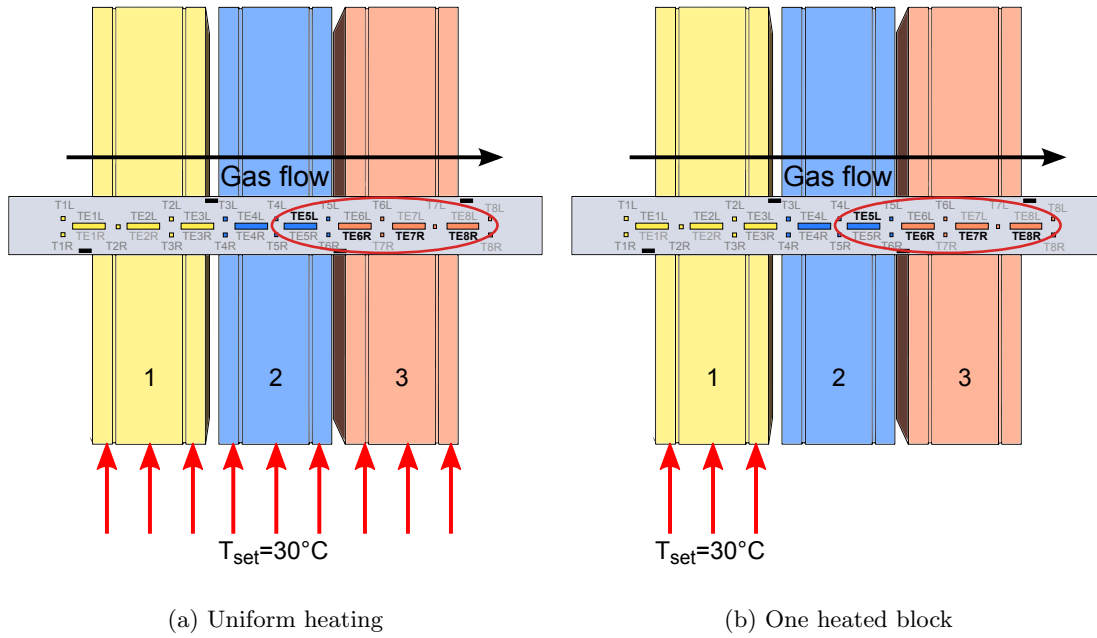


Figure 5.36.: Schematic layout for the two thermopile test sequences. In the first case all blocks are uniformly heated (a). In the second sequence only the first block is heated (b). The sensors considered to compare the results are highlighted within the red circles.

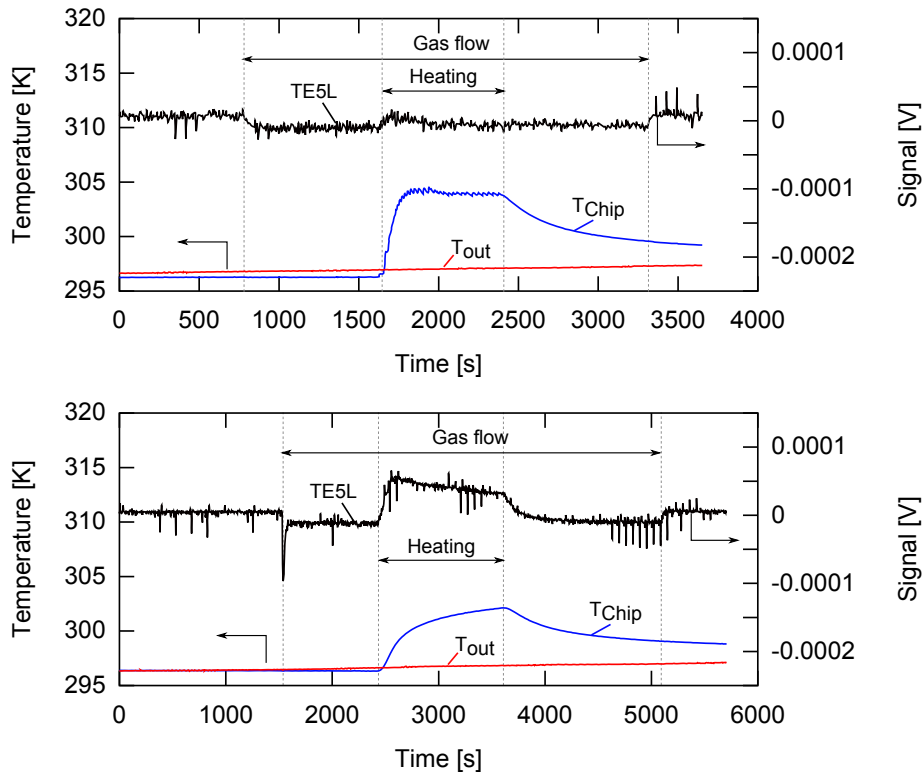


Figure 5.37.: Test sequences results for the thermopile TE5L positioned on the second block. The first plot refers to a uniform block temperature of 30 °C (top). In the second sequence only the first block is heated up to 30 °C (bottom).

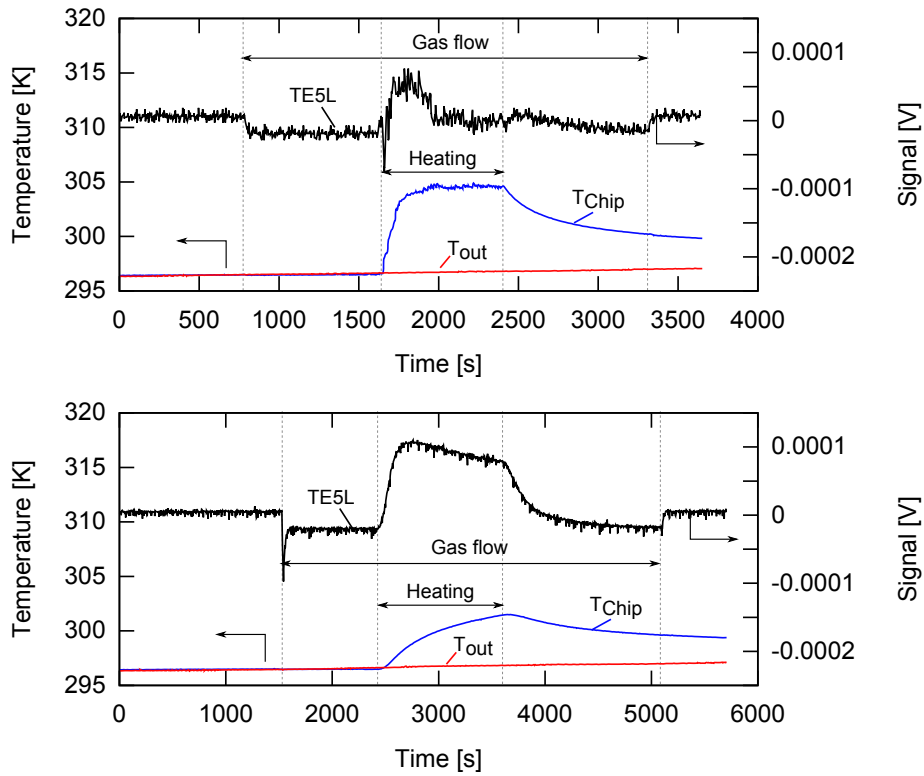


Figure 5.38.: Test sequences results for the thermopile TE6R positioned between the second and the third blocks. The first plot refers to a uniform block temperature of 30 °C (top). In the second sequence only the first block is heated up to 30 °C (bottom).

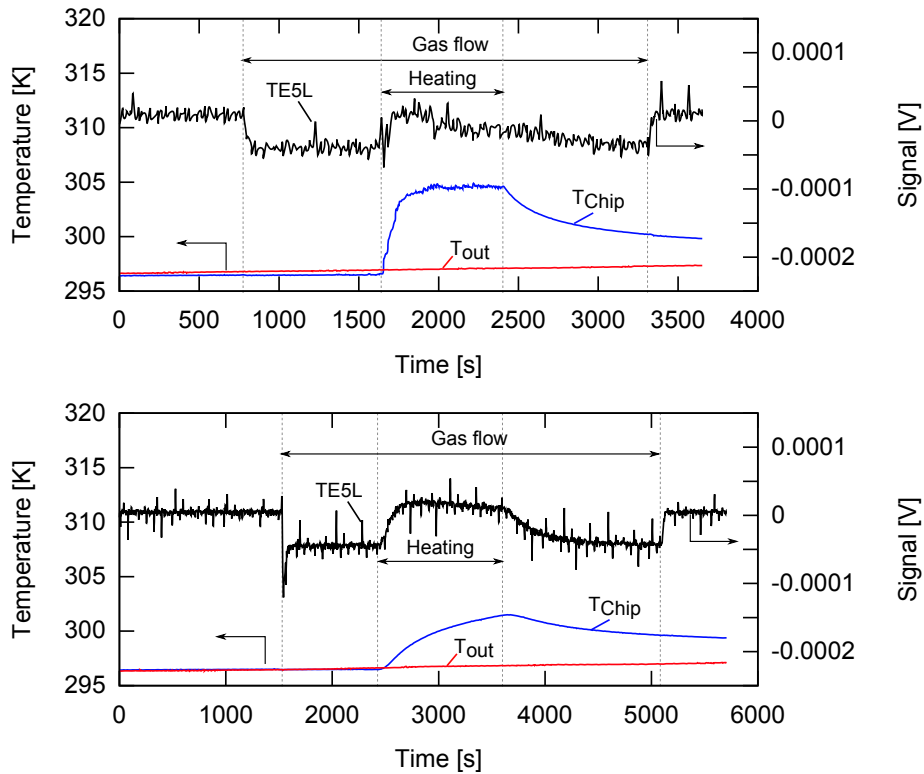


Figure 5.39.: Test sequences results for the thermopile TE7R positioned on the third block. The first plot refers to a uniform block temperature of 30 °C (top). In the second sequence only the first block is heated up to 30 °C (bottom).

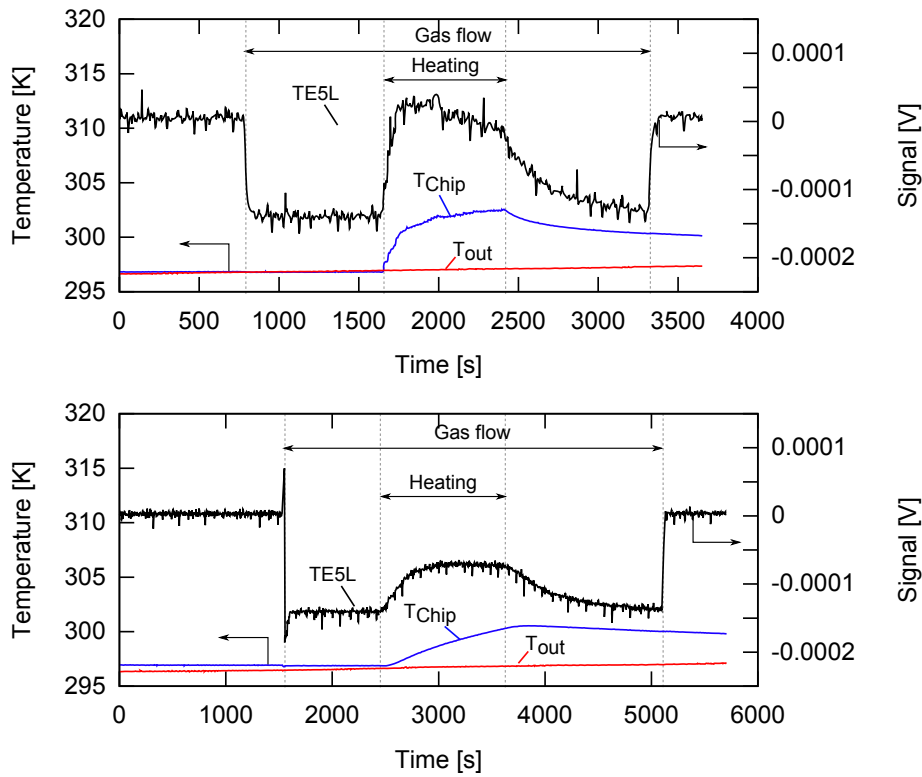


Figure 5.40.: Test sequences results for the thermopile TE8R positioned outside from the heated area. The first plot refers to a uniform block temperature of 30 °C (top). In the second sequence only the first block is heated up to 30 °C (bottom).

For the thermopile TE5L (Fig. 5.37) the voltage signal throughout the experiments is almost constant and deviates only slightly from its zero level. In particular, in the first test, where all three copper blocks are heated, the signal remains unvaried except for a small step at the beginning of the heating phase and a small reduction throughout the whole period of gas flow. As the sensor is positioned almost in the middle of the chip, the gas reaching the membrane has time to heat up along the first block, and very small or no temperature differences can be detected in correspondence of the sensor. When only the first block is heated the voltage variations are larger than in the first case. The gas is heated along the first part of the microchannel and thus is hotter than the chip, resulting in a positive voltage signal. However, by keeping the first block at constant temperature, the chip at the thermopile positions is gradually heated by heat conduction from the upstream area and by the flow of heated gas, and the thermopile signal progressively decreases as the  $\Delta T$  between the chip and the membrane is reduced.

The membrane of the thermopile TE6R (Fig. 5.38) is positioned at the beginning of the the third block. As in the previous case, the signal relative to the first test has a rather constant behavior compared to second case. The voltage step at the beginning of the heating phase in the first sequence is rapidly compensated as the chip is heated and the  $\Delta T$  decreases. The reduction of the signal in presence of the gas flow is more pronounced than for TE5L. The second test sequence presents a quite different behavior. The chip at the sensor position is further downstream with respect to the thermopile TE5L and has therefore a lower temperature. This results in larger temperature and voltage variations. Again, as the chip is eventually heated by heat conduction, a decreasing profile for the voltage is detected during the heating phase.

The signal corresponding to the thermopile TE7R (5.39) shows a similar behavior to the

sensor TE6R (i.e., small voltage variations in the test with the three heated blocks and positive step in the second test in correspondence of the first block heating). Compared to TE5L and TE6R the reduction of the signal in presence of the gas flow is further enhanced. The voltage variation in the second test is smaller than for the thermopile TE6R and the signal remains around its zero level, without reaching a positive value. This behavior can be explained again by looking at the sensors relative positions. The thermopile TE7R is positioned further downstream, where heat exchange between the gas and the chip has taken place to a larger extent reducing the temperature difference. This results in a smaller temperature difference with the chip at the position corresponding to the thermopile TE7R.

Figure 5.40 refers to the last sensor before the microchannel exit (TE8R). In this case the whole sensor area faces a non directly heated part of the microchannel and the thermopile signal variations are quite large. The signal is greatly reduced by the onset of the gas flow. In the first test, from the negative voltage level reached after the onset of the gas flow, the signal raises following the temperature variations of the third block. The gas is heated before reaching the thermopile position. The  $\Delta T$  is reduced and the  $\Delta V$  decreases accordingly. In particular the thermopile signal reaches zero when the gas and the chip are at the same temperature. In the second experiment (with only one heated block) the signal variations are still detectable, but the voltage absolute value remains negative for the whole time interval where the gas flow is active. The gas temperature rapidly decreases right after leaving the directly heated zone, while the chip is heated by conduction from the upstream area.

From the described test sequences it is evident that the gas flow temperature varies according to the position along the microchannel. Along the inlet and outlet unheated lengths, the wall temperature is lower than in the heated areas and the gas temperature decreases too. It is not possible to correctly evaluate the temperature differences at the membrane positions, even though the temperatures of the heating blocks are controlled. A direct calibration of the thermopiles is therefore not possible. A potential solution could be an indirect calibration, based on the measurement of the reference signals with an alternative method. For this purpose the embedded thermocouples in the PEEK cover were employed to calculate the reference temperature differences between the gas and the microchannel top wall (as described in Section 5.3.5).

#### 5.3.4. PEEK-cover tests

By substituting the device cover with the PEEK frame including the embedded thermocouples, it is possible to access the microchannel for temperature measurements with conventional sensors. However, this measuring technique must at first be validated to ensure that the recorded signal corresponds to the gas temperature and not to the temperature of the cover itself. For this purpose, a series of tests have been performed with the PEEK cover.

The first sequence consisted of the following steps:

1. The zero signal is recorded before the gas flow and the heating are activated.
2. A gas flow of nitrogen is imposed with a mass flow rate of 100 ml/min (regulated by the mass flow controller at the inlet) and an inlet pressure of about 2 bar.
3. The heating of the first block is activated with a set temperature of 32 °C. The second and the third block are left unheated.
4. The heating is stopped.
5. The gas flow is stopped.

The results of the test sequence are shown in Fig. 5.41, where the thermocouple signals corresponding to the onset and stop of the gas flow are enlarged in detail. Contrary to what has been registered with the integrated thermopiles, no signal variation in correspondence of these two phases was detected. The thermocouples are indeed affected by the surrounding cover material, which spoils the overall sensitivity preventing the recording of small temperature differences.

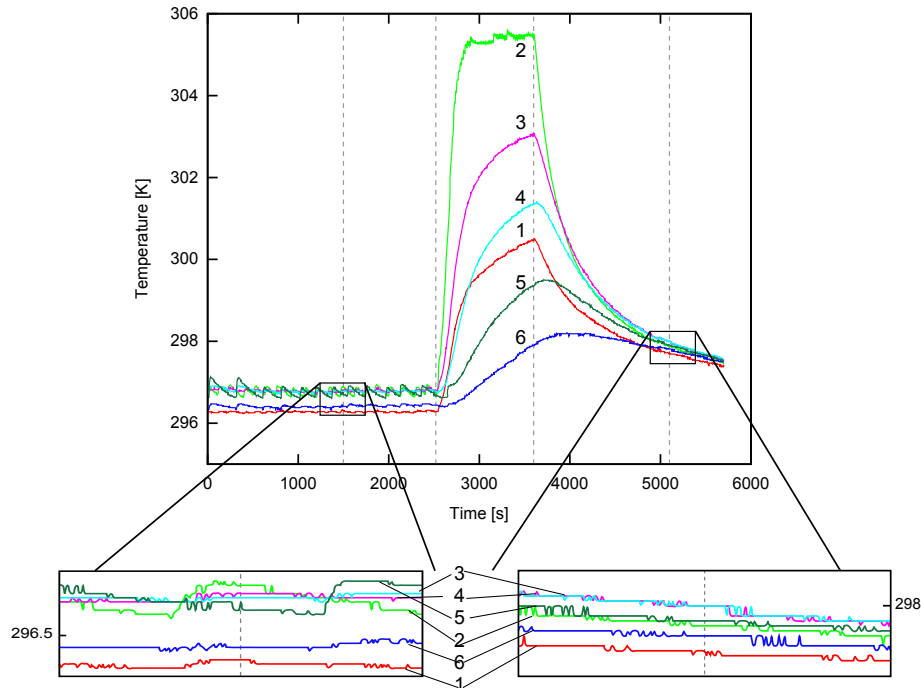


Figure 5.41.: Test sequence performed with the PEEK cover and an imposed mass flow rate of 100 ml/min.

To probe the system sensitivity the same test sequence has been repeated with a higher mass flow rate (about 250 ml/min). The results of the second sequence are presented in Fig. 5.42. In this case it is possible to detect two temperature steps corresponding to the imposition and the shutting off of the gas flow. The steps are evident especially for the two thermocouples positioned at the microchannel extremities (i.e. on the unheated areas). The central sensors (from 2 to 5) correspond to the heated area, where the gas reaches almost the same temperature of the wall, as already found with the thermopiles.

To investigate the temperature dependence of the measuring system, a second test sequence has been performed. Two different temperature levels (namely 30 °C and 40 °C) were set on the third copper block, close to the exit. A flow rate of 200 ml/min was imposed and turned on and off at different times to evaluate the thermocouples time response. The results of this test sequence are reported in Fig. 5.43, with details of the three time windows where the gas flow was turned on and off. These correspond to three different temperature levels: one before the beginning of the heating, the second when the third block was heated at 30 °C and the third when the temperature of the third block was raised up to 40 °C. The response of the embedded thermocouples at a given mass flow rate depends on the absolute temperature level. In particular, at higher temperatures, the signal variations detecting the gas presence are larger. Moreover, in this case the thermal entry region is longer and the temperature step is detectable also for the thermocouples inside the heated area (e.g. thermocouple 3 for period III).

In conclusion, the embedded thermocouples on the PEEK cover can be employed to mea-



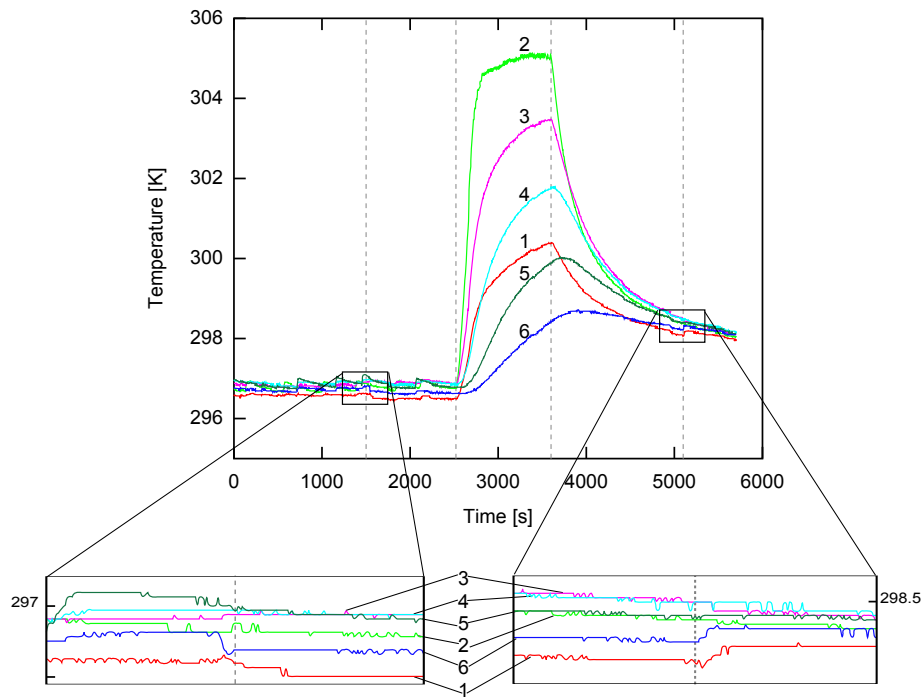


Figure 5.42.: Test sequence with the PEEK cover, with an imposed mass flow rate of 200 ml/min.

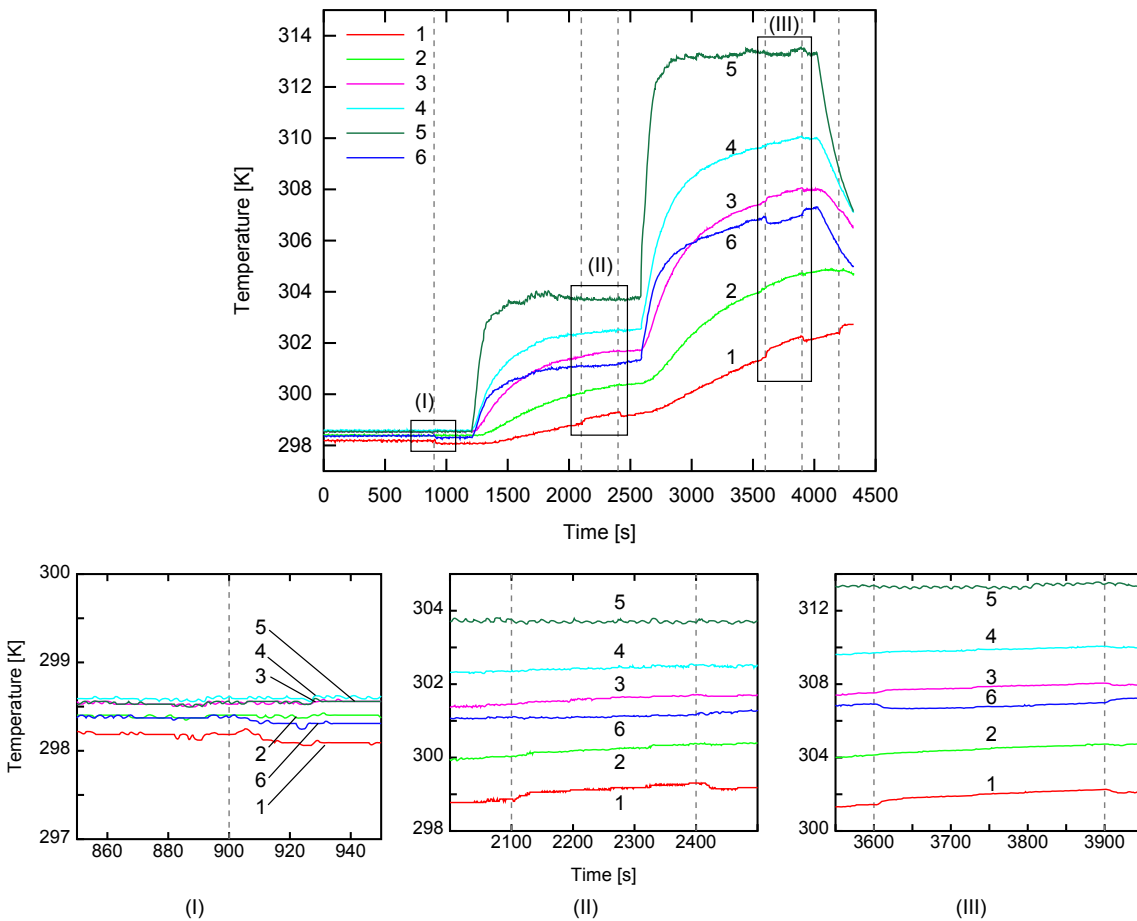


Figure 5.43.: Test sequence for the PEEK cover at three different temperatures imposed on the heating blocks.

sure the gas temperature distribution in the microchannel, provided that a sufficiently high mass flow rate or temperature level are assured. For small mass flow rates and low absolute temperatures it is not possible, from the thermocouple signals, to assess the presence of a gas flow and the actual axial temperature distribution.

### 5.3.5. Comparative approach

To compare the results obtained from the integrated thermopiles and those from the PEEK cover, three similar tests have been performed. The same experimental procedure is repeated at first with the PEEK cover and the blind foil to evaluate the top wall temperature distribution, then with the microchannel foil installed, to evaluate the gas temperature distribution and finally with the silicon sensor chip to register the corresponding thermopile signals. By using the blind foil to measure the top wall reference temperature it is possible to eliminate the influence of the inlet and outlet openings. This solution represents the best option to retrieve the equivalent upper wall temperature with the embedded thermocouples. However, the difference between these values and those recorded by the RTDs during similar experiments is negligible. The experimental sequence has been performed as follows:

1. The signal is recorded without a gas flow and with no heating.
2. A gas flow of nitrogen is imposed with an inlet pressure of 2 bar and with a mass flow of 200 ml/min.
3. The third block is heated up to 40 °C.
4. The gas flow is turned temporarily off and then on again (this is meant to compare the transient behavior of the thermopiles and the thermocouples).
5. The heating and the gas flow are turned off.

The reference temperature difference for the thermopile signals is calculated by subtracting the wall temperature registered with the blind foil to the gas temperature registered with the microchannel foil. The resulting curve is plotted against the thermopile signal as shown in Fig. 5.44-5.46 for three different positions along the microchannel. Figure 5.44 refers to a thermopile and a thermocouple positioned on the unheated length close to the microchannel entrance. Figure 5.45 presents the results referred to the center of the first unheated block. Finally Fig. 5.46 shows the results relative to the second unheated block. In correspondence of the third heated block the temperature difference between the wall and the gas is too small to be detected by the thermocouples.

For each examined position the temperatures of the blind foil, the gas and the heating block are reported (cf. Fig. 5.44-a). In a separate plot the comparison between the thermopile signal and the temperature difference calculated from the first plot is shown (cf. Fig. 5.44-b).

A good qualitative agreement between the voltage and temperature difference variations has been found for all the examined sensors. The oscillations for the calculated  $\Delta T$  derive from the impossibility of synchronizing the heating cycles imposed by the temperature controllers during the two tests with the PEEK cover.

In the transient behavior (time lapse where the gas flow is turned off), the thermopile signals go back to zero with no detectable delay. This is due to the very small thermal inertia of the membranes. When the flow is stopped, the gas around the membranes rapidly reaches the same temperature as the chip and thus a zero signal is delivered. The thermocouples on the chip have a larger response time due to the thermal inertia of the bulk material around the tips. When the flow is stopped, the calculated  $\Delta T$  progressively

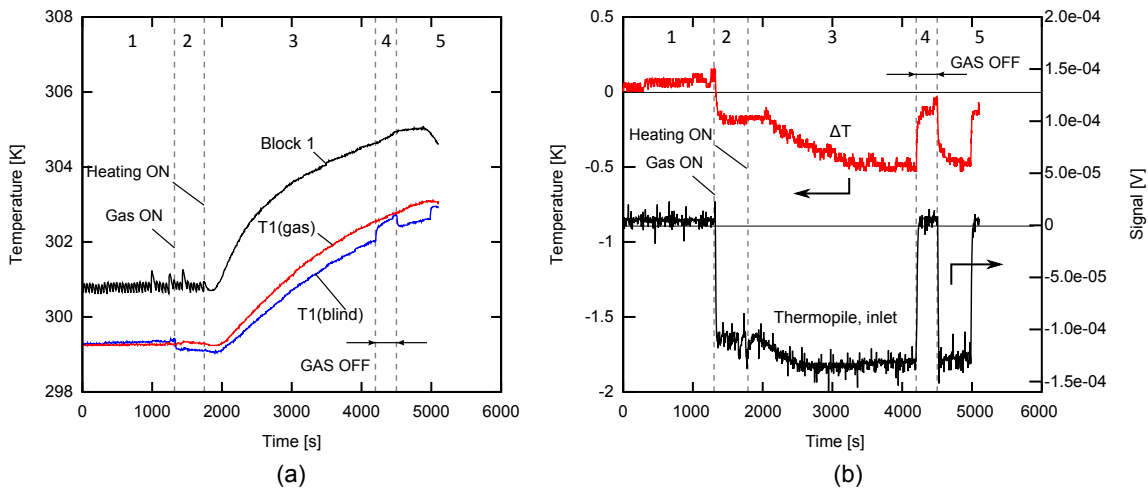


Figure 5.44.: Comparison between the data from the integrated thermopiles and the PEEK cover thermocouples for a position close to the microchannel entrance. (a): for the calculation of the reference temperature difference the signals from the first embedded thermocouples recorded with the unstructured foil (red) and with the microchannel foil (black) have been considered and plotted with the temperature of the unheated first block. (b): the thermopile signal (black) is plotted with the calculated temperature difference (red).

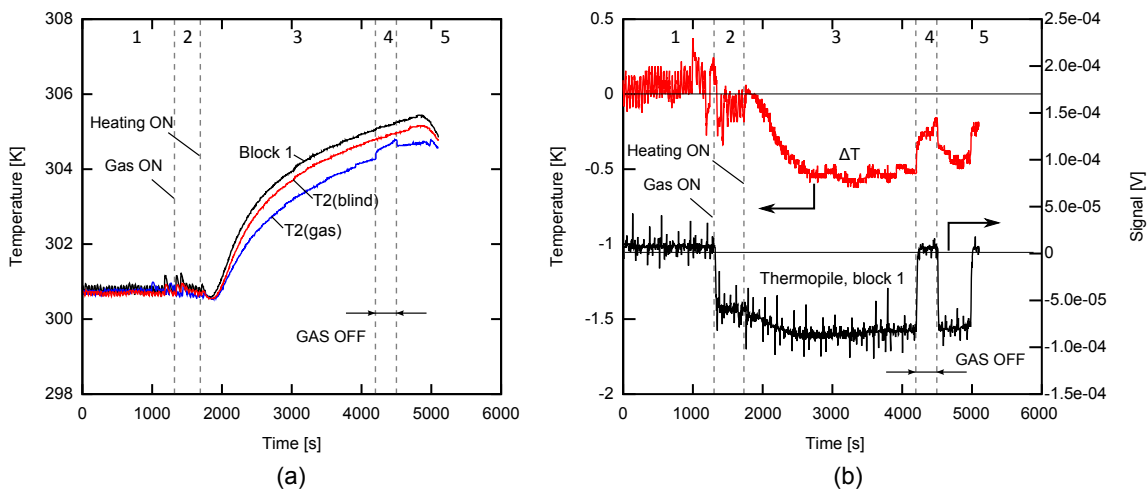


Figure 5.45.: Comparison between the data from the integrated thermopiles and the PEEK cover thermocouples recorded for the first unheated block. (a): for the calculation of the reference temperature difference the signals from the second embedded thermocouples recorded with the unstructured foil (red) and with the microchannel foil (black) have been considered and plotted with the temperature of the unheated first block. (b): the thermopile signal (black) is plotted with the calculated temperature difference (red).

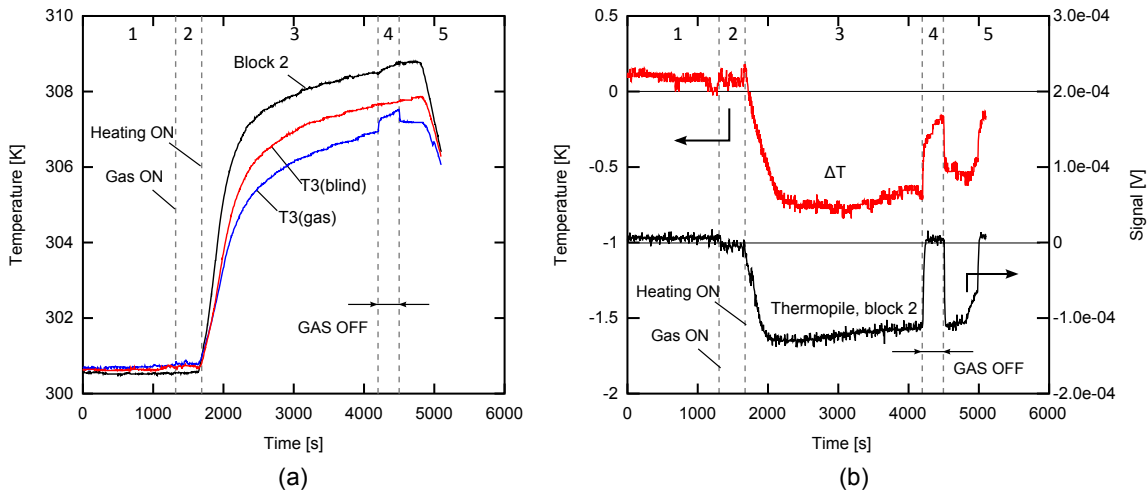


Figure 5.46.: Comparison between the data from the integrated thermopiles and the PEEK cover thermocouples recorded for the second unheated block. (a): for the calculation of the reference temperature difference the signals from the third embedded thermocouples recorded with the unstructured foil (red) and with the microchannel foil (black) have been considered and plotted with the temperature of the unheated first block. (b): the thermopile signal (black) is plotted with the calculated temperature difference (red).

tends to zero as the thermocouple tip (and the material around) accommodates to the new gas temperature.

The comparative analysis between the data obtained with the PEEK cover and the integrated thermopiles has given consistent results. The reproducibility of the thermopile signals with conventional thermocouples has validated the integrated chip measuring principle. In particular, by combining the two methods it is possible to provide the reference signals for the calibration of the thermopiles.

Due to the problems encountered during the sensor implementation, it was not possible, within the frame of this work, to perform the flow characterization under rarefied conditions by means of the integrated silicon sensors. In particular, major delays were faced due to the failure of many chips during operation. The fabrication of new sensors and their implementation was not possible, since the whole process is rather time and cost consuming. For these reasons, a numerical model of the sensor assembly was developed to further assist the understanding of the chip thermal behavior. Numerical simulations represent a valid tool to have an insight of the sensor functioning and predict the assembly performances. Moreover, by comparing the numerical and the experimental results it was possible to validate the integrated sensor measuring principle. The results of the numerical studies are reported in Chapter 6.

## 5.4. Heat transfer analysis

### 5.4.1. Microchannel material effects

The materials employed in microstructured devices may strongly affect the thermal behavior and the temperature profile development along the microchannels. To analyze these effects, a series of tests have been performed with the different manufactured microchannels. The gas and the wall temperature profiles, for a temperature of 50 °C imposed on the heating blocks, were measured with the PEEK cover. The wall temperature was measured separately, with an unstructured foil of the same material as the examined microchannel.

The gas temperature is measured for a flow at an inlet pressure of 2 bar and an average mass flow rate of 200 ml/min. Both sequences are recorded at steady state after turning on the heating of the three copper blocks.

Figures 5.47-5.51 reports the results for the micromachined stainless steel, copper, PEEK and wet chemically etched stainless steel microchannels, respectively. For each test section the plots show the temperature of the top wall and of the gas close to it as recorded by the embedded thermocouples on the PEEK cover. The block temperatures were also recorded to allow verifying that the boundary conditions in the test for the wall temperature measurement and the one for the gas temperature measurement were the same, and thus that the two result sets can be compared. The error bars reported for the data points include the instrumental error of the type-K thermocouples, as indicated by the manufacturer ( $\pm 0.25$  K).

Figure 5.47 refers to the micromachined stainless steel microchannel. Only small variations between the gas and the wall temperature can be detected. In particular, the gas temperature after the second thermocouple is systematically higher than the wall temperature recorded at the same position. This is because the gas is in contact with the heated bottom wall of the microchannel which is at a higher temperature than the top wall. An axial temperature gradient between the two non heated areas, at the entrance and exit of the microchannel, and the central, directly heated area is also established.

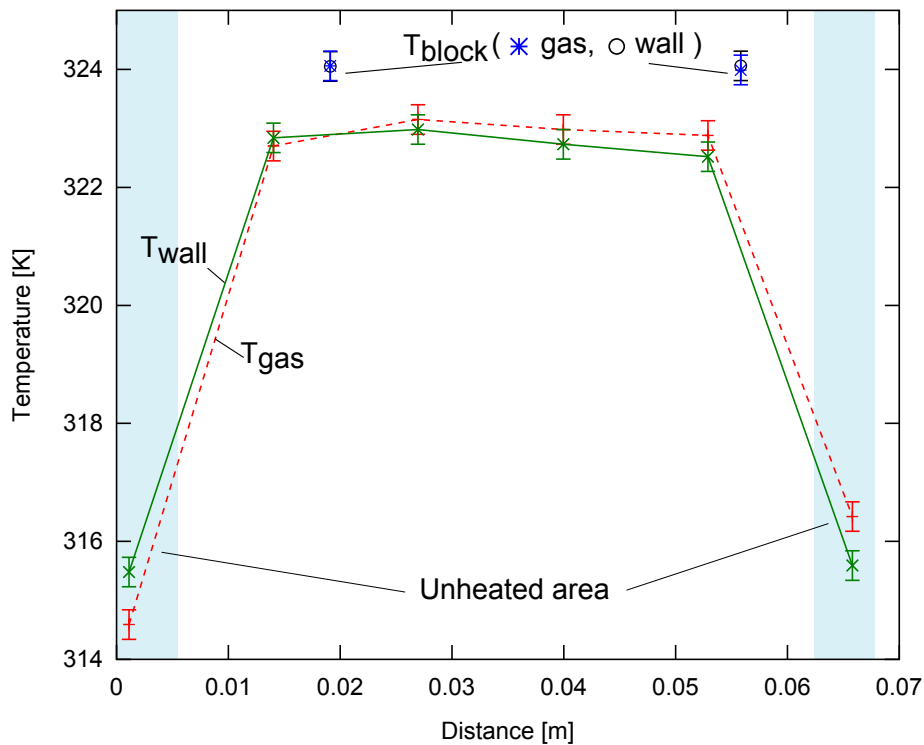


Figure 5.47.: Axial temperature distribution for the machined stainless steel microchannel as recorded by the PEEK cover embedded thermocouples for a temperature of 50 °C imposed on the three heating blocks. The wall temperature is measured during a similar test sequence with an unstructured foil.

The copper microchannel has a larger thermal conductivity which results in a fully developed profile reached already in correspondence of the second thermopile position. The axial temperature profile is showed in Fig. 5.48 (and in Fig. 5.49 with an enlarged scale). In this case, the temperature gradient from the unheated to the heated areas is smaller, resulting in a flatter axial temperature profile with respect to the stainless steel microchannel.

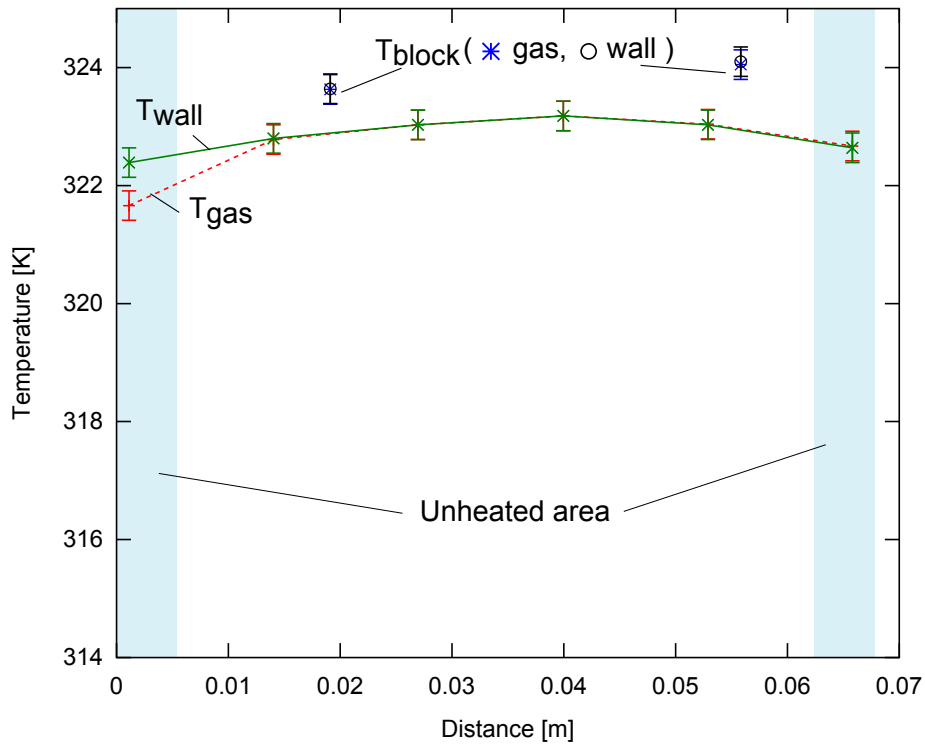


Figure 5.48.: Axial temperature distribution for the machined copper microchannel as recorded by the PEEK cover embedded thermocouples for a temperature of 50 °C imposed on the three heating blocks. The wall temperature is measured during a similar test sequence with an unstructured foil.

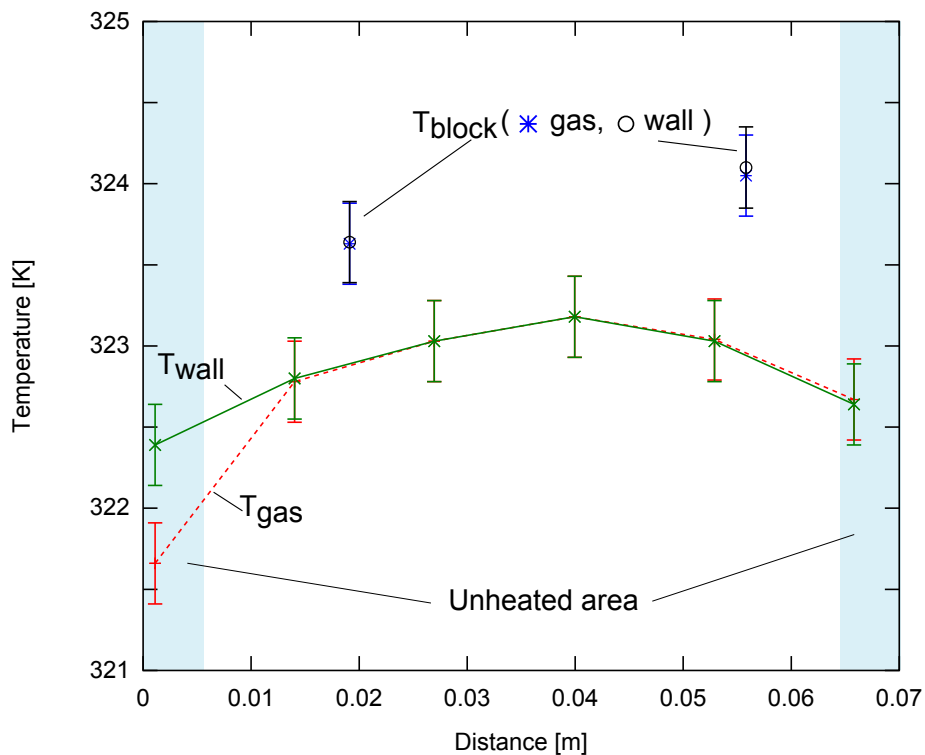


Figure 5.49.: Enlargement of Fig. 5.48 to highlight the details of the temperature distribution.

In Fig. 5.50 the temperature profiles recorded for the PEEK microchannel are shown. Higher temperature differences between the wall and the gas can be measured. As a result of the very low thermal conductivity of the polymer (about three orders of magnitude lower than copper), the vertical heat conduction from the blocks to the internal bottom wall of the microchannel is lower. As a consequence, even with the same temperature levels set on the heating blocks, the real boundary conditions at the channel inner walls are lower for PEEK than for the metallic structures. Moreover, also the axial conduction is lower, resulting in a larger thermal entry region length than the previous cases.

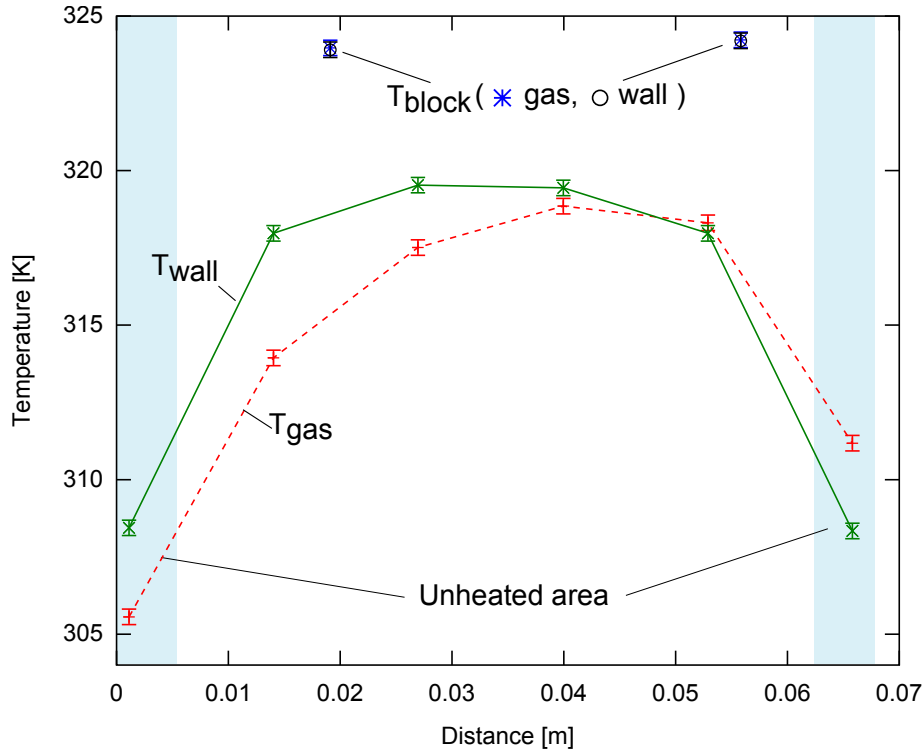


Figure 5.50.: Axial temperature distribution for the machined PEEK microchannel as recorded by the PEEK cover embedded thermocouples for a temperature of 50 °C imposed on the three heating blocks. The wall temperature of the wall is measured during a similar test sequence with an unstructured foil.

The last tested section is the wet chemically etched stainless steel microchannel. The results are shown in Fig. 5.51. The test section has a rougher finish (see Section 5.2) and a larger hydraulic diameter than the others (see Tab. 4.1), as a result of the specific manufacturing technique. However, the established temperature profile is similar to the micromachined stainless steel channel, confirming that the constituting material plays a major role in determining the heat transfer behavior. The higher temperature difference for the microchannel first sections is probably due to the larger cross sectional area, rather than to roughness effects.

Figure 5.52 presents a summary for a direct comparison of the gas temperature profiles resulting from the different tested sections. Thanks to its good thermal properties, copper allows to achieve a rather flat temperature profile. Stainless steel (either etched or machined) grants good heat transfer properties and the rapid achievement of thermally developed flows. With a thermal conductivity significantly lower than copper, it allows the presence of axial temperature gradients. Finally, PEEK offers insulating characteristics, which can be suitable when the thermal development region is to be studied. Long entry lengths and smooth gradients between the heated and non-heated areas can be produced.

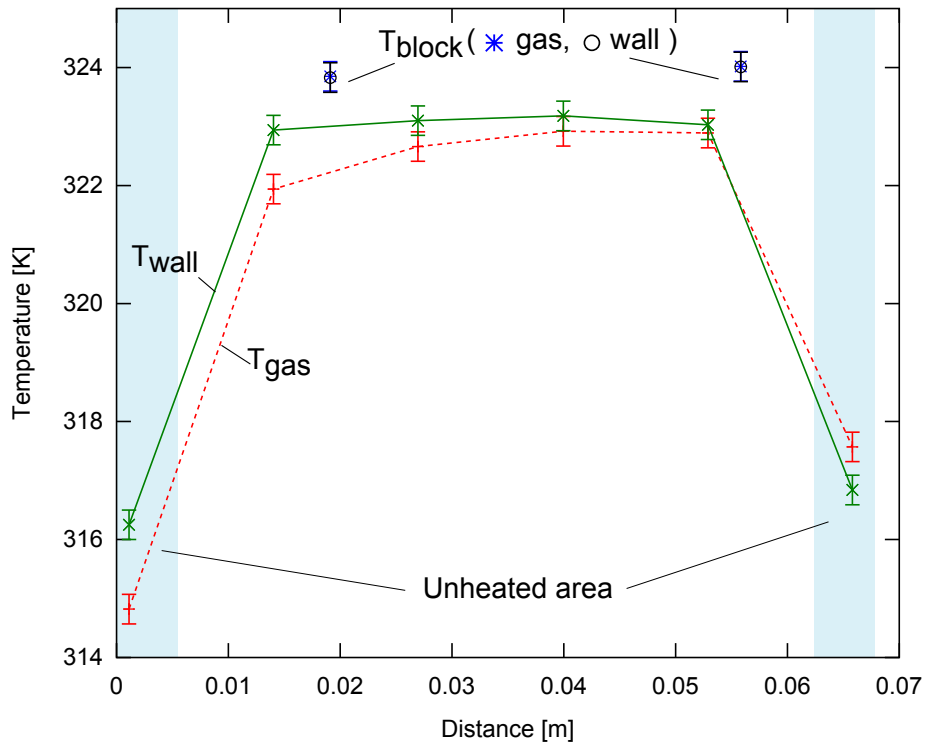


Figure 5.51.: Axial temperature distribution for the etched stainless steel microchannel as recorded by the PEEK cover embedded thermocouples for a temperature of 50 °C imposed on the three heating blocks. The wall temperature is measured during a similar test sequence with an unstructured foil.

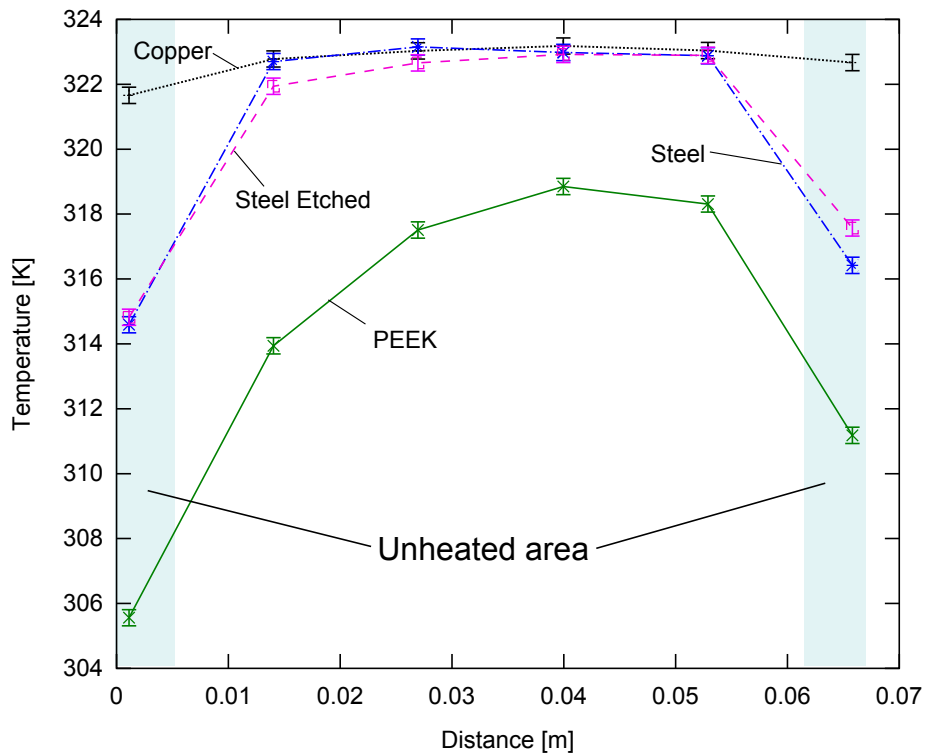


Figure 5.52.: Comparison of the axial temperature distributions recorded with the PEEK cover and microchannels of different materials for the same thermal boundary conditions.



### 5.4.2. Roughness effects

Surface roughness has been claimed to have relevant effects on the heat transfer behavior of microchannels [10]. To directly investigate this issue, one of the microchannel test sections employed for the previously described tests has been treated to alter its surface characteristics. In particular, the micromachined stainless steel microchannel has been processed with abrasive blasting, using glass particles with average sizes ranging between  $10\ \mu\text{m}$  and  $20\ \mu\text{m}$ . Figure 5.53 shows a comparison between the SEM pictures of the microchannel bottom surface before (a) and after (b) the treatment.

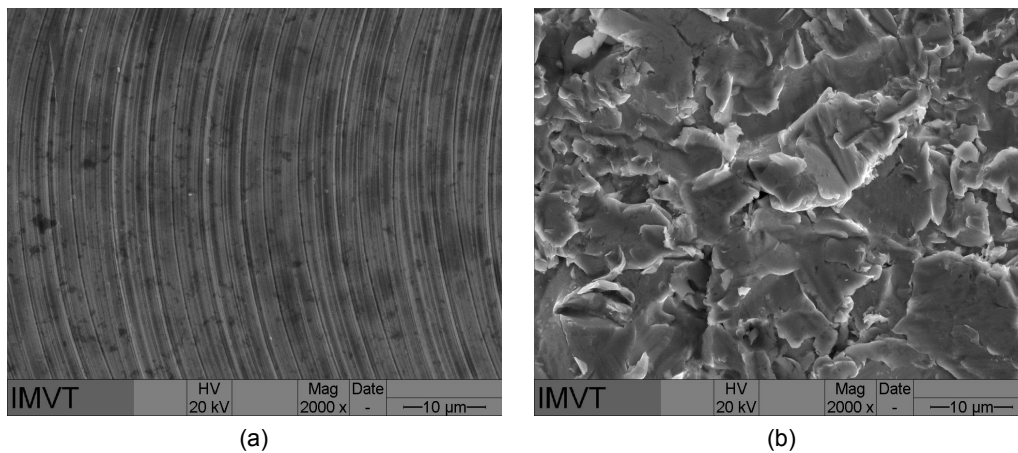


Figure 5.53.: SEM picture of the stainless steel microchannel surface after the micromachining (a) and after the additional treatment with glass particles (b).

The same test sequence described in Section 5.4.1 has been repeated with the treated microchannel. The results are plotted in Fig. 5.54 along with the experimental data obtained for the same section, prior to the surface treatment.

The axial temperature profile developed along the microchannel axis does not show any substantial difference between the two tests. The small deviations between the two data sets fall within the experimental uncertainty and can be interpreted as statistical fluctuations. These results suggest that, within the investigated flow conditions (i.e. continuum and laminar flow regime), the surface finish characteristics do not have major effects on the heat transfer performances of the microchannels. The temperature profile is determined by macroscopic properties such as the mass flow rate, the temperature boundary conditions and the microchannel material rather than by the microscopic surface characteristics. This might be different for different flow conditions, such as rarefied gas flows, for which the gas-surface interactions are expected to have a stronger effect on the flow behavior (e.g., appearance of a temperature jump at the wall).

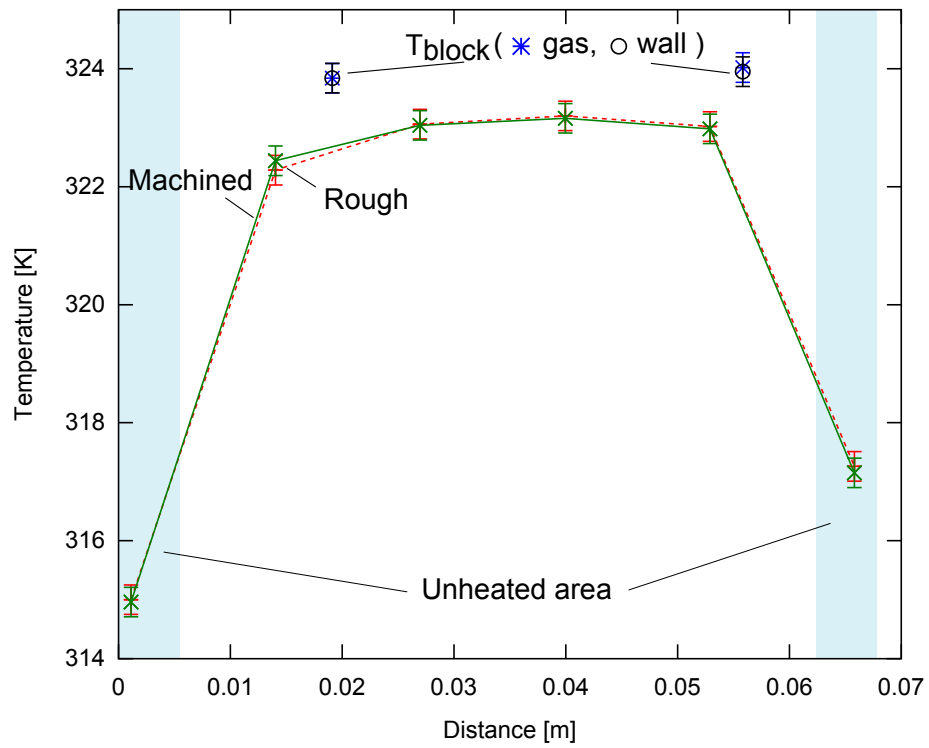


Figure 5.54.: Comparison of the axial temperature distributions for the machined stainless steel microchannel recorded with the PEEK cover before and after the roughness enhancement surface treatment.

## 6. Numerical results

Computational fluid dynamics (CFD) is a powerful numerical tool to solve fluid mechanics problems. It is generally based on the numerical solution of the conservations laws for mass, momentum and energy for the flow through the geometry of interest, taking the form of particular differential equations. Most of the finite volume methods are applied for discretization. In most commercial CFD codes the calculation scheme includes the definition of a geometry, the creation of a mesh for the volume occupied by the fluid, the definition of the physical models to be applied for the problem and the definition of the boundary conditions for the geometrical structure. The simulation routine solves the governing equations to calculate the flow properties for every cell of the mesh domain. The underlying partial differential equations are based on the assumption of a fluid with continuous properties. Hence CFD methods are normally restricted to flows in the continuum regime. However, the possibility of re-formulating the boundary conditions or adding special terms to the basic equations to include extra effects make these tools very appealing also for applications including slightly rarefied flows.

Among the different available commercial software packages for CFD simulations, ANSYS FLUENT<sup>®</sup> is one of the most commonly employed in practical engineering problems. Within this software it is possible to develop custom designed geometries, define material properties for both solid and fluid parts, impose different types of boundary conditions and eventually include custom field functions (CFF) for the modification of the default features of the program.

For the present work, CFD simulation techniques have been chosen to model the microchannel integrated sensor assembly. The geometry of the problem has been developed under GAMBIT<sup>®</sup>, a pre-processing tool for the creation of the geometry and the meshing, while the calculations and the post-processing have been performed with FLUENT<sup>®</sup>. The main aim of the simulations is the implementation of the same boundary conditions recorded during the experiments and the comparison of the numerical predictions with the experimental data. This allows a further validation of the integrated sensor functioning, as well as an insight on the heat transfer performances of the assembly. Moreover, also the simulation of different microchannel materials and the comparison with the experimental data obtained in Sec. 5.4.1 was performed.

## 6.1. Geometries and physical models

A schematic view of the developed geometry for the channel-chip assembly is shown in Fig. 6.1, along with a representation of the coordinate system.

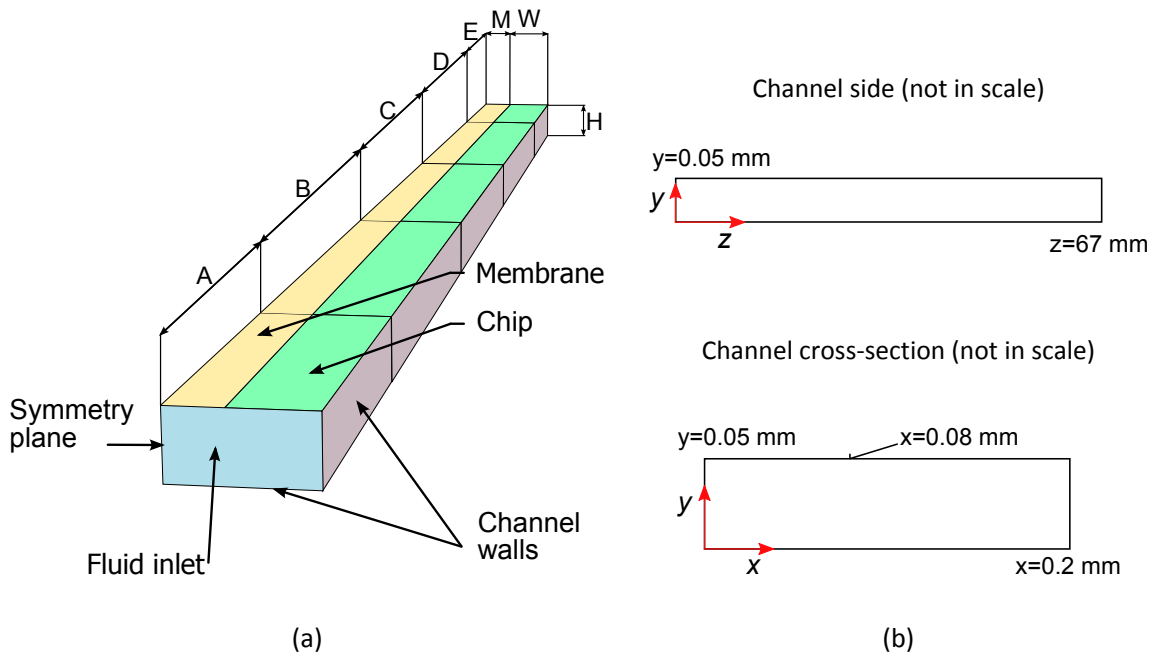


Figure 6.1.: Schematic representation of the channel-chip geometry developed with GAMBIT<sup>®</sup> (a) and of the employed coordinate system (b). The full set of dimensions is given in Tab. 6.1.

Based on symmetry considerations, only one half of the microchannel geometry is simulated. A symmetry boundary condition is imposed on the vertical plane corresponding to the microchannel central axis. To reproduce the actual thermal boundary conditions established with the three copper blocks during the experiments, the channel length has been split into five areas, corresponding to the unheated entrance and exit lengths and to the three heated lengths, respectively. For the chip, i.e. the microchannel top wall, a simplified geometry has been implemented. Two main areas have been identified, the actual chip substrate (the outermost part) and the membrane area (the inner part). In the real chip, the membranes do not occupy the entire length of the channel, but are separated from each other. With the present model the heat conduction across the material separating the membranes is not considered and thus, the resulting axial heat transfer would be underestimated. The microchannel zones defined with the created geometry are listed and described in Tab. 6.1. Different boundary conditions can be set to evaluate the best thermal model reproducing the actual membrane behavior.

With the meshing tool of GAMBIT<sup>®</sup> the channel geometry has been divided into small control volumes, for which the governing equations are solved. The simulation domain has been divided with a structured mesh, presenting also a boundary layer to refine the solution where needed. Structured meshes are characterized by a regular connectivity which limits the element type for 3D problems to hexahedra only. The boundary layer option allows the creation of small cells close to areas where a more detailed solution is needed. For the present model a progressive refinement boundary layer has been applied, as represented in Fig. 6.2.

Table 6.1.: Specification of the channel geometry created for the CFD simulations.

Channel area	Description	Dimensions
A	Unheated entrance length	3.5 mm
B	First heating block	20 mm
C	Second heating block	20 mm
D	Third heating block	20 mm
E	Unheated exit length	3.5 mm
H	Height	0.1 mm
M	Membrane (half)	0.08 mm
W	Chip	0.12 mm

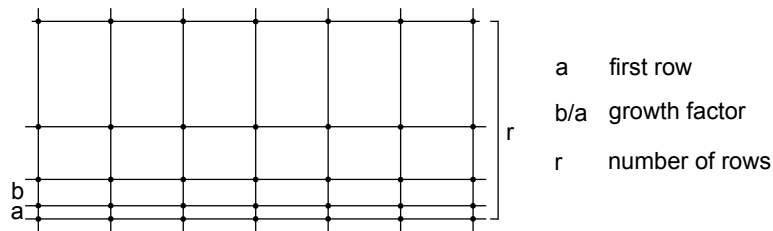


Figure 6.2.: Schematic layout of the boundary layer option for the geometry meshing.

When setting up the geometry it is also possible to assign a specific boundary type for every zone, depending on which different input parameters are required to initiate the calculations. Based on the experimental conditions encountered during the tests, the boundary types listed in Tab. 6.2 have been assigned.

Table 6.2.: Boundary conditions type chosen for the different geometry areas, with respective input parameter given for the simulation.

Zone	Boundary type	Input parameters
Inlet cross section	Pressure Inlet	- Total inlet pressure - Inlet temperature
Channel bottom/ side walls Top wall, chip Top wall, membrane (A-B-C-D-E)	Solid wall	<b>Momentum:</b> - Stationary walls - Slip (TMAC=TAC=1) <b>Thermal:</b> - Constant heat flux/ wall temperature - Wall thickness - Material
Outlet cross section	Pressure outlet	- Static outlet pressure

The boundary conditions can be varied for every studied problem to match the same conditions recorded during the experiments and allow for comparison between the numerical and the experimental results. FLUENT<sup>®</sup> allows the definition of different materials both for the solid and the fluid parts as well as the choice among different models to be included for the specific problem. By properly choosing among the various options it is possible to include effects such as compressibility and, to some extent, rarefaction to the simulation.

When modeling compressible flows, the density changes across the domain must be taken into account to calculate the pressure distribution. This is done automatically by FLUENT<sup>®</sup> if the option of *ideal gas law* is picked for the fluid density model. In this case the solver calculates for every cell the density as:

$$\rho = \frac{p_{op} + p}{\frac{\bar{R}}{M}T} \quad (6.1)$$

where  $p_{op}$  is the operative pressure properly defined along with the boundary conditions (e.g. inlet pressure),  $p$  is the pressure change computed by the solver,  $\bar{R}$  is the universal gas constant,  $M$  is the fluid molecular weight and  $T$  is the calculated temperature. The numerator in Eq. 6.1 represents the absolute static pressure for the considered cell.

Similarly to what is done for the density model definition, specific viscosity models can be imposed too. In particular it is possible to take the temperature dependence of the viscosity with appropriate laws into account. For dilute gases, the power law derived from the Chapman-Enskog theory [68] is very often employed (see e.g. [64]). In this case, the solver calculates the viscosity of every cell in the domain as:

$$\mu = \mu_0 \left( \frac{T}{T_0} \right)^n \quad (6.2)$$

where  $\mu$  and  $T$  are the effective viscosity and temperature,  $\mu_0$  and  $T_0$  are the respective reference values and  $n$  is the exponent of the power law, changing according to the specific fluid.

It is possible to take rarefaction effects into account, e.g. imposing slip boundary conditions, with the option *laminar flow* for the viscous model. The *low pressure boundary slip* (LPBS) option automatically sets velocity slip and temperature jump boundary conditions for the equations to be solved. With this option it is also possible to define the momentum and the thermal accommodation coefficients as fluid properties.

Additional and detailed information about the different available models, boundary condition types and options for FLUENT<sup>®</sup> can be found in [99] and [100].

Details about the material properties and other relevant parameters employed in the simulations are give in Appendix B

## 6.2. Isothermal flow analysis

The first simulations to test the developed microchannel geometry have been focused on the study of a well known problem for which the analytical solution is known and can be used as reference for the numerical results. In particular, the isothermal slip-flow of a gas in a rectangular duct, for which the analytical solution has been proposed by Erbert and Sparrow [101], has been chosen. The authors solved the Navier-Stokes equations for a fully developed isothermal flow of gas, including first order slip flow boundary conditions. This problem has been preferred to the one presented by Deissler [102], who developed second order boundary conditions, since the slip boundary condition used by default in FLUENT<sup>®</sup> are of the first order.

To study the mesh dependence of the microchannel model, four different meshes have been created, mainly differing from each other for the boundary layer disposition and configuration and for the total number of elements. The main characteristics for the four tested meshes are reported in Tab. 6.3.

The inlet and walls temperatures have been set to a constant value of 296 K. The LPBS option has been included to take slip at the walls into account. As gas, air with both tangential momentum and thermal accommodation coefficients set to 1 has been considered. The ideal-gas option has been chosen to calculate the gas density at each node. Finally the inlet and outlet pressure have been set respectively to 20000 Pa and 2000 Pa.

As the analytical solution refers to a fully developed flow, the comparisons for the axial velocity profile along the  $y$ -coordinate have been done in correspondence of the microchannel exit section. The results are reported in Fig. 6.3.

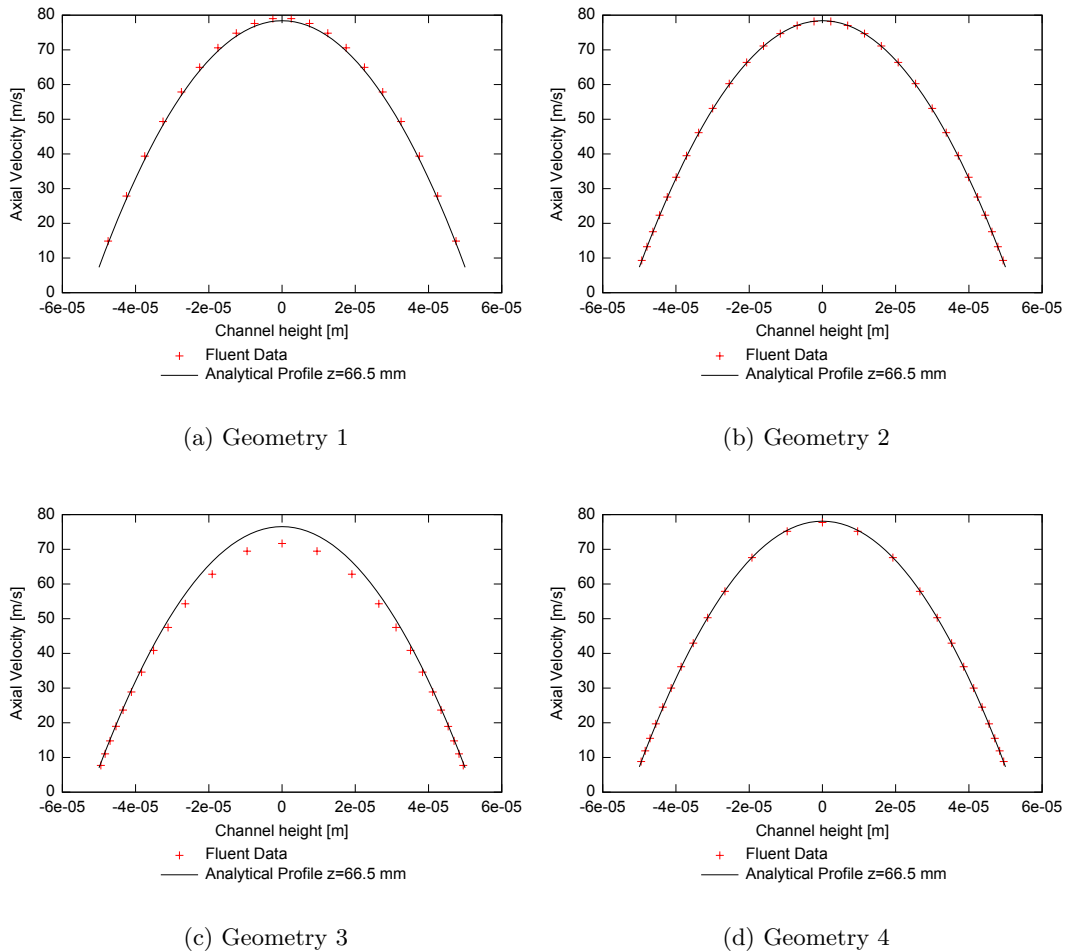


Figure 6.3.: Axial velocity close to the channel exit ( $z=66.5$  mm) for an isothermal slip flow, calculated with the four different meshes. The numerical results (crosses) are plotted together with the corresponding analytical solutions (solid line).

Geometry 1 and 3 show some disagreement with the analytical solution, while a good agreement is found for Geometry 2 and 4. The number of cells in the first mesh is much higher than in the second case, and thus a larger computational effort is required. For this reason Geometry 4 has also been employed for the non-isothermal simulations, provided that for each case finer meshes have been tested as well, with no detected dependence of the results.

Table 6.3.: Details of the four different meshes created with GAMBIT for the isothermal flow simulations.

Geometry	Zone	Boundary Layer	Meshing	Total number of cells
Geometry 1	Inlet	No	Interval size =5	536000
	Outlet	No	Interval size =5	
	A	-	Interval size = 100	
	B	-	Interval size = 100	
	C	-	Interval size = 100	
	D	-	Interval size = 100	
Geometry 2	Inlet	a=1 b/a=1.2 r=10	Elements=20	604800
	Outlet	a=1 b/a=1.2 r=10	No. of elements=30	
	A	-	Interval size = 200	
	B	-	Interval size = 200	
	C	-	Interval size = 200	
	D	-	Interval size = 200	
Geometry 3	Inlet	a=1 b/a=1.2 r=18	No. of elements=20	233750
	Outlet	a=1 b/a=1.2 r=8	No. of elements=20	
	A	a=4 b/a=1.2 r=10	Interval size=200	
	B	-	Interval size = 400	
	C	-	Interval size = 400	
	D	-	Interval size = 400	
Geometry 4	Inlet	-	No. of elements=25	273750
	Outlet	a=1 b/a=1.2 r=10	Elements=25	
	A	-	Interval size = 350	
	B	-	Interval size = 350	
	C	-	Interval size = 350	
	D	-	Interval size = 350	
	E	a=4 b/a=1.2 r=30	Interval size=350	



### 6.3. Simplified simulation of the membrane behavior

The first implemented simulation to analyze the membrane behavior refers to an ideal case where the microchannel bottom and side walls are all at the same constant temperature (no distinction between the heated and unheated areas). In this case the simulations are performed for a flow under continuum regime to decouple the actual effects of the channel configuration from the slip effects. These appeared during the experiments in the last sections of the microchannel, due to the small pressure reached by the gas flow at the exit, and can be added successively by modifying the boundary conditions.

To investigate the membrane thermal performances, two opposite situations have been chosen: in the first the membrane is treated as adiabatic, while in the second the membrane is considered isothermal to the silicon chip. Although the real membrane characteristics would most likely be intermediate between the two extremes, these cases are interesting as they would help to understand the actual working conditions of the integrated sensors. For the adiabatic simulations a zero heat flux condition is imposed on the microchannel areas corresponding to the membrane. For the isothermal approach the membrane is set at the same temperature imposed on the chip. The boundary conditions used for the different microchannel areas are listed in Tab. 6.4. These are distinguished between adiabatic and isothermal membrane cases.

Table 6.4.: Boundary conditions imposed for the simulation of the microchannel heat transfer performances. Two different cases are considered, for which the membrane is treated either as adiabatic or isothermal thermal boundary.

Zone	Adiabatic membrane	Isothermal membrane
Inlet	$p_{in}=150000$ Pa $T_{in}=296$ K	$p_{in}=150000$ Pa $T_{in}=296$ K
Outlet	$p_{out}=100000$ Pa	$p_{out}=100000$ Pa
Bottom & side walls: (A-B-C-D-E)	Thickness=0 $T=308$ K	Thickness=0 $T=308$ K
Chip (A-B-C-D-E)	Thickness=0 $T=308$ K	Thickness=0 $T=308$ K
Membrane (A-B-C-D-E)	Thickness=0 Heat Flux=0	Thickness=0 $T=308$ K

Figure 6.4 shows the calculated pressure and Knudsen number profiles along the microchannel axis, for the two membrane models. The Knudsen number is fully included within the continuous flow limits, confirming that in this case rarefaction effects can be dismissed. The axial pressure distribution is not perfectly linear, as a result of compressibility effects along the channel. However, no major differences in terms of pressure profiles between the two membrane thermal models have been found. This is not surprising since the area of the membrane is small compared to the total wall area.

Small discrepancies for the Knudsen number are visible at the channel inlet. However, since the Knudsen number temperature dependence is weak, the differences between the two approaches are negligible.

Figure 6.5 reports the calculated axial temperature distributions at different positions of the microchannel cross section and for the two membrane models. In particular, the temperature distribution along the microchannel central axis is plotted together with the

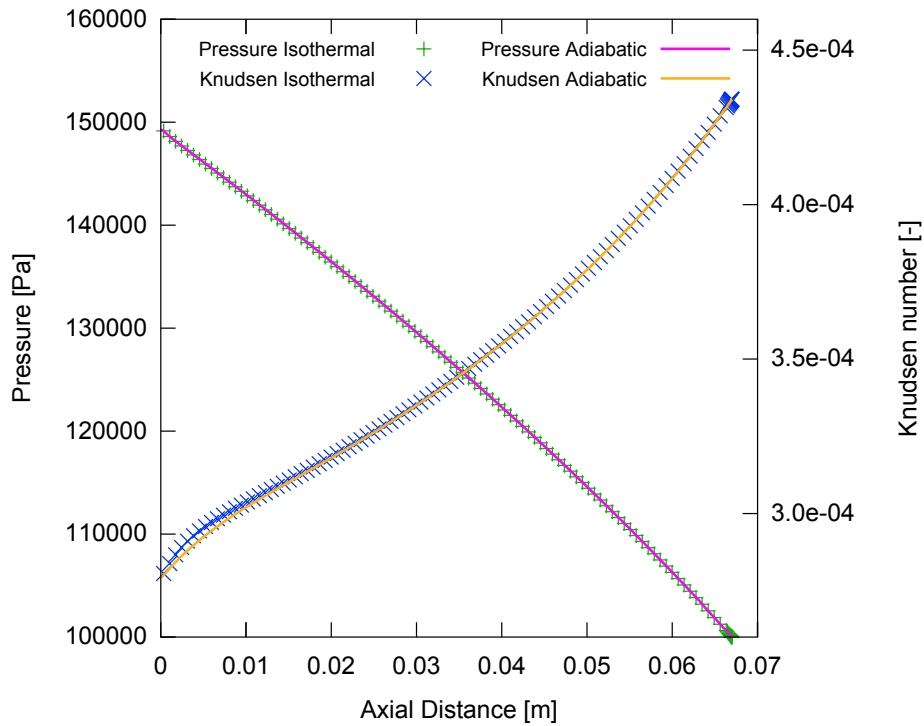


Figure 6.4.: Axial pressure and Knudsen number distribution calculated for the isothermal and adiabatic membrane models.

profiles along the microchannel top wall in correspondence of the chip and the membrane, respectively. In the isothermal case the temperature of the membrane and of the chip coincide.

The gas temperature distribution along the microchannel axis converges from the imposed inlet value to the microchannel wall temperature. In the isothermal membrane case, the convergence is steeper, since the exchange area includes also the membrane. In the adiabatic case the thermal entry region is longer.

The chip temperature distribution is the same in both cases, since its value is imposed as boundary condition and no conjugate effect is considered (the chip thickness is set to zero). More realistic boundary conditions, including non-zero wall thickness of the chip are treated in Sec. 6.4.

The main difference between the two cases is in the membrane temperature distribution. In the adiabatic case the membrane temperature distribution is closer to the axial temperature profile.

The results have been analyzed also in terms of temperature distribution across the channel width at different axial positions from the inlet. This allows understanding the influence of the membrane thermal boundary conditions on the length of the thermal entry region. Figures 6.6-6.9 show the transversal temperature distribution for the microchannel top wall at four different positions (corresponding to the inlet and the first three thermopiles, respectively). The 2d plots for both the adiabatic and the isothermal membrane are reported. This allows estimating the maximum theoretical temperature difference the thermopile could sense, i.e. in the case of a perfectly adiabatic membrane. From the third membrane position to the microchannel exit the temperature distribution is uniform across the section and the same for both cases.

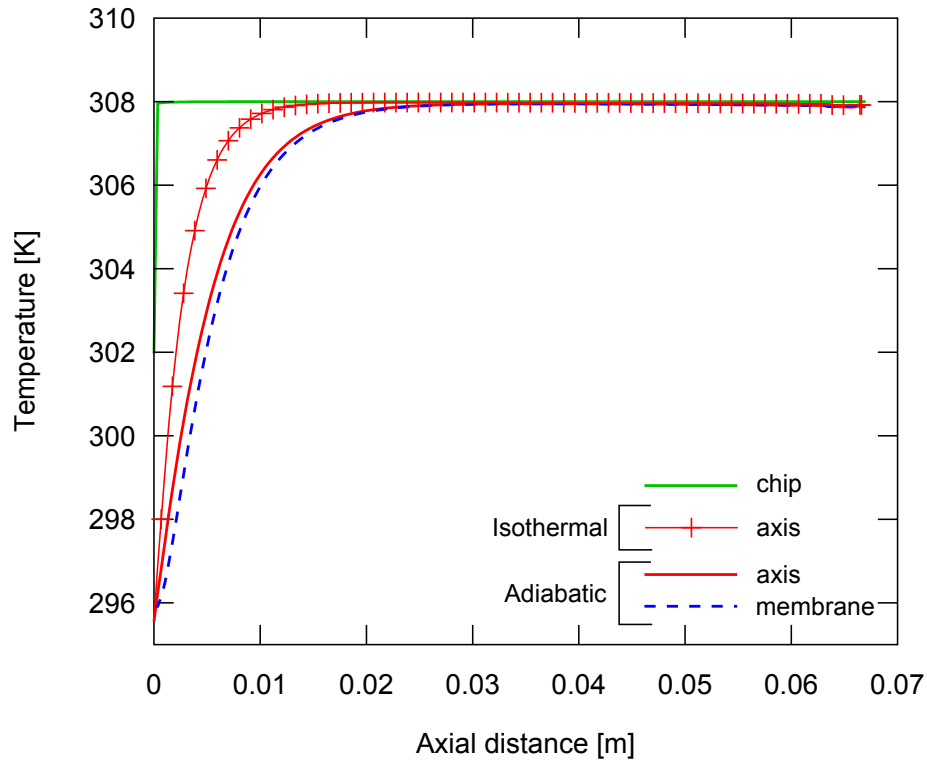


Figure 6.5.: Axial temperature distribution along the microchannel axis (red), the chip (green) and the membrane (blue) calculated for the isothermal and adiabatic thermal model.

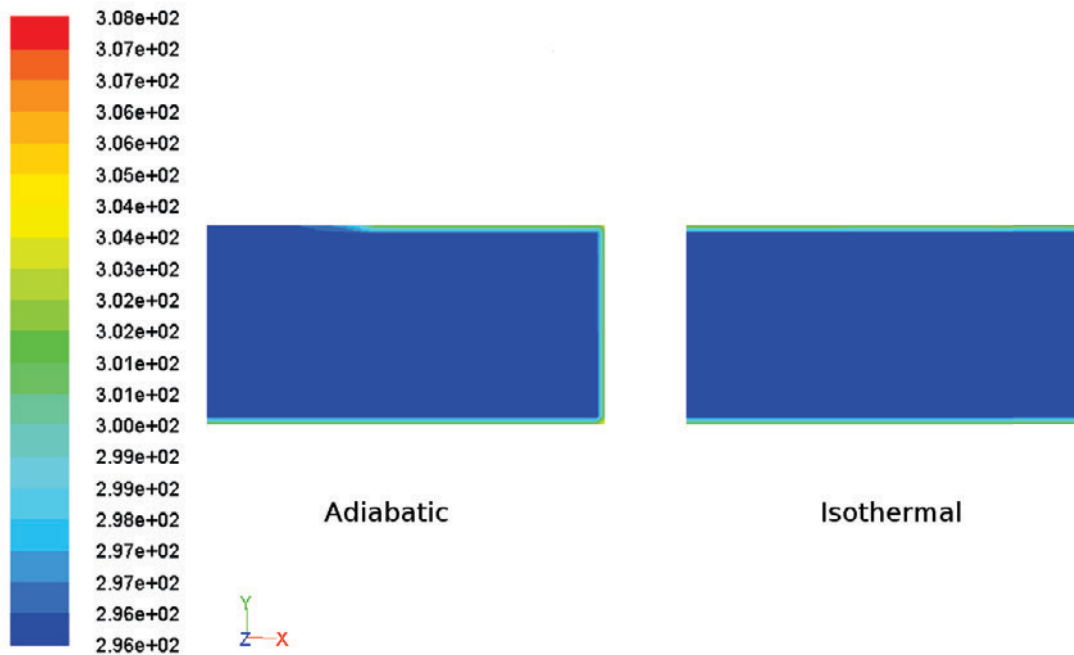


Figure 6.6.: Temperature distribution across the microchannel inlet cross section, compared for the two membrane models.

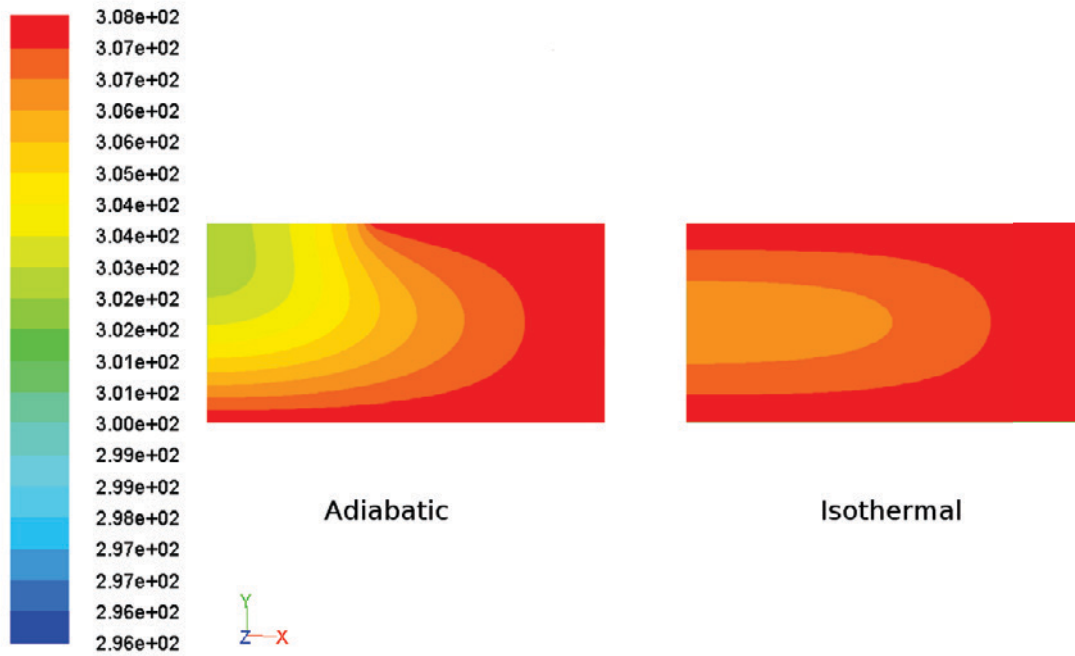


Figure 6.7.: Temperature distribution across the microchannel cross section corresponding to the first membrane, compared for the two thermal boundary conditions sets.

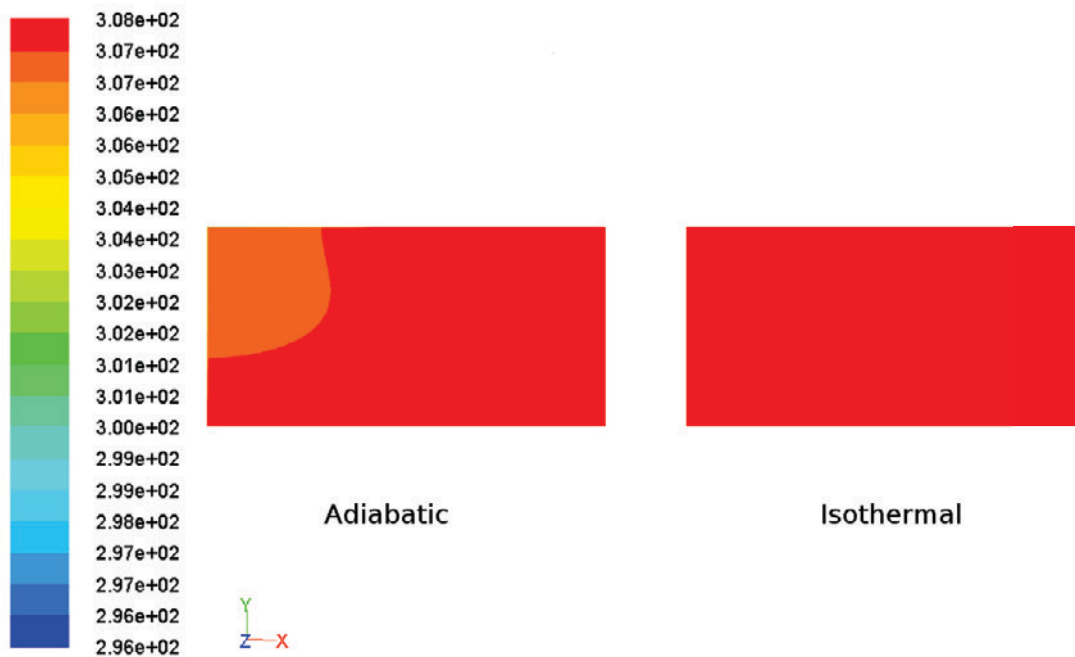


Figure 6.8.: Temperature distribution across the microchannel cross section corresponding to the second membrane, compared for the two thermal boundary conditions sets.

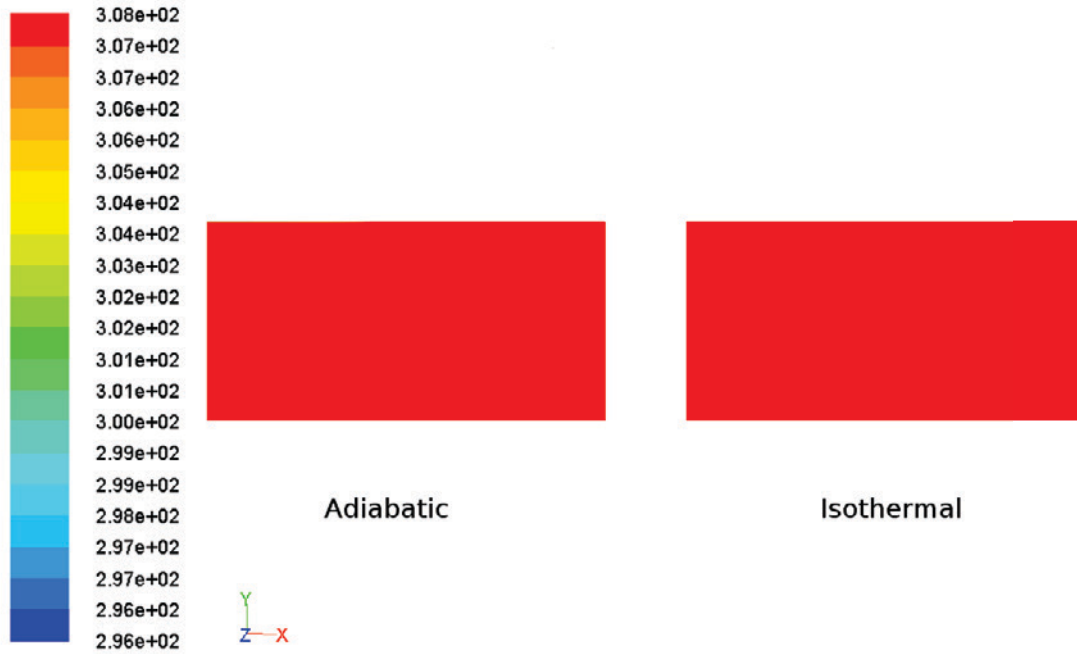


Figure 6.9.: Temperature distribution across the microchannel cross section corresponding to the third membrane, compared for the two thermal boundary conditions sets.

## 6.4. Full simulation of the membrane behavior

To better investigate the real thermal behavior of the sensor chip and the membranes, a simulation with boundary conditions extrapolated from the experimental data has been implemented. For a given set of inlet and outlet parameters, the bottom wall temperature distribution along the heated area, measured with the thermocouples installed on the heating blocks, has been considered. The wall temperatures of the entrance and exit regions have been measured separately, employing the PEEK cover and the unstructured foil in a similar test sequence. The chip temperature has been measured with the RTDs on the silicon chip. To include the effects of the axial heat conduction along the microchannel material (conjugate effects), the real wall thicknesses have been used for the microchannel foil and the chip. The membrane thickness has been kept to zero, being negligible compared to the other two components. To compare the experimental data to the simulation results, the test sequence described in Section 5.3.5 has been taken as reference. In particular, since the sequence includes also transient states, two steady state time windows for the evaluation of the boundary conditions have been identified. The first corresponds to the initial phase, where the gas flow is activated but the microchannel is not yet heated. The second is fixed when the microchannel is heated and the axial temperature profile is established.

Both the adiabatic and isothermal conditions for the membrane have been simulated. The boundary conditions implemented for the two periods are listed in Tab. 6.5. The values for the membrane are not included since they correspond to zero heat flux in the adiabatic case and are the same than those imposed for the chip in the isothermal case.

The pressure and Knudsen number distributions, plotted in Fig. 6.10, do not significantly vary between the two periods due to the weak temperature dependence.

Compared to the previous simulations the pressure drop is substantially larger and compressibility effects are more evident. This results in a non linear pressure profile, with an

Table 6.5.: Boundary conditions imposed for the microchannel simulation as recorded during one of the integrated sensors experiments at two different periods. The thickness of the microchannel and chip surfaces are set to the real values, while the membrane is set to zero thickness.

<b>Zone</b>	<b>Period 1</b>	<b>Period 2</b>			
Inlet	$p_{in}=110000$ Pa $T_{in}=298.8$ K	$p_{in}=110000$ Pa $T_{in}=299$ K			
Outlet	$p_{out}=21000$ Pa	$p_{out}=21000$ Pa			
Bottom & side walls:	Material: Steel Thickness=1 mm $T_A=300$ K $T_B=300.9$ K $T_C=300.7$ K $T_D=300.9$ K $T_E=300$ K	Material: Steel Thickness=1 mm $T_A=302$ K $T_B=303.8$ K $T_C=305.7$ K $T_D=312.5$ K $T_E=307$			
	Chip	Material: Silicon Thickness=0.5 mm $T_A=300$ K $T_B=300.6$ K $T_C=300.6$ K $T_D=300.6$ K $T_E=300$ K	Material: Silicon Thickness=0.5 mm $T_A=302.1$ K $T_B=304.1$ K $T_C=305.8$ K $T_D=312.5$ K $T_E=307.2$		
		Membrane (isothermal case)	Thickness=0 $T_A=300$ K $T_B=300.6$ K $T_C=300.6$ K $T_D=300.6$ K $T_E=300$ K	Thickness=0 $T_A=302.1$ K $T_B=304.1$ K $T_C=305.8$ K $T_D=312.5$ K $T_E=307.2$	
			Membrane (adiabatic case)	Thickness=0 Heat Flux=0	Thickness=0 Heat Flux=0

acceleration effect towards the channel exit (the calculated Mach number at the outlet section is 0.67). The last sections of the microchannel also fall within the slip flow regime, as the Knudsen number gets above 0.001. Both effects are included in the simulation with a compressible ideal gas model and the LPBS option for the viscous model.

Figures 6.11 and 6.12 show the axial temperature distributions corresponding to the first and the second period, for the membrane axis (line parallel to the  $z$ -axis at  $x=0$ ) and the chip axis (line parallel to the  $z$ -axis at  $x=0.14$  mm).

In the second period an axial temperature profile is established due to the fact that the third block is directly heated by the power supply, while the first and the second block are heated only by heat conduction along the device.

In the isothermal cases the membrane has the same temperature as the chip (as imposed in the boundary conditions), except for the locations where the axial temperature variations occur. Here the chip has a smoother transitory due to its non-zero thickness and to the axial heat losses.

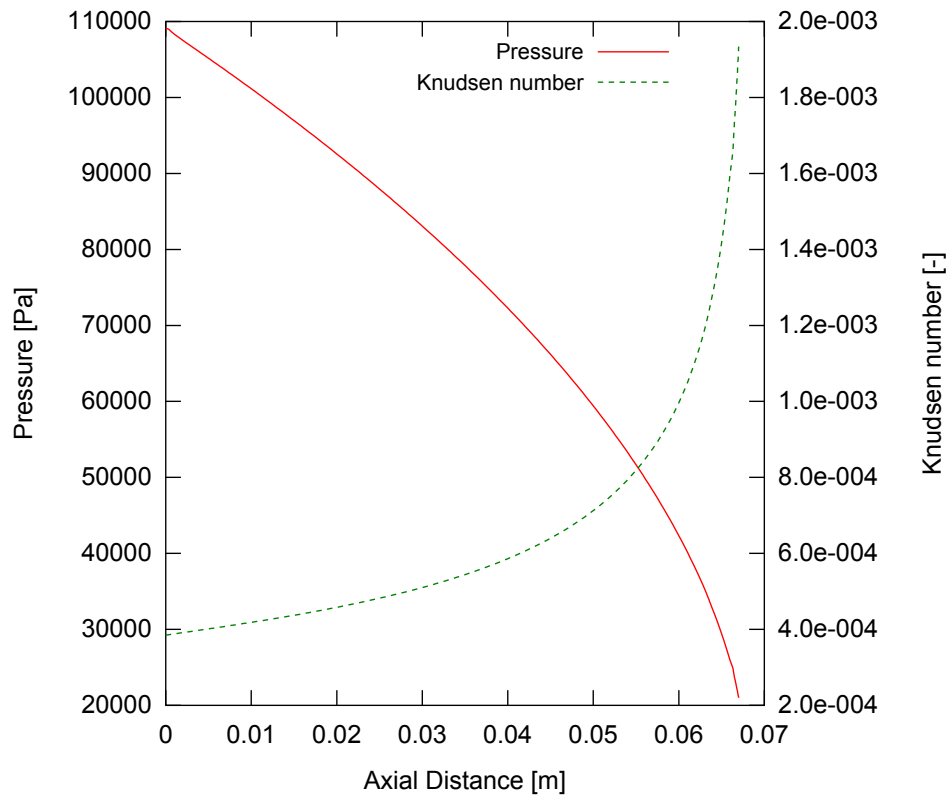


Figure 6.10.: Pressure and Knudsen number distributions along the microchannel axis calculated for the boundary conditions encountered during the chip tests.

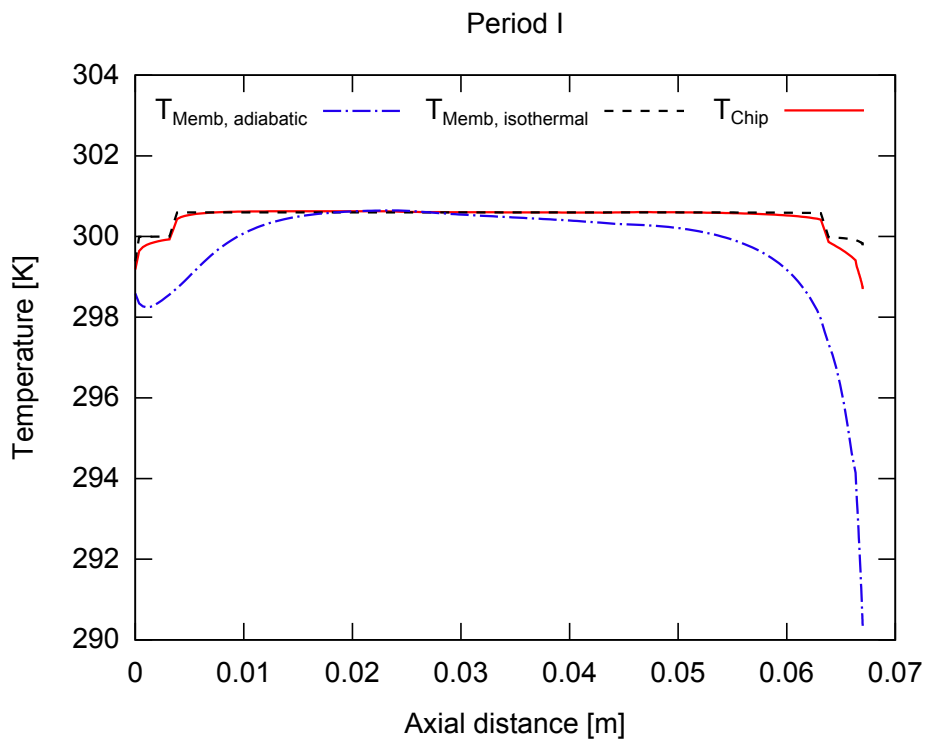


Figure 6.11.: Comparison of the axial temperature distributions along the chip and the membrane (in the isothermal and adiabatic cases) relative to the first set of boundary conditions listed in Tab. 6.5.

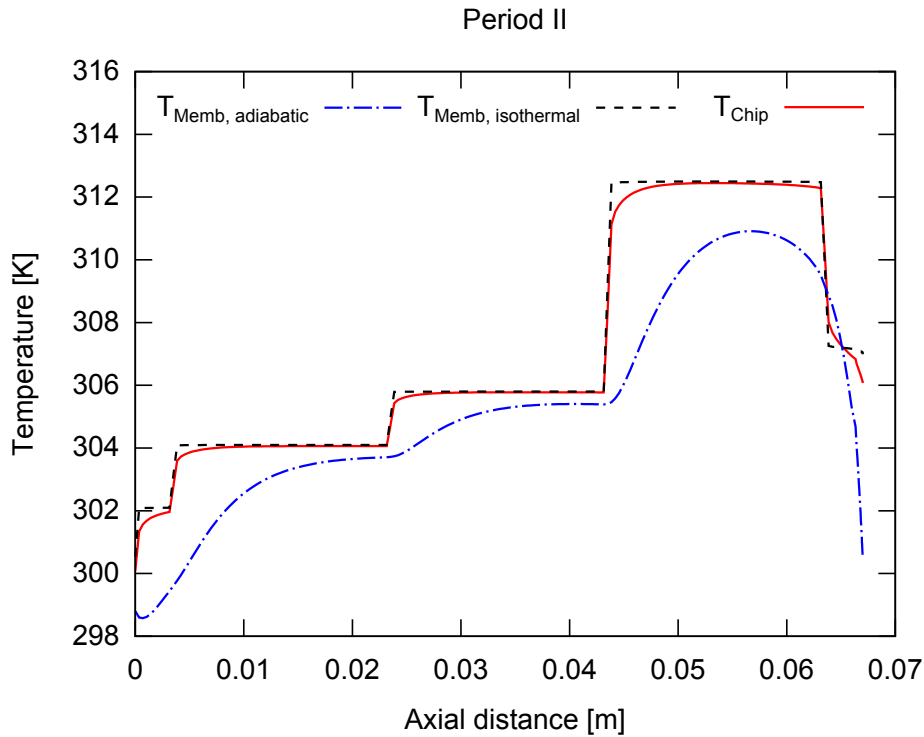


Figure 6.12.: Comparison of the axial temperature distributions along the chip and the membrane (in the isothermal and adiabatic cases) relative to the second set of boundary conditions listed in Tab. 6.5.

In the adiabatic case, the length necessary for the membrane to accommodate to the chip temperature is larger. In particular, when the microchannel is heated, the membrane temperature is always lower than the chip and its temperature profile is not fully developed.

Towards the microchannel exit the gas temperature drastically drops, cooling down the membrane in contact with the gas. This is mainly an effect of the gas acceleration at the microchannel exit, where a localized expansion of the gas takes place (cf. Fig. 6.10).

Figures 6.13 and 6.14 present, for the two analyzed periods, the comparison between the voltage drops measured by the thermopiles and the theoretical temperature differences between the chip and the membranes, calculated from the numerical results. The voltage drops are evaluated with respect to the initial phase of the experiment when no temperature difference was present and the thermopile signal average was zero. The theoretical temperature differences are calculated at the axial position of the thermopiles and for adiabatic membranes.

Since the two signals are of different nature, the comparison can be qualitative only, but it helps understanding whether the real sensor behavior can be predicted by the developed numerical model and how far it is from the ideal conditions. Quantitative comparisons between the numerical model and the experimental results from the calibrated integrated sensors could be useful to fully validate their measuring principle. However, due to their structural fragility, all the manufactured sensor chips broke before completion of the heat transfer test campaign. The manufacturing of a new set of sensors with optimized design to improve the mechanical stability could not be accomplished within the time schedule of the present work, as this would have implied the design of new masks and the modification of the integration layout as well as of the data acquisition system.

For both analyzed periods the temperature and voltage difference trends are comparable. The discrepancies may be explained by considering that the numerical model, apart for the



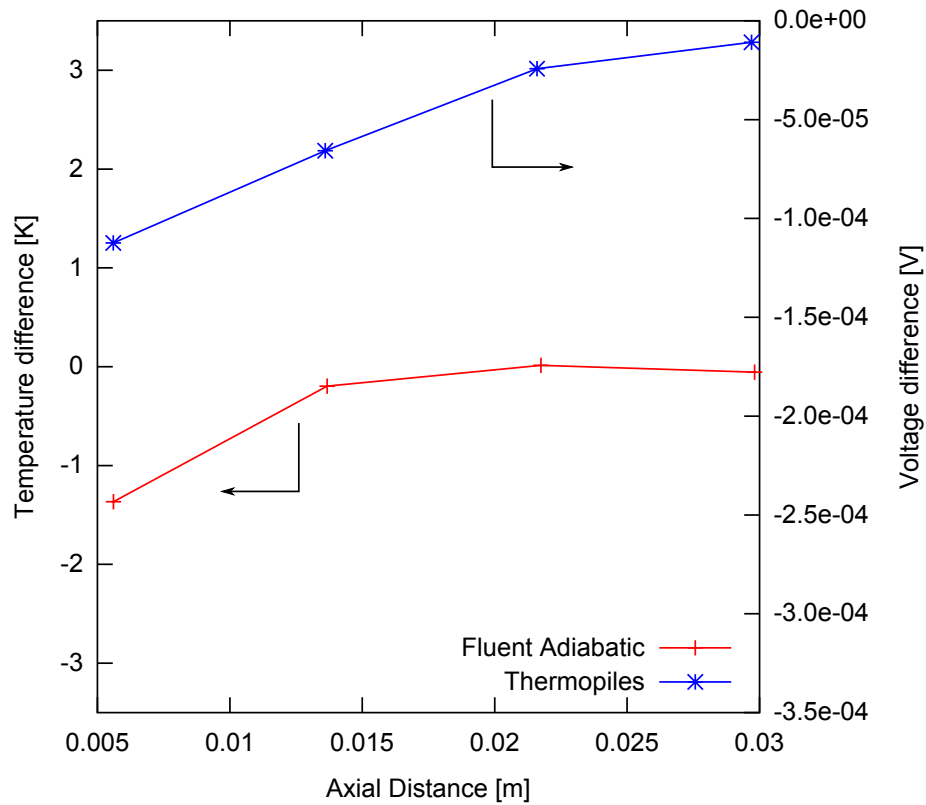


Figure 6.13.: Qualitative comparison between the measured thermopiles voltage differences and the temperature differences calculated at the membrane positions. The data refer to the boundary conditions of Period 1 in Tab. 6.5.

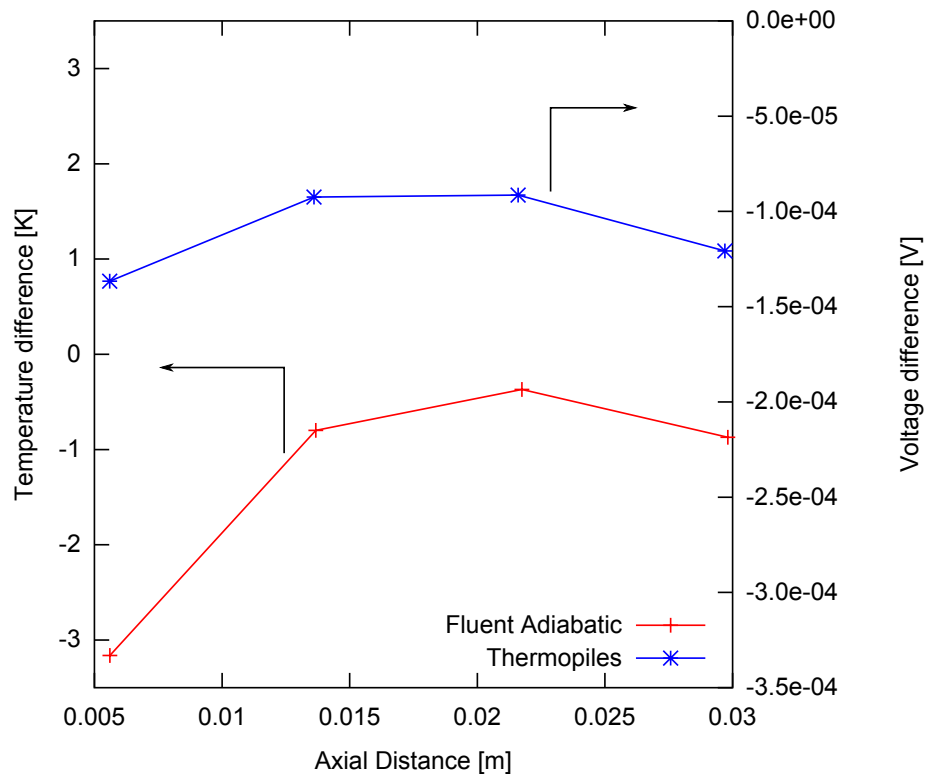


Figure 6.14.: Qualitative comparison between the measured thermopiles voltage differences and the temperature differences calculated at the membrane positions. The data refer to the boundary conditions of Period 2 in Tab. 6.5.

conjugate affect across the imposed material thicknesses, does not take heat losses to the ambient into account. Moreover, despite its low thickness the membrane is not perfectly adiabatic and some heat conduction effects are present.

## 6.5. Microchannel material effects

A set of numerical simulations has been performed to compare the results to the experimental data obtained with the PEEK cover (cf. Sec. 5.4.1). The main goal was to assess whether the numerical model can be used to predict the thermal performance of the microchannels and validate, at the same time, the data obtained from the embedded thermocouples. The material properties imposed on the walls have been varied according to the materials tested during the experimental campaign.

Differently from the membrane simulations, the top wall of the microchannel was now treated as a single layer. The distinction between the 5 different axial sections of the microchannel was kept to take into account the unheated entrance and exit regions. The real thicknesses of both the cover and the microchannel sections have been used to include the axial heat conduction in the calculations.

The imposed boundary conditions have been directly derived from the experiments. These include the inlet and outlet pressures and the inlet and wall temperatures for the different microchannel sections. In particular, the bottom wall temperatures are set as recorded by the reference thermocouples installed below the microchannel section, while the top wall temperatures have been measured with the PEEK cover and an unstructured foil of the same material.

The reference experimental data are the ones presented in Section 5.3.1. In Fig. 6.15- 6.16 the numerical and experimental results for the micromachined stainless steel, copper and PEEK sections are compared. The plots include both the wall and the gas temperature profiles, as recorded with the blind and the micromachined foils, respectively. The data referring to the top wall are the same used as boundary conditions for the simulations. The temperature profiles from the simulation are calculated in the microchannel symmetry plane at different heights, including the top wall ( $y=0.05$ ) and other positions inside the microchannel.

The stainless steel section (Fig. 6.15) shows a flat temperature profile in the central heated area, with temperature steps at the boundaries to the two outer unheated regions. Both experiments and simulations show small differences between the wall and the gas temperatures. The entry regions in the microchannel inlet/outlet and between the heated and unheated areas are relatively short. The best fit between the numerical and experimental data for the gas axial temperature profile occurs between  $y=0.04$  and  $y=0.03$ .

Figure 6.16 presents the results obtained for the copper microchannel section. In this case the axial gradients between the unheated and heated areas are smaller than for stainless steel. This results from a higher axial conduction along the microchannel walls due to the higher conductivity of copper. The experimental points show that, after a short thermal entry length, the wall and the gas temperatures coincide. The calculated profiles show some minor differences with each other, which are however below the thermocouple precision and could not be recorded experimentally. In this case the best fit for the gas temperature between the experimental and numerical data occurs for  $y=0.04$  mm, close to the top wall.

The data for the PEEK section are presented in Fig. 6.17. As a result of the characteristic thermal conductivity of PEEK (about three orders of magnitude smaller than copper and about two smaller than steel), heat conduction both in the vertical and the axial directions is limited. As recorded during the experiments, the internal wall temperature is smaller

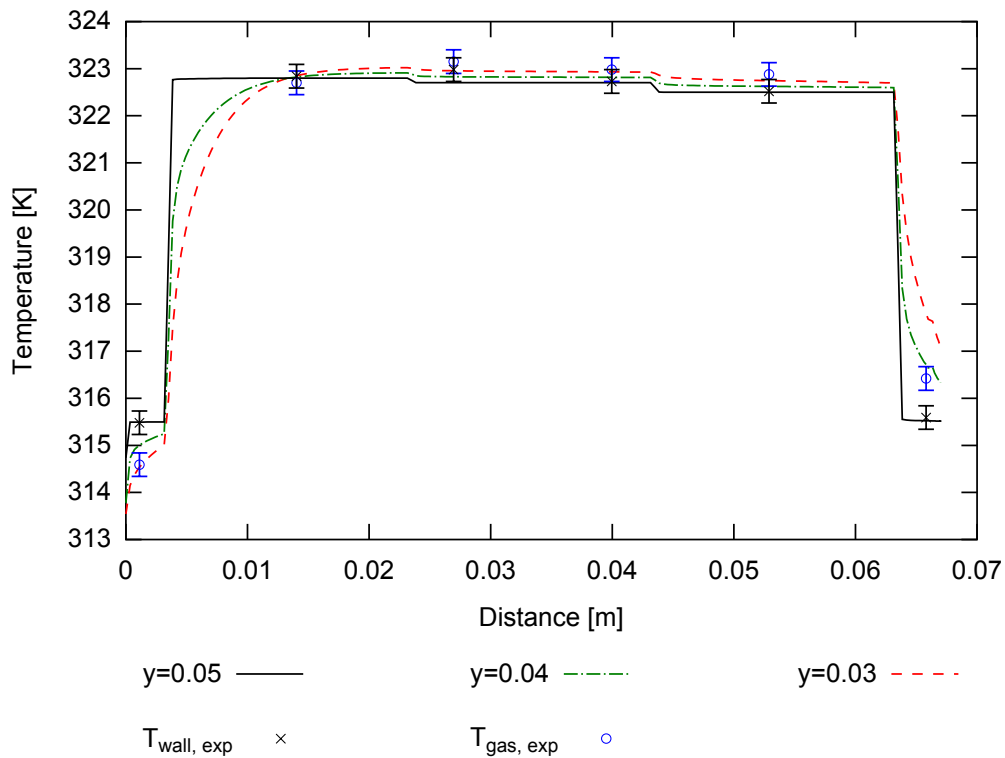


Figure 6.15.: Comparison between the experimental and numerical results for the axial temperature distribution along the machined stainless steel microchannel. The numerical results are plotted for the microchannel wall ( $y=0.05$ ) and for two different channel heights ( $y=0.04$  and  $y=0.03$ ).

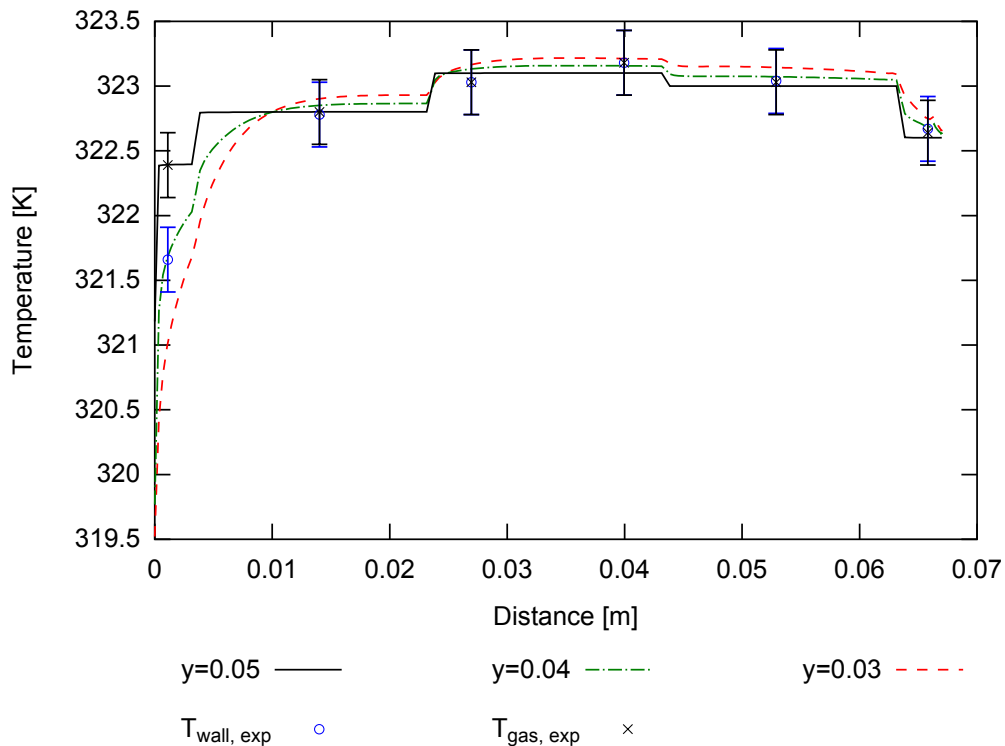


Figure 6.16.: Comparison between the experimental and numerical results for the axial temperature distribution along the machined copper microchannel. The numerical results are plotted for the microchannel wall ( $y=0.05$ ) and for two different channel heights ( $y=0.04$  and  $y=0.03$ ).

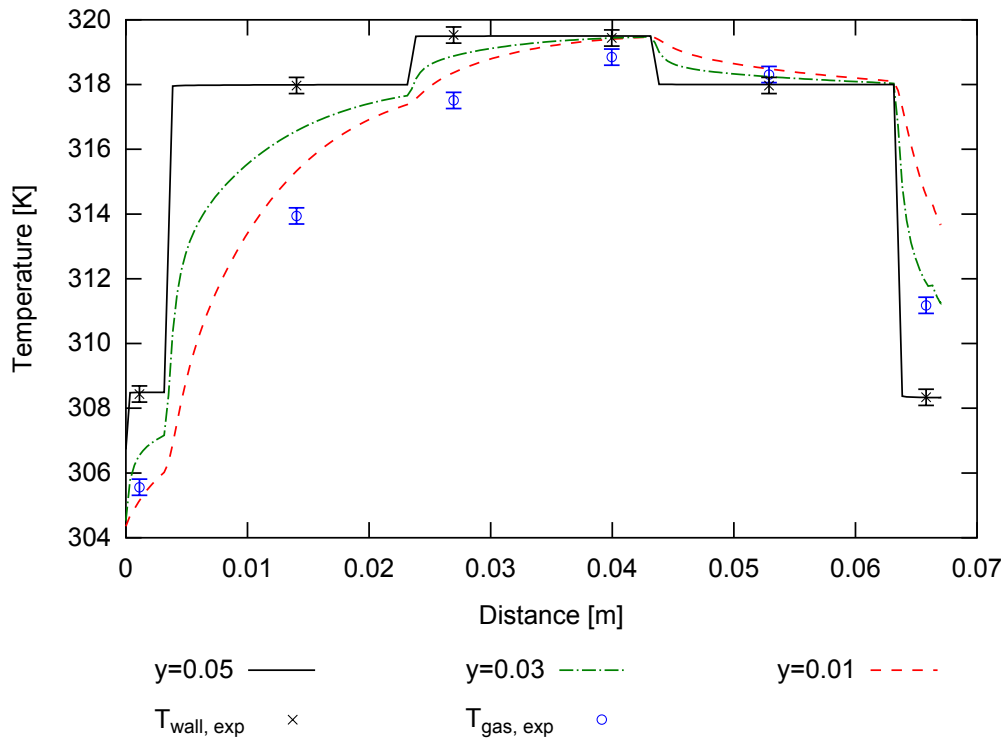


Figure 6.17.: Comparison between the experimental and numerical results for the axial temperature distribution along the machined PEEK microchannel. The numerical results are plotted for the microchannel wall ( $y=0.05$ ) and for two different channel heights ( $y=0.04$  and  $y=0.03$ ).

than in the two previous cases, and the resulting axial wall temperature profile presents large differences between the heated and unheated areas. Both experimental and numerical results show relatively large entry lengths for the gas approaching the wall temperature. The best fitting profile is closer to the microchannel axis and ranging between  $y=0.01$  mm and  $y=0.03$  mm. Contrary to the two previous cases, the experimental results for PEEK are overestimated by the numerical simulation. This can be due to a non optimal choice of the polymer thermal properties for the numerical model (differently from most engineering materials, no standard reference values are available for PEEK).

To compare the results from the different test sections, the experimental and numerical gas temperature profiles for the three microchannel materials are plotted together in Fig. 6.18.

With metallic microchannels, the gas temperature along the heated area is almost constant and uniform (and similar in the two cases), while a developing temperature profile characterizes the PEEK section. Thanks to the good thermal properties, copper is the most suitable material when uniform and flat temperature distributions are desired. On the contrary, PEEK has rather insulating properties, offering poor axial and vertical heat conduction rates. Finally, steel allows the achievement of steep axial gradients, with intermediate values for the thermal conductivity coefficient.

The comparisons between experimental and numerical results showed good qualitative agreement and therefore seem to validate the integration design developed for the commercial sensors. The thermal properties of the microchannel material play a major role in determining the final gas temperature distribution. Provided that the material choice for the design of microstructured devices is mainly driven by practical choices (e.g., the best material withstanding the desired working conditions or offering the best compromise

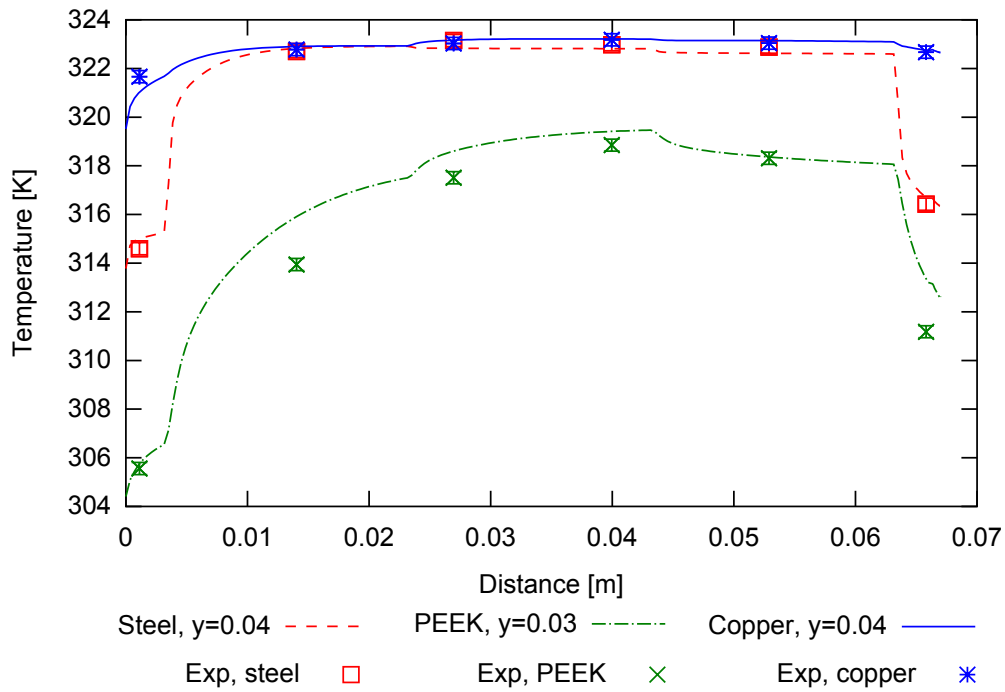


Figure 6.18.: Comparison between the theoretical and experimental temperature profiles for the different microchannel materials.

between durability and costs), the considerations mentioned above might be very useful when dealing with fundamental studies in microchannels. If, e.g., processes under uniform temperature boundary conditions are to be studied, metals with a high conductivity such as copper are the best choice. On the contrary, when thermal transients are to be investigated, polymers such as PEEK should be preferred.



## 7. Conclusions and Outlook

### 7.1. Conclusions

This work addresses the issue of local flow characterization in microstructures by proposing two integrated sensors designs and a novel experimental device for heat transfer studies in microchannels. The main goal was to take advantage of local measurements techniques to investigate the effects of the microchannel material and surface characteristics on the heat transfer of gases at different flow regimes (spanning from the continuum to the early transition regime). Many open issues still present for gaseous microflows could indeed benefit from the implementation of local measuring systems.

The two proposed configurations include a MEMS-based microsensor system, prepared with silicon microfabrication technologies, and a set of commercial thermocouples arranged on a PEEK substrate. Both designs are integrated as microchannel cover and top wall. The experimental device allows an easy exchange of the test sections while the measuring system is fixed. This represents a novelty in the field of micro-integrated systems, since the designs proposed so far are usually limited to few specific materials and do not present many degree of freedom concerning the flexibility of applications.

The first part of the experimental work has been concentrated on the design, implementation and characterization of the two measuring systems. This included the calibration of the MEMS-based microsensors and the assessment of the proper functioning for the thermocouples integration system.

The commercial thermoelements are embedded into a PEEK support, which covers the microchannel. This grants a minimal flow disturbance but spoils the overall sensor sensitivity due to the additional thermal inertia of the material surrounding the sensing elements. For this reason the range of boundary conditions for which the system can be employed is limited to relatively high mass flow rates and temperature levels. This excludes, e.g., the possibility of studying flows under rarefied conditions as it was intended.

The employment of custom-made silicon microsensors requires the definition of appropriate calibration procedures. The proposed layout includes two kind of sensors: resistance temperature detectors (RTD) for the monitoring of the top wall temperature, and thermopiles with a closed membrane configuration to record the temperature difference between the wall and the gas flowing close to the wall.

The calibration of the RTDs was performed by employing external absolute temperature references. Particular attention should be paid in choosing the proper references to as-

sess the actual boundary conditions of the experimental system. A direct calibration for the thermopiles was not possible, since the reference temperature differences cannot be imposed or measured simultaneously. A comparative method employing the integrated commercial sensors in a reference test sequence was demonstrated to be a possible approach to solve the issue. In this case, the calibration must be carried out under working conditions suitable for the commercial sensors. However, the thermopiles showed good resolutions also for relatively small flow rates and temperature differences. Moreover, the MEMS-based measuring system ensures very short response times (no detectable delay even for the maximum data acquisition rate) and a small thermal inertia compared to the conventional thermocouple systems. The main drawback of the integrated silicon sensor design is related to the fragility of the assembly. The overall dimensions of the silicon substrate lead to frequent mechanical failures of the chip during the installation of the assembly or during the operation (if pressure and thermal stresses occur along the chip). This issue made the implementation of the sensors a challenging task. Proper integration solution and limits for the device working conditions had to be defined, in order to assure the mechanical and thermal stability of the sensor assembly. The unanticipated complexity of the integrated sensor system employment did not allow for a systematic analysis in the rarefied flow regime. Nonetheless, differently from the PEEK system, the miniaturized silicon sensors proved to be suitable to be employed within these conditions, too.

Finally, the PEEK cover system was also employed to study the effects of the microchannel material and surface characteristics on the microchannels thermal behavior. For this purpose different materials and micromanufacturing techniques were employed, resulting in different surface characteristics for the microchannel walls. The experimental campaign was performed under laminar and continuum flow regime. The results showed that the main features determining the microchannel thermal behavior are the thermal properties of the material itself. By modifying the surface roughness of the microchannel no detectable differences in the heat transfer behavior could be found. However, this might not hold for other flow regimes, e.g. under rarefied conditions.

In addition to the experimental campaign, a numerical model has been developed to perform CFD simulations of the microchannel-sensor assembly. Two different types of boundary conditions for the thin membranes containing the thermopiles have been implemented corresponding to an isothermal and an adiabatic case, respectively. The last situation corresponds to an ideal case of perfectly insulated membrane which would ensure the best sensitivities to record the inner gas temperatures. By comparing the numerical results with the experimental data it was found that the real behavior of the membranes is intermediate between the two opposite models, but closer to the adiabatic case. This confirms that the developed system allows the measuring of the internal gas temperature, although some heat losses are unavoidable.

The experimental data for the different tested microchannel sections have been employed for comparison with the numerical model. In this case the presence of the membrane has been neglected, since the data were recorded with the commercial thermocouples. The reproducibility of the experimental data has validated the employed numerical model. At the same time it has confirmed the major differences between the thermal behavior of the different microchannel materials. The numerical tool can be very useful in supporting fundamental studies on heat transfer in microchannel and predict their performances.

As a final remark it must be highlighted that the proposed integrated measuring systems have proved the possibility of accessing local information in microchannels, overcoming the material limitations of previously proposed configurations. Despite their simpler layout, conventional sensors showed some sensitivity issues, whereas silicon miniaturized sensors offers better performances in terms of time response and signal resolution. The possibility



of a local characterization of gas flows in microchannels has been proved, too.

## 7.2. Outlook

The main limitation of the two proposed integrated measuring systems concerns the allowable working conditions, due to either sensitivity issues or fragility problems. In the first case no practical solution is foreseen, since the system is based on commercial sensors. On the contrary some efforts should be done for the optimization of the silicon microsensors design. This would allow the broadening of the allowable working conditions, increasing the possible applications, too.

Improvement seems possible with a new design with smaller sensing units. Smaller chips would be less subject to bending fractures and could stand higher mechanical stresses. The new chips could be integrated in substrates of different materials (metal or polymer) without requiring large silicon areas (which results in brittle structures). By reducing the mechanical stress, it would also be possible to increase the working temperatures, up to the sensor material limits.

Another foreseen continuation of the present work concerns the study of gaseous flows which should be extended to different regimes, including rarefied gases. In this case the heat transfer behavior is likely to be influenced not only by the microchannel material, but also by the surface microscale characteristics. One interesting aspect to be analyzed for gas flows under rarefied conditions, is the possibility with the proposed integrated sensors system of detecting and quantifying the temperature jump at the wall. In continuum regime a temperature difference can be detected only along the thermal entry region (where the temperature profile is not fully developed), while in slip flow regime a temperature difference exists also in the fully developed flow region. The possibility of measuring this quantity would be of advantage, e.g., for an indirect evaluation of the thermal accommodation coefficient and its dependence on the microchannel material.

Besides research activities, many other fields could benefit of fully integrated MEMS devices. The developed integrated measuring system is indeed not suitable for gas flow studies only. The main advantage of the proposed design is the flexibility of applications, which allows its employment in a variety of situations, other than the one presented in this work. To demonstrate the potential of integrated MEMS technologies, new prototype designs with integrated sensors and microstructured devices should be developed for the monitoring of some representative technical processes. In the micro process engineering and microfluidic fields the employment of such system would allow to switch from off-line to in-line monitoring and control, speeding up the processes and enhancing their overall efficiencies.

The proposed integration technique could also be suitable for other kind of sensors, i.e. pressure transducers, flow sensors, gas detectors, PH detectors, etc.. Future researches in this field should be aimed at the integration of multiple sensing units into one single system, for the simultaneous characterization of different process quality parameters.

The CFD numerical model could also be further developed and improved to include some characteristic complexities of the real system (e.g. heat conduction and heat losses across the membrane and the sensors) and reduce the idealizations of the model developed so far. By comparing the simulation findings with the experimental data, a better understanding of the system and its performances could be achieved.



# Bibliography

- [1] M. Gad-el-Hak, "The fluid mechanics of microdevices," *J. Fluids Eng.*, vol. 121, pp. 5–33, 1999.
- [2] M. Madou, *Fundamentals of Microfabrication*. Boca Raton, FL: CRC Press, 1997.
- [3] S. C. Terry, J. H. Jerman, and J.-B. Angeli, "A gas chromatographic air analyzer fabricated on a silicon wafer," *IEEE Trans. Electron Devices*, vol. 26, no. 12, pp. 1880–1886, 1979.
- [4] E. Bassous, H. Taub, and L. Kuhn, "Ink jet printing nozzle arrays etched in silicon," *Appl. Phys. Lett.*, vol. 31, no. 2, pp. 135–137, 1977.
- [5] M. Mehregany, K. J. Gabriel, and W. S. N. Trimmer, "Integrated fabrication of polysilicon mechanisms," *IEEE Trans. Electron Devices*, vol. 45, no. 6, pp. 719–723, 1988.
- [6] I. Amato, "Fomenting a revolution in miniature," *Science*, vol. 282, no. 5388, pp. 402–405, 1998.
- [7] P. Gravesen, J. Branebjerg, and O. S. Jensen, "Microfluidics - a review," *J. Micromech. Microeng.*, vol. 3, pp. 168–182, 1993.
- [8] C. M. Ho and Y. C. Tai, "Micro-electro-mechanical systems (MEMS) and fluid flows," *Annu. Rev. Fluid. Mech.*, vol. 30, pp. 579–612, 1998.
- [9] T. Hsu, *MEMS and Microsystems. Design Manufacture and Nanoscale Engineering*. Hoboken, NJ: John Wiley & Sons, Inc., 2008.
- [10] G. Morini, "Single-phase convective heat transfer in microchannels: a review of experimental results," *Int. J. Therm. Sci.*, vol. 43, no. 7, pp. 631–651, 2004.
- [11] A. A. Rostami, A. S. Mujumdar, and N. Saniei, "Flow and heat transfer for gas flowing in microchannels: a review," *Heat Mass Transfer*, vol. 38, no. 4-5, pp. 359–367, 2002.
- [12] S. Colin, "Gas microflows in the slip flow regime: a critical review on convective heat transfer," *J. Heat Transfer*, vol. 134, no. 020908, 2012.
- [13] J. Liu and Y. C. Tai, "MEMS for pressure distribution studies of gaseous flows in microchannels," in *Proc. of IEEE Conference on Micro Electro Mechanical Systems*, Amsterdam, The Netherlands, Feb. 1995, pp. 209–215.
- [14] M. J. Kohl, S. I. Abdel-Khalik, S. M. Jeter, and D. L. Sadowski, "An experimental investigation of microchannel flow with internal pressure measurements," *Int. J. Heat Mass Transfer*, vol. 48, no. 8, pp. 1518–1533, 2005.
- [15] S. E. Turner, L. C. Lam, M. Faghri, and O. J. Gregory, "Experimental investigation of gas flow in microchannels," *J. Heat Transfer*, vol. 126, no. 5, pp. 753–763, 2004.

- 
- [16] E. B. Arkilic, "Measurement of the mass flow and tangential momentum accommodation coefficient in silicon micromachined channels," Ph.D. dissertation, Fluid Dynamics Research Laboratory Department of Aeronautics and Astronautics, Massachusetts Institute of Technology, Cambridge, MA, 1997.
- [17] S. Colin, P. Lalonde, and R. Caen, "Validation of a second-order slip flow model in rectangular microchannels," *Heat Transfer Engineering*, vol. 25, no. 3, pp. 23–30, 2004.
- [18] S. B. Choi, R. F. Barron, and R. O. Warrington, "Fluid flow and heat transfer in microtubes," in *Micromechanical Sensors, Actuat. Syst.*, vol. DSC-32. New York: ASME, 1991, pp. 123–134.
- [19] J. Pfahler, J. Harley, H. Bau, and J. Zemel, "Gas and liquid flow in small channels," vol. DSC-32, pp. 49–60, 1991.
- [20] P. Wu and W. A. Little, "Measurement of friction factors for the flow of gases in very fine channels used for microminiature joule-thomson refrigerators," *Cryogenics*, vol. 23, no. 5, pp. 273–277, 1983.
- [21] D. Yu, R. O. Warrington, R. F. Barron, and T. A. Ameel, "An experimental and theoretical investigation of fluid flow and heat transfer in microtubes," in *Proc. of ASME/JSME Thermal Engineering Joint Conference*, Maui, HI, March 1995, pp. 520–530.
- [22] R. K. Shah and A. L. London, *Laminar flow forced convection in ducts*. New York: Academic Press, 1978.
- [23] Z. Y. Guo and Z. X. Li, "Size effects on single-phase channel flow and heat transfer at microscale," *Int. J. Heat Fluid Flow*, vol. 24, pp. 284–298, 2003.
- [24] G. L. Morini, "Scaling effects for liquid flows in microchannels," *Heat Transfer Engineering*, vol. 27, no. 4, pp. 64–73, 2006.
- [25] G. L. Morini, M. Lorenzini, S. Salvigni, and G. P. Celata, "Experimental analysis of micro-convective heat transfer in the transition region," in *Proc. of the 1st European Conference on Microfluidics*, no.  $\mu$ -FLU08-102, Bologna, Italy, Dec. 2008.
- [26] Z. Y. Guo and X. B. Wu, "Compressibility effects on the gas flow heat transfer in a microtube," *Int. J. Heat Mass Transfer*, vol. 40, no. 13, pp. 3251–3254, 1997.
- [27] Z. Guo and X. B. Wu, "Further study on compressibility effects on the gas flow and heat transfer in a microtube," *Microscale Thermophys. Eng.*, vol. 2, no. 2, pp. 111–120, 1998.
- [28] G. L. Morini, M. Lorenzini, and S. Salvigni, "Friction characteristics of compressible gas flows in microtubes," *Exp. Therm Fluid Sci.*, vol. 30, pp. 733–744, 2006.
- [29] G. H. Tang, Z. Li, Y. L. He, and W. Q. Tao, "Experimental study of compressibility, roughness and rarefaction influences on microchannel flow," *Int. J. Heat Mass Transfer*, vol. 50, pp. 2282–2295, 2007.
- [30] G. P. Celata, M. Cumo, and G. Zummo, "Thermal-hydraulic characteristics of single phase flow in capillary tubes," in *Proc. of the International Symposium on Compact Heat Exchangers*, Grenoble, France, Aug. 2002.
- [31] M. Elwenspoek, "Thermal flow microsensors," in *Proc. of the IEEE International Semiconductor Conference*, Sinaia, Romania, October 1999.
- [32] B. van Oudheusden, "Integrated silicon slow sensors," Ph.D. dissertation, TU Delft, The Netherlands, November 1989.

- [33] M. A. Schmidt, R. T. Howe, S. D. Senturia, and J. H. Haritonidis, "Design and calibration of a microfabricated floating-element shear-stress sensor," *IEEE Trans. Electr. Devices*, vol. 35, pp. 750–757, 1988.
- [34] L. N. Krause and G. C. Fralick, "Miniature drag force anemometer," NASA, Tech. Rep. TM-X3507, 1977.
- [35] O. Tabata, H. Inagaki, and I. Igarashi, "Monolithic pressure-flow sensor," *IEEE Trans. Electr. Devices*, vol. 34, no. 12, pp. 2456–2462, 1987.
- [36] A. van Herwaarden, D. van Duyn, B. van Oudheusden, and P. Sarro, "Integrated thermopile sensors," *Sens. Actuators, A*, vol. 22, pp. 621–630, 1989.
- [37] S. Wu, J. Mai, Y. Zohar, Y. Tai, and C. Ho, "A suspended microchannel with integrated temperature sensors for high pressure flow studies," in *Proc. of the 11th International Workshop on Micro Electro Mechanical Systems*, Piscataway, NJ, 1998, pp. 87–92.
- [38] H. Park, J. J. Pak, S. Y. Son, G. Lim, and I. Song, "Fabrication of a microchannel integrated with inner sensors and the analysis of its laminar flow characteristics," *Sens. Actuators, A*, vol. 103, p. 317, 2003.
- [39] Z. Xue and H. Qiu, "Integrating micromachined fast response temperature sensor array in a glass microchannel," *Sens. Actuators, A*, vol. 122, pp. 189–195, 2005.
- [40] C. W. Liu, C. Gau, H. S. Ko, C. S. Yang, and B. T. Dai, "Fabrication challenges for a complicated micro-flow channel system at low temperature process," *Sens. Actuators, A*, vol. 131, pp. 575–582, 2006.
- [41] H. Ko, C. W. Liu, and C. G. C. S. Yang, "Fabrication and design of a heat transfer micro-channel system by a low temperature mems technique," *J. Micromech. Microeng.*, vol. 17, pp. 983–993, 2007.
- [42] Y. Yang, G. L. Morini, H. Chalabi, and M. Lorenzini, "Experimental Nusselt number determination for gas flows through commercial microtubes," in *Proceedings of the 3rd International GASMEMS Workshop*, no. 21, Bertinoro, Italy, June 2011.
- [43] J. J. Brandner, T. Gietzelt, T. Henning, M. Kraut, H. Mortiz, and W. Pflöging, "Microfabrication in metals and polymers," in *Micro Process Engineering: Fundamentals, Devices, Fabrication and Applications*, N. Kockmann ed. Weinheim, Germany: WILEY-VHC, 2006, ch. 10.
- [44] F. Goldschmidtböing, M. Engler, and A. Doll, "Silicon microfabrication for microfluidics," in *Micro Process Engineering: Fundamentals, Devices, Fabrication and Applications*, N. Kockmann ed. Weinheim, Germany: WILEY-VHC, 2006, ch. 11.
- [45] D. Resnik, D. Vrtacnik, U. Aljancic, M. Mozek, and S. Amon, "Different aspect ratio pyramid tips obtained by wet etching of (100) and (111) silicon," *Microelectron. J.*, vol. 34, pp. 591–593, 2003.
- [46] G. T. A. Kovacs, N. I. Maluf, and K. E. Petersen, "Bulk micromachining of silicon," in *Proc. of the IEEE*, vol. 86, no. 8, 1998.
- [47] M. J. Madou, "MEMS fabrication," in *The MEMS Handbook*, M. Gad-el-Hak, Ed. Boca Raton, FL: CRC Press, 2002, ch. 16.
- [48] C. Khan-Malek, "Polymer and glass manufacturing," in *GASMEMS 2nd Summer School*, Les-Embiez, France, 2010.

- 
- [49] “Microfluidics and bio polymer microcomponents,” *The Yole Développement magazine for MEMS, Nanotechnology, Optics, Bio & Microfluidic Chips and Semiconductors*, no. 29, pp. 4–5, October 2004.
- [50] A. C. Liou and R. Chen, “Injection molding of polymer micro- and sub-micron-structures with high aspect ratios,” *Int. J. Advanced Manufacturing Technology*, vol. 28, no. 11-12, pp. 1097–1103, 2006.
- [51] M. Worgull, *Hot Embossing: Theory and Technology of Microreplications*, Oxford, UK, 2009.
- [52] R. Knitter and T. Dietrich, “Microfabrication in ceramics and glass,” in *Micro Process Engineering: Fundamentals, Devices, Fabrication and Applications*, N. Kockmann ed. Weinheim, Germany: WILEY-VHC, 2006, ch. 12.
- [53] J. J. Brandner, “Manufacturing techniques for microstructures - an overview,” in *GASMEMS 2nd Summer School*, Les-Embiez, France, 2010.
- [54] M. Madou, “LIGA and other replication techniques,” in *The MEMS Handbook*, M. Gad-el-Hak, Ed. Boca Raton, FL: CRC Press, 2002, ch. 17.
- [55] E. W. Backer, W. Ehrfeld, D. Münchmeyer, H. Betz, A. Heuberger, S. Pongratz, W. Glashauser, H. J. Michel, and R. Siemens, “Production of separation-nozzle system for uranium enrichment by a combination of x-ray lithography and galvanoplastics,” *Naturwissenschaften*, vol. 69, no. 11, pp. 520–523, 1982.
- [56] V. Haverkamp, W. Ehrfeld, K. Gebauer, V. Hessel, H. Löwe, T. Richter, and C. Wille, “The potential of micromixers for contacting of disperse liquid phases,” *Fresenius Journal of Analytical Chemistry*, vol. 364, pp. 617–624, 1999.
- [57] W. Heywang, *Sensorik*. Berlin-Heidelberg-New York- Tokio: Springer-Verlag, 1984.
- [58] H. Schaumburg, *Sensoren*. Stuttgart: Teubner, 1992.
- [59] C. Liu, *Foundations of MEMS*. Upper Saddke River, New Jersey: Pearson Prentice Hall, 2006.
- [60] S. Sugiyama, M. Takigawa, and I. Igarashi, “Integrated piezoresistive pressure sensor with both voltage and frequency output,” *Sens. Actuators A*, vol. 4, pp. 113–120, 1983.
- [61] G. T. A. Kovacs, *Micromachined Transducers Sourcebook*. New York: McGraw-Hill, 1998.
- [62] X. Fan, I. M. White, S. I. Shopova, H. Zhu, J. D. Suter, and Y. Sun, “Sensitive optical biosensors for unlabeled targets: a review,” *Analytica Chimica Acta*, no. 6200, pp. 8–26, 2008.
- [63] F. S. Ligler and C. A. R. Taitt, Eds., *Optical Biosensors - Present and Future*. Amsterdam, The Netherlands: Elsevier, 2002.
- [64] S. Colin, “Single-phase gas flow in microchannels,” in *Heat Transfer and fluid flow in minichannels and microchannels*, S. Kandlikar, Ed. Elsevier, 2006, ch. 2.
- [65] K. Koura and H. Matsumoto, “Variable soft sphere molecular model for inverse-power-law or lennard-jones potential,” *Physics of Fluids A*, vol. 3, no. 10, pp. 2459 – 2465, 1991.
- [66] E. H. Kennard, *Kinetic theory of gases*. New York: McGraw-Hill, 1938.
- [67] F. Sharipov and V. Seleznev, “Data on internal rarefied gas flows,” *J. Phys. Chem. Ref. Data*, vol. 27, no. 3, pp. 657–706, 1998.

- [68] S. Chapman and T. Cowling, *The mathematical theory of non-uniform gases*. London, UK: Cambridge University Press, 1988.
- [69] G. A. Bird, *Molecular gas dynamics and the direct simulation of gas flows*. Oxford, UK: Clarendon Press, 1994.
- [70] M. Gad-el-Hak, "Flow physics," in *The MEMS Handbook*, M. Gad-el-Hak, Ed. Boca Raton, FL: CRC Press, 2002, ch. 4.
- [71] J. Maxwell, "On stresses in rarefied gases arising from inequalities of temperature," *Trans. R. Soc. Part I*, vol. 170, pp. 231–256, 1879.
- [72] L. B. Thomas and R. G. Lord, "Comparative measurements of tangential momentum and thermal accommodations on polished and on roughened steel spheres," in *Rarefied gas dynamics*, K. Karamcheti, Ed. New York: Academic Press, 1974, vol. 8.
- [73] B. T. Porodnov, P. E. Suetin, S. F. Borisov, and V. D. Akinshin, "Experimental investigation of rarefied gas flow in different channels," *J. Fluid Mech.*, vol. 64, pp. 417–437, 1974.
- [74] E. B. Arkilic, K. S. Breuer, and M. A. Schmidt, "Mass flow and tangential momentum accommodation in silicon micromachined channels," *J. Fluid Mech.*, vol. 437, pp. 29–43, 2001.
- [75] M. Smoluchowski, "Über Wärmeleitung in verdünnten Gasen," *Annalen der Physik und Chemie*, vol. 64, pp. 101–130, 1898.
- [76] J. Pitakarnnop, "Analyse expérimentale et simulation numérique d'écoulements raréfiés de gaz simples et de mélanges gazeux dans les microcanaux," Ph.D. dissertation, École doctorale Mécanique, Énergétique, Génie civil et Procédés Unité de recherche : Laboratoire de Génie Mécanique de Toulouse, 2009.
- [77] S. V. Gaastra-Nedea, A. J. Markvoort, A. J. H. Frijns, A. A. van Steenhoven, and P. Hilbers, "Hybrid method coupling molecular dynamics and monte carlo simulations to study the properties of gases in micro and nanochannels," *Phys. Rev. E*, vol. 72, no. 016705, 2005.
- [78] A. J. H. Frijns, S. V. Gastra-Nedea, A. J. Markvoort, A. A. van Steenhoven, and P. Hilbers, "Molecular dynamics and monte carlo simulations for heat transfer in micro- and nanochannels," *Int. J. Multiscale Comp. Eng.*, vol. 4, no. 3, pp. 391–397, 2006.
- [79] L. Boltzmann, *Lectures on gas theory*. London, UK: Cambridge University Press, 1964.
- [80] C. Cercignani, *The Boltzmann equation and its applications*. Berlin: Springer-Verlag, 1988.
- [81] G. E. Karniadakis and A. Beskok, *Microflows: fundamentals and simulation*. New York: Springer-Verlag, 2002.
- [82] S. Maikowske, "A novel device for the optical investigation of phase transition in micro channel array evaporators," *Appl. Therm. Eng.*, vol. 30, no. 13, pp. 1872–1876, 2010.
- [83] A. van Herwaarden and P. Sarro, "Floating-membrane thermal vacuum sensor," *Sens. Actuators*, vol. 14, pp. 259–268, 1988.
- [84] D. Moser, R. Lenggenhager, and H. Baltes, "Silicon gas flow sensors using industrial cmos and bipolar ic technology," *Sens. Actuators*, vol. A21-A23, pp. 1019–1022, 1990.

- 
- [85] A. Schaufelbuhl, N. Schneeberger, U. Munch, M. Waelti, O. Paul, O. Brand, H. Baltes, C. Menolfi, Q. Huang, and E. Doering, “Uncooled low-cost thermal imager based on micromachined cmos integrated sensor array,” *IEEE J. Microelectromechanical Systems*, vol. 10, no. 40, pp. 503–510, 2001.
- [86] S. Kisban, J. Kenntner, P. Janssen, R. Metzen, S. Herwik, U. Bartsch, T. Stieglitz, O. Paul, and P. Ruther, “A novel assembly method for silicon-based neural devices,” in *Proc. of World Congress on Medical Physics and Biomedical Engineering*.
- [87] G. Hamacher, “Helium leak test of fuel systems in mass production,” in *Proc. of TankTech 2003*, Fruestenfeldbruck bei Muenchen, Nov. 2003.
- [88] H. Darcy, *Recherches experimentales relative au mouvement de l’Eau dan le Tuyaux*, Maller-Bachelier, Ed., Paris, 1857.
- [89] J. T. Fanning, *A practical treatise on hydraulic and water supply engineering*, V. Nosstrand, Ed., New York, 1877.
- [90] J. Nikuradse, “Stromungsgesetze in rauhen rohren,” *VDI-Forschungsheft*, vol. 361, 1933.
- [91] J. B. Taylor, A. L. Cerrano, and S. G. Kandlikar, “Characterization of the effect of surface roughness and texture on fluid flow - past, present and future,” *Interantional Journal of Thermal Sciences*, vol. 45, pp. 962–968, 2006.
- [92] T. V. Vorburger and J. Raja, “Surface finish metrology tutorial,” National Institute of Standards and Technology, Tech. Rep. NISTIR 89-4088, 1990.
- [93] D. Whitehouse, “Improved type of wave filter for use in surface finish measurement,” in *Proc. Inst. Mech. Engrs.*, vol. 182, no. 3k, 1967, p. 306.
- [94] *DIN EN ISO 4287/A1 - Geometrical Product Specifications (GPS) - Surface texture: Profile method - Terms, definitions and surface texture parameters*.
- [95] T. Vorburger, J. dagata, G. Wilkening, and K. Iizuka, “Characterization of surface topography,” in *Beam Effects, Surface Topography, and Depth Profiling in Surface Analysis - Methods of Surface Characterization*, A. Czanderna, T. Madey, and C. Powell, Eds. Springer US, 2002, vol. 5, pp. 275–354.
- [96] A. Calvimontes, “Topographic characterization of polymer materials at different length scales and the mechanistic understanding of wetting phenomena,” Ph.D. dissertation, Technischen Universität Dresden, 2009.
- [97] *Geometrical Product Specifications (GPS). Surface texture: profile method - rules and procedures for the assessment of surface texture*, ISO Standard Std. ISO 4288, 1998.
- [98] R. J. Moffat, “Describing the uncertainties in experimental results,” *Exp. Therm. Fluid Sci.*, vol. 1, pp. 3–17, 1988.
- [99] *ANSYS Fluent 6.2 User Guide*, Fluent Inc., Centerra Resource Park, 10 Cavendish Court, Lebanon, NH 03766, USA, 2005.
- [100] *ANSYS Fluent 12.0 Theory Guide*, Fluent Inc., Centerra Resource Park, 10 Cavendish Court, Lebanon, NH 03766, USA, 2009.
- [101] W. A. Erbert and E. Sparrow, “Slip flow in rectangular and annular ducts,” *Journal of Basic Engineering*, vol. 87, pp. 1018–1024, 1965.
- [102] R. G. Deissler, “An analysis of second-order slip flow and temperature jump boundary conditions for rarefied gases,” *Int. J. Heat Mass Transfer*, vol. 7, pp. 681–694, 1964.



# Appendix

## A. Test-rig Specifications

The list of measuring systems and control devices employed for the experimental test rig described in Section 4.4 is given in Tab. A.1. The accuracies corresponding to the different instruments are listed in Tab. A.2.

Table A.1.: List of the test-rig parts and instruments.

Part	Manufacturer	Ref. No.	Description/Notes
Mass flow Controller	BROOKS	SLA5850	Different mass flow ranges available
Control unit	Westphal	WMR4008	Display and data acquisition for the mass flow controller
Pressure sensors	BD Sensors	DMP331	Pressure ranges 0-1 bar; 0-200 mbar
Pressure sensors	Pfeiffer Vacuum	CMR 263	Pressure range 0-10 mbar
Thermocouples	Conatex	T5	NiCr-Ni (Type K) thermoelements
Pump	Edwards	A37132919	Two stage oil sealed rotary vane pump
Acquisition modules	National Instruments	FP-TC-120	8-Channels thermocouple input
Acquisition modules	National Instruments	FP-RTD-124	8-Channels resistance input
Acquisition modules	National Instruments	FP-AI-110	8-Channels analog input

Table A.2.: Accuracies of the different instruments as given by vendors.

---

<b>Instrument</b>	<b>Accuracy</b>
Mass flow Controller	$\pm 0.1$ % Full Scale
Pressure sensors BD	$\leq 0.1$ % reading
Pressure sensors Pfeiffer Vacuum	0.2 % reading
Thermocouples	$\pm 0.25$ K
FP-TC-120	$\pm 0.15$ K
FP-RTD-124	0.03 $\Omega$ offset, 0.06 % gain
FP-AI-110	$\pm 0.5$ % reading

---

## B. Material properties for the CFD simulations

The material properties employed for the simulations described in Chapter 6 are listed in the following tables.

### B.1. Isothermal flow analysis simulations

Table B.1.: List of material properties used for the isothermal flow simulations (cf. Sec. 6.2).

<b><math>\mu</math>-channel material</b>		
Steel	Density $\rho$	8030 kg/m <sup>3</sup>
	Specific heat $c_p$	504 J/kg K
	Thermal conductivity $\kappa$	16.27 W/m K
Silicon	Density $\rho$	2.329 kg/m <sup>3</sup>
	Specific heat $c_p$	700 J/kg K
	Thermal conductivity $\kappa$	148 W/m K
<b>Gas</b>		
Air	Density $\rho$	<i>ideal gas law</i>
	Specific heat $c_p$	1006.43 J/kg K
	Thermal conductivity $\kappa$	0.0242 W/m K
	Viscosity $\mu$	$\mu = \mu_0 \left(\frac{T}{T_0}\right)^n$ $\mu_0 = 1,716 \cdot 10^{-5}$ kg/m s, $T_0 = 273.15$ K, $n = 0.76$
	Molecular weight $M$	28.966 kg/kmol
	Thermal Accommodation Coefficient (TAC)	1
	Tangential Momentum Accommodation Coefficient (TMAC)	1

## B.2. Simplified simulations of the membrane behavior

Table B.2.: List of material properties used for the simplified simulation of the membrane behavior (cf. Sec. 6.3).

<b><math>\mu</math>-channel material</b>		
Steel 1.4301	Density $\rho$	7900 kg/m <sup>3</sup>
	Specific heat $c_p$	500 J/kg K
	Thermal conductivity $\kappa$	15 W/m K
Silicon	Density $\rho$	2.329 kg/m <sup>3</sup>
	Specific heat $c_p$	700 J/kg K
	Thermal conductivity $\kappa$	148 W/m K
<b>Gas</b>		
Air	Density $\rho$	<i>ideal gas law</i>
	Specific heat $c_p$	1006.43 J/kg K
	Thermal conductivity $\kappa$	0.0242 W/m K
	Viscosity $\mu$	$\mu = \mu_0 \left(\frac{T}{T_0}\right)^n$ $\mu_0 = 1,716 \cdot 10^{-5}$ kg/m s, $T_0 = 273.15$ K, $n = 0.76$
	Molecular weight $M$	28.966 kg/kmol
	Thermal Accommodation Coefficient (TAC)	1
	Tangential Momentum Accommodation Coefficient (TMAC)	1

### B.3. Full simulations of the membrane behavior

Table B.3.: List of material properties used for the full simulation of the membrane behavior (cf. Sec. 6.4).

<b><math>\mu</math>-channel material</b>		
Steel 1.4301	Density $\rho$	7900 kg/m <sup>3</sup>
	Specific heat $c_p$	500 J/kg K
	Thermal conductivity $\kappa$	15 W/m K
Silicon	Density $\rho$	2.329 kg/m <sup>3</sup>
	Specific heat $c_p$	700 J/kg K
	Thermal conductivity $\kappa$	148 W/m K
<b>Gas</b>		
Nitrogen	Density $\rho$	<i>ideal gas law</i>
	Specific heat $c_p$	$c_p = a + bT + cT^2 + dT^3 + eT^4$ J/kg K a=979.043, b=0.4179639, c=-0.001176279, d=1.674394·10 <sup>-6</sup> , e=-7.256297·10 <sup>-10</sup>
	Thermal conductivity $\kappa$	0.0242 W/m K
	Viscosity $\mu$	$\mu = \mu_0 \left(\frac{T}{T_0}\right)^n$ $\mu_0=1.656\cdot 10^{-5}$ kg/m s, $T_0=273.15$ K, n=0.74
	Molecular weight $M$	28.0134 kg/kmol
	Thermal Accommodation Coefficient (TAC)	1
	Tangential Momentum Accommodation Coefficient (TMAC)	1

---

#### B.4. Microchannel material effects simulations

Table B.4.: List of material properties used for the microchannel material effects simulations (cf. Sec. 6.5).

<b><math>\mu</math>-channel material</b>		
Steel 1.4301	Density $\rho$	7900 kg/m <sup>3</sup>
	Specific heat $c_p$	500 J/kg K
	Thermal conductivity $\kappa$	15 W/m K
Copper	Density $\rho$	8978 kg/m <sup>3</sup>
	Specific heat $c_p$	381 J/kg K
	Thermal conductivity $\kappa$	387.6 W/m K
PEEK	Density $\rho$	1300 kg/m <sup>3</sup>
	Specific heat $c_p$	320 J/kg K
	Thermal conductivity $\kappa$	0.25 W/m K
<b>Gas</b>		
Nitrogen	Density $\rho$	<i>ideal gas law</i>
	Specific heat $c_p$	$c_p = a + bT + cT^2 + dT^3 + eT^4$ J/kg K a=979.043, b=0.4179639, c=-0.001176279, d=1.674394·10 <sup>-6</sup> , e=-7.256297·10 <sup>-10</sup>
	Thermal conductivity $\kappa$	0.0242 W/m K
	Viscosity $\mu$	$\mu = \mu_0 \left(\frac{T}{T_0}\right)^n$ $\mu_0=1.656\cdot 10^{-5}$ kg/m s, $T_0=273.15$ K, n=0.74
	Molecular weight $M$	28.0134 kg/kgmol
	Thermal Accommodation Coefficient (TAC)	1
	Tangential Momentum Accommodation Coefficient (TMAC)	1

# List of Publications

## International Journals

Maikowske, S., Vittoriosi, A., Brandner, J.J., “Optical measurement of evaporation processes using microstructured evaporators”, *Flow Measurement and Instrumentation*, In Press, Accepted Manuscript.

Brandner, J.J., Maikowske, S., Vittoriosi, A., “A new microstructure device for efficient evaporation of liquids”, *International Journal of Thermal Science and Technology*, vol. 7, No. 3, pp. 414-423, 2012.

Vittoriosi, A., Brandner, J.J., Dittmeyer, R., “A sensor-equipped microchannel system for the thermal characterization of rarefied gas flows”, *Experimental Thermal and Fluid Science*, vol. 41, pp. 112-120, 2012.

## National Journals

Brandner, J.J., Hansjosten, E., Maikowske, S., Vittoriosi, A., “Mikrostrukturapparate zur Verdampfung von Flüssigkeiten”, *Chemie Ingenieur Technik*, vol.82, No. 9. pp. 1318, 2010.

## Book Chapters

Vittoriosi, A., Hecht, K., Brandner, J.J., Dittmeyer, R., “Surface characterization for microstructured systems: methods and examples”, in *Jahrbuch Oberflächentechnik*. Bad Saulgau, Germany: Eugen G. Leuze Verlag, submitted manuscript.

## International Conferences - Talks with Proceedings

Vittoriosi, A., Brandner, J.J., “Role and influence of scaling effects on micro gas-flows: a review of results and theory”, in *Proceedings of 1st International GASMEMS Workshop (GASMEMS09)*, Eindhoven, The Netherlands, No. 02, 2009.

Vittoriosi, A., Brandner, J.J., “Optical characterization of microstructured evaporators”, in *Proceedings of Workshop on Microprocess Engineering and Nanotechnology Applications*, Congress-GEO-SIBERIA, Novosibirsk, Russia, pp. 1-10, 2010.

Vittoriosi, A., Brandner, J.J., Dittmeyer, R., “Integrated sensors in MEMS: characterization of roughness effects for rarefied gas flows”, in *Proceedings of 2nd International GASMEMS Workshop (GASMEMS10)*, Les Embiez, France, No. GM01, 2010.

Vittoriosi, A., Brandner, J.J., Dittmeyer, R., “Gas-wall interactions of rarefied gases in MEMS: a new experimental device with integrated sensors”, in *Proceedings of the 3rd Joint US-European Fluids Engineering Summer Meeting and 8th International Conference on Nanochannels, Microchannels and Minichannels (FEDSM-ICNMM2010)*, Montréal, Canada. ASME (Publisher), No. 30488, 2010.

Brandner, J.J., Anurjew, E., Hansjosten, E., Maikowske, S., Schygulla, U., Vittoriosi, A., “Microstructure devices for water evaporation”, in *Proceedings of the 3rd Joint US-European Fluids Engineering Summer Meeting and 8th International Conference on Nanochannels, Microchannels and Minichannels (FEDSM-ICNMM2010)*, Montréal, Canada. ASME (Publisher), No. 30700, 2010.

Vittoriosi, A., Brandner, J.J., Dittmeyer, R., “Experimental device for the characterization of the gas-wall interactions under slip-flow”, in *Proceedings of 2nd European Conference on Microfluidics ( $\mu$ Flu’10)*, Toulouse, France, S. Colin and G. L. Morini, Eds. SHF (Publisher), No. 23, 2010.

Vittoriosi, A., Brandner, J.J., Dittmeyer, R., “Integrated measuring system for gas flows in MEMS”, in *Proceedings of 3rd International GASMEMS Workshop (GASMEMS11)*, Bertinoro, Italy, No. 4, 2011.

Vittoriosi, A., Brandner, J.J., Dittmeyer, R., “Experimental design with integrated temperature sensors in MEMS: an example of application for rarefied gases”, in *Proceedings of 3rd Micro and Nanoflow Conference (MNF2011)*, Thessaloniki, Greece, No. 75, 2011.

Brandner, J.J., Maikowske, S., Vittoriosi, A., “A new microstructure device for efficient evaporation of liquids”, in *Proceedings of 4th International Conference on Heat Transfer and Fluid Flow in Microscale (HTFFM-IV)*, Fukuoka, Japan, No. HTFFM-IV, 2011.

Vittoriosi, A., Brandner, J.J., Dittmeyer, R., “Integrated temperature micro sensors for the characterization of gas heat transfer”, in *Proceedings of 1st European Conference on Gas MicroFlows (GASMEMS2012)*, vol. 362, Skiathos, Greece, pp. 012021, 2012.

Vittoriosi, A., Brandner, J.J., Ruther, P., Paul, O., Dittmeyer, R., “Design and characterization of integrated microsensors for heat transfer studies in microchannels”, in *Proceedings of the 3rd European Conference on Microfluidics ( $\mu$ Flu’12)*, Heidelberg, Germany, submitted full length paper.

### International Conferences - Talks

Vittoriosi, A., Brandner, J.J., Dittmeyer, R., “Integrated measuring system for the thermal characterization of gas flows in MEMS under slip-flow regime”, presented at *64th IUVSTA Workshop on Practical Applications and Methods of Gas Dynamics for Vacuum Science and Technology*, Leinsweiler, Germany, May 16-19, 2011.

Maikowske, S., Vittoriosi, A., Brandner, J.J., “Microstructure evaporators: design, properties and application example”, presented at *5th International Topical Team Workshop on Two-Phase Systems for Ground and Space Applications*, Kyoto, Japan, 2010.

Brandner, J.J., Vittoriosi, A., Yang, Y., Morini, G. L., “Microstructure devices for heat transfer studies in gas flows”, presented at *28th International Symposium on Rarefied Gas Dynamics (RGD28)*, Zaragoza, Spain, July 9-13, 2012.

Brandner (on behalf of the GASMEMS members), “The GASMEMS Network: Design and Manufacturing of MEMS and Experiments for Rarefied Gas Flows in Microscale”, invited paper at *28th International Symposium on Rarefied Gas Dynamics (RGD28)*, Zaragoza, Spain, July 9-13, 2012.



### International Conferences - Posters

Vittoriosi, A., Morini, G. L., Brandner, J.J., “Characterization of microstructured evaporators with optical measurements”, presented at *11th International Conference on Microreaction Technology (IMRET11)*, Kyoto, Japan, March 8-10, 2010.

A. Vittoriosi, J.J. Brandner, R. Dittmeyer, “Integrated Sensors in MEMS: Characterization of Roughness Effects for Rarefied Gas Flows”, presented at *2nd International GASMEMS Workshop (GASMEMS10)*, Les Embiez, France, July 9-10, 2010.

A. Vittoriosi, J.J. Brandner, R. Dittmeyer, “Integrated Measuring System for Gas Flows in MEMS”, presented at *3rd International GASMEMS Workshop (GASMEMS11)*, Bertinoro, Italy, June 9-11, 2011

### National Conferences - Posters

Vittoriosi, A., Ruther, P., Brandner, J.J., “Internal measurements in micro channels”, presented at *VIM Workshop for the NanoMikro Program of KIT*, Karlsruhe, Germany, 2009.



**ALICE VITTORIOSI** (\* 29 September 1984)

**PRESENT ADDRESS**

Lachnerstr. 14  
76131 Karlsruhe, Germany  
alice.vittoriosi@kit.edu  
+49 176 85021724

**PERMANENT ADDRESS**

Loc. Patrignone, Via Pozzo Nuovo 34  
52100 Arezzo, Italy  
alivitto@gmail.com  
+39 328 7411044

**EDUCATION**

UNIVERSITY OF BOLOGNA, Faculty of Engineering, Italy

- Master of Science, Energy Engineering (March 2009)
- Bachelor of Science, Energy Engineering (October 2006)

**RESEARCH EXPERIENCE**

KARLSRUHE INSTITUTE OF TECHNOLOGY (KIT), Institute for Micro Process Engineering (IMVT), Germany

- PhD student (April 2009 - present)
- Master Thesis student (July 2008 - January 2009)

Worked in the group of Thermal Micro Processes Engineering. Testing of microstructured devices for heat transfer in single and two-phase flows. Fundamental research on the heat transfer of gases at microscale. Development and implementation of integrated microsensors.

UNIVERSITY OF TOULOUSE, National Institute of Applied Sciences (INSA), France

- Visiting PhD within the frame of a Marie-Curie Project secondment. (March 2011, September 2011)

Experimental and numerical studies for gas flows in microchannels.

TECHNICAL UNIVERSITY OF DRESDEN, Institute for Process and Environmental Engineering, Germany

- Visiting PhD within the frame of a Marie-Curie Project secondment. (September 2010)

Development of a data acquisition routine under LabView.

**FELLOWSHIPS AND AWARDS**

Marie-Curie fellow in the frame of the EU-Project GASMEMS as Early Stage Researcher, (April 2009 - March 2012)

Award "Le Migliori Laureate 2009" (best female graduated student in engineering faculties), Bologna (May 2009)

2009 Master Thesis Award "Claudio Pisoni" from the Italian Union of Thermal-Fluid Dynamics (UIT), Brescia (June 2009)

2009 Master Thesis Award "Piergiorgio Berardi" from the faculty of Mechanical Engineering, Salerno (November 2009)